

# **The Development of Glass Compositions for the Vitrification of Ion Exchange Resin Wastes from the Nuclear Industry**

**Owen J. McGann**

A Thesis submitted to the Department of Materials Science and Engineering at the University of Sheffield in partial fulfilment of the requirement for the Degree of Doctor of Philosophy.

**30<sup>th</sup> September 2013**



## **Acknowledgements**

Firstly, I would like to acknowledge the vast amount of support, advice and guidance which I have received from each of my supervisors, Prof. Neil Hyatt and Dr. Paul Bingham, over the course of my PhD. Without their guidance during the early stages of my work and their feedback later on in my studies I could not have produced the work contained within this thesis. I must thank Neil in particular for his great patience and perseverance in directing my work throughout my PhD and in recent months for helping me to shape this thesis and in proof-reading its many revisions. I would like to thank Paul for teaching me a great deal and giving me some excellent opportunities for experience. I would also like to thank him for introducing me to many members of the wider glass research community.

In addition I would like to acknowledge and thank all of the people who helped with the experimental work which was conducted during the course of my PhD. Specifically I would like to thank Mr. Ian Watts, Mr. Dean Haylock and Dr. Lisa Hollands for their assistance in the countless glass melts. The experience and knowledge that they have imparted to me, and their capacity for (and resistance to) vague personal abuse certainly should not go without mention. I would also like to thank Ms. Bev Lane, Mr. Ben Palmer and Mr. Philip Staton for all of the help and training which they provided. Also, I would like to specially thank Dr. Sue Forder of Sheffield Hallam University for making available her institution's Mossbauer spectrometer, and for all of her help and advice.

I also cannot fail to acknowledge the vast amount of help and support that I have received from my family, and in particular from my wife Elspeth, over the course of my PhD. Her loving encouragement and support throughout the course of my PhD has been key to its accomplishment, especially when the work has been stressful and when things haven't been going to plan.

Finally, I must acknowledge the provision that I have received from the Lord God in all that has been achieved throughout the course of my studies. Nothing that is presented in this thesis, and indeed none of the work which I have conducted throughout my studies, could have been achieved without the gracious provision of the Father and indeed I attribute all of the support which I have received to his love and grace. I therefore submit all that I have accomplished before the Lord and acknowledge that all has been achieved through his gracious provision and ultimately for the glory of the Father, the Son and the Holy Spirit.

## Abstract

Ion exchange resin (IEX) wastes from the nuclear power generation are a growing problem faced by the nuclear industry both in the UK and abroad. Vitrification of these wastes offers a route for their disposal by which these wastes can be immobilised in a durable waste-form. However, vitrification of these wastes possessed three major problems due to the anionic content of the waste, the organic content of the waste and the volatile radionuclides present in the waste which are problematic for vitrification.

In order to identify routes by which these wastes may be successfully vitrified, systematic development experiments were carried out on three glass systems, an alkali borosilicate glass system, an alkali alkaline-earth glass system and a calcium silicate glass system. These development experiments identified a number of novel glass compositions which possessed improved properties in terms of reduced melting temperatures, increased capacities for sulphur species, increased capacities for reduction, amongst other improvements to physical properties. These improvements were attributed to changes to the glass forming network due to additive species.

Glass compositions were waste-loaded with simulant IEX waste. ZnO containing alkali alkaline-earth silicate glass waste-forms demonstrated high levels of sulphur retention and near total caesium retention. These results were attributed to the physical properties of the novel glass compositions. Developed waste-forms were demonstrated to possess superior aqueous durability and radiation stability due to low alkali content and the presence of Fe in their composition. A mechanism was identified by which Fe acted to prevent the accumulation of  $\gamma$ -radiation induced defects in the waste-forms.

ZnO-containing alkali alkaline-earth silicate glass compositions were shown to have a low melting temperature, high density, increased capacity for anionic species and the ability to achieve high Cs retentions.

## Contents

Chapter 1 - Introduction .....	8
Chapter 2 - Literature Review: A review of the Vitrification of Ion-Exchange Resin Wastes from the Nuclear Fuel Cycle in the UK and Abroad.....	12
2.1. Overview of Ion-Exchange (IEX) resin Waste.....	12
2.1.1 Sources of IEX Resin Waste .....	12
2.1.2 Composition of typical IEX resin wastes.....	13
2.1.3 Disposal of IEX resin wastes.....	14
2.2 IEX Resin Vitrification .....	16
2.3 Problems Surrounding IEX Resin Vitrification .....	17
2.4 Approaches to mitigate for the problems associated with IEX resin vitrification .....	20
2.4.1 Resin Pre-treatment.....	20
2.4.2 Glass Composition Variation.....	23
2.4.3 Modifications to the Vitrification Process .....	27
2.4.4 Comparison of pre-treatment, process modification and composition modification options. .....	28
2.5 Summary .....	29
Chapter 3.1 - Systematic Development of an Alkali Alkaline-Earth Silicate Glass for the purpose of Cs-loaded Ion Exchange Resin Vitrification.....	31
3.1.1 Experimental Procedures.....	32
3.1.1.1 Sample Preparation.....	32
3.1.1.2 Characterisation Techniques.....	32
3.1.2 Results .....	36
3.1.2.1 Variation in ratio of component Alkaline-Earth species (BaO and CaO).....	36
3.1.2.2 Replacement of CaO with divalent oxides .....	41
3.1.2.3 Variation in content of alkali species (Na <sub>2</sub> O and Li <sub>2</sub> O).....	45
3.1.2.4 Fe-free solid-state NMR series .....	50
3.1.3 Discussion.....	59
3.1.3.1 Variation of alkaline-earth component composition .....	59
3.1.3.2 Replacement of 4 mol% CaO with divalent oxides.....	61
3.1.3.3 Variation in the content of alkali species .....	64
3.1.4 Conclusions.....	65
Chapter 3.2 - Development of Hybrid Alkali Alkaline-Earth Silicate Glasses for the Purpose of Cs-Loaded Ion Exchange Resin Vitrification. ....	67

3.2.1 Experimental Procedures.....	68
3.2.2 Results .....	70
3.2.3 Discussion.....	75
3.2.4 Conclusion .....	77
Chapter 3.3 - Systematic Development of Alkali Borosilicate and Calcium Aluminosilicate Glass for the purpose of Cs-loaded Ion Exchange Resin Vitrification.....	79
3.3.1 Experimental Procedures.....	81
3.3.2 Results .....	82
3.3.2.1 Alkali Borosilicate Series - Variation in Na <sub>2</sub> O : Li <sub>2</sub> O ratio.....	82
3.3.2.2 Calcium Alumino-silicate glasses - Replacement of Al <sub>2</sub> O <sub>3</sub> .....	85
3.3.2.3 Calcium Alumino-Silicate glasses - Replacement of CaO.....	89
3.3.3 Discussion.....	93
3.3.3.1 Variation in alkali oxide component of Alkali Borosilicate glass.....	93
3.3.3.2 Replacement of Al <sub>2</sub> O <sub>3</sub> content of Calcium Aluminosilicate glass .....	95
3.3.3.3 Replacement of CaO content of Calcium Aluminosilicate glass .....	96
3.3.4 Conclusion .....	97
Chapter 4.1 - The Effect of Waste Loading Novel Glass Compositions Developed for the Vitrification of Cs loaded Ion Exchange Resin Wastes .....	100
4.1.1 Experimental Procedures.....	101
4.1.2 Results .....	103
4.1.2.1 Base Glass Waste-Loading and the Determination of Optimum Waste-Loading.....	103
4.1.2.2 Waste Loading of Developed Waste-Forms.....	112
4.1.3 Discussion.....	129
4.1.3.1 Initial Waste-loading Experiments .....	129
4.1.3.2 Effects of Waste-loading on Developed Host Glasses.....	131
4.1.4 Conclusion .....	145
Chapter 4.2 - Investigation of the Off-Gas Released from the Vitrification of Ion-Exchange Resin Wastes in Alkali Borosilicate and Alkali Alkaline-Earth Silicate Glass Compositions.....	147
4.2.1 Experimental Procedures.....	148
4.2.2 Results .....	150
4.2.3 Discussion.....	156
4.2.3.1 Implications for IEX Resin Vitrification.....	158
4.2.4 Conclusion .....	159
Chapter 5.1 - The effects of $\gamma$ -radiation on model vitreous wasteforms intended for the disposal of intermediate and high level radioactive wastes in the United Kingdom.* .....	161

5.1.1 Experimental Procedures.....	163
5.1.1.1 Mechanical Techniques.....	165
5.1.1.2 Spectroscopic Techniques .....	166
5.1.2 Results .....	168
5.1.2.1 Mechanical Techniques.....	168
5.1.2.2 Spectroscopic Techniques .....	172
5.1.3 Discussion.....	190
5.1.3.1 Mechanical property variation. ....	190
5.1.3.2 Glass structure variation as detected by Raman and FTIR spectroscopy.....	191
5.1.3.3 Fe analysis by optical absorption, EPR and Mössbauer spectroscopy.....	191
5.1.3.4 X-ray absorption and X-ray emission spectroscopy at the S K-edge. ....	194
5.1.4 Conclusion .....	195
Chapter 5.2 - Investigation of the Durability of Novel Glass Compositions Developed for the Purpose of Cs loaded Ion Exchange Resin Vitrification. ....	196
5.2.1 Experimental Procedures.....	197
5.2.1.1 Sample Preparation.....	197
5.2.1.2 Durability Experiments .....	198
5.2.2 Results .....	198
5.2.2.1 Alkali Alkaline-Earth Silicate glasses.....	198
5.2.2.2 Alkali Borosilicate Glasses.....	203
5.2.2.3. Calcium Silicate Glasses .....	207
5.2.2.4 Waste-loaded Glasses .....	210
5.2.3 Discussion.....	216
5.2.3.1 Alkali Alkaline-Earth Silicate System. ....	216
5.2.3.2 Alkali Borosilicate System.....	218
5.2.3.3 Calcium Silicate System.....	218
5.2.3.4 Waste-loaded Samples .....	219
5.2.3.5 Durability of Base and Development Glasses.....	221
5.2.4 Conclusion .....	223
Chapter 6. - Summary, Conclusion and Future Work.....	225
6.1 Summary .....	225
6.2 Conclusion.....	229
6.3 Recommendation for Future Work.....	231
7. References.....	233

<b>8. Appendix</b> .....	244
<b>8.1 Overview of Experimental Procedures</b> .....	244
8.1.1 Glass Batch Preparation.....	244
8.1.2 Glass Melting and Fabrication.....	244
8.1.3 Sample Preparation.....	245
8.1.4 Density Measurement.....	246
8.1.5 Liquidus Temperature Determination.....	246
8.1.6 Differential Thermal Analysis.....	247
8.1.7 Melt Viscosity Determination.....	247
8.1.8 X-ray Diffractometry.....	248
8.1.9 Scanning Electron Microscopy and Energy Dispersive X-ray Spectroscopy.....	249
8.1.10 Fourier Transform Infrared Spectroscopy.....	251
8.1.11 Raman Spectroscopy.....	253
8.1.12 Optical absorption spectroscopy.....	254
8.1.13 Mossbauer spectroscopy.....	255
8.1.14 Electron Paramagnetic Resonance spectroscopy.....	257
8.1.15 Solid State Nuclear Magnetic Resonance spectroscopy.....	258
8.1.16 X-ray Absorption Near Edge Spectroscopy.....	259
8.1.17 X-ray Emission Spectroscopy.....	261
8.1.18 Chemical Durability (PCT).....	262

## Chapter 1 - Introduction

Ion exchange (IEX) resin wastes are a growing concern for the nuclear industry both in the UK and in other nations who use nuclear energy for power generation. Over the past 20 years, IEX resin wastes have been generated by the nuclear industry through the process of treating aqueous waste-streams containing water soluble radionuclides such as  $^{137}\text{Cs}$ ,  $^{60}\text{Co}$ , and  $^{99}\text{Tc}$ . Even though the organic ion-exchange resins used for this process are highly effective in removing these radionuclides from solution, they are themselves problematic to immobilise or safely store. As a result a large, and growing, inventory of this type of waste now exists globally which requires a route for disposal.

A range of disposal routes for IEX resin has been considered. However, of the options explored, the vitrification of these wastes, that is, the incorporation of the waste material into a vitreous waste-form with the addition of a suitable host glass, has been shown to possess a number of benefits over other immobilisation techniques which had been previously explored. These include the capacity of vitrification to reduce the volume of waste requiring subsequent storage and the relatively high durability of the waste-forms produced. However, it has been shown by the work of Herman *et al*<sup>(1)</sup>, and Hutson *et al*<sup>(2)</sup> that the vitrification of these IEX resin wastes is complicated by three factors. These are the presence of anionic species from the resin which are insoluble in silicate glasses, the presence of organic material which are reducing to the oxide content of silicate glasses, and the volatility of radionuclides present in IEX resin wastes, such as  $^{137}\text{Cs}$ , at high temperatures.

A range of solutions to these problems has been explored. However at present no definitive solution exists to these issues. Approaches which have been explored include the pre-treatment of the resin waste to eliminate the problematic anionic and organic portion of the material, the modification of the melter technology in order to practically eliminate the cold-cap and salt gall layer produced during IEX resin vitrification, and the development of new glass compositions with improved capacities for anionic and organic species and improved physical properties allowing increased retention of volatile radionuclides.

This thesis adds to the body of knowledge which exists with regards to the third of these routes, that is, the development of glass compositions possessing improved capacities for anionic species, reduction by organics and retention of volatile species. These are addressed in three chapters, which cover the development of novel glass compositions from three initial glass systems, the waste-loading and lab-scale vitrification

of simulant ion exchange resin wastes with the use of these developed glasses, and finally, an analysis of the radiation stability and durability of the resultant waste-forms.

In terms of structure, the three thesis chapters are further subdivided into seven sections, with a self-contained description of experimental methods, results, a discussion of results, and conclusions as pertinent to the subject of the particular section. Preceding these three sections is a literature review (Chapter 2) which discusses past work and developments with regards to the immobilization of ion exchange resin wastes, and more specifically, the vitrification of these wastes. The details of these three results sections in this thesis are as follows:-

Chapter 3, comprising three sections, addresses the systematic compositional development of three glass systems with the aim of producing glass compositions with modified chemical and physical properties which improve their capacity for the vitrification of ion exchange resin wastes.

The first of these three sections, 'Systematic Development of an Alkali Alkaline-Earth Silicate Glass for the purpose of Cs loaded Ion Exchange Resin Vitrification' on the development of an Alkali Alkaline-Earth Silicate glass system which has previously been investigated by Bingham *et al*<sup>(3)</sup> and Kaushik *et al*<sup>(4)</sup> for its superior properties in terms of durability and anion retention. Optimised compositions were identified and described which yielded improved physical properties such as reduced melting temperature, increased densities and improved capacity for reduction. Specifically, compositions containing increased proportion of BaO and ZnO were highlighted and the improved physical properties were linked to changes to the bonding of glass forming network, the coordination of networking cations and the effect of Zn<sup>2+</sup> cations as intermediate network modifiers.

The second section, 'Development of Hybrid Alkali Alkaline-Earth Silicate Glasses for the Purpose of Cs-Loaded Ion Exchange Resin Vitrification' investigated further compositional development of the alkali alkaline-earth silicate glass system, specifically with regards to glasses developed in the initial compositional development of the glass system. The replacement of CaO with ZnO and the replacement of CaO with BaO, both of which resulted in reductions to the melting temperature of the glass, and increases in the density of the glass, were determined to be supported by separate mechanisms. This section describes the glass composition derived from the addition of both ZnO and BaO to the initial glass system. The resulting 'hybrid' glass composition was found to demonstrate a large decrease in the melting temperature of the system and further increases

in glass density, whilst retaining the other beneficial properties of the system. A second glass composition, containing a reduced alkali content, was also described.

The third section, 'Systematic Development of Alkali Borosilicate and Calcium Aluminosilicate Glass Systems for the purpose of Cs loaded Ion Exchange Resin Vitrification' addresses the systematic compositional development of an alkali borosilicate glass system, derived from the MW type glass composition, and a calcium silicate glass system based upon the work of Schofield *et al* <sup>(5)</sup>. These glasses were selected for their melting properties and capacity for anionic species respectively. The glasses were developed through a number of series, modifying the ratio of alkali species present in the alkali borosilicate system and replacing the RO and R<sub>2</sub>O<sub>3</sub> components of the calcium silicate system. It was found that the replacement of Al<sub>2</sub>O<sub>3</sub> with Fe<sub>2</sub>O<sub>3</sub> in the calcium silicate glass system yielded a composition with improved melting properties.

Chapter 4, comprising two sections, investigates the waste-loading of a selection of these developed glass compositions in terms of the physical effects of waste-loading, the retention of radioactive species and also the emission of these species through off-gases during the vitrification process. The first section, 'The Effect of Waste Loading Novel Glass Compositions Developed for the Vitrification of Cs loaded Ion Exchange Resin Wastes' investigated the waste-loading of the three base glass compositions and five developed glass compositions produced by the systematic development work described in the first section of the thesis. Waste-loading experiments demonstrated the formation of a phase-separated salt phase, consistent with previous reports, in several waste-loaded alkali alkaline-earth silicate and alkali borosilicate glass compositions. ZnO-containing alkali alkaline-earth silicate glasses demonstrated higher degrees of retention for both calcium and sulphur species.

The second section in Chapter 4, 'Investigation of the Off-Gas Released from the Vitrification of Ion-Exchange Resin Wastes in Alkali Borosilicate and Alkali Alkaline-Earth Silicate Glass Compositions' investigates the nature and quantity of species lost through off-gases during the vitrification. An alkali borosilicate and alkali alkaline-earth silicate glass composition were investigated through the use of an off-gas capturing system which allowed the collection of soluble species from the off-gases for later analysis via ICP-MS. The experiment demonstrated both the impact of the physical properties of the glass upon the loss of sulphur and caesium species during vitrification and gave information on the mechanism by which sulphur species are lost during vitrification. The experiments also demonstrated that there is no connection between the volatilisation of sulphur species and the volatilization of caesium, which was found only to occur at temperatures in excess of 1000 °C.

Chapter 5 comprises two sections and examines the developed glasses and waste-forms derived from them in terms of aqueous durability and radiation stability. The first section in Chapter 5, 'The Effects of  $\gamma$ -radiation on Model Vitreous Waste-forms Intended for the Disposal of Intermediate and High-Level Radioactive Wastes in the United Kingdom' investigated the effect of significant  $\gamma$ -radiation doses upon four waste-loaded vitreous waste-forms. The waste-forms investigated were based upon developed alkali borosilicate and alkali alkaline-earth silicate compositions and also included a sample of simulated HLW loaded MW type glass. The aim of this work was to explore the effect of  $\gamma$ -radiation, such as would be emitted from an immobilized waste, upon the structural, physical and chemical properties of the waste-forms. It was determined that in all four of the waste-forms investigated  $\gamma$ -radiation induced defects did not occur, as opposed to observations made on the control unloaded alkali borosilicate glass. These defects were prevented from forming due to the presence of Fe in the waste-forms investigated. A mechanism, first reported by Debnath *et al* <sup>(6)</sup> in glasses irradiated by  $\beta$ -radiation, was identified by which the Fe content of the samples removed the electronic defects generated by  $\gamma$  radiation by changing oxidation state. To the knowledge of the author, this is the first instance that this mechanism has been reported in relation to  $\gamma$ -irradiation. This work was published in the Journal of Nuclear Materials\*.

The second section in Chapter 5, 'Investigation of the Durability of Novel Glass Compositions Developed for the Purpose of Cs loaded Ion Exchange Resin Vitrification' addresses the aqueous durability of the developed glasses and of four waste-forms derived from developed glass compositions. The aqueous durability of these glasses and waste-forms were explored through a series of 28-day PCT B experiments, allowing the normalised mass loss of various species to be determined. It was determined that the alkali alkaline-earth glasses and calcium silicate glasses presented lower overall values of normalised mass loss over the course of the 28 day experiment than the alkali borosilicate composition explored. This was primarily attributed to the effect of the low proportion and/or absence of alkali species in the composition of the alkali alkaline earth borosilicate and calcium silicate glasses respectively.

Finally, a summary of conclusions from these sections is presented and suggestions for future work are made.

---

\* O. J. McGann, P. A. Bingham, R. J. Hand, A. S. Gandy, M. Kavcic, M. Zitnik, K. Bucar, R. Edge and N. C. Hyatt, "The effects of  $\gamma$ -radiation on model vitreous waste-forms intended for the disposal on intermediate and high level wastes in the United Kingdom," *J. Nuc. Mater.*, 429 353-367 (2012).

## **Chapter 2 - Literature Review: A review of the Vitrification of Ion-Exchange Resin Wastes from the Nuclear Fuel Cycle in the UK and Abroad.**

Over the past 57 years, nuclear power has been utilised in the UK for the generation of electricity for civil use. As a by-product of the generation of nuclear energy, a large and varied inventory of radioactive waste materials has been produced which require treatment and immobilisation prior to disposal or storage in a repository. A particularly problematic form of waste is ion-exchange resins contaminated with radionuclides. The resin wastes, produced through the treatment of aqueous waste streams contaminated with water soluble radionuclides, are a growing inventory in the UK and globally, with as much as 4000 m<sup>3</sup> being produced each year <sup>(7)</sup>, and present a significant challenge since there is currently no satisfactory method by which the radionuclide inventory of these wastes can be immobilised <sup>(1,2,8)</sup>.

This review presents an overview of the methods which have been explored for the safe immobilisation of waste radioactive ion-exchange resins. The focus of the review is the application of vitrification processes in the immobilisation of ion exchange resin wastes, the problems that are typically encountered in application of this conditioning technology, and describes the various routes by which these problems may be overcome.

### **2.1. Overview of Ion-Exchange (IEX) resin Waste.**

#### **2.1.1 Sources of IEX Resin Waste**

Currently IEX resins are used for two primary purposes in the nuclear industry. The first is the selective removal of uranium from leaching solutions, as discussed in detail in the work of Kunin *et al* and Eccles *et al* <sup>(9,10)</sup>. The second use is for the removal of waste radioactive and toxic ions from aqueous solutions comprising processing effluent from waste storage ponds and coolant water or from effluents produced during fuel reprocessing <sup>(1,9)</sup>.

Large quantities of resin waste are produced globally due to the prevalence of water based reactor technology, in which water is used as a coolant and is therefore exposed to radioactive materials <sup>(1)</sup>. In addition to this, IEX resins are also used in the treatment of

legacy waste sludge, so producing further quantities of IEX resin waste <sup>(2)</sup>. Relatively little information is published on the overall quantities of contaminated IEX resin being produced on a yearly basis. However, the following examples provide some insight into the volumes involved. In the US, it has been reported that 45 tons of resin waste, rich in iron oxide, is being produced by BWR type reactors each year and similarly 136 tons of resin waste is produced by PWR type reactors <sup>(1,11)</sup>. In Argentina, power stations produce 12.3 m<sup>3</sup> of resin waste each year, and have now accumulated more than 178 m<sup>3</sup> of material for disposal <sup>(2)</sup>. It has been estimated that a 1000 MW PWR type reactor will produce 40m<sup>3</sup> waste IEX resin each year <sup>(7)</sup>, and due to the prevalence of these designs it has been estimated the global product of IEX resin wastes may be as high as 4000 m<sup>3</sup> per year <sup>(12)</sup>. In the UK, despite the prevalence of the Magnox and AGR reactor designs over either PWR or BWR designs, a large inventory of IEX resin type wastes also exists, arising from the treatment of effluent and waste waters sourced from power stations where the storage of fuel elements in ponds has resulted in water becoming contaminated by fission products <sup>(13)</sup>.

In the treatment of radionuclide-contaminated liquid waste streams, the IEX resin is utilised to adsorb and remove soluble radioactive species from waste waters, effectively removing the majority of the contaminating species <sup>(1,11,14,15)</sup>. In so doing, IEX resins allow more costly processes for the removal of soluble radioactive species, such as the use of chelating agents as described by Doherty *et al* <sup>(16)</sup>, to be avoided, providing significant gains in terms of cost and implementation <sup>(17)</sup>. As such, these IEX resins can be used to treat large volumes of solution or sludge, only limited by the capacity of the resin material for the adsorption of the radioactive species. Once the resin material has become saturated it must either be regenerated or replaced <sup>(1)</sup>. Typically, resin is not regenerated but is stored for disposal since regeneration of the resin materials is not cost effective in comparison to replacing the resins <sup>(1)</sup>. This process produces an inventory of radionuclide-loaded IEX resin which requires immobilisation and disposal.

### 2.1.2 Composition of typical IEX resin wastes

The IEX resins used for the purpose of radionuclide removal are typically a copolymer, such as a copolymer of styrene and divinyl-benzene, which possess either sulphonate groups or other strongly acidic species which provide functional sites for waste ions to interact with <sup>(7,15,18)</sup>. These resins may be tailored through modifying the functional groups coordinated to the copolymer to be selective for specific species. As a result of this, and due to the diversity of manufacturers involved in the production of IEX resin for various purposes, a wide range

of different IEX resins is commercially available. This is clearly demonstrated in the report of Baumgarten *et al* <sup>(15)</sup>, in which a wide range of different types of IEX resin was investigated for use by the US DOE. As a consequence of this, the inventory of IEX resin wastes is highly varied in terms of resin composition, albeit with similarities in terms of the proportion of organic material present and the acidic nature of the resins. As examples, Figures 2.1 and 2.2 show images of the Lewatit and Duolite IEX resins which are both used in aqueous waste-stream purification in the UK.

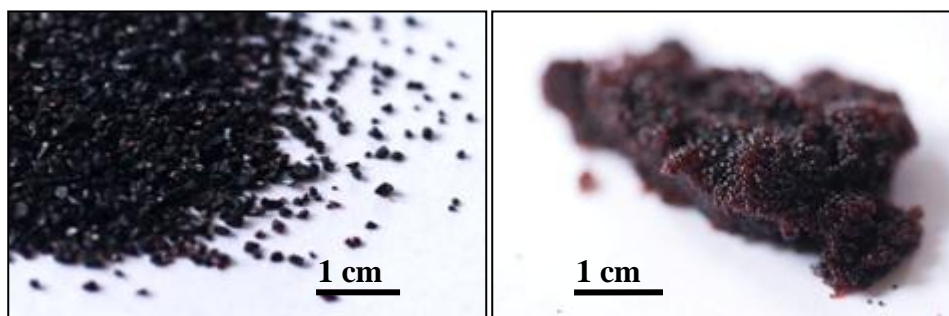


**Figure 2.1 & 2.2** - Duolite and Lewatit commercial IEX resins respectively.

It is also necessary to consider the waste radionuclides that are present in these wastes. Typically IEX resin wastes are loaded with a range of water soluble radionuclides including direct fission products which may range widely in terms of half-life and activity. As described by Sargent *et al* <sup>(17)</sup>, the most significant radionuclide present in these wastes in terms of both the proportion of the radionuclide and its overall activity is <sup>137</sup>Cs, although significant proportions of the isotopes <sup>90</sup>Sr, <sup>60</sup>Co, <sup>14</sup>C, <sup>99</sup>Tc and <sup>3</sup>H are also present in IEX resin wastes and may also have a significant impact upon their radioactive properties. Due to the prevalence of <sup>137</sup>Cs in most IEX resin wastes it is the most commonly addressed radionuclide in publications relating to IEX resin waste immobilisation <sup>(7,17,19,20)</sup>.

### 2.1.3 Disposal of IEX resin wastes

At present, there is no route for the disposal of radionuclide loaded ion-exchange resins <sup>(1,2,8)</sup>, and so the current practice in the UK and globally is to place these wastes into interim storage. In the UK, this storage is planned to take the form of the “ILW Mini-Store” units.

However as with other forms of storage available these do not represent an acceptable long-term solution, and do not represent an acceptable form of final disposal in line with the multi-barrier approach required by the generic disposal system safety case (DSSC) for nuclear waste storage in the UK. The DSSC specifies that nuclear waste material should be immobilised in order to add an additional passive barrier against the release of radioactive species. An additional issue associated with the storage of these wastes is the generation of reactive gas by IEX resin material in storage. A study undertaken in 1997 concluded that because of radiolysis, reactive gases were produced which meant that storage of these resins could present a fire hazard <sup>(2)</sup>. This effect could be mitigated by some forms of immobilisation, further underlining the need for the immobilisation of these wastes and the relative adequacy of interim or long-term storage for these wastes <sup>(18)</sup>.

Vitrification of IEX resins is problematic due to the incompatibility of the sulphur and chlorine content with silicate glass compositions and the significant organic content of the resin which imposes strongly reducing melt conditions <sup>(11)</sup>. The radionuclides themselves present problems for long-term storage due to their radioactivity which has been shown by various authors <sup>(1,2,14,17,18)</sup> to produce radiation-induced hydrolysis, changes in volume and mechanical failure. In addition to this, in the case of <sup>137</sup>Cs, further problems are presented due to the volatility of the element at high temperatures <sup>(19)</sup>. A wide variety of approaches for immobilising the IEX resin wastes have been explored <sup>(20-22)</sup>. However, of these approaches, cementation and vitrification are currently seen as the most suitable for IEX resin immobilisation.

The incorporation of waste materials into cement has been used as a form of radioactive waste immobilisation since the mid 1960s, and has a significant appeal on the basis of its low cost, relative ease of processing and the good mechanical, chemical and physical properties of the final waste-form <sup>(23-24)</sup>. In the context of IEX immobilisation, cementation is advantageous due to its simplicity, in that the resin is mixed with the cement which sets through interaction with the waste water present with the ion exchange resin material. However, despite the advantages offered by the relative ease and cost efficiency of cementation there are significant problems with the approach. Firstly, the process of cementation increases the overall volume of material which needs to be placed into a repository, which represents a significant expense. In addition, the alkaline nature of cement and the acidic nature of the ion exchange resin leads to detrimental interactions between the resin and the cement binder, where the strongly acidic resin reacts with the primary constituent of the cement, CaCO<sub>3</sub>. This reaction can lead to the breakdown of the cement binder over time and the failure of the waste-form, in some case in a time scale as short as few

weeks <sup>(25)</sup>. As a consequence, the waste-loading of these cementitious waste-forms are typically limited to between 10-15 wt%, which further exacerbates the problems associated with the increased volume of the waste-form. A body of research has been carried out by various groups <sup>(26)</sup> with the aim of circumventing the interaction between the cement grout and the resin, such as non-standard cement formulations and the pre-treatment of the resin <sup>(23-24)</sup>. Further information on the immobilisation of IEX resin in cement can be found in the review paper of Li *et al* <sup>(23)</sup>.

## 2.2 IEX Resin Vitrification

Vitrification has become the internationally recognised standard for minimizing the impact of nuclear waste on the environment and reducing waste volumes for conditioned waste <sup>(27)</sup>. Vitreous waste-forms are produced through the mixing of a waste material with a molten host glass, producing a waste-form <sup>(28)</sup>. In France, vitrification has now been used since 1977 <sup>(21)</sup>. More than 11,000 canisters of vitreous glass waste-forms have now been produced <sup>(27)</sup>. Vitrification technology is now used around the world, and in the United States the EPA (Environmental Protection Agency) have declared that vitrification was the ‘best demonstrable available technology’ (BDAT) for the immobilisation of radioactive waste <sup>(11,17,29)</sup>.

Vitreous waste-forms are generally thought to produce more stable waste-forms than cement <sup>(30)</sup> due to the chemical integration of waste into the glass matrix, and their relatively homogenous nature <sup>(43)</sup>. Waste elements are incorporated into the glass through the formation of chemical bonds between the waste species and the glass forming network, which directly incorporates the waste species into the glass waste-form <sup>(29)</sup>. Furthermore, glasses are tolerant to variation in compositions <sup>(11)</sup>, require relatively low temperatures for synthesis, possess a reasonable degree of chemical durability, are largely radiation resistant by virtue of their amorphous structure. They are also flexible enough to accommodate radiation-induced structural changes <sup>(28)</sup>. The use of vitrification also has a number of benefits on an industrial scale. Many wastes do not require pre-treatment in order for them to be integrated into a vitreous waste-form <sup>(11)</sup> and the melter technology required for vitrification is widely available and relatively inexpensive, with newer designs such as the cold-crucible melter possessing some resistance to corrosive phases that maybe generated during the vitrification process <sup>(11)</sup>.

The vitrification of IEX resins has a number of major advantages over the other options that have been considered for the immobilisation and disposal of these resins. The foremost of these is that vitrification reduces the volume of the IEX resin by a significant fraction, through organic destruction, moisture evaporation and reduction in porosity<sup>(1)</sup>. This sets it apart from other methods available that increase the volume of material requiring disposal, such as cementation.<sup>(1,22)</sup> Alongside this benefit, vitreous waste-forms possess superior long-term durability and are less vulnerable to radiation, chemical and mechanical damage than other waste-forms which have been considered<sup>(1,22)</sup>.

### 2.3 Problems Surrounding IEX Resin Vitrification

Despite the advantages possessed by vitrification in general there are a number of problematic problems associated with the vitrification of IEX resin materials. Specially these relate to the high concentrations of organic material, anionic species and radionuclides present in IEX resin wastes<sup>(1,29)</sup>. The waste loadings that can be achieved are highly dependent upon the type and composition of the IEX resin which is being vitrified<sup>(1-2)</sup>.

One of the most comprehensive studies undertaken on the vitrification of IEX resins was performed by Hutson *et al*, in a study looking at the vitrification of IEX resin from two Argentine nuclear power stations<sup>(29)</sup>. They utilised technology developed by the US DOE (Department of Energy) for waste vitrification to vitrify resin waste in a iron doped borosilicate host glass<sup>(2,29)</sup>. In their studies, performed in a lab environment, vitreous waste-forms were produced with 30 wt% loadings, and an overall reduction in waste volume of 65%<sup>(11)</sup>. These lab-scale glasses were seen to be both homogenous and durable<sup>(2)</sup>, however, when the technology was scaled up to an industrial scale, melt crystallisation was observed in the final product, due to interactions between the glass and the simulant waste, and a significant quantity of off-gases were recorded<sup>(2,29)</sup>. However, a 70% volume reduction was recorded for the IEX resin and the retention rates for the radio-isotope surrogates were near 100%<sup>(29)</sup>. This study showed that IEX resins may be effectively treated and immobilised via vitrification technology<sup>(29)</sup>.

Further work by Herman *et al* determined that waste loadings from 38 – 70 grams of resin per 100 grams of glass could be achieved<sup>(2)</sup>, but that these were dependent upon the chemistry of the resin<sup>(1)</sup>. The sulphonated styrene resins were found to have the greatest waste loading limitations due to the sulphate content<sup>(1)</sup>. Sulphate has a very low solubility in silicate glass, and is limited to about 1 wt% loading<sup>(22)</sup>, and, in general, a loading that

exceeds 3-5 wt% has been shown to result in phase separation occurring during the glass melt <sup>(22,31)</sup>, though the exact figure varies depending on oxidation state <sup>(32)</sup>. Phase separation leads to the formation of a 'yellow phase' of sulphate salts on top of the glass <sup>(33)</sup>. This is soluble in water, and can contain dissolved radionuclides <sup>(22)</sup>, and is known to increase the volatility of species such as caesium by between 5 and 10 fold <sup>(33)</sup>. Waste loadings limited to 3-5 wt% would lead to excessive amounts of vitrified low activity waste being produced <sup>(32)</sup>. The formation of the salt phase during melting is a major problem, since it adversely effects the melter. The salt layer increases corrosion of the melter, and because the salt layer is conductive the layer can cause a short circuit to occur in joule heated melters <sup>(30-31)</sup>. Off-gases from sulphur and chloride-bearing wastes are also often corrosive due to the effect of pyrohydrolysis, and so the off-gas system needs to be acid resistant <sup>(11)</sup>. In experiments, sulphate dust was seen to be formed from the melt and escape into the environment <sup>(34)</sup>.

It is known that over time, the salt layer will volatilise as it is removed from the glass by a process of salt dissociation. Initially a small quantity of sulphate is incorporated into the glass, and the rest forms a secondary salt phase. This salt phase will float on the surface of the glass melt, held by the surface tension of the sulphate salt. Over time, sulphate species were reported to diffuse slowly to the depleted region at the surface of the glass resulting in the emission of SO<sub>3</sub> gas <sup>(32)</sup>.

The organic content of the resins was also found to be problematic due to their reductive effect on the oxide constituent of the glass <sup>(17)</sup>. Reduction in the glass melt is generally undesirable, as it risks the reduction of metal oxides to the native metal which may cause corrosion of the melter at industrial scale, potentially damaging off-gas systems and electrodes <sup>(11)</sup>. Furthermore, it has also been shown that reduced glasses possess inferior durability compared to oxide counterparts <sup>(1,19)</sup>.

The study of Herman et. al. <sup>(1)</sup>, in which the vitrification of caesium-contaminated sulphonated IEX resin in borosilicate glass compositions were explored, it was determined that despite a higher extent of reduction being achieved due to the organic content of the resin, the durability of the final waste-form was found to be satisfactory <sup>(1)</sup>. In some melts, inhomogeneous pellets were found within the glass which were not durable and could be extracted from the glass. The pellets were found to be metal sulphides, which formed when the glass became too reduced <sup>(1,11)</sup>. This is an excellent example of the consequence of reduction in a waste glass. As a consequence of this study, IEX resin vitrification at the Savannah River site was limited to only 5 g of waste per 100 g of glass in order to avoid the

reduction of metals from the melt <sup>(19)</sup>, and due to the requirement to avoid the formation sulphur salts that can corrode the melter <sup>(19)</sup>.

In the same study, Herman *et al* <sup>(1)</sup> also identified problems associated with the volatility of caesium radionuclides in that the study demonstrated a retention rate for the caesium simulant ranging from 73 – 84 wt% <sup>(1,2)</sup>. This indicated that the loss of caesium due to volatilisation was a significant issue, and that off-gas collection would be necessary for the full scale vitrification of these wastes in order to prevent the loss of radionuclides into the environment <sup>(1)</sup>.

A review paper produced by Herman *et al* summarised the problems associated with the vitrification of IEX resins <sup>(11)</sup>;

1. The organic content of the resin causes the glass to be reduced leading to impaired durability.
2. Low density resin material forms a 'cold cap' on the top of the glass melt impairing the mixing of the waste with the glass phase.
3. The volatility of radio-caesium at high temperatures leads to difficulties in retaining all radioactive species from the resin.
4. The emission of toxic and environmentally harmful off-gas, such as SO<sub>x</sub>, NO<sub>x</sub> and CO<sub>2</sub>
5. Anionic species from the resin are not sufficiently soluble in glass compositions typically used for waste vitrification. This can lead the formation of a phase separated salt phase.
6. The reduced nature of the melt and the presence of phase separated material can lead to corrosion of the melting vessel.
7. Tritium present in the waste is not readily retained during vitrification.

This comprehensive list includes a variety of problems with differing degrees of importance. A number of these described by Herman *et. al.* can be addressed through modification to the vitrification process and technology, such as the problems associated with the cold cap and melter corrosion. However, the list also highlights more fundamental issues

posed by the vitrification of IEX resin wastes which are independent of the technology used in the vitrification process. These issues can be summarised as:-

1. The volatility of the  $^{137}\text{Cs}$  radionuclide and other radionuclides present in the waste, which may be lost during vitrification due to the high temperatures involved.
2. The reducing action of the organic content upon the oxide glass melt, which can lead to a final waste-form with impaired durability, the increased corrosion of the melter, and to the phase separation of some metallic species.
3. The insolubility of the anionic species in the glass, which leads to the formation of a separated salt phase which has the potential to exacerbate problems such as a radio-caesium loss, melter corrosion and the volatilisation of dangerous off-gas species such as  $\text{SO}_x$ .

Each of these problems relates to the interaction of the ion exchange resin with the oxide glass, and as such can only be solved either through the modification of the chemistry of the resin through pre-treatment or through the modification of the glass chemistry.

## **2.4 Approaches to mitigate for the problems associated with IEX resin vitrification**

A range of approaches has been explored to find a viable route which allows the vitrification of IEX resins which is not significantly affected by the problems discussed above. For vitrification these approaches tend to fall into two groups, either attempting to modify the properties of the IEX resin itself before vitrification through some means of pre-treatment, or changing the composition of the glass used in vitrification in order to reduce the problematic effects encountered from the anionic and organic species present in the IEX resin.

### **2.4.1 Resin Pre-treatment**

Some form of pre-treatment has been applied in almost all previous investigations into IEX resin vitrification, typically with the aim of converting the initial waste stream into a form which is more suitable for vitrification. This can cover a wide range of possible processes, from the simple de-watering of the IEX resin material through low temperature heating

(3,12,35), to forms of pre-treatment which completely breakdown the IEX resin material (1,7, 22,37). These more active processes typically have the goal of removing or reducing the quantity of organic and anionic phases present in the waste, thereby allowing vitrification of the remaining material without the issues presented by the organic or anionic content of the resin (12,18).

The simplest form of pre-treatment is incineration. The waste is heated, typically in the presence of an oxidising atmosphere, to a point where any moisture present is lost and the organic material decomposes (7). Typically, 400 °C is sufficient to destroy the organic material and cause the release of sulphur-bearing species as SO<sub>x</sub> (7), but often higher temperatures are used in order to assure the oxidation of the organic compounds and reduce the volume to the maximum extent possible (7). Hamodi *et al* determined that H<sub>2</sub>O is lost at a temperature range up to 150 °C, sulphur species between 150 °C and 490 °C and the organic phases from 490 to 650 °C. From 650 to 950°C the radio-caesium and metallic content oxidises. Finally, above 1050 °C the radio-caesium content is lost to volatilisation. At lower temperatures, around 400 °C, the process results in an ash containing the majority of the waste in the form of oxides and produces a large quantity of off-gas containing carbon dioxide, SO<sub>x</sub> and other volatile species depending on the temperature at which incineration is conducted (1,11). The ash would then be vitrified or disposed of through some other route (37). Incineration is not 100% efficient at removing heavier organics which may be pyrolysed by the process instead of being oxidised (17). Incineration has a number of disadvantages in that it poses a significant risk of losing radionuclides into the environment through volatilisation. This causes scrubbing of the off-gases to be required (7), and is a relatively time consuming process (7). Sulphur species must be scrubbed from off-gases to prevent environmental contamination by SO<sub>x</sub> emissions (18).

Pyrolysis or thermal decomposition describes a number of possible processes similar to incineration, which use heat to decompose organic materials but that avoid the volatilisation and corrosion problems of incineration (37). This is achieved through the reaction of waste materials in the absence of oxygen (30,38). The process breaks down the organic compounds, although it does not change them chemically, and so allows them to be integrated with a greater range of glasses and reduces the risk of radionuclides being lost. With IEX resins, temperatures of between 300 °C and 400 °C are used, depending on the polymers present with the aim having sufficient temperature to break down the organic structure but not enough to risk volatilisation of the radionuclides (30). A temperature which is too low may not be sufficient to break down the cross-linked polymers of the IEX resin (30). Oxidation is required to oxidise the carbon content of the organic species (30) and is catalysed by metal

oxides present which react with anionic species. It is worth noting that higher temperatures would be required for oxidation of the residue than for the initial pyrolysis process in order to achieve complete oxidisation of all of the constituents<sup>(30)</sup>. Generally, a multistage process of increasing temperature is used, first to evaporate fluids, then to decompose the material and finally to combust the polymer matrix<sup>(30)</sup>. One method for thermal decomposition of organics explored by the Russian nuclear institute Radon looked at mixing IEX resin with a pulverised metal fuel (PMF)<sup>(22)</sup>. The PMF reacts with the moisture from the IEX resin generating heat, evaporating moisture and gasifying the IEX resin<sup>(7)</sup>. The products of the IEX gasification are then burned out through combustion with air, which is pumped into the chamber, as a neutral atmosphere had been used up to this point<sup>(7)</sup>. This causes the formation of an ash residue and a gas phase, with the majority of radionuclides held within the ash<sup>(7,22)</sup>. The off-gases from this process were determined to contain SO<sub>x</sub>, NO<sub>x</sub> and CO<sub>2</sub>. Volatile radionuclides such as Cs were found to be bound to sulphides in the waste, although formation of Cs gas compounds is possible through this method<sup>(7)</sup>. The ash produced would require further stabilisation, through a process such as vitrification prior to disposal<sup>(22)</sup>.

Oxygen plasma decomposition is one of the more recent forms of pre-treatment which have been developed. The process, which has been developed by Fuji Electric, uses oxygen plasma to decompose a material into its component oxides and reduce the volume of the material significantly. Oxygen plasma is used due to its high chemical activity<sup>(37)</sup>, which allows more complete combustion to be achieved<sup>(18)</sup>. The treatment is effected by a two stage process, the waste material is exposed to a high-frequency inductively coupled plasma, which burns the material in a reduced oxygen pressure of 2 -4 kPa<sup>(37)</sup>. In the first stage, thermal decomposition of the resin is achieved by heating it to 400 °C through the effect of the plasma, and this decomposes volatiles to gas. The plasma is then used to heat the remaining materials to 700 °C in the second stage of the process, which causes the formation of oxides and decomposes all remaining organics<sup>(37)</sup>. An IEX resin would be oxidised to H<sub>2</sub>O, CO<sub>2</sub>, NO<sub>x</sub> and SO<sub>x</sub> and exhausted as a gas. Light compounds such as sulphur are therefore not retained and would need to be filtered from off-gases<sup>(18)</sup>. All the other components would be converted into an oxide form retained in the ash<sup>(37)</sup>, and metal oxides would not be reduced in the process<sup>(18)</sup>. In principle, the process could reduce the volume of the waste material by 90%, though in testing it only achieved 78- 84% reduction<sup>(37)</sup>. In experiments, the process took 30.1 hours to convert a volume of 16 litres, though a significant proportion of this was due to cooling time which could be reduced<sup>(37)</sup>. Though a large volume of off-gas would be produced via the process, the transfer of radionuclides into the environment should be low<sup>(37)</sup>, although it is worth noting that in some experiments the retention of Cs within the ash was reported to be as low as 25%<sup>(18)</sup>. As an oxide mixture, the

final ash product could be easily incorporated into a glass <sup>(18)</sup>, although Fuji Electric only demonstrated its incorporation into a cement <sup>(37)</sup>.

Chemical treatment utilising nitrates presents a further route for the pre-treatment of IEX resins, and have been used for the treatment of IEX resin in Argentina <sup>(1)</sup>. The addition of nitrites allows the reducing nature of the material to be decreased and allows a greater quantity of organic material to be incorporated into the glass <sup>(1,11)</sup>. Experiments have been conducted using  $\text{Fe}(\text{NO}_3)_3$ ,  $\text{HNO}_3$  and  $\text{NaNO}_3$  <sup>(19)</sup> for this purpose, where these chemicals were reacted at low temperatures with IEX resin.  $\text{HNO}_3$  was found to be the most effective in attacking the IEX resin material, however, long reaction times were required in order to achieve a significant effect <sup>(1)</sup>. A further possibility of this chemical treatment is that the use of nitrates can be combined with acids so that the organic component can be decomposed. For example nitric-phosphoric acid solution can be used to completely destroy the organic content of a resin leaving a waste residue in solution, which can be stabilised in an iron phosphate glass with a potential 50% reduction in volume <sup>(1,37)</sup>.

It is important to note that with most of these forms of pre-treatment, it is still necessary for the material to undergo vitrification in order to form a stable immobilised waste-form which can retain the radionuclides for the required period of time. It is also important to note that the problematic effect associated with radionuclides volatility, most notably in the case of radio-caesium, must still be addressed in the final immobilisation of the waste material. The work of Hamodi *et al* <sup>(12)</sup> provides an example of this in a pre-treated resin in which a pre-treated IEX resin waste failed to form a suitable waste-form on vitrification due to the effect of retained sulphur species and due to the caesium and cobalt loading of the simulant waste. It is clear that the glass composition used in the vitrification is of vital importance to the successful immobilisation of ion exchange resin wastes regardless of the pre-treatment that may have been previously used.

#### **2.4.2 Glass Composition Variation**

Conventional borosilicate glass compositions typically used in the vitrification of nuclear waste material in the UK and elsewhere are not well suited to the vitrification of IEX resin type wastes due to their low capacity for anionic species, typically sulphur, and due to their vulnerability to reduction by organic species <sup>(1,7)</sup>. The work of Herman *et al* and others <sup>(1,7,43)</sup> has shown that it is necessary to produce novel glass compositions in order to produce a composition which may successfully incorporate IEX resin wastes into a vitreous waste-form.

In order to achieve this, the problems associated with organic, anionic and volatile species present must be accounted for in the glass composition.

#### 2.4.2.1 Compensation for Reduction by Organics

Addressing first the modification of glass compositions in order to compensate for the effects the reducing organic species, the most frequently used addition to counter reduction is iron (III) oxide. Fe(III) can function as a buffer to reduction, as in a glass melt it is reduced to Fe(II), mitigating the reducing effect on other components of the glass and the waste <sup>(1,3,35)</sup>. However as Fe(II) is a glass modifier, the durability of the glass will be reduced with increasing proportions of Fe(II) <sup>(11)</sup>. An added benefit of using iron as a buffer is that it can be used to determine the extent of reduction in the glass through Mossbauer spectroscopy <sup>(36)</sup>. Iron oxides have been used since the 1990's to increase the possible loading of organic wastes in vitreous waste-forms by lowering of their reduction potential <sup>(19)</sup>. It is probable that other polyvalent species could also perform a similar buffer function in silicate glass compositions. However, the presence of Fe<sub>2</sub>O<sub>3</sub> in some IEX resin associated waste streams cause it to be favoured since it can be introduced to the final waste-form through the waste-stream itself <sup>(3,35)</sup>.

#### 2.4.2.2 Compensating for Anionic Content

The incorporation of anions into the glass is probably the most difficult of these three challenges to overcome. Typically the only solutions are to either reduce the content of waste in the glass, resulting in large volumes of waste at high cost <sup>(19)</sup>, or to modify the composition of the glass in order to allow the incorporation of higher quantities of anions into the glass. Sulphates, chlorides, phosphates and chromates are the most notable anions, which have limited solubility in silicate glasses. <sup>(11)</sup>

A range of solutions has been considered by various groups in order to find a possible route to circumvent the problems caused by the presence of sulphates, and broadly anionic species. Work has been undertaken by Donald *et al* in order to identify additives that would be beneficial to a host glass for the vitrification of IEX resin <sup>(28)</sup>, and the broad conclusions were that glass containing high quantities of alumina and silica would be ideal for the disposal of IEX resins since these compositions would provide sufficient durability despite

the effect of sulphates. However, CaO and Na<sub>2</sub>O were determined to have detrimental effects on durability in this study<sup>(22)</sup>. Studies carried out on the ternary system PbSiO<sub>3</sub>-PbSO<sub>4</sub>-PbO showed that at high concentrations of PbSiO<sub>3</sub>, and low PbO, a region of glass formation existed which has the potential to incorporate as much as 10 to 20 wt% of sulphates in the glass matrix<sup>(39)</sup>. The upper melting point for these compounds was defined as 1100 °C, and the T<sub>liq</sub> was defined as 982 °C<sup>(39)</sup>. It should be noted that specific research to assess the suitability of this glass for waste immobilisation purposes has yet to be undertaken, and the durability of such a glass is not known. It has been suggested that the element vanadium, specifically its oxide V<sub>2</sub>O<sub>5</sub>, can increase the amount of sulphate that can be retained in a glass. However the mechanism by which this is achieved is disputed, and not fully understood, with some research groups indicating that vanadium oxide does not have the effect that has been reported<sup>(32,40)</sup>. The leading explanation is that V<sub>2</sub>O<sub>5</sub> increases the liquid state miscibility of sulphates in the glass melt, allowing a higher amount to be incorporated<sup>(32)</sup>. During long melts the immiscible sulphate layer is seen to decrease as has been described, and disappears with a long enough period of time, and the addition of vanadium oxide accelerates the process<sup>(32)</sup>. In borosilicate type glasses, vanadium was seen not to directly interact with the sulphates, but instead acts instead as a network modifier<sup>(32)</sup>. Therefore, one explanation is that the depolymerisation of the borate network in the borosilicate glass leads to the increased kinetics of sulphur incorporation<sup>(32)</sup>.

In addition to the modification of borosilicate and silicate glass compositions, work has also been carried out exploring other glass systems. Phosphate glasses are known to possess a glass-forming region in which higher concentrations of sulphates may be dissolved<sup>(22)</sup>. Though phosphate glasses are typically overlooked, they have been shown to possess a higher capacity for sulphates than silicate glasses<sup>(31)</sup>. Compositions containing up to 25 wt% sulphate have been produced. However, these tended to possess poor durability in comparison to other waste glasses<sup>(31)</sup>. Where iron phosphate glasses do offer the possibility of improved durability, they have a much lower sulphur solubility<sup>(31)</sup>.

A study carried out by Bingham and Hand<sup>(31)</sup>, based upon the work of Dietzal *et al*<sup>(41-42)</sup> demonstrated a relationship between the cation field strength ( $z/a^2$ ), or the cation field index ( $\Sigma(z/a^2)$ ) as described in the paper, and the capacity for a glass system to incorporate sulphur. This was demonstrated to work for both borosilicate and phosphate glass systems and provides a qualitative basis for the prediction of sulphate incorporation in glass compositions. In the most general sense, this work implies that the inclusion of low field strength cations, such as Ba<sup>2+</sup>, in glass compositions is preferable for the incorporation of sulphur into glass systems. This work was applied by Bingham *et al*<sup>(3)</sup> in a study of various

borosilicate glass compositions intended to determine their effectiveness or IEX resin vitrification and sulphur incorporation. Glass compositions which were selected on the basis of their predicted high capacity for sulphur incorporation were shown to indeed demonstrate superior extents of sulphur incorporation than other glasses explored, demonstrating that cation field strength may be related to sulphur incorporation on a qualitative basis. Furthermore the three glass compositions identified by Bingham *et al*, most notably in the case of the G73 composition, demonstrated little evidence of gall layer formation due to sulphate insolubility showing that these compositions are close to optimal for IEX resin vitrification at the waste-loadings explored. Figure 2.3 shows the correlation between cation field index and sulphur incorporation as shown by Bingham *et al* <sup>(3)</sup>.

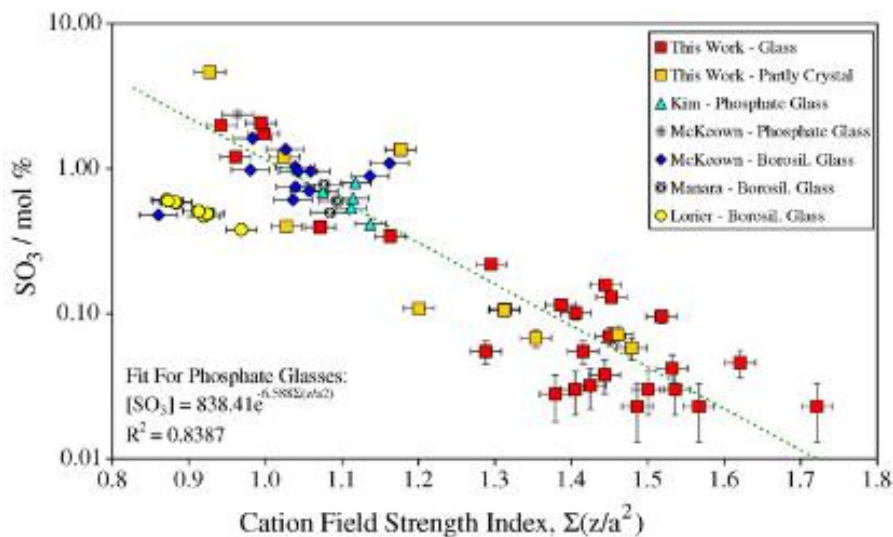


**Figure 2.3.** The correlation between sulphate content and cation field strength in a range of glasses as presented in the work of Bingham *et al* <sup>(31)</sup> and glasses surveyed in the same work.

#### 2.4.2.3 Compensating for Volatile Content

The retention of volatiles, such as the radio-caesium content of the IEX resin waste, is governed to a large extent by the composition of the glass used for vitrification and by the waste components that the volatiles are combined with <sup>(3)</sup>. A survey of results carried out by Bingham *et al* <sup>(3)</sup> demonstrated that over a range of composition, waste-loadings and processing parameters a wide variety of caesium retentions were achieved, between 70.5 –

93.5 % retention <sup>(3)</sup>. It is not possible to determine the common factors between the various surveyed references due to the diversity of parameter and experimental conditions that are explored. Despite this, it is likely that the retention of caesium can be attributed primarily to the temperatures at which the glasses were melted, as governed by the liquidus temperature ( $T_{liq}$ ) of the glass composition used, the viscosity of the glass composition and to the extent of reduction and solubility of anions in the system, since the presence of a volatile gall layer will significantly increase the rate at which volatiles are lost to the off-gas. As a consequence of this, two parameters must be considered in the maximisation of caesium retention. Firstly the compositional problems presented by the anionic and organic content of the resin waste must be considered, but in addition the liquidus temperature of the glass must be minimised, allowing vitrification processes to take place with reduced volatilisation and increase glass viscosity.

#### **2.4.3 Modifications to the Vitrification Process**

In addition to the routes which have already been described for resolving the issues associated with the vitrification of IEX resin wastes, changing the host glass composition and various pre-treatment routes, work has also been performed with the aim of modifying the vitrification process itself.

One approach which uses the modification of the vitrification process to reduce the reducing effect of organic species in a glass melt involves the adjustment of the melting conditions in order to compensate for reduction by increasing the proportion of oxygen available to the composition. Oxygen gas is fed into the glass melt in order to increase the quantity of oxidisers present in the glass, and in effect balance out the increased presence of reducing agents provided by the organic compounds <sup>(11)</sup>. This method has been used in vitrification plants in Korea, utilising an adjustable feed to compensate for variable quantities of reducing material <sup>(34)</sup>. Tests in 1999 showed that vitrified IEX wastes, vitrified without oxygen feeding, contained entrained solids and were over-reduced <sup>(2)</sup>. It has been suggested that stirring will have a similar effect through introducing oxygen into the melt, assuming the melt is conducted under an oxidising atmosphere <sup>(11)</sup>. In general, even the diffusion of  $O_2$  into the glass at high temperatures may reduce the extent of reduction <sup>(19)</sup>.

In a similar way, the problem of sulphate insolubility can potentially be resolved through changing the conditions of the melt in order to prevent the occurrence of phase separation in the melt. One approach is to add reducing agents to the slag crust which

inhibits the formation of a salt phase <sup>(33)</sup>, and causes the sulphates to be volatilised at an increased rate <sup>(27)</sup>. However, this approach is time consuming <sup>(33)</sup> and difficult due to the control required to avoid over reducing the glass melt <sup>(27)</sup>. Unfortunately not all radionuclides are transferred back to the glass phase, the addition of reducing agents also increases the volatility of cations that may be present in the salt phase, such as caesium, increasing the requirements for effective scrubbing <sup>(33)</sup>. As this approach clearly has a number of problems, other approaches have also been considered, such as supplying the melt with divalent cations in an attempt to preferentially form a sulphate salt layer with these cations, which could then be extracted and treated separately to the melt <sup>(33)</sup>. A second approach which has been considered in instances where the salt forming species cannot be incorporated into the glass matrix is to remove the species from the glass melt itself. To achieve this, melters can be designed include salt drains to remove salt phases either from under the melt or from on top of it <sup>(33)</sup>, allowing the glass to form unaffected by the sulphate salt, which is handled as a separate waste <sup>(11)</sup>.

The problems associated with volatilisation of the radio-caesium from the melt during the process of vitrification are not as easily solved through the modification of the processing conditions. Minimising the temperatures involved in the vitrification process has been demonstrated to be an effective route by which the proportion of radio-caesium lost to volatilisation can be minimised. However, it is important to note that the melting temperature is constrained by the glass composition <sup>(39,43)</sup>. Further possibilities include the possible collection of radio-caesium lost to off-gases by the means of filtration, allowing lost radio-caesium to re-input for vitrification or another form of immobilisation.

#### **2.4.4 Comparison of pre-treatment, process modification and composition modification options.**

As can be seen from the literature discussed above, the various possible approaches presented for eliminating the problems encountered with IEX resin vitrification have varying degrees of effectiveness. The work of Hamodi *et al* and others <sup>(7,12,17,25,31)</sup> shows that pre-treatment, was effective at eliminating some or all of the problematic chemistry associated with the resin wastes, does not guarantee the successful vitrification of the materials produced after pre-treatment, and in addition to this, the cost associated with pre-treatment, in terms of equipment and chemical emissions (SO<sub>x</sub> notably) mean that pre-treatment may not be entirely economically viable. Similarly, the approaches which involve the modification of the melting process itself can be seen to be non-optimal, since in most cases these approaches lead to the

production of additional waste streams, such as volatilised radionuclides or molten salts containing radionuclides. It therefore seems apparent that despite the useful benefits that can be gained either from the pre-treatment of the IEX resin or from the modification of the vitrification process the most promising approach can only come from the modification of the host glasses used in vitrification. This assessment can be supported in view of the fact that the three primary issues encountered in the vitrification of IEX resin wastes arise due to interactions between the host glass and the waste itself, and as such can only be resolved through the modification of the host glass chemistry, although pre-treatment of the IEX material can also provide partial solutions in this regard. In addition it should be noted that if the issues presented by IEX resin vitrification can be resolved through the modification of the host glass composition, pre-treatment steps and further modifications to the melting process may not be necessary.

Given this analysis, probably the most promising research which has been covered by this review is that presented by Bingham *et al* in which three potential glass compositions are identified which possess characteristics which are ideal for IEX resin vitrification, those being <sup>(1)</sup> resistance to reduction through the presence of an Fe<sub>2</sub>O<sub>3</sub> buffer, <sup>(2)</sup> high capacity for the incorporation of sulphur species which prevents the formation of a significant gall layer and <sup>(3)</sup> high levels of caesium retention. These glass compositions, or compositions developed from these, present exciting prospects with regards to the vitrification of IEX resin wastes.

## 2.5 Summary

In summary, it can be seen in this review that the IEX resin wastes represent a growing problem of the global nuclear industry, and for the UK nuclear industry, which as yet does not have an adequate solution. Current practice for these wastes advocates the long-term storage of the materials. However, this has been shown to be inadequate due to the emission of combustible gases and due to the time scales required for the decay of the radioactive species present in the wastes. Over the past four decades a range of possible routes for immobilisation have been investigated, but most have been found inadequate to the task either due to the expenses associated with the volume increases caused by the encapsulation of IEX resin materials or due to chemical incompatibility of the resin materials with potential waste-forms, such as the cements commonly used in the UK for ILW waste immobilisation.

Vitrification has been shown to possess a wide range of desirable factors in relation to the immobilisation of IEX resin wastes, most notably in terms of the durability and low

volume of the final waste-form which could potentially be produced through the vitrification of IEX resin wastes. However, the vitrification of IEX resin is complicated by a number of factors relating to the chemistry of the resin itself. Firstly, the presence of anionic species, most typically sulphur, is problematic due to the low solubility of these species in most silicate glass compositions which are typically used for nuclear waste vitrification. These phases are known to phase separate if the solubility limit of the glass melt is exceeded and form problematic glass layers which are water soluble and can preferentially contain radioactive species from the IEX resin waste. Secondly, the presence of significant organic content of these wastes presents problems due to the reducing effect they have upon the oxide components of the host glass. This can lead to the separation of metallic and metal sulphide phases, and in addition has been shown to impair the durability of a final waste-form due to the impact of the organic materials upon the glass network. Finally, the primary radioactive component of most types of IEX resin waste, <sup>137</sup>Cs, presents a problem due to its volatility at high temperatures, such as those used for the process of vitrification.

In order to compensate for these various issues a wide range of approaches have been investigated in order to identify routes which may allow these problems to be overcome. These solutions in general may be categorised into three groupings; modification to the vitrification process itself, pre-treatment of the IEX resin in order to eliminate the problematic chemistry of the resin material and the modification of conventional waste glass compositions in order to allow the glass to avoid the problematic interactions with the chemistry of the IEX resin. These approaches have been reviewed above and have had a range of success in application. However, it is apparent from the literature that regardless to the implementation of pre-treatment for the IEX resin waste or to modification of the melter design, the most effective and economically viable solutions lie in the modification of the composition of the waste glass material. Research has been identified by Hand *et al* and Bingham *et al*<sup>(31)</sup> which demonstrates the potential of a number of glass compositions for use in the vitrification of ion exchange resin wastes. These glasses, through their compositions which includes Fe<sub>2</sub>O<sub>3</sub> which acts as a buffer against reduction, and other components which have been shown to allow increased retention of sulphur species, have been shown to be able to successfully incorporate and immobilise IEX resin wastes at relatively high waste-loading levels and with negligible loss of volatile radio-nuclides. As such, these glass compositions, and glass compositions which could potentially be developed from them, represent probably the optimal solution to the lingering problem posed by the growing inventory of radionuclide contaminated IEX resin wastes in the UK and around the world.

## **Chapter 3.1 - Systematic Development of an Alkali Alkaline-Earth Silicate Glass for the purpose of Cs-loaded Ion Exchange Resin Vitrification.**

Radioisotope loaded ion exchange (IEX) resins are a problematic form of waste originating from the treatment of aqueous wastes streams from nuclear applications. Due to their organic, acidic and anion rich nature they are generally not appropriate for encapsulation by Ordinary Portland Cement blends<sup>(23-24)</sup>. Vitrification offers an attractive potential route for the disposal of these resin wastes, leading to a reduction in the overall volume of the waste and to enhanced passive safety for the final waste-form. However the anionic and organic content of the waste, as well the volatility of the primary radioisotope Cs-137, means that current vitrification techniques and materials are not optimised for resin treatment<sup>(1-2)</sup>

The aim of this work was to explore the effect of composition variation in an alkali alkaline-earth silicate glass system, with the goal of producing a ‘tool-box’ of compositions, allowing the system to be tailored for specific waste streams. The composition of the base glass system, to be optimised in this study, is reported in table 3.1.1. This system was selected for development due to its high capacity for the incorporation of anionic species, superior durability<sup>(3,35)</sup>, and proven tolerance to gamma radiation effects<sup>(44)</sup>. In the context of ion exchange resin vitrification the base glass system may not be optimal due to a high melting temperature which increases the risk of radio-caesium volatilisation<sup>(2)</sup>. Three series of compositional development experiments were carried out, aimed at improving upon the characteristics and performance of the base glass composition.

The following experimental series are described and discussed in this section. The first series considered modification of the constituent alkaline-earth species, to determine the effects of varying the ratio of BaO to CaO on the charge density of network modifying components of the system. The second series considered the replacement of 5 mol% of the CaO content with an equimolar quantity of MgO, SrO, MnO and ZnO on the liquidus temperature ( $T_{liq}$ ), glass transition temperature ( $T_g$ ), density and change in viscosity over temperature. The final series considers the reduction of the overall alkali content of the system, to explore the effect of reducing the Na<sub>2</sub>O and Li<sub>2</sub>O content, whilst retaining the same ratio of Na<sub>2</sub>O and Li<sub>2</sub>O, on melting properties of the system ( $T_{liq}$  and  $T_g$ ) to determine the feasibility of reducing the alkali content of the system, since high alkali content is generally linked to impaired glass durability<sup>(47)</sup>.

Compositions from both the first and second series (+4 mol% BaO and +5 mol% ZnO, MnO and MgO) exhibited reduced values of  $T_{liq}$ , representing significant improvements, from the perspective of ion exchange resin waste vitrification, over the original base glass composition. In addition compositions from the second series (+5 mol% MnO and ZnO) were found to contain Fe as exclusively  $Fe^{3+}$  species, thereby maximising their capacity for mitigating the effects of reduction by organic species via the reduction of  $Fe^{3+}$  to  $Fe^{2+}$  during melting. The results of the third series revealed that reducing the alkali content of the system from ca. 13.4 to ca. 8 mol% was possible without adversely affecting the melting properties of the glass, if the compositional improvements of the first and second series were applied.

### **3.1.1 Experimental Procedures**

#### **3.1.1.1 Sample Preparation**

Each sample was prepared from its component chemicals using either oxide or carbonate compounds of 99.9% purity or greater. These were subsequently melted at 1200 °C for 3 hours in a Zr-stabilised Pt crucible. Samples were stirred for the latter 2 hours of the melting period (at 30 rpm), poured into block moulds and annealed at 500 °C for 1 hour before being cooled to room temperature at a rate of 1 °C per min. Approximately 200g of material was produced for each sample. This procedure was applied for all samples with exception of fully alkali depleted sampled which was, by necessity, melted at 1400 °C.

#### **3.1.1.2 Characterisation Techniques**

Sample density was determined through Archimedes method. Three measurements were taken per sample and the results were adjusted to compensate for the density change in the deionised water due to ambient temperature changes. The glass transition onset ( $T_g$ ) and crystallisation onset ( $T_x$ ) temperatures for the glasses were determined through the use of Differential Thermal Analysis (DTA). DTA experiments were all performed in air and using Pt crucibles and measurements were taken automatically by a computer operated system (Perkin Elmer DTA 7).

Table 3.1.1. Nominal glass compositions for development experiments.

Sample ID	Component (mol%)											
	SiO <sub>2</sub>	B <sub>2</sub> O <sub>3</sub>	Al <sub>2</sub> O <sub>3</sub>	Fe <sub>2</sub> O <sub>3</sub>	CaO	BaO	Li <sub>2</sub> O	Na <sub>2</sub> O	MgO	SrO	MnO	ZnO
AS Base	51.72	2.23	0.38	2.92	11.08	18.23	7.80	5.64	-	-	-	-
Full BaO	51.72	2.23	0.38	2.92	0	29.31	7.80	5.64	-	-	-	-
+ 8 mol% BaO	51.72	2.23	0.38	2.92	3.08	26.23	7.80	5.64	-	-	-	-
+ 4 mol% BaO	51.72	2.23	0.38	2.92	7.08	22.23	7.80	5.64	-	-	-	-
+4 mol% CaO	51.72	2.23	0.38	2.92	15.08	14.23	7.80	5.64	-	-	-	-
+8 mol% CaO	51.72	2.23	0.38	2.92	19.08	10.23	7.80	5.64	-	-	-	-
+12 mol% CaO	51.72	2.23	0.38	2.92	23.08	6.23	7.80	5.64	-	-	-	-
Full CaO	51.72	2.23	0.38	2.92	29.31	0	7.80	5.64	-	-	-	-
AS + MgO	51.72	2.23	0.38	2.92	6.08	18.23	7.80	5.64	5.00	-	-	-
AS + SrO	51.72	2.23	0.38	2.92	6.08	18.23	7.80	5.64	-	5.00	-	-
AS + MnO	51.72	2.23	0.38	2.92	6.08	18.23	7.80	5.64	-	-	5.00	-
AS + ZnO	51.72	2.23	0.38	2.92	6.08	18.23	7.80	5.64	-	-	-	5.00
12 mol% Alkali	52.58	2.27	0.39	2.97	11.27	18.53	6.96	5.04	-	-	-	-
8 mol% Alkali	54.97	2.37	0.40	3.10	11.77	19.37	4.64	3.36	-	-	-	-
4 mol% Alkali	57.36	2.47	0.42	3.24	12.29	20.21	2.32	1.68	-	-	-	-
0 mol% Alkali	59.74	2.57	0.44	3.37	12.80	21.06	-	-	-	-	-	-

The liquidus temperature ( $T_{\text{liq}}$ ) was determined using a tube furnace in which a fritted sample was heated across a known temperature gradient. By determining the temperature across the length of the sample (contained within an  $\text{Al}_2\text{O}_3$  boat of ~10cm length) the  $T_{\text{liq}}$  could be identified by visually locating the point to within the nearest centimetre at which crystal growth begins to occur and matching that to the known temperature at that displacement. This technique can produce results accurate to within  $\pm 10$  °C. In order to discriminate between glass compositions the melting temperature ( $T_{\text{melt}}$ ) was defined as being 50 °C above the  $T_{\text{liq}}$ . It should be noted that this does not take into account properties such as viscosity which also effect the temperature at which a glass can be melted.

The viscosity of the samples was determined using a Viscometer setup (Theta Industries) including a rheometer (Brookfield DV-III-Ultra) and a specially designed vertical muffle furnace (Theta Industries). This setup allows the viscosity of a sample to be determined by measuring the torque experienced by an alumina spindle rotating in a molten sample across a range of temperatures. The instrument was calibrated using a control fluid prior to use.

Electron dispersive X-ray spectroscopy (EDS) was utilised to quantify and confirm the compositions of the samples produced. A Philips P500 SEM/EDS system was utilised to collect the data and a Co standard was used as a calibration standard. The produced emission spectra were automatically quantified utilising standard data previously input into the EDS system.

Fourier Transform Infra-Red (FT-IR) spectroscopy was applied to investigate the changes in glass structure as a function of composition. Samples were ground and polished manually using SiC abrasive discs and diamond suspension respectively. A Perkin Elmer Spectrum 2000 FT-IR spectrometer was used to collect spectra over the 500 – 1500 nm range. FTIR data were collected using reflectance and as such was corrected utilising a Kramers-Kronig transform. FT-IR spectra were fitted with Gaussian line-shapes in order to determine band areas. The initial parameters used in fitting were constrained based on literature values.<sup>(48)(49)</sup> It is important to note that the values produced for Q-speciation involve contributions from multiple oxide bonds associated with the 9-10 components present in each sample. As such the fitted band areas can only be considered as an indicative average of the contributions from the oscillations of these multiple oxide bonds.

<sup>57</sup>Fe Mössbauer spectroscopy was utilised to determine the oxidation state and co-ordination of Fe within the samples. A WissEl <sup>57</sup>Fe Mössbauer spectrometer setup was utilised operating in a constant acceleration mode with a <sup>57</sup>Co source (activity ~9000

$\mu\text{Ci}$ ). Mössbauer spectra were fitted using single Lorentzian line shapes each set to represent the  $\text{Fe}^{2+}$  and  $\text{Fe}^{3+}$  environments, using the software package Recoil 1.03. The recoil free fraction was assumed to be equal in the  $\text{Fe}^{2+}$  and  $\text{Fe}^{3+}$  environments. Sample calibration was performed relative to  $\alpha\text{-Fe}$ .

Solid state NMR of the  $^{29}\text{Si}$ ,  $^{27}\text{Al}$ ,  $^7\text{Li}$ ,  $^{23}\text{Na}$  and  $^{11}\text{B}$  nuclei was applied to study the co-ordination and environment of network forming and network modifying components of the system. Spectra were recorded at the frequencies listed in table 3.1.2. below using a Varian VNMRS 400 spectrometer and a 4mm (rotor o.d.) MAS probe. They were obtained using a cross-polarisation with a 0.5 or 1 s recycle delay and a 1 ms contact time. Between 1000 – 10000 repetitions were accumulated. Spectral referencing was with respect to an external sample of 1M aqueous  $\text{AlCl}_3$ , neat  $\text{BF}_3/\text{OEt}_2$ , 1M  $\text{LiCl}$  and 1 M  $\text{NaCl}$  respectively and neat tetramethylsilane.

More detailed descriptions of these techniques are provided in appendix 8.1.

**Table 3.1.2.** Solid State NMR experiment parameters.

	$^{27}\text{Al}$	$^{11}\text{B}$	$^7\text{Li}$	$^{23}\text{Na}$	$^{29}\text{Si}$
<b>Frequency</b>	104.197 MHz	128.3 MHz	155.406 MHz	105.782 MHz	59.557 MHz
<b>Spectral Width</b>	416.7 kHz	416.7 kHz	416.7 kHz	416.7 kHz	2.996 kHz
<b>Acquisition Time</b>	20.0 ms	40.0 ms	20.0 ms	20.0 ms	20.0 ms
<b>Recycle Time</b>	0.5 s	1.0 s	1.0 s	1.0 s	90 s
<b>Pulse Duration</b>	1.0 $\mu\text{s}$				

MAS-NMR spectra for all nuclei were fitted by Gaussian line-shapes based upon and constrained to within  $\pm 2$  ppm of literature values<sup>(50-56)</sup>. All MAS-NMR spectra included contributions from multiple groups, associated with the interactions of the numerous components in the system with the target nuclei, for each fitted site. Due to the complexity of fitting potentially 8 or 9 different groups for each site the  $^{29}\text{Si}$  MAS-NMR spectra were fitted only for what was judged to be the dominant group (e.g.  $\text{Q}^4(4\text{Si})$  excluding  $\text{Q}^4(1\text{B})$ ).

### 3.1.2 Results

#### 3.1.2.1 Variation in ratio of component Alkaline-Earth species (BaO and CaO)

This series of compositions comprised 8 glasses, including the original base glass (Table 3.1.1), spanning the base glass with full replacement of CaO with BaO to the full replacement of BaO with CaO. X-ray diffraction data revealed the glasses produced to be amorphous within the limit of detection estimated at 5 % of crystalline material by volume.

The density of the glasses was observed to increase linearly, within experimental errors, upon increasing BaO replacement of CaO, as shown in figure 3.1.1, due to the higher molar mass of BaO relative to CaO<sup>(57)</sup>.

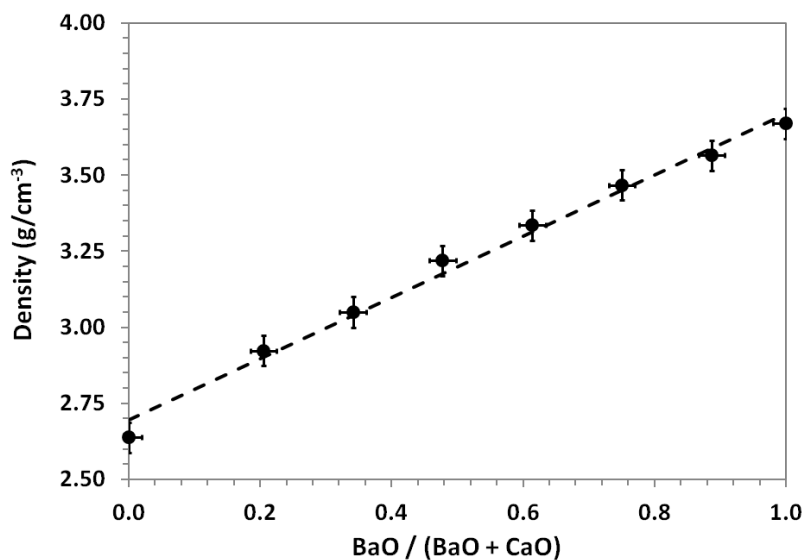


**Figure 3.1.1.** Variation in density across the BaO : CaO variation series. Density error bars determined from deviation of three measurements. Composition error determined from error associated with of EDS analysis.

$T_g$  and the  $T_{liq}$  were found to vary in a non-linear manner in proportion to the ratio of BaO and CaO, both achieving a minimum point between  $BaO / (CaO + BaO) = 0.60$  and  $0.75$ . The variation in  $T_g$  across the full range of compositions is approximately  $40^\circ C$ . The

variation of  $T_{liq}$  across the range of samples is 260 °C between its maximum point in the series, at full replacement of BaO with CaO, and the minimum point. The dependence of  $T_{liq}$  and  $T_g$  on composition are plotted in figures 3.1.2 and 3.1.3, respectively. The observed variation in  $T_{liq}$  is in broad agreement with the ternary  $SiO_2$ -BaO-CaO phase diagram published by Toropov *et al.*<sup>(60)</sup> which implies a non-linear variation in  $T_{liq}$  across the range of compositions explored, although at a smaller magnitude than was observed in this study.

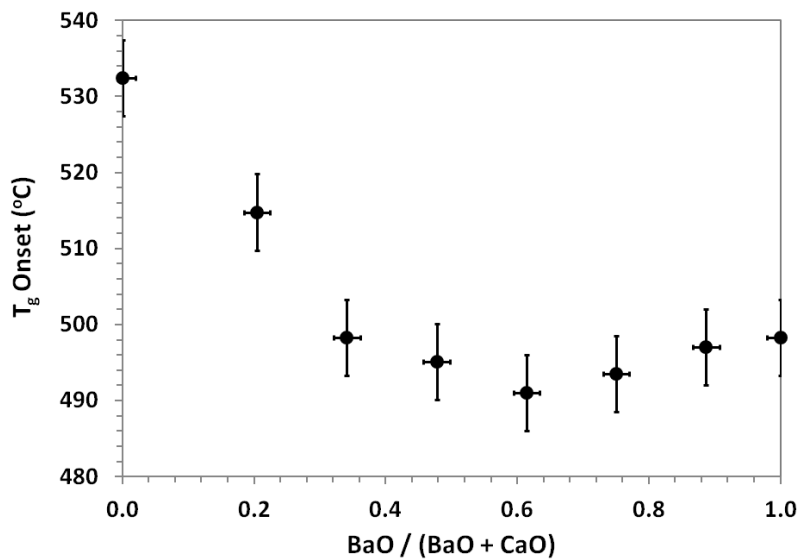


**Figure 3.1.2.** Variation in  $T_g$  onset across the BaO : CaO variation series. Error bars for  $T_g$  determined from experimental error associated with technique and fitting. Composition error determined from error associated with of EDS analysis.

The viscosity of the samples was determined to change only by a small extent across the series, showing evidence of decreasing viscosity across all temperatures with an increasing proportion of BaO<sup>(50)</sup>. Figure 3.1.4 shows the variation in change in viscosity across the series. This in agreement with the observations made by Stebbins *et al.*<sup>(61)</sup> concerning the dependence of change in viscosity over temperature on the proportion of heavier alkaline-earth oxide constituents in silicate glasses.

Mössbauer spectroscopy was utilised to probe the oxidation state and co-ordination environment of the Fe content in the samples. It was found that throughout the series the Fe oxidation state was invariant at  $Fe^{3+} / (Fe^{3+} + Fe^{2+}) = 0.96 \pm 0.02$  in all but one sample, within the limits of error. The full CaO sample showed a slightly higher extent of reduction with

$\text{Fe}^{3+} / (\text{Fe}^{3+} + \text{Fe}^{2+}) = 0.87 \pm 0.02$ . The centre shift and quadrupole splitting parameters of the fitted Mössbauer spectra (not shown) showed no significant variation across the samples investigated, within the limits of error indicating no change in average co-ordination state of either  $\text{Fe}^{2+}$  or  $\text{Fe}^{3+}$  across the compositional series. This result is in agreement with the work of Mysen *et al.*<sup>(62)</sup> and Bingham *et al.*<sup>(63)</sup>. The proportion of  $\text{Fe}^{2+}$  across the series is shown in figure 3.1.5.

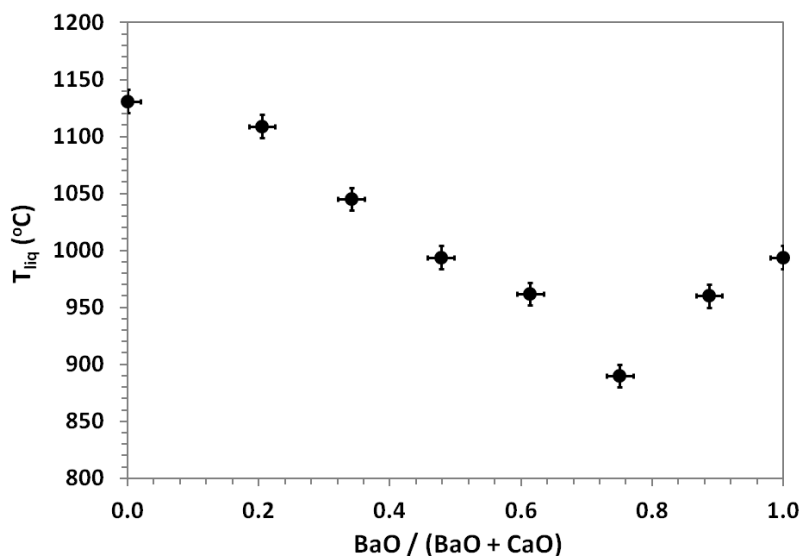


**Figure 3.1.3** Variation in  $T_{\text{liq}}$  across the BaO : CaO variation series. Error determined from experimental error associated with technique. Composition error determined from error associated with of EDS analysis.

FT-IR spectroscopy showed the Q-speciation the glasses to be split between two distributions indicative of  $Q^2$  and  $Q^3$  silicate tetrahedral units, as shown in Figure 3.1.6. This feature was present in spectra from all glasses of the BaO:CaO series and is seen to be present in the base glass spectrum. It can be connected to the relatively large content of alkaline earth oxides (BaO and CaO) which has been linked to the formation of a strong  $Q^2$  band, associated with combinations of alkali and alkali-earth modifiers coordinated to silicate tetrahedral units<sup>(4,45-46)</sup>. In this series, it can be seen that this  $Q^2$  band varies in relative intensity and wavenumber, relative to the  $Q^3$  band which remains unchanged within experimental resolution. As the relative content of BaO is increased, the  $Q^2$  band increased in intensity and decreased in wavenumber. This is shown in figure 3.1.6 and 3.1.7.

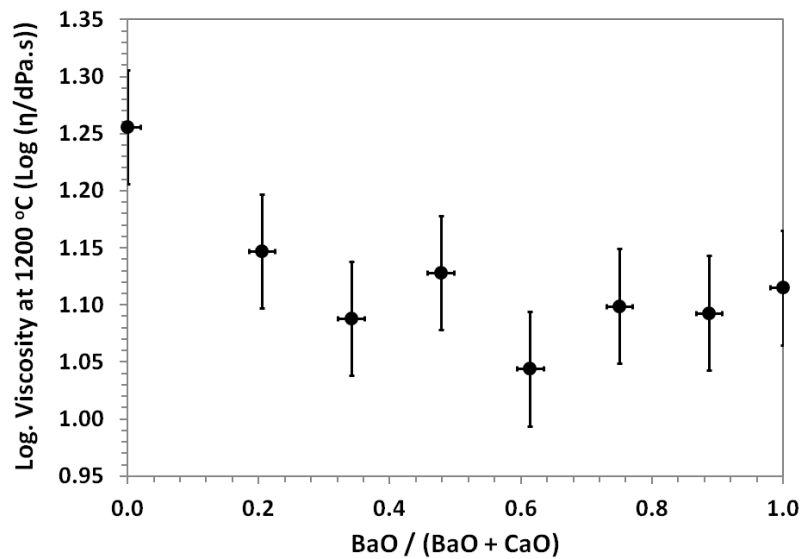


**Figure 3.1.4.** Variation in Log (viscosity) at 1200 °C over the BaO : CaO variation series. Error determined from experimental errors associated with measurement. Composition error determined from error associated with of EDS analysis.

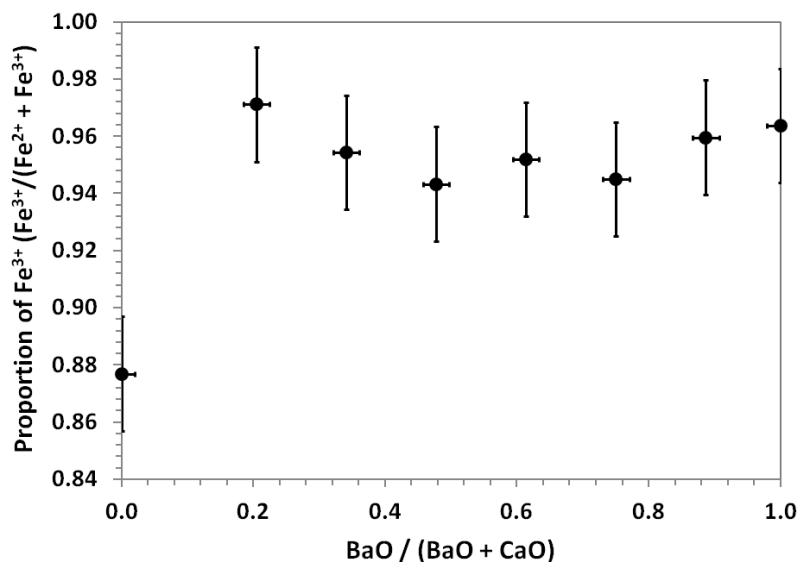


**Figure 3.1.5.** Comparison of Fe oxidation state in across BaO : CaO variation series. Derived from Lorentzian fitting of Mössbauer spectra. Error bar represents three standard deviations, derived from three independent measurements. Composition error determined from error associated with EDS analysis.

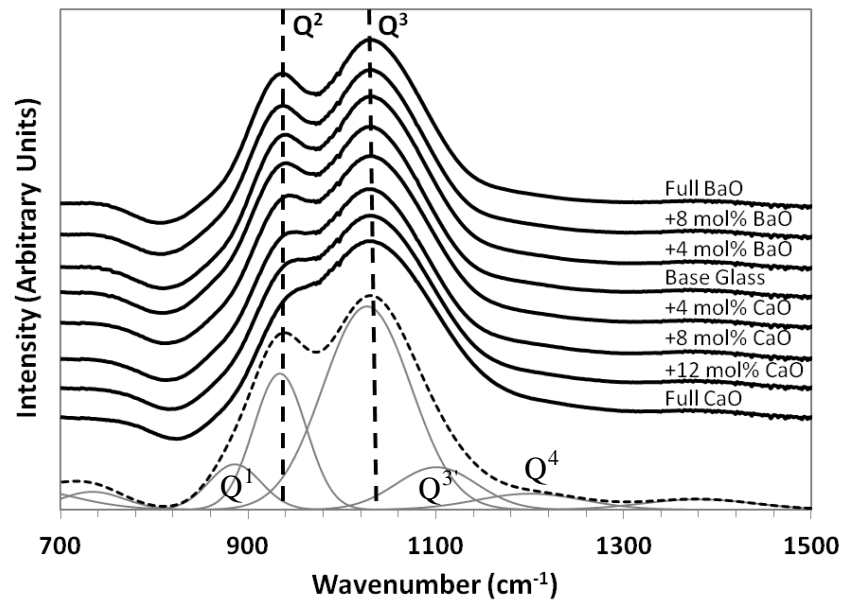


**Figure 3.1.6.** FT-IR spectra of samples from BaO : CaO variation series. Fitted bands and convolution shown below. Lines serve as guide for eyes only, indicating  $Q^2$  and  $Q^3$  band.

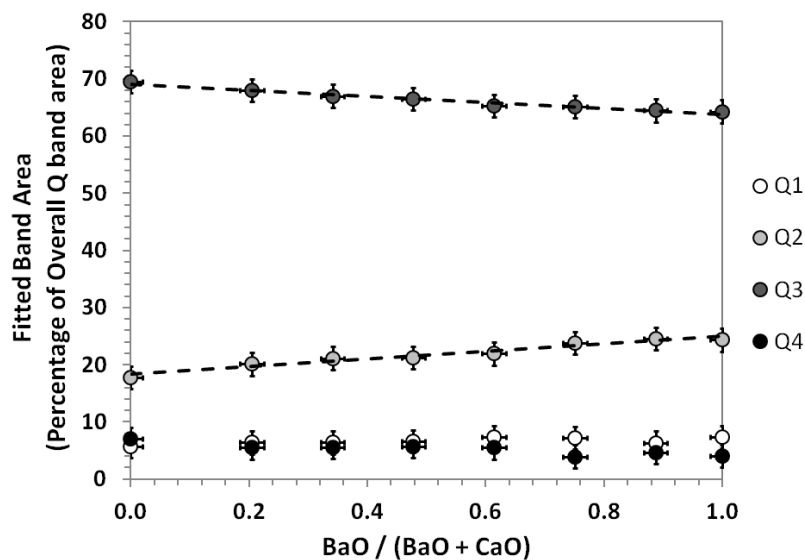


**Figure 3.1.7.** Variation in proportion of  $Q^n$  bands across BaO : CaO variation series. Determined by fitting of bands with Gaussian line-shapes. Error determined from deviation of fit. Composition error determined from error associated with EDS analysis. Line is guide for the eyes only.

### 3.1.2.2 Replacement of CaO with divalent oxides

This series consisted of four samples, which individually contained a 5 mol% replacement of CaO with MgO, SrO, MnO and ZnO. The results of these four samples were compared with the base glass and the 5 mol% BaO sample from the BaO : CaO variation series. X-ray diffraction experiments conducted on the series revealed the produced glasses to be amorphous within the limit of detection estimated at 5 % of crystalline material by volume.

Marked variations in samples density were observed with a discernible trend being apparent in the ZnO ( $3.50 \pm 0.01 \text{ gcm}^{-3}$ ) and MnO ( $3.49 \pm 0.01 \text{ gcm}^{-3}$ ) samples between increased density and higher relative molecular mass relative to CaO, as shown in Figure 3.1.8, consistent with the work of Huggins *et al*<sup>(57)</sup>. This does not apply in the alkaline-earth samples as the density of the SrO sample ( $3.41 \pm 0.01 \text{ gcm}^{-3}$ ) is lower than that of the MgO ( $3.47 \pm 0.01 \text{ gcm}^{-3}$ ) despite the higher relative molecular mass.

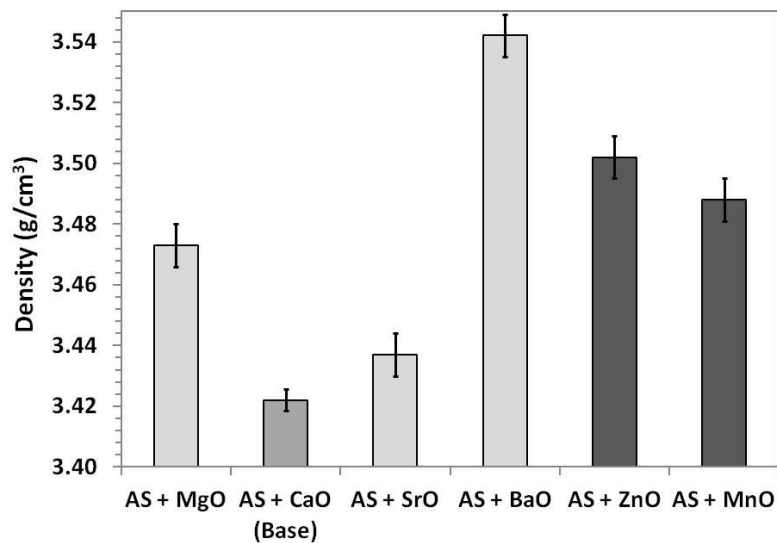


**Figure 3.1.8.** Variation in density across samples in Ca replacement series. Error bars derived from deviation of three measurements.

$T_g$  was determined to vary by  $17 \pm 5^\circ\text{C}$  depending upon the replacement oxide, as shown in Figure 3.1.9. The maximum was apparent at  $506 \pm 5^\circ\text{C}$  in the MgO composition and the minimum in the MnO composition at  $493 \pm 5^\circ\text{C}$ , close to the  $T_g = 491 \pm 5^\circ\text{C}$  of the initial base glass composition. These results differ from the results observed in the BaO : CaO variations series, since all four samples demonstrate higher  $T_g$  than observed in the BaO : CaO series. This is consistent with literature expectations in the case of the MgO sample only, which possesses a higher  $T_{\text{melt}}$  than CaO as an oxide ( $T_g$  of a glass was linked to  $T_{\text{melt}}$  of an additive oxide by Islam *et. al.* <sup>(58)</sup>).

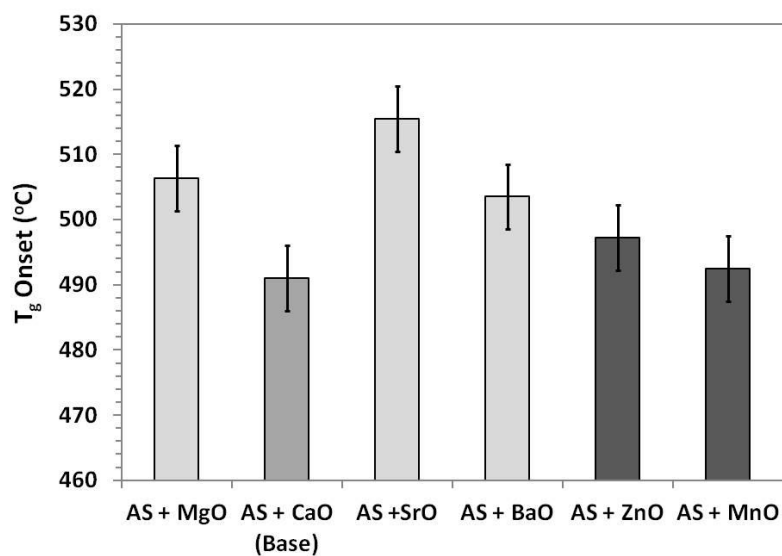


**Figure 3.1.9.** Variation in  $T_g$  onset across CaO replacement series. Error determined from experimental error associated with technique and fitting.

The variation in  $T_{\text{liq}}$  as a result of CaO replacement covers a temperature range of  $132 \pm 5^\circ\text{C}$ . All compositions, with the exception of the SrO sample, show reductions in  $T_{\text{liq}}$  as a result of the replacement of CaO. These compositions exhibit a reduction in  $T_{\text{liq}}$  of up to  $110 \pm 5^\circ\text{C}$  from the  $T_{\text{liq}}$  of the initial base glass composition. This is most apparent in the ZnO sample, which exhibits a lower  $T_{\text{liq}}$  than that previously determined in the BaO : CaO compositional series sample (labelled as AE + BaO in figure 3.1.10).

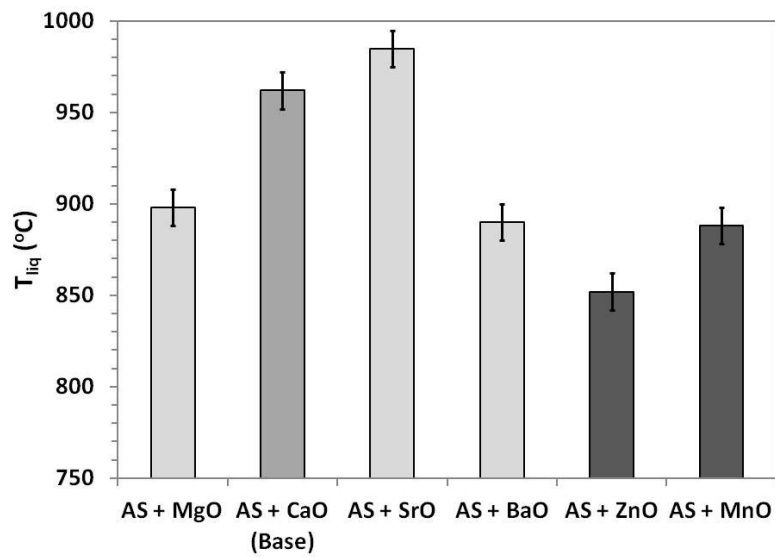


**Figure 3.1.10.** Variation in  $T_{liq}$  across samples in Ca replacement series, where 5 mol% CaO has been replaced with alternative divalent oxides. Error derived from experimental errors associated with measurement.

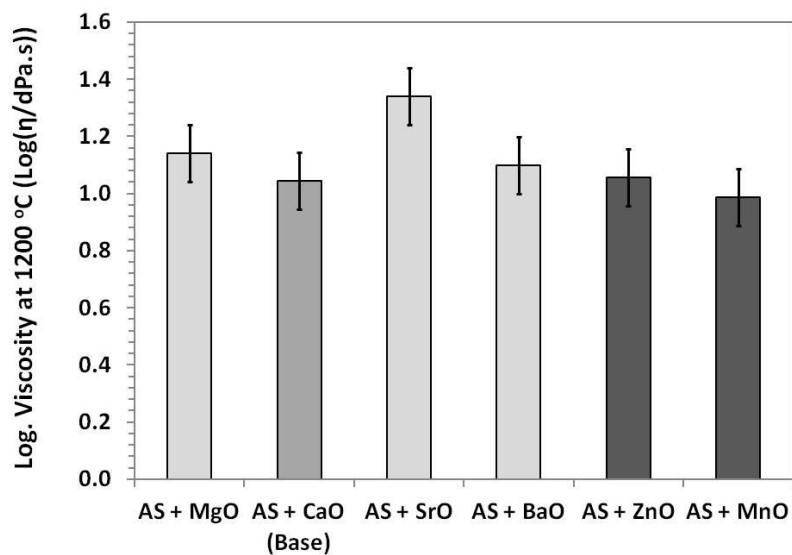


**Figure 3.1.11.** Variation in log (viscosity) at 1200 °C over the CaO replacement series. Error determined from experimental errors associated with measurement.

The  $\log \eta$  for the CaO replacement samples was found to vary by a significant extent in only a few samples, indicating that the replacement of CaO has little effect upon the viscosity of the samples. The most significant variations in viscosity occurred in relation to the SrO sample which demonstrated a significantly higher viscosity relative to the other samples in the series and a smaller increase seen in the MgO sample which can be connected to observations made in the previous series which connected alkaline-earth components with a smaller ionic radius with higher viscosities. The measured  $\log$  (viscosity) of each sample at 1200 °C is shown in figure 3.1.11.

Both alkali-earth replacement samples (MgO and SrO) showed evidence of a small increase in the proportion of iron present as  $\text{Fe}^{2+}$  ( $5 \pm 2$  %). In both the MnO and ZnO samples the Fe content was determined to be fully oxidised  $\text{Fe}^{3+}$ . In the case of ZnO this implies that the overall divalent modifier content of the sample may have resulted in an increased basicity, leading to lower fraction of  $\text{Fe}^{2+}$  species, in agreement with previous studies<sup>(59-60)</sup>. Figure 3.1.12 shows the variation in overall  $\text{Fe}^{2+}$  content in the samples. Mutual redox interactions between Fe and Mn can be expected to occur in the MnO-doped sample and support the oxidation of all Fe by Mn to the  $\text{Fe}^{3+}$  state.

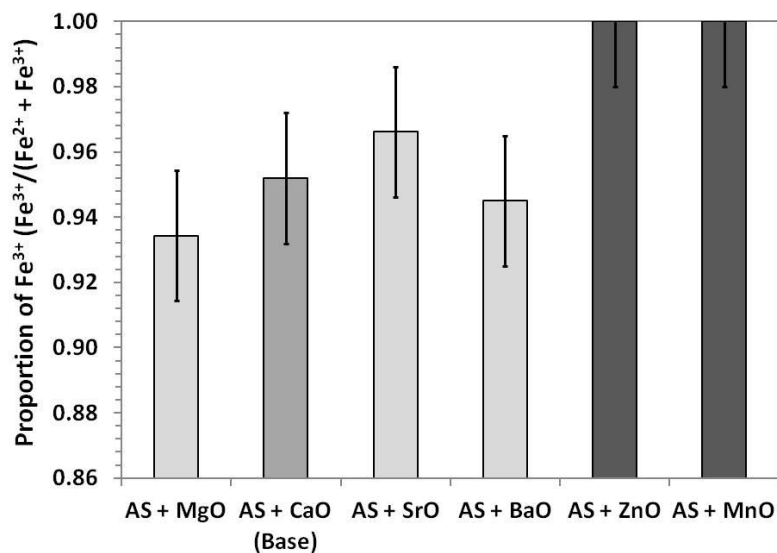


**Figure 3.1.12.** Comparison of Fe oxidation state in across Ca replacement series. Derived from Lorentzian fitting of Mössbauer spectra. Error bar represents three standard deviations, derived from three independent measurements.

FT-IR spectra of the CaO replacement samples demonstrated distinct  $Q^2$  and  $Q^3$  bands. A clear variation in the relative intensity of the  $Q^2$  band relative to the  $Q^3$  band was apparent, with increasing BaO content. The MgO, ZnO and MnO replacement samples showed a similar  $Q^2$  and  $Q^3$  distribution to the base glass. The SrO sample shows a distinct shift in the apparent position of the  $Q^2$  and  $Q^3$  bands. This could be attributable either to a shift in Q-speciation due to a move towards higher order polymerisation or to a shift in the position of the  $Q^n$  bands themselves due to changes in modifier to oxygen bond length. It is possible that the latter effect may contribute to the anomalous viscosity behaviour of the SrO sample, however further investigation would be required to confirm this hypothesis. The FT-IR spectra are shown in figure 3.1.13.

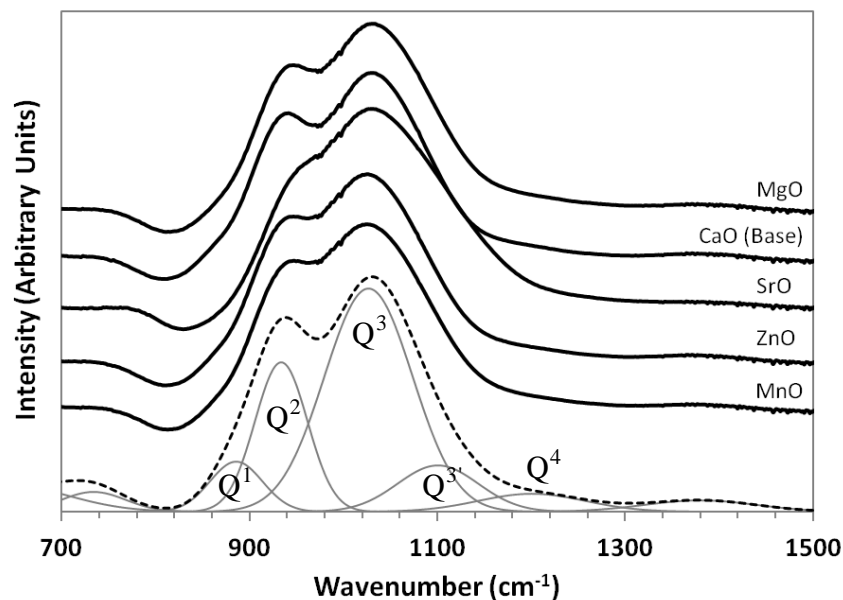


**Figure 3.1.13.** FT-IR spectra of samples from the Ca replacement series. Fitting bands and convolution displayed below.

### 3.1.2.3 Variation in content of alkali species ( $Na_2O$ and $Li_2O$ )

The alkali variation series consisted of four samples with alkali oxide content ranging from 0 to 12 mol%. These samples were compared against the base glass which has an alkali oxide content of ca. 13.4 mol%. X-ray diffraction revealed the glasses produced to be amorphous within the limit of detection, estimated at 5 % of crystalline material by volume.

The density,  $T_g$  and  $T_{liq}$  were determined utilising the methods already discussed. The density of the alkali variation series was determined to decrease in proportion to the increase in alkali oxide content in the composition, as shown in Figure 3.1.14. This is in good agreement with previous work on similar systems<sup>(57)</sup> wherein a decrease in the average relative molecular mass of the components of the system led to a decrease in the density of the system.

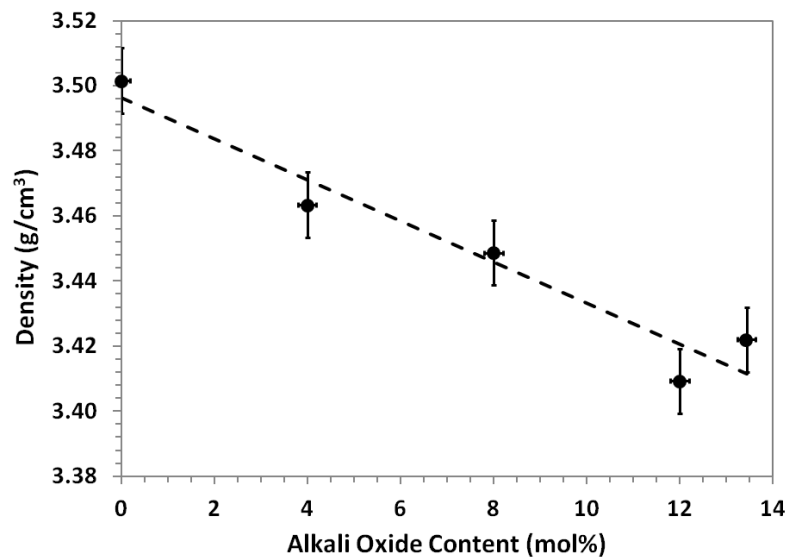


**Figure 3.1.14.** Variation in density across the  $R_2O$  variation series. Error bars correspond to three deviations on measured density. Composition error determined from error associated with of EDS analysis.

$T_g$  was found to vary in inverse proportion to the relative content of alkali elements in the glass composition, achieving a  $T_g$  temperature of  $657 \pm 5$  °C, approximately 175 °C above the  $T_g$  of the base glass composition at 0 mol% alkali oxide content. Figure 3.1.15 shows the variation in  $T_g$  across the series.

$T_{liq}$  was to vary over a range of  $263 \pm 10$  °C across the alkali replacement series, increasing with depletion of alkali species from the system, as shown in Figure 16. A maximum value of  $1245 \pm 10$  °C was reached with the complete removal of alkali elements from the system. This behaviour is consistent with the general understanding of the  $T_{liq}$  reducing effect of alkali elements in silicate glass systems<sup>(59)</sup>.

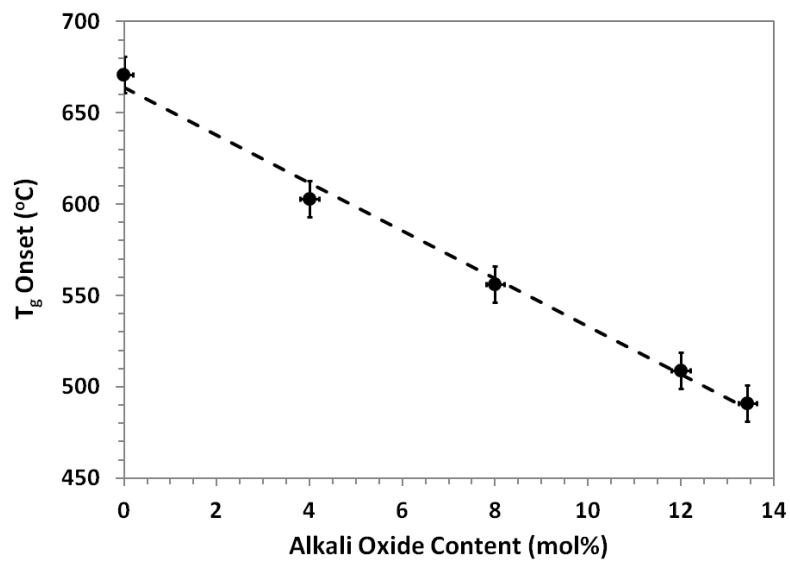


**Figure 3.1.15.** Variation in  $T_g$  onset across the  $R_2O$  variation series. Error based on experimental error associated with technique and fitting. Composition error determined from error associated with of EDS analysis.

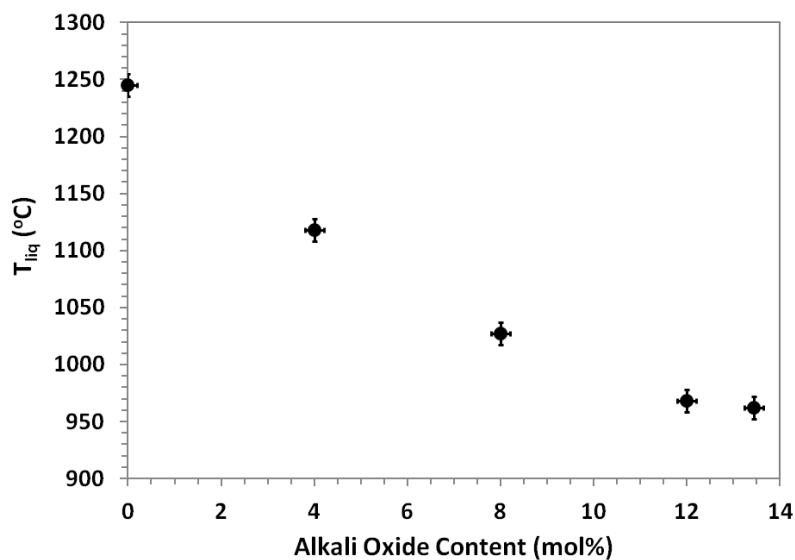


**Figure 3.1.16.** Variation in  $T_{liq}$  across the BaO : CaO variation series. Error determined from experimental error associated with technique and fitting. Composition error determined from error associated with of EDS analysis.

The log (viscosity) increased in proportion with the reduction of the alkali content of the samples. This is consistent with accepted convention<sup>(47)</sup> since the reduction of alkali species in the system results in an increase in the proportion of the overall SiO<sub>2</sub> content, increase in the average value of Q and the overall network connectivity, and hence increased viscosity. The viscosities of the samples considered remain within acceptable limits for vitrification at higher temperatures. The variation in the change in viscosity per unit temperature in this series can be seen in figure 3.1.17.

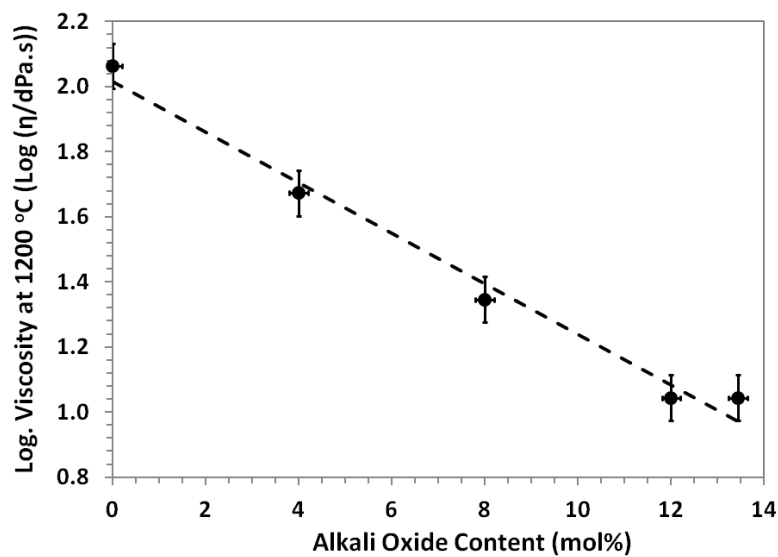


**Figure 3.1.17.** Variation in the viscosity change per unit temperature over the R<sub>2</sub>O variation series. Error determined from experimental errors associated with measurement. Composition error determined from error associated with of EDS analysis.

Mössbauer spectroscopy carried out on all samples in the series indicated no change in overall Fe oxidation state within the limits of error associated with the technique. All samples showed a uniform Fe<sup>3+</sup> / (Fe<sup>3+</sup> + Fe<sup>2+</sup>) ratio of 0.96 ± 0.02 consistent with results from both other series.

FT-IR spectroscopy showed that the Q<sup>2</sup> band varied in intensity in a linear relationship to the alkali content of the glass composition. The Q<sup>2</sup> band can be seen in figure 3.1.19 to be most apparent in the high alkali content samples, and almost absent in the alkali depleted sample. In parallel to this, it can be seen, in figure 3.1.18, that the Q<sup>3</sup> band shifts to a lower wavenumber with the removal of alkali oxides from the composition.

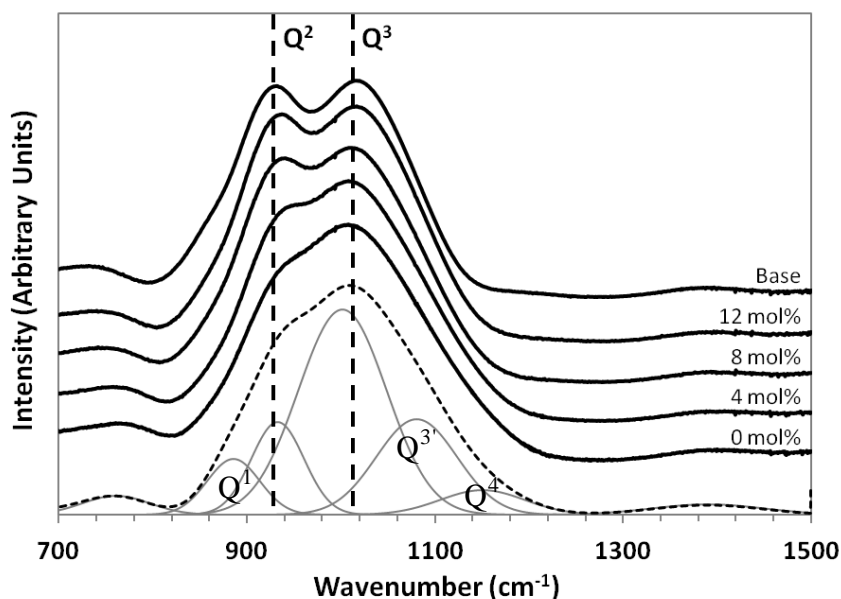


**Figure 3.1.18.** FT-IR spectra of samples from  $R_2O$  variation series. Lines serve as guide for eyes, marking  $Q^2$  and  $Q^3$  band. Bands used for fitting and convolution displayed below.

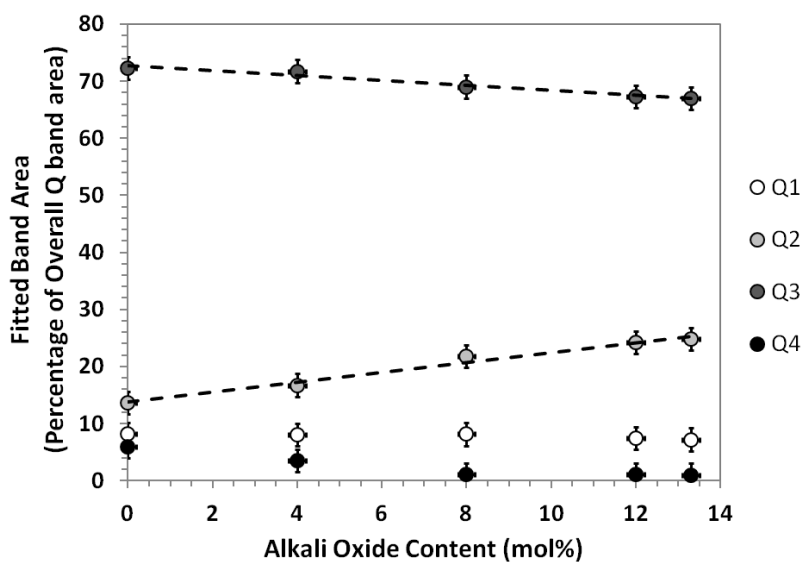


**Figure 3.1.19** Variation in proportion of  $Q^n$  bands against alkali content of sample, determined by the fitting of  $Q^n$  bands with Gaussian line-shapes. Error determined from deviation of fit. Composition error determined from error associated with of EDS analysis. Line is guide for the eyes only.

### 3.1.2.4 Fe-free solid-state NMR series

In order to obtain solid state NMR data for the compositional series studied it was necessary to produce samples which were identical in composition but with the omission of Fe<sub>2</sub>O<sub>3</sub>, since paramagnetic effects associated with Fe nuclei are known to interfere with MAS NMR. These glasses were produced using the same techniques as the samples in the original series and were subjected to the full range of characterisation techniques. The samples were found to exhibit identical trends across T<sub>g</sub>, T<sub>liq</sub>, change in viscosity and density as were observed for the Fe containing samples.

#### 3.1.2.4.1 <sup>29</sup>Si, <sup>27</sup>Al and <sup>11</sup>B MAS NMR

Considering the variation in ratio of alkaline-earth (BaO and CaO) species it was seen that the <sup>29</sup>Si NMR provided further information on the distribution of the Si Q units, supporting the observations made in FT-IR spectroscopy in that a small but statistically significant increase in the Q<sup>2</sup> band was indicated with the increasing proportion of BaO in the system. Figure 3.1.20 shows the variation in Q unit speciation as determined by <sup>29</sup>Si NMR. While there is broad agreement between FT-IR and <sup>29</sup>Si NMR results concerning the distribution of Si Q units on composition, it is notable that there are some small differences between the exact Q speciation determined by the two techniques. This difference can be attributed to the absence of Fe in the samples studied utilising <sup>29</sup>Si NMR, which impacts the proportion of network modifying species in the system. Furthermore, <sup>29</sup>Si NMR is a direct probe of Si speciation, since it is sensitive to the local environment of the resonating Si nuclei. In contrast, FT-IR spectroscopy is an indirect probe of Si speciation since it is sensitive to the vibrational frequency of Si-O bonds (which may be significantly influenced by the nature of charge balancing species in the case of non-bridging oxygen atoms). Consequently, the <sup>29</sup>Si NMR data are considered more reliable, where available.

<sup>11</sup>B NMR results indicated the proportion of the boron population in 3 or 4 fold coordination, N<sup>3</sup> and N<sup>4</sup> respectively. This is typically expressed as the boron ratio (N<sub>4</sub>/N<sub>3</sub>). The boron ratio, as determined from fitting of the <sup>11</sup>B NMR, is shown in figure 3.1.21. It can be seen that the ratio generally increases across the series, in proportion to an increased content of BaO, indicating an increase in the proportion of the more polymeric BO<sub>4</sub> units. This can be shown to be consistent with the work of Zhao *et al*<sup>(50)</sup> and Islam *et al*<sup>(58)</sup> in which increased proportions of BO<sub>4</sub> units were reported to occur in response to the increase availability of units available for the charge compensation of BO<sub>4</sub> units. The increased

proportion of NBOs made available from the decrease in polymerisation of the silicate network, as the content of BaO increases across the series, could provide the necessary charge compensation for the  $\text{BO}_4$  units. The direct influence of the ratio of BaO to CaO can be discounted since the work of Feller *et al*<sup>(63)</sup> shows that charge compensation of  $\text{BO}_4$  units is equally shared by  $\text{Ba}^{2+}$  and  $\text{Ca}^{2+}$  ions.

$^{27}\text{Al}$  NMR indicated the presence of Al in 3 co-ordination states across the series (4, 5 and 6 coordinated Al). A significant non-linear trend in the proportion of  $^{6}\text{Al}$  was apparent across the series, achieving a maximum point at a ratio of  $0.75 \pm 0.07$  BaO : (CaO + BaO). This point closely matches the point at which the minimum  $T_{\text{liq}}$  was observed. Aside from this, a general trend was observed in a small reduction in the proportion of  $^{5}\text{Al}$  and a slight increase in  $^{4}\text{Al}$  on increasing proportion of BaO. Variation in Al co-ordination is shown in figure 3.1.22. These results are atypical of alkali rich borosilicate compositions in which a large proportion of  $^{4}\text{Al}$  is typical<sup>(51)</sup>.

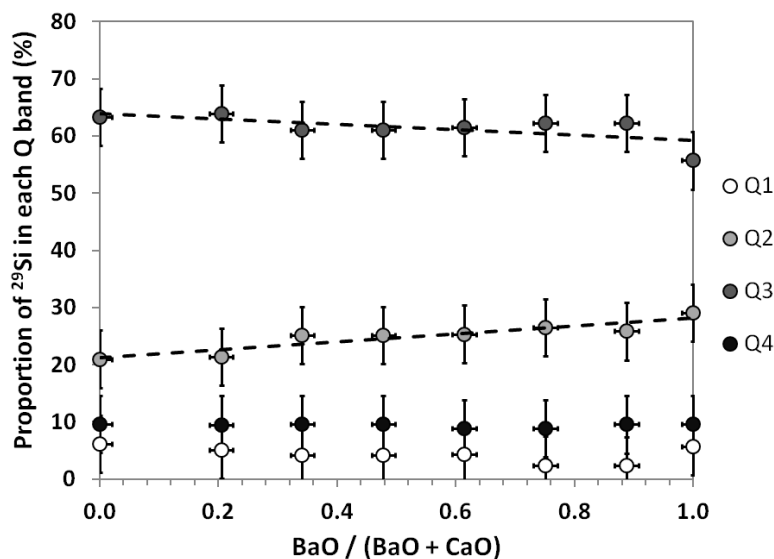


**Figure 3.1.20.** Variation in  $Q^n$  speciation as determined from fitting of  $^{29}\text{Si}$  MAS NMR with Gaussian line-shapes. Error derived from systematic error associated with fitting. Composition error determined from error associated with of EDS analysis.

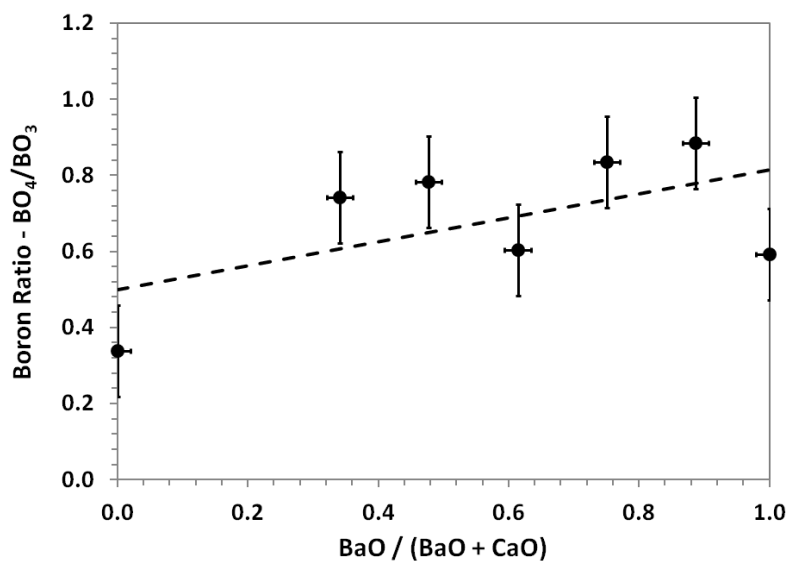


**Figure 3.1.21.** Variation in boron ratio ( $\text{BO}_4/\text{BO}_3$ ) as determined from fitting of  $^{11}\text{B}$  MAS NMR with Gaussian line-shapes. Error derived from systematic error associated with fitting. Composition error determined from error associated with of EDS analysis.

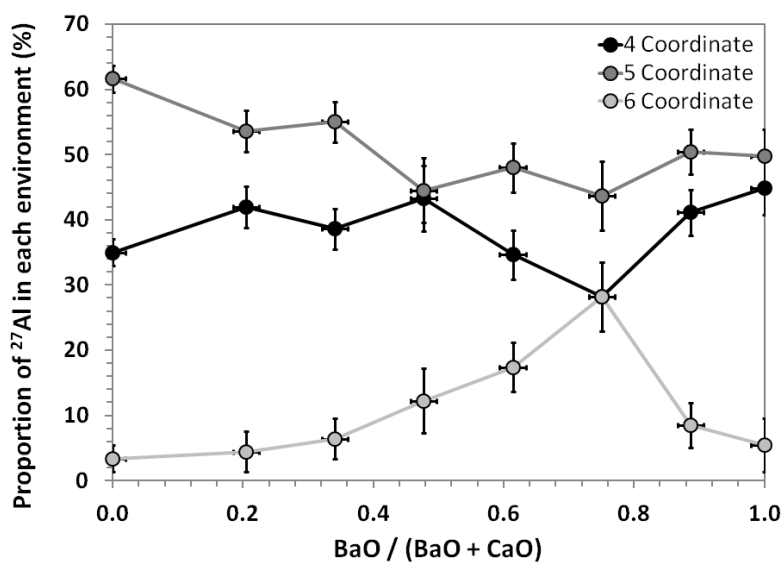


**Figure 3.1.22.** Variation in Al co-ordination as determined from fitting of  $^{27}\text{Al}$  MAS NMR with Gaussian line-shapes. Error derived from systematic error associated with fitting. Composition error determined from error associated with of EDS analysis.

Considering the replacement of CaO with divalent oxides it was seen that the  $^{29}\text{Si}$  NMR results for the ZnO, SrO and MgO replacement indicated no significant variation in Si  $Q^n$  speciation compared to the corresponding base glass composition (the MnO replacement sample was not investigated, due to the paramagnetic nature of MnO). As such the observed variation in FT-IR bands in the SrO replacement composition must be attributable to a shift in the wavenumber position of the  $Q^n$  bands themselves (due to change the vibrational frequency of Si-O bonds) rather than a change in the proportion of Q units in different environments.

$^{11}\text{B}$  NMR results showed a small degree of variation between the samples in terms of  $N^4 / N^3$  ratio, as shown in figure 3.1.23. All CaO replacement samples presented higher  $N^4 / N^3$  ratio values than were seen in the initial glass system, with the exception of the SrO sample which showed no significant variation compared to the base glass composition within statistical limits. This shows that a greater proportion of  $\text{BO}_4$  units are present in the Zn, Ba and Mg samples.

$^{27}\text{Al}$  NMR indicated a range of Al environments were present across the series, as shown in Figure 3.1.24. In the alkaline-earth replacement sample it is apparent that as the mass of the replacing alkaline-earth elements increases the proportion of Al in 5 or 6 coordination increases and 4 coordinated Al decreases. In considering the ZnO sample it is apparent that a higher proportion of 4 coordinate Al is present than in any other sample in all three series.

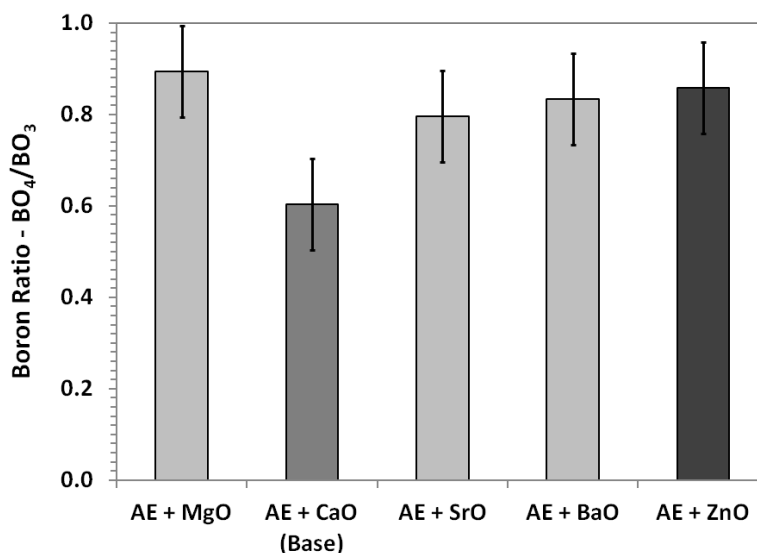


**Figure 3.1.23.** Variation in boron ratio ( $\text{BO}_4/\text{BO}_3$ ) as determined from fitting of  $^{11}\text{B}$  MAS NMR with Gaussian line-shapes. Error derived from systematic error associated with fitting.

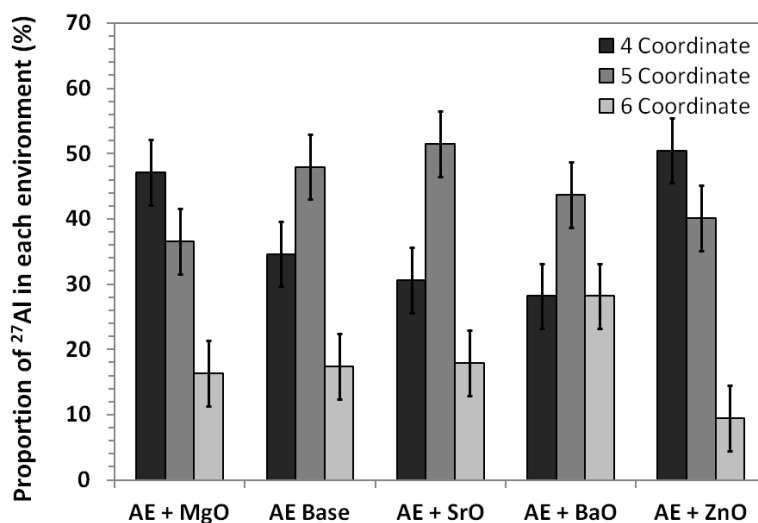


**Figure 3.1.24** Variation in Al co-ordination as determined from fitting of  $^{27}\text{Al}$  MAS NMR with Gaussian line-shapes. Error derived from systematic error associated with fitting.

In considering the variation in the content of alkali species  $^{29}\text{Si}$  NMR showed a clear trend in  $\text{Q}^n$  speciation in response to the variation of alkali content in the system. It can be seen that as the proportion of alkali in the system increases, the  $\text{Q}^2$  band increases and the  $\text{Q}^3$  band decreases in area, indicating a decrease in network polymerisation. This trend can be seen in figure 3.1.25. This result is in good agreement with the trend seen in the FT-IR spectroscopy, although there is some difference in the exact proportion of  $\text{Q}^n$  species. This can be attributed to the absence of Fe from those samples investigated by NMR spectroscopy, as well as the direct / indirect nature of the NMR/FT-IR probes of glass structure.

$^{27}\text{Al}$  NMR results show a complex compositional dependence of Al co-ordination environment, as evident in Figure 3.1.26. With increasing alkali content the proportion of 4 coordinate Al increases from  $30 \pm 2\%$  at 0 mol%  $\text{R}_2\text{O}$  to  $39 \pm 2\%$  at 8 mol%  $\text{R}_2\text{O}$ . This then decreases to a value of  $36 \pm 2\%$  at 12 mol% alkali content. There is a similar increase in 6 coordinate Al, increasing from  $30 \pm 2\%$  at 0 mol%  $\text{R}_2\text{O}$  to  $39 \pm 2\%$  at 8 mol% before decreasing to  $17 \pm 2\%$  at 12 mol%  $\text{R}_2\text{O}$ . 5 coordinate Al exhibits an increase in proportion across the series from to  $32 \pm 2\%$  at 0 mol%  $\text{R}_2\text{O}$  to  $48 \pm 2\%$  at 12 mol%  $\text{R}_2\text{O}$ .

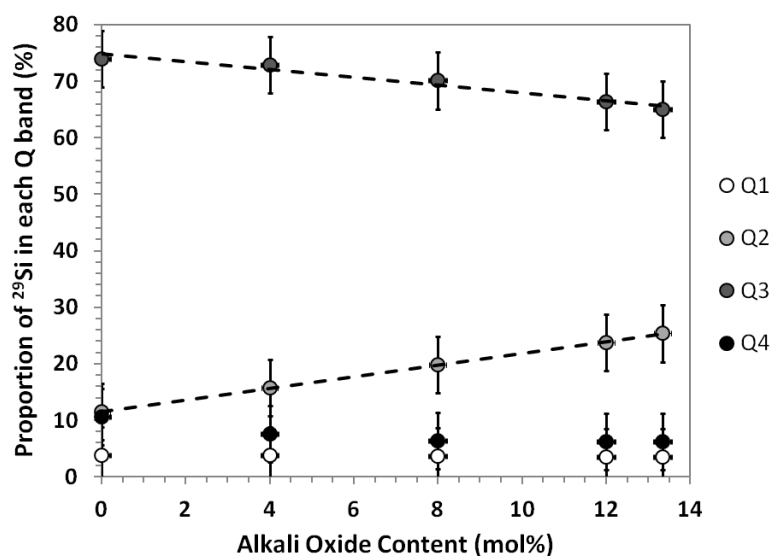


**Figure 3.1.25.** Variation in Q speciation across R<sub>2</sub>O variation series as determined from fitting of <sup>29</sup>Si MAS NMR with Gaussian line-shapes. Error derived from systematic error associated with fitting. Composition error determined from error associated with of EDS analysis. Lines are guide for the eyes only.

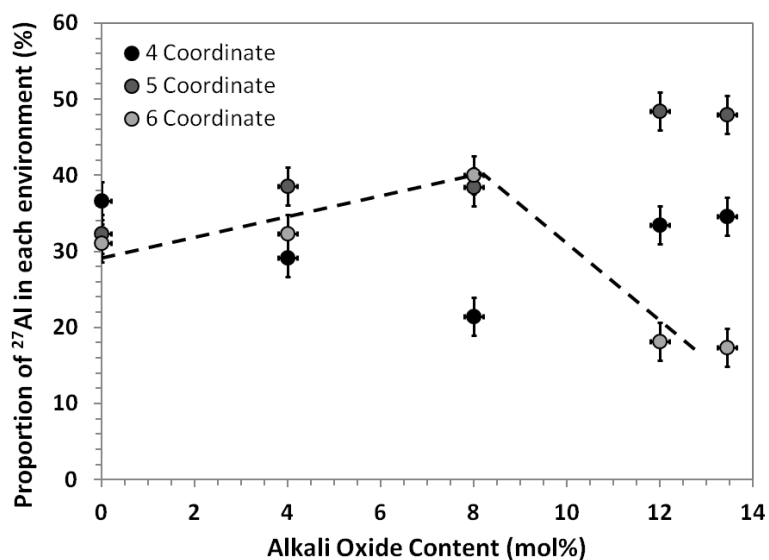


**Figure 3.1.26.** Variation in Al co-ordination across R<sub>2</sub>O variation series as determined from fitting of <sup>27</sup>Al MAS NMR with Gaussian line-shapes. Error derived from systematic error associated with fitting. Composition error determined from error associated with of EDS analysis. Line serves as guide to eyes only.

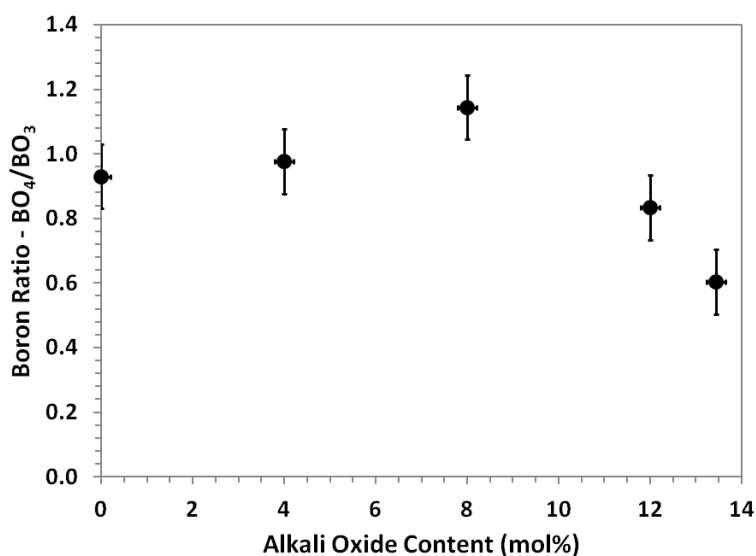


**Figure 3.1.27.** Variation in boron ratio ( $\text{BO}_4/\text{BO}_3$ ) as determined from fitting of  $^{11}\text{B}$  MAS NMR with Gaussian line-shapes. Error derived from systematic error associated with fitting. Composition error determined from error associated with of EDS analysis.

$^{11}\text{B}$  MAS NMR results showed a small, but statistically significant, variation across the series which was roughly proportional to the observations made in  $^{41}\text{Al}$  and  $^{67}\text{Al}$ . A boron ratio of  $0.93 \pm 0.1$  was determined at 0 mol%  $\text{R}_2\text{O}$ , which increased up to a maximum of  $1.15 \pm 0.1$  at 8 mol%  $\text{R}_2\text{O}$  before dropping down to  $0.83 \pm 0.1$  at 12 mol%  $\text{R}_2\text{O}$ . This variation can be seen in figure 3.1.27.

#### 3.1.2.4.2 $^{23}\text{Na}$ and $^7\text{Li}$ MAS NMR

Considering the variation in ratio of alkaline-earth component species the fitting of the  $^{23}\text{Na}$  MAS NMR and  $^7\text{Li}$  MAS NMR showed that the chemical shift of the NMR signals varied by a statistically significant amount across the series. It can be seen from figures 3.1.28 and 3.1.29 that on increasing the proportion of BaO in the system (from full CaO) the chemical shift increased, from -13.5 ppm to -10.3 ppm ( $\pm 0.5$ ) for  $^{23}\text{Na}$  and from 0.45 ppm to 1.10 ppm ( $\pm 0.1$ ) for  $^7\text{Li}$ . Based on the analysis of Angeli *et al.* this increase in chemical shift is consistent with a decrease in Li-O and Na-O bond lengths, with increasing BaO content up to  $\text{BaO} : (\text{CaO} + \text{BaO}) = 0.75 \pm 0.10$ <sup>(52)</sup>.

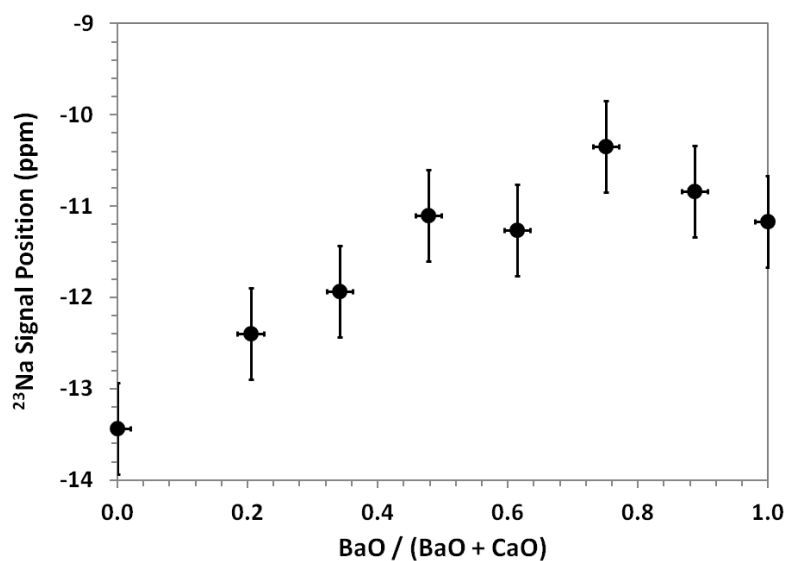


**Figure 3.1.28.** Variation in <sup>23</sup>Na MAS NMR band position across the BaO : CaO variation series. Bands fitted with Gaussian line-shape. Error derived from systematic error associated with fitting. Composition error determined from error associated with of EDS analysis.

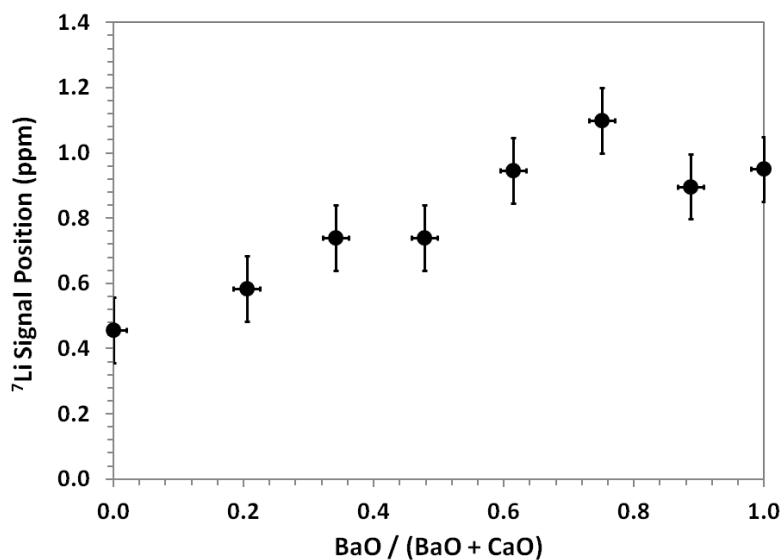


**Figure 3.1.29.** Variation in <sup>7</sup>Li MAS NMR band position across the BaO : CaO variation series. Bands fitted with Gaussian line-shape. Error derived from systematic error associated with fitting. Composition error determined from error associated with of EDS analysis.

Considering the replacement of CaO with divalent oxides  $^{23}\text{Na}$  NMR revealed significant differences between the initial system and the MgO and ZnO samples from the replacement series, as shown in figure 3.1.30. These samples show a significant increase in the chemical shift of  $^{23}\text{Na}$  from  $-11.3 \pm 0.5$  to  $-9.0 \pm 0.5$  ppm for the MgO sample and to  $-9.4 \pm 0.5$  ppm for the ZnO sample. Following the analysis of Angelie *et al.* this indicates a decrease in Na-O and Li-O bond lengths in these samples<sup>(52)</sup>. In contrast, the chemical shift of  $^{23}\text{Na}$  showed no variation within statistical limits for the SrO sample.  $^7\text{Li}$  NMR indicated that there was no significant variation in the signal position across the samples, within the limits of error.

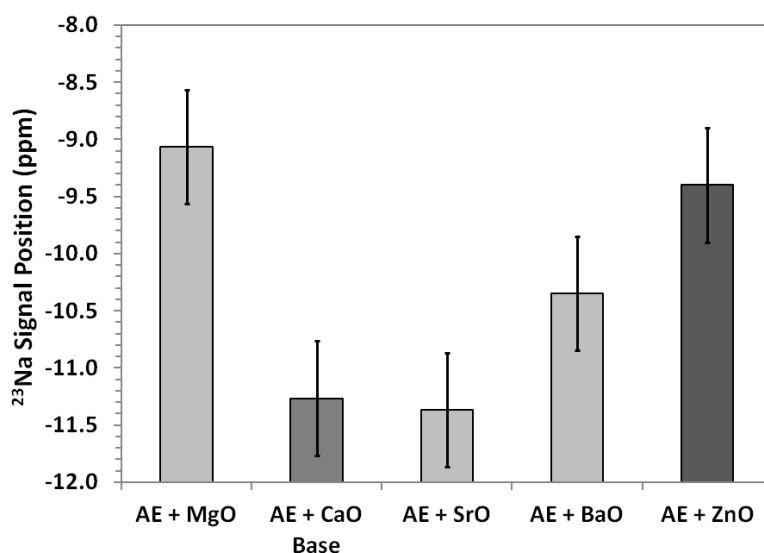


**Figure 3.1.30.** Variation in  $^{23}\text{Na}$  MAS NMR band position across the Ca replacement series. Bands fitted with Gaussian line-shape. Error derived from systematic error associated with fitting.

Considering the variation in the content of alkali species  $^{23}\text{Na}$  and  $^7\text{Li}$  NMR was undertaken on all samples in the alkali variation series with the exception of the 0 mol%  $\text{R}_2\text{O}$  sample, due to the lack of  $\text{Na}_2\text{O}$  or  $\text{Li}_2\text{O}$ . Fitting of  $^{23}\text{Na}$  and  $^7\text{Li}$  NMR fitting indicated that there was no statistically significant variation in chemical shift, within the limits of precision.

### 3.1.3 Discussion

#### 3.1.3.1 Variation of alkaline-earth component composition

Varying the proportion of BaO and CaO in the base glass system was found to have a significant effect on the  $T_g$ ,  $T_{liq}$ , change in viscosity, density and glass structure. In the context of ion exchange resin waste vitrification, the most interesting result of the series can be seen in the variation in  $T_{liq}$ , specifically in the +4 mol% BaO sample which exhibits a reduction in  $T_{liq}$  of  $\sim 80$  °C. This decrease in  $T_{liq}$  potentially translates to a reduced minimum melting temperature for the glass, which has the potential for increasing the retention of  $^{137}\text{Cs}$  by the system. This minimum in  $T_{liq}$  is supported by the work of Toropov *et al.*<sup>(60)</sup> in which a similar minimum  $T_{liq}$  is reported in a CaO, BaO, SiO<sub>2</sub> ternary system.

The trend apparent in  $^{61}\text{Al}$  shows an increase in the proportion of  $^{61}\text{Al}$  to a maximum at  $\text{BaO} / (\text{CaO} + \text{BaO}) \approx 0.75$ , followed by a sharp decrease. This is roughly inversely proportional to the observed composition dependence of  $T_{liq}$ . Similarly, in both  $^{23}\text{Na}$  and  $^7\text{Li}$  MAS NMR the chemical shift of the NMR signal can be seen to increase up to a maximum point again at  $\text{BaO} / (\text{CaO} + \text{BaO}) \approx 0.75$ . Based on the work of Toplis *et al.*, Angeli *et al.* and Mysen *et al.*<sup>(51-53)</sup> these results can be interpreted in terms of variation in the extent to which the bond forming tetrahedra are distorted by highly charged cations.  $^{61}\text{Al}$  forms only in the absence of alkali elements which are required for the charge compensation of  $^{41}\text{Al}$  in silicate networks, or in networks where charge compensation of  $^{41}\text{Al}$  is not possible due to changes in network coordination. Since  $\text{Na}^+$  and  $\text{Li}^+$  cations are abundant in the system it is plausible that the increase in  $^{61}\text{Al}$  observed is attributable to a change in the coordination of the alkali species present in the glass system. It is implied by the results that the combination of  $\text{Ca}^{2+}$  and  $\text{Ba}^{2+}$  cations effect the coordination of alkali species in the glass leading to a minimum in average alkali coordination at  $\text{BaO} / (\text{CaO} + \text{BaO}) \approx 0.75$ . This minimum results in alkali cations being unavailable for coordination with  $\text{Al}^{3+}$  producing an increased proportion of  $^{61}\text{Al}$  in the glass and also resulting in increased alkali to oxygen bond lengths as shown by the NMR results. Where these increased bond lengths may contribute to the decreases in  $T_{liq}$  and  $T_g$  which were observed as  $\text{BaO} / (\text{CaO} + \text{BaO}) \approx 0.75$  it is unlikely that they are solely responsible, since the eutectic in the BaO-CaO-SiO<sub>2</sub> ternary system, as described by Toropov *et al.*<sup>(60)</sup> exists in the absence of alkali species. It is probable that the decrease in  $T_{liq}$  observed in these glass compositions occurs due to the same effects which produce the eutectic in the BaO-CaO-SiO<sub>2</sub> ternary system. It is not possible to provide a

detailed explanation for this minimum in  $T_{\text{liq}}$  without obtaining additional detailed structural and coordination information for the alkaline-earth constituents of the glass.

The observed variation in the  $T_g$  can also be attributed in part to the effect of the mixing of differently sized alkali-earth cations. Over the range from full CaO to BaO / (CaO + BaO)  $\approx$  0.6 the decrease in  $T_g$  can be attributed directly to the effect of the BaO addition, which is known to reduce  $T_g$  due to its lower enthalpy of formation in relation to CaO<sup>(58)</sup>. The invariance in  $T_g$  observed from BaO / (CaO + BaO)  $\approx$  0.6 to full BaO can be attributed to the decrease in the average coordination of the alkali cations due to the increased BaO content which has been noted as having the effect of increasing  $T_g$ <sup>(58)</sup>, mitigating the decrease caused by the enthalpy of formation for BaO.

Density and change in viscosity over temperature both show linear trends in response to the replacement of CaO with BaO. The density can be seen to increase with increasing proportion of BaO, in agreement with the work of Stebbins *et al.*<sup>(61)</sup> and relative atomic mass of the alkaline earth species. This result can be correlated with variation in the polymerisation of the silicate network as evidenced by the FT-IR and <sup>29</sup>Si MAS NMR results. FTIR and <sup>29</sup>Si NMR both show an increase in the Q<sup>2</sup> band in proportion to the overall BaO content of the system, indicating the increased formation of non-bridging oxygen atoms (NBOs) as Ba<sup>2+</sup> cations are added to the system. This is consistent with the work of Rajyasree *et al.*, Shelby *et al.* and Lee *et al.*<sup>(54-56)</sup> in which increasing proportion of Ba<sup>2+</sup> cations in analogous silicate systems resulted in bond length variation and increased in the formation of NBOs, suggesting that Ba<sup>2+</sup> cations have a greater impact on the silicate network than Ca<sup>2+</sup> cations. The work of Islam *et al.*<sup>(58)</sup> indicates that this can be associated with the larger ion size of Ba<sup>2+</sup> relative to Ca<sup>2+</sup>. The increase in the proportion on NBOs in the system translates to a decrease in the degree of polymerisation in the silicate network which provides an explanation for the decrease in viscosity due to the increased mobility of the silicate network as suggested by the model of Mysen *et al.*<sup>(64)</sup> Concurrently with this decrease in silicate network polymerisation, the <sup>11</sup>B NMR results show an increase in the proportion of BO<sub>4</sub> units, an explanation for this can be found in the work of Eremyashev *et al.*<sup>(65)</sup> and Zhao *et al.*<sup>(50)</sup> in which the same increase in NBOs indicated in the Si network similarly affects the network forming boron content of the glass, resulting in an increase in charge compensated BO<sub>4</sub>.

Finally, <sup>57</sup>Fe Mössbauer spectroscopy results show that throughout the series almost all samples show a uniform and very small reduction (~2%) of Fe<sup>3+</sup> to Fe<sup>2+</sup>. This slight Fe reduction is attributable to the high optical basicity and to the acidity of the system as

reported by Bingham *et al.*<sup>(35)</sup>. Only the full CaO sample shows a higher extent of Fe<sup>2+</sup> however it unclear why this is the case, and further data would be required.

### 3.1.3.2 Replacement of 4 mol% CaO with divalent oxides.

The replacement of a small portion of CaO in the system with other divalent oxides was found to have significant effects on the physical properties of the glass. In the context of IEX resin vitrification some of these results show modifications to physical properties which have useful potential for the optimisation of the system. Specifically, the significantly reduced  $T_{liq}$  apparent in the ZnO, MnO and MgO replacement compositions indicates that these glasses could be melted at lower temperature, potentially increasing the retention of volatile radionuclides. In addition to this, the ZnO and MnO compositions evidence increased density and uniquely show no evidence of partial Fe reduction, potentially allowing reduced waste form volumes and an increased tolerance for highly reducing melt conditions imposed by organic ion exchange resins. However, it should be noted that the change in viscosity of the MgO, MnO and ZnO samples were all increased relative to the original system, which is less helpful for IEX resin vitrification as it may inhibit the combination of resin with glass and will affect the melting character of the vitrified material.

Considering first the MgO, ZnO and MnO samples, it can be seen from the results of FT-IR spectroscopy, and from <sup>29</sup>Si NMR spectroscopy, that there is no significant change in the silicate Q<sup>n</sup> speciation as a result of the CaO replacement. This indicates that the small changes in composition do not significantly affect the silicate network polymerisation of either of the glasses. Similarly, when the results of <sup>27</sup>Al NMR spectroscopy are considered for the MgO and ZnO samples it is apparent that the samples exhibit an increased proportion of <sup>[4]</sup>Al and reduced proportions of <sup>[5]</sup>Al and <sup>[6]</sup>Al relative to the base glass. This result shows that the extent of changes to the coordination of modifier cations in the glass is reduced. The implication of both of these results is that the reduced  $T_{liq}$  observed in the MgO, MnO and ZnO samples is the result of a different mechanism to that which was seen in the first series. <sup>23</sup>Na and <sup>7</sup>Li NMR produced results indicative of reduced alkali-oxygen bond lengths and <sup>11</sup>B NMR results indicated a higher proportion of BO<sub>4</sub> units in all three compositions, this shows that the replacement of CaO with MgO, MnO and ZnO does have an effect on the glass network, causing changes to the boron and alkali co-ordination; however the Al co-ordination shows an increased availability of alkali cations, as is consistent with the work of Toplis *et al.*<sup>(51)</sup>. The reduced  $T_{liq}$  observed in the MgO, ZnO and MnO samples cannot be attributed to the same factors. It is plausible that the reduced  $T_{liq}$  seen in conjunction with the

MgO sample can be attributed to the increasingly modifying  $\text{Mg}^{2+}$  cation which would decrease the  $T_{\text{liq}}$  by virtue of its high charge density and strong oxygen bonding increasing the thermodynamic barrier to crystallisation and hence reducing its  $T_{\text{liq}}$ . However  $\text{Mn}^{2+}$  and  $\text{Zn}^{2+}$  do not possess the strong modifying character of  $\text{Mg}^{2+}$  and instead act as intermediate network forming cations<sup>(59)</sup>. It is possible that these cations may act as network formers in the system, as has been observed of  $\text{Zn}^{2+}$  in similar alkali borosilicate compositions<sup>(58)</sup>, as such they would reduce the  $T_{\text{liq}}$  through another mechanism. The reduced  $T_{\text{liq}}$  observed in the ZnO and MnO replacement samples may therefore be attributed to the action of these weak network formers on the system, which increases the thermodynamic barrier to crystallisation and hence reduce the  $T_{\text{liq}}$ . This is supported by work presented by Volf *et al*<sup>(59)</sup>. The role of  $\text{Zn}^{2+}$  and  $\text{Mn}^{2+}$  as intermediate network formers also provides an explanation for the increased  $T_g$  observed in the MnO and ZnO samples, since the  $\text{Zn}^{2+}$  and  $\text{Mn}^{2+}$  structural units, alongside the large  $\text{Sr}^{2+}$  and  $\text{Ba}^{2+}$  cations, would decrease the average coordination of the alkali and cations which is known to increase the  $T_g$  of glass systems<sup>(58)</sup>.

The increase in density seen in the MgO, MnO and ZnO sample can be attributed to two different effects. The increased density of the MnO and ZnO sample can be attributed to the higher relative atomic mass of the replacement oxide, based on the analysis by Huggins *et al*<sup>(57)</sup>. However the MgO sample possesses a lower atomic mass and as such cannot be attributed to the same argument. It is instead likely that the higher density seen in this sample may instead be attributable to the shorter bond distances associated with the small  $\text{Mg}^{2+}$  cation and its preference for tetrahedral coordination. This is supported by the work of Islam *et al* in which  $\text{Mg}^{2+}$  additions had a similar impact of the density of an alkali borosilicate sample and in which the same explanation was presented<sup>(58)</sup>.

The fully oxidised condition of the Fe content in the MnO and ZnO samples can be attributed to the effect of replacing the CaO content specifically with a transition metal cation, since the effect was not apparent in any of the glasses where CaO was replaced by another alkaline-earth cation. The effect can be explained through two mechanisms. The first possibility is that the  $\text{Zn}^{2+}$  or  $\text{Mn}^{2+}$  cation charge compensates for the  $\text{Fe}^{2+}$  present in the system since it is known that in the case of manganese additions,  $\text{Mn}^{3+}$  cations will undergo mutual redox interactions with  $\text{Fe}^{2+}$  to form  $\text{Fe}^{3+}$ <sup>(59)</sup>. Alternatively it is possible that the acidity and optical basicity of the system are reduced due to the reduction in overall alkaline-earth cation content leads to a change in the equilibrium conditions in the system with the result of decreased  $\text{Fe}^{2+}$  formation<sup>(62)</sup>.

Considering the alkaline earth replacement samples, including the AE + BaO sample derived from the first series, it is apparent in the  $^{27}\text{Al}$  NMR results that there is a linear correlation between the size of the alkaline-earth cation and the coordination of Al. This demonstrates that the effect previously described in these glasses, where alkali coordination is decreased reducing the availability of alkali cations for the charge stabilisation of  $^{[4]}\text{Al}$  tetrahedra, is related to the ionic radius of the alkaline-earth cations that are present. This trend indicates that the availability of alkali cations for Al charge stabilisation decreases in proportion to the ionic radius of the substituted alkaline-earth cation. This can be seen in figure 3.1.31.

This trend implies that steric effects or cation field effects are primarily responsible for the coordination changes observed in these samples. However, the lack of linear variation across the physical properties ( $T_{\text{liq}}$ ,  $T_{\text{g}}$ , density, viscosity) of the samples doped with alkaline-earth elements indicates that the variation in network coordination has negligible impact upon the physical properties of the glasses in comparison to other effects.

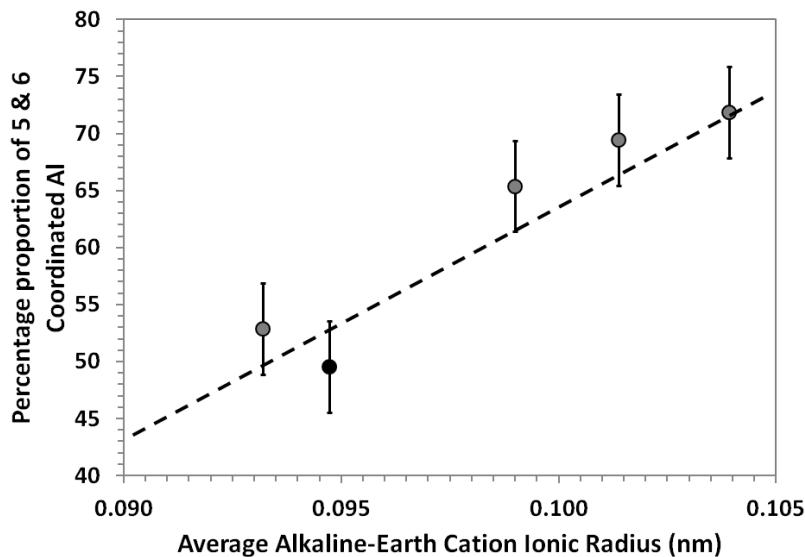


**Figure 3.3.31.** Proportion of  $^{[5]}\text{Al}$  and  $^{[6]}\text{Al}$  compared against average ionic radius of alkaline-earth (light) or transition metal (black) content as derived from literature values<sup>(66)</sup>. Error bars derived from fitting deviation. Line is guide for the eyes only.

The SrO replacement sample presents a set of unusual physical properties with respect to the other properties of the other samples in the system in that it displays a notably

increased  $T_{liq}$  and  $T_g$  which is unique amongst the samples in the series. Furthermore the FT-IR spectrum of the sample indicates Q-bands at higher wave number positions than is seen in other samples.  $^{29}\text{Si}$  NMR spectroscopy indicates that there is no significant change in the Q speciation of the system relative to the base glass; consequentially the observed shift in FT-IR spectra can only be associated to a wavenumber shift in the band position as opposed to a change in Q speciation. Further investigation is required to fully understand these issue, however, the physical properties of the SrO modified composition are not desirable for the purpose of IEX resin vitrification.

### 3.1.3.3 Variation in the content of alkali species

The removal of alkali elements from the system was found to have significant effects on the properties of the system in-line with expectations. In the context of IEX resin vitrification, none of the compositions produced in the series represent improvements on the original system in themselves. However, samples with 8 mol%  $\text{R}_2\text{O}$  content or greater did present an increase in  $T_{liq}$  of  $\sim 60$  °C and as such may be combined with systems described in the first two series to produce a viable glass composition with reduced alkali content and therefore potentially improved durability.

On the removal of alkali content, the  $T_g$  and  $T_{liq}$  were both seen to increase significantly ( $\sim 300$  °C in  $T_{liq}$  and  $\sim 150$  °C in  $T_g$ ). These results are consistent with generally accepted theory on the interaction with alkali cations in silicate glasses. However, it was notable that the increase in  $T_{liq}$  was not in linear proportion with alkali content, creating the compositional window indicated above. The viscosity for the system was seen to significantly increase on alkali removal. This is again consistent with the work of Mysen *et al.*<sup>(64)</sup> in that increased network polymerisation increases the viscosity of the system. Finally the density of the system was seen to increase on the removal of alkali species. This is consistent with work of Stebbins *et al.*<sup>(61)</sup> as the removal of alkali species from the system leads to an increase in the average atomic mass of the system.

FT-IR spectroscopy and  $^{29}\text{Si}$  NMR both indicated that as alkali species were removed from the system the extent of network polymerisation increased. This result is again consistent with generally accepted theory since alkali cations act as network modifiers and their depletion results in an increase in the number of bridging oxygen atoms in the system and hence network polymerisation.  $^7\text{Li}$  and  $^{23}\text{Na}$  NMR data indicated no change in the alkali environment as a function of composition. In  $^{27}\text{Al}$  NMR the proportion of  $^{[6]}\text{Al}$  was seen to increase with the removal of alkali species from the system. This is consistent with the work of Toplis *et al.*<sup>(51)</sup> since alkali elements are known to stabilise  $^{[4]}\text{Al}$  and  $^{[5]}\text{Al}$ , and as such the

removal of alkalis prevents this stabilisation from occurring. The boron ratio presented a similar variation where the proportion of  $\text{BO}_4$  units was seen to decrease with the removal of alkali elements. This observation is in line with expectations based upon Zhao *et al.*<sup>(50)</sup> where alkali content is shown to be required to charge compensate  $\text{BO}_4$  units.

### 3.1.4 Conclusions

Through the various compositions development series which have been described by the work a number of glass compositions have been identified which possess properties that improve their applicability for the vitrification of ion exchange resin wastes. These compositions provide a tool kit which can be applied to the further optimisation of compositions for immobilisation of wastes from a range of ILW waste streams. Specifically it has been shown that the replacement of 4-5 mol% of CaO with BaO, MgO, ZnO and MnO can effect significant reduction in the  $T_{\text{liq}}$  of the glass, which translates to a potential reduction in  $T_{\text{melt}}$  by as much as 110 °C which should translate to concomitant improvements in the retention of volatile waste species. In addition it has been shown that replacement by MnO and ZnO results in the formation of  $\text{Fe}^{3+}$  exclusively, improving the tolerance toward reducing conditions imposed by organic ion exchange resins by increasing capacity for reduction of  $\text{Fe}^{3+}$  to  $\text{Fe}^{2+}$ . Finally, it has been shown that there is sufficient flexibility in the composition of the system to reduce the alkali content by ~30% without seriously effecting the melting characteristics of the system, potentially allowing improvements to the durability of the system. Through FTIR and NMR spectroscopy detailed insights into the origins of the changes in physical properties observed, providing the necessary information for further development of the system and linking the observed physical property changes to changes in the bonding and coordination of the glass network.

These developed compositions therefore provide a tool-box of compositions which may be used to mitigate some of the problems associated with ion exchange resin vitrification. The reduced  $T_{\text{melt}}$  associated with the MgO, ZnO, MnO and BaO enriched compositions allow vitrification at lower temperatures, reducing the proportion of volatile  $^{137}\text{Cs}$  lost to off-gasses, and these compositions with a 4 mol% decrease in alkali oxide content would produce a waste form with improved durability. The MnO or ZnO enriched compositions would provide an increased proportion of buffering against organic species, allowing increased waste loading. With these improvements to the physical properties of the original glass composition, and taking into account the favourable properties of the original composition itself<sup>(3,35,44)</sup>, it can be seen that the developed compositions represent significant

improvements upon the original composition for the vitrification of ion exchange resins wastes. Furthermore it is probable that these compositions may be applicable to a wider range of waste streams where contamination with organics, anionic and volatile species is problematic.

## Chapter 3.2 - Development of Hybrid Alkali Alkaline-Earth Silicate Glasses for the Purpose of Cs-Loaded Ion Exchange Resin Vitrification.

As described in Chapter 3.1, alkali alkaline-earth silicate glasses have been previously identified as having significant potential for the vitrification of ion exchange wastes<sup>(67)(12)</sup> due to their superior durability and high capacity for the incorporation of anionic species. The aim of this section is to further develop promising alkali alkaline-earth silicate glass compositions which were identified in Chapter 3.1. In this section, three compositions were identified to have potential for further developing the alkali alkaline-earth silicate glass system for the ion exchange resin vitrification. These compositions involved the replacement of CaO in the intermediate glass formulation with BaO and ZnO, which was shown to significantly reduce the liquidus and melting temperatures ( $T_{liq}$  and  $T_{melt}$ ), and increase the density of the system. A third composition was also described in which the overall alkali content of the system was reduced with the purpose of improving the durability of the system. In the case of the BaO and ZnO additions, the mechanisms behind the observed changes in the physical properties were identified. BaO was found to decrease the average coordination of modifier species in the glass network, leading to an average decrease bond strengths and decreasing the  $T_{liq}$ , whereas ZnO was found to decrease the  $T_{liq}$  through the effect of the  $Zn^{2+}$  cation acting as a weak network former in the glass system. Since these mechanisms are independent of each other, there is a possibility that the effects could be combined to produce a further improved composition.

This section explores these possibilities through two hybrid glass compositions (ASZ1 & ASZ2), which combine the compositional modifications previously highlighted. These glass systems are termed 'hybrid' throughout, whereas the intermediate glass systems with ZnO and BaO replacement are termed 'intermediate' throughout. The compositions of these glass systems and the original base glass composition are given in Table 3.2.1. In composition ASZ1, the replacement of CaO in the intermediate glass composition by both BaO and ZnO was explored with the aim of producing a hybrid composition with further improved physical properties. Composition ASZ2 is derived from ASZ1, with a reduced proportion of alkali oxides, with the aim of producing a hybrid composition with improved chemical durability, whilst maintaining an acceptable melting temperature.

Glasses based upon these compositions were produced and characterised in order to identify their physical properties. The ASZ1 hybrid system was found to possess a

significantly reduced  $T_{liq}$  and  $T_g$ , compared to the intermediate glass composition. The ASZ2 system showed an increased value of  $T_{liq}$  relative to the intermediate glass but this was lower than would normally be expected with a ~40% decrease in alkali content. Both hybrid systems were found to possess a significantly higher density than the previous systems, and both were found to contain a small proportion of reduced  $Fe^{2+}$ .

**Table 3.2.1.** Nominal glass compositions for all reported samples.

Sample ID	Component (mol%)								
	SiO <sub>2</sub>	B <sub>2</sub> O <sub>3</sub>	Al <sub>2</sub> O <sub>3</sub>	Fe <sub>2</sub> O <sub>3</sub>	CaO	BaO	Li <sub>2</sub> O	Na <sub>2</sub> O	ZnO
Base Glass	51.72	2.23	0.38	2.92	11.08	18.23	7.80	5.64	-
ASB	51.72	2.23	0.38	2.92	7.08	22.23	7.80	5.64	-
ASZ	51.72	2.23	0.38	2.92	6.08	18.23	7.80	5.64	5.00
ASZ1	51.72	2.23	0.38	2.92	2.08	22.23	7.80	5.64	5.00
ASZ2	54.97	2.37	0.40	3.10	2.21	23.63	4.64	3.36	5.31

### 3.2.1 Experimental Procedures

Each sample was prepared using either oxide or carbonate reagents as appropriate. All chemicals used were of a grade of purity of 99.9% or greater. These compositions were melted for three hours at 1200 °C. The melt was stirred at a rate of 30 rpm over the last two hours. The glass melt was poured into a block mould and then annealed at 500 °C for 1 hour before being allowed to cool at a rate of 1 °C per minute to room temperature. Glasses were melted in a Zr-stabilised Pt crucible and 200g of glass was produced for each sample.

Sample density was determined using Archimedes' method. De-ionised water was used for the experiment and each of the three pieces from each sample was measured independently. The density of the deionised water was corrected to allow for the ambient temperature at the time of measurement. The glass transition onset ( $T_g$ ) was determined through differential thermal analysis (DTA). DTA experiments were performed using Pt crucibles and measurements were taken automatically by a computer-operated system (Perkin Elmer DTA7).

The liquidus temperature ( $T_{liq}$ ) was determined using a tube furnace to create a temperature gradient along the length of a refractory boat containing powdered sample

material. By determining the temperature gradient along the length of the sample the  $T_{liq}$  could be determined visually by locating the position on the boat, having been air quenched, at which crystallisation was observed to occur and comparing that to the known temperature gradient. The boat was held at temperature for 24 hours in order to allow thermodynamic equilibrium to be achieved. The estimated accuracy of this method is ca.  $\pm 10$  °C.

The viscosity of the samples was determined through using a Theta Industries viscometer. This comprised a rheometer (Brookfield DV-III-Ultra) mounted above a bespoke vertically mounted electrical furnace (Theta Industries). The setup allowed for the direct measurement of the viscosity of a glass melt at temperature by means of measuring the torque exerted upon a re-crystallised alumina spindle rotating within the molten glass sample. The setup was calibrated before use by using a control fluid of known viscosity at room temperature.

Fourier transform infra-red (FT-IR) spectroscopy was applied to investigate glass structure. FT-IR spectroscopy was carried out using a Perkin Elmer Spectrum 2000 FT-IR spectrometer over the 500 - 1500 nm wavelength range. Data was collected using a reflectance set-up by which the incident laser was reflected off a polished surface of the sample. The data was subsequently corrected using a Kramers-Kronig transform. Samples were polished using SiC grinding discs and a diamond polishing suspension. FT-IR spectra were fitted with Gaussian line-shapes in order to determine the area of the absorption band which was present. The initial parameters used for fitting were constrained based upon literature values<sup>(48)(49)</sup>. An average value for the  $Q^n$  speciation of the silicate network was calculated from the normalised fractional areas of the  $Q^1$ - $Q^4$  bands by means of finding the weighted mean of the band areas (eg.  $Q^1$  equivalent to 1,  $Q^2$  equivalent to 2 etc.). The bands seen in FT-IR spectroscopy are composed of contributions from multiple oxide bonds. Due to the complexity and number of components present in the systems studied, the fitted bands can only be considered as an indicative average of the contributions associated with these multiple oxide bonds.

<sup>57</sup>Fe Mossbauer spectroscopy was carried out in order to determine the oxidation state of the Fe content of the samples. A WissEl <sup>57</sup>Fe Mossbauer spectrometer was used to collect data. The spectrometer was operated in constant acceleration mode over a range of 6 mms<sup>-1</sup> calibrated using an  $\alpha$ -Fe calibration sample. A <sup>57</sup>Co source with an activity of ~9000  $\mu$ Ci was used as a  $\gamma$ -radiation source. Mossbauer spectra were fitted using single Lorentzian line shapes to represent the Fe<sup>2+</sup> and Fe<sup>3+</sup>, using the software Recoil 1.03. The recoil free fraction was assumed to be equal in the Fe<sup>2+</sup> and Fe<sup>3+</sup> environments.

X-ray fluorescence spectroscopy (XRF) was utilised to quantify and confirm the composition of the samples which were produced. XRF experiments were performed at the Manchester University XRF facility at the School of Earth, Atmospheric and Environmental Sciences.

More detailed descriptions of these techniques are provided in appendix 8.1.

### 3.2.2 Results

The densities of both of the hybrid compositions were found to be significantly higher than the base system or either of the two intermediate compositions (ASB and ASZ). The alkali-depleted hybrid sample ASZ2 demonstrated the highest density at a value of  $3.66 \pm 0.03 \text{ gcm}^{-3}$ . The straightforward hybrid composition ASZ1 demonstrated a lower density at  $3.60 \pm 0.03 \text{ gcm}^{-3}$ . The variation in density is shown in Table 3.2.2.

The  $T_g$  onset was found to vary significantly in both of the hybrid glass compositions. ASZ1 composition demonstrated a significantly reduced value of  $T_g$  relative to the intermediate glass composition, with  $T_g = 474 \pm 5 \text{ }^\circ\text{C}$ . The ASZ2 composition presented a  $T_g = 509 \pm 5 \text{ }^\circ\text{C}$ , comparable to that of the intermediate compositions. The DTA plots can be seen in Figure 3.2.1 and the variation in  $T_g$  onset can be found in Table 3.2.2. The peak denoted as ' $T_x$ ' in Figure 3.2.1 indicates exotherms associated with the formation of a crystalline phase within the glass at the specified temperature. The  $T_{liq}$  of both hybrid systems were seen to vary significantly from the values associated with the base glass composition and the two intermediate compositions. The ASZ1 hybrid composition demonstrated a significantly reduced  $T_{liq}$  below that which was seen in either of the intermediate compositions with a value of  $802 \pm 10 \text{ }^\circ\text{C}$ . The ASZ2 hybrid demonstrated a value of  $T_{liq}$  at  $989 \pm 10 \text{ }^\circ\text{C}$ , putting it at a higher value than the base glass composition which can be attributed the decreased alkali content of the ASZ2 composition. The variation in  $T_{liq}$  is shown in Table 3.2.2. In order to discriminate between glass compositions the melting temperature ( $T_{melt}$ ) was defined as being  $50 \text{ }^\circ\text{C}$  above the  $T_{liq}$ . It should be noted that this does not take into account properties such as viscosity which also effect the temperature at which a glass can be melted. Considering the viscosity of the hybrid systems it is apparent that the ASZ1 hybrid system shows no significant change in viscosity relative to the base glass composition or to either of the intermediate glass compositions. However in considering the ASZ2 system it can be seen that there is a clear increase in the viscosity of the system, showing an increase in  $\text{Log } \eta$  from 1.04 to  $1.44 \pm 0.1 \text{ Log } (\eta / \text{ dpa.s})$ . This increase

in viscosity can be attributed to the effect of the reduced alkali content upon the composition. The variation in  $\log \eta$  is shown in Figure 3.2.2.

**Table 3.2.2.** Values of density,  $T_g$ ,  $T_{liq}$  and Viscosity in the base glass, intermediate and hybrid glass compositions.

Glass Composition	Density ( $\text{gcm}^{-3}$ )	$T_g$ Onset ( $^{\circ}\text{C}$ )	$T_{liq}$ ( $^{\circ}\text{C}$ )	Log $\eta$ at 1200 $^{\circ}\text{C}$ (Log ( $\eta/\text{dPa.s}$ ))
AS0	$3.42 \pm 0.034$	$491.0 \pm 5$	$962 \pm 10$	$1.044 \pm 0.005$
ASB	$3.54 \pm 0.031$	$503.5 \pm 5$	$890 \pm 10$	$1.099 \pm 0.005$
ASZ	$3.50 \pm 0.028$	$497.2 \pm 5$	$852 \pm 10$	$1.056 \pm 0.005$
ASZ1	$3.60 \pm 0.028$	$474.2 \pm 5$	$802 \pm 10$	$1.026 \pm 0.005$
ASZ2	$3.66 \pm 0.033$	$508.8 \pm 5$	$987 \pm 10$	$1.444 \pm 0.005$

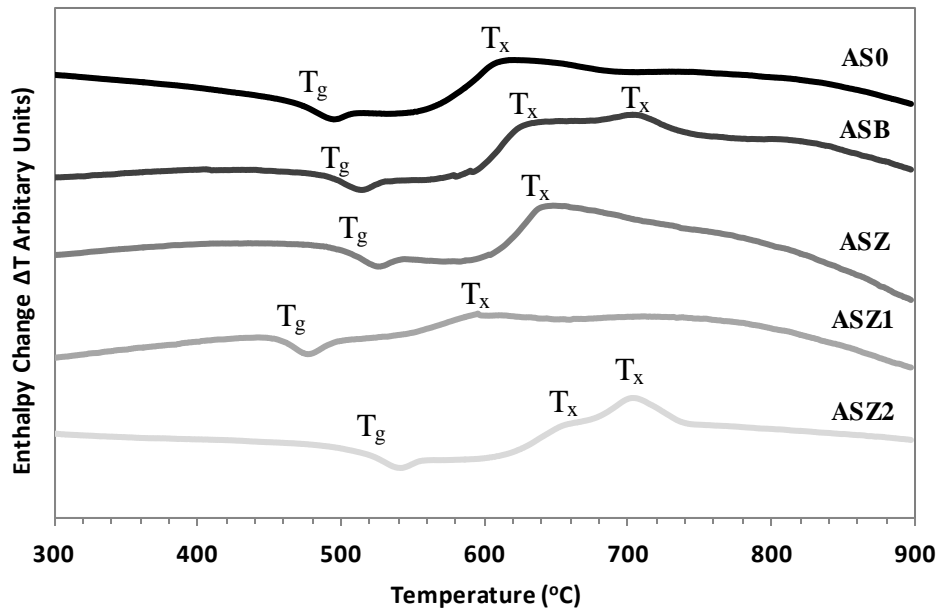


**Figure 3.2.1.** DTA plots showing variation in  $T_g$  across base glass and all four samples. Data points and error are given in Table 3.2.2.

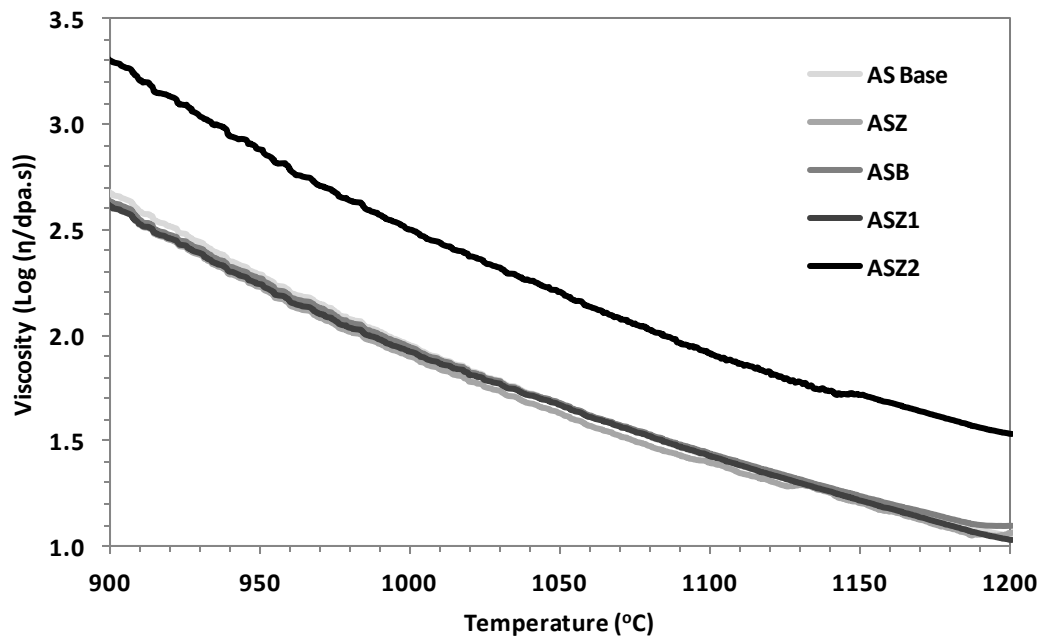


**Figure 3.2.2.** Variation in Log  $\eta$  across all samples. Data values for viscosity at 1200 °C shown in Table 3.2.2.

The FT-IR spectra obtained from the samples were fitted with Gaussian line shapes in order to determine the area associated with each absorption band. The bands were assigned based upon literature values<sup>(68)(69)(70)</sup> and an average value of  $Q^n$  speciation for the silicate Q-bands was determined through the method previously described. FT-IR results for the base glass system and the two intermediate systems demonstrated the  $Q^n$  speciation of the silicate network in these glasses to be similar, showing only a small degree of variation between the samples. As shown in Figure 3.2.3, the two intermediate systems both demonstrate a lower range of values for the Q-bands than was demonstrated by the base glass, with average  $Q^n$  speciations of  $2.804 \pm 0.005$  relative to the average  $Q^n$  speciation of the base glass  $2.821 \pm 0.005$ . Investigation of the two hybrid systems shows that these systems show a greater degree of variation relative to the base glass system, with average  $Q^n$  values for ASZ1 and ASZ2 of  $2.772 \pm 0.005$  and  $2.863 \pm 0.005$  respectively. The system ASZ1 demonstrates a significant decrease in its average  $Q^n$  speciation, indicating a decrease in the extent of polymerisation in the silicate network. With an average  $Q^n$  speciation of  $2.863 \pm 0.005$  ASZ2 demonstrates a significantly increased value of average  $Q^n$  speciation, exceeding all of the other developed glass compositions and the base glass composition. This increase in  $Q^n$  speciation can be directly correlated to the removal of network modifying alkali cations from

the system. The FT-IR spectra and average  $Q^n$  speciation as derived from the fitting of the FT-IR bands can be seen in Figure 3.2.3 and Table 3.2.3 respectively.

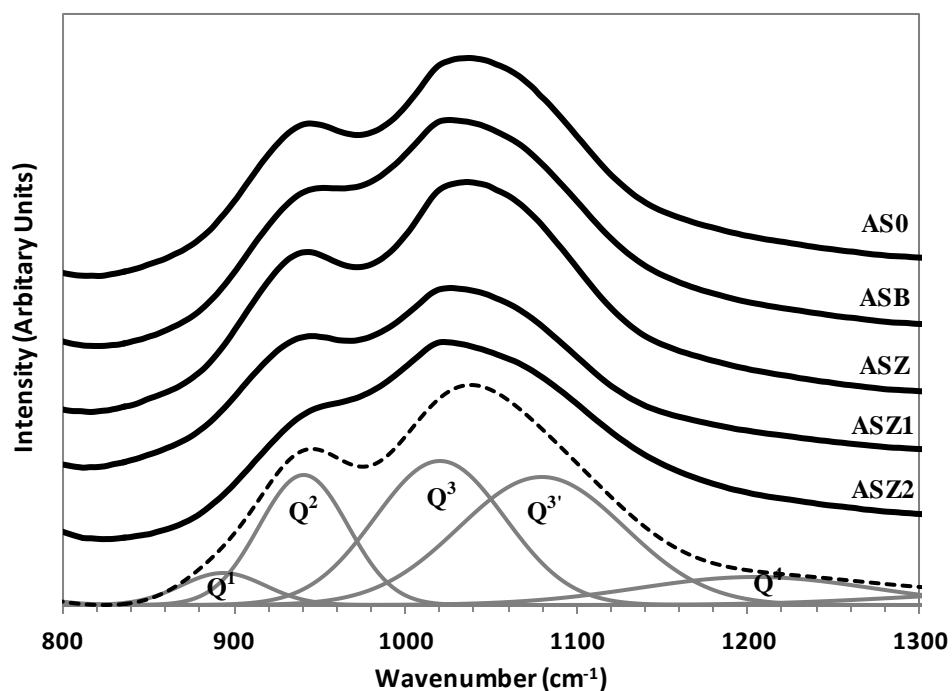


**Figure 3.2.3** FT-IR spectra of base glass, intermediate glass compositions and hybrid compositions. Fitted bands and convolution shown below.

**Table 3.2.3.** Average  $Q^n$  speciation of all developed glasses as determined from the fitting of FT-IR spectra. Hybrid systems ASZ1 and ASZ2 highlighted. Error determined from variation between fit and collected data.

Glass Composition	Avg. $Q^n$ Speciation (Avg. Si Coordination)
AS0	$2.82 \pm 0.01$
ASB	$2.80 \pm 0.01$
ASZ	$2.80 \pm 0.01$
ASZ1	$2.77 \pm 0.01$
ASZ2	$2.86 \pm 0.01$

Mossbauer spectroscopy of the all samples demonstrated the presence of a small degree of variation of proportion of Fe<sup>3+</sup> in the samples. The base glass and ASB developed glass were found to contain primarily Fe<sup>3+</sup> but evidenced a small proportion of Fe<sup>2+</sup> ( $4 \pm 2\%$  Fe<sup>2+</sup>). The ASZ glass was determined to be 100% Fe<sup>3+</sup>. The hybrid glass samples, ASZ1 and ASZ2, were found to contain primarily Fe<sup>3+</sup>. However, a low level of Fe<sup>2+</sup> was found to be present ( $3 \pm 2\%$  Fe<sup>2+</sup>). The variation between the proportion of Fe<sup>2+</sup> in the base, ASB, ASZ1 and ASZ2 glasses was not statistically significant. The Fe<sup>3+</sup> content of all glasses was found to be 6-fold coordinated, as determined from the dipole and quadrupole shift values derived from the fitting of the Mössbauer spectra with reference to the work of Darby-Dyar *et al*<sup>(71)</sup>. The precise values reported for the proportion of Fe<sup>3+</sup> and coordination can be found in Table 3.2.4. Figure 3.2.4 shows the variation in overall Fe<sup>3+</sup> content between the samples.

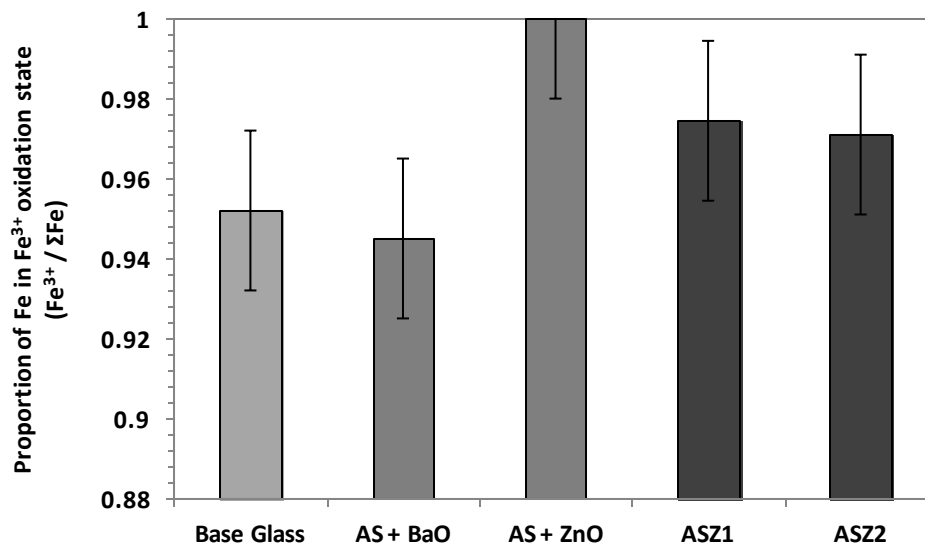


**Figure 3.2.4.** The proportion of iron in the Fe<sup>3+</sup> oxidation state in all investigated glasses. Error based on systematic error associated with fitting of Mossbauer spectra.

**Table 3.2.3.** Data from fitting of Mossbauer spectra showing coordination environment as derived from Derby-Dyar *et al*<sup>(71)</sup>.

Glass Composition	Proportion of Fe <sup>3+</sup> (Fe <sup>3+</sup> / ΣFe)	Fe <sup>3+</sup> Dipole Shift (mms <sup>-1</sup> )	Fe <sup>3+</sup> Quad. Shift (mms <sup>-1</sup> )	Fe <sup>3+</sup> Coordination
AS0	0.952 ± 0.02	0.297 ± 0.05	0.883 ± 0.05	6 fold
ASB	0.945 ± 0.02	0.312 ± 0.05	0.921 ± 0.05	6 fold
ASZ	1.0 ± 0.02	0.460 ± 0.05	1.630 ± 0.05	6 fold
ASZ1	0.974 ± 0.02	0.462 ± 0.05	1.504 ± 0.05	6 fold
ASZ2	0.971 ± 0.02	0.439 ± 0.05	1.556 ± 0.05	6 fold

### 3.2.3 Discussion

In comparing the physical properties of the hybrid glass compositions against the previously developed glass compositions it is clear that the hybrid compositions possess properties which are significantly different from those of the other systems. Notably the physical properties of the ASZ1 composition provides clear evidence for the additive nature of the effects from ZnO and BaO additions, as was previously discussed in chapter 3.1.

Considering the hybrid glasses in the context of ion exchange resin waste vitrification it is apparent that both systems possess properties which would be advantageous for the application. The ASZ1 composition demonstrated significantly reduced values of  $T_{liq}$  and  $T_g$  in comparison to both the base glass and the intermediate glass systems, demonstrating a reduction of  $160 \pm 10$  °C in the  $T_{liq}$  and a reduction of  $16.8 \pm 5$  °C in the  $T_g$ . This potentially would allow for waste vitrification to be achieved at significantly lower temperatures with benefits to both the retention of radio-caesium in the waste-form and to the operational life-span of the melter. The lack of change observed in the viscosity in this sample, along with the reduced  $T_g$ , shows that the glass should be sufficiently workable to be practical for waste vitrification. ASZ2 does not share the low  $T_{liq}$  or  $T_g$  of the previous system, and therefore lacks the obvious benefits associated with these properties. It also demonstrates an increased viscosity at melting temperatures which may impair the workability of the system. However, it should be noted that most of these properties can be associated with the 30% decrease in alkali oxide content in the compositions, relative to the other compositions investigated, and that despite this the composition demonstrates physical properties which are not far removed from those displayed by the base glass composition. The decrease in alkali oxide content should, in principle, lead to an increased chemical durability which is essential for the retention of hazardous radio-caesium. Both ASZ1 and ASZ2 demonstrate a significant increase in density relative to the other glasses. This means that a higher waste-loading, on a per unit volume basis, should be possible with these glass compositions.

The increase in density observed in the hybrid glasses is consistent with the increase in the average relative molecular mass of the glasses as suggested by Huggins *et al*<sup>(57)</sup> and Islam *et al*<sup>(58)</sup>. Since the replacement of Ca with either Ba or Zn would increase the average molecular mass of the system, the higher density of ASZ1 relative to ASB and ASZ is within expectations. The further increase in density seen in ASZ2 can be connected to the loss of low relative molecular mass alkali oxide species, which would further increase the average relative molecular mass of the system as is consistent with the work of Stebbins *et al*<sup>(61)</sup>.

The increase in viscosity observed in the ASZ2 sample can also be attributed to the reduced alkali oxide content of the system, since the reduced proportion of network modifying alkali cations in the glass allows the glass to possess a higher degree of network polymerisation. This increased degree of network polymerisation can be seen in the increased average  $Q^n$  speciation of the glass as determined by FT-IR spectroscopy. As such, these results are consistent with the work of Mysen *et al*<sup>(65)</sup> in which the increased polymerisation of the silicate network was connected with increased viscosity of the system.

The decrease in  $T_g$  and  $T_{liq}$  observed in the ASZ1 hybrid glass can be attributed to the combination of these effects which were previously described in the ASZ and AS+ BaO systems. In these systems, the reduced  $T_{liq}$  was attributed to the action of  $Zn^{2+}$  cations as weak network-forming species on the silicate network and upon the disruptive effect of the large  $Ba^{2+}$  cation upon the silicate network. The further decrease in  $T_{liq}$  in the ASZ1 glass demonstrates that both of these effects are still present in the sample, and do not appear to interact with each other in any manner which diminishes their effect upon the enthalpy of crystallisation. This allows the decrease in  $T_{liq}$  connected to both effects to be combined producing the low observed low  $T_{liq}$  of the ASZ1 glass.

The reduced value of  $T_g$  in ASZ1 is inconsistent with the raised values of  $T_g$  which were reported for the ASZ and ASB systems. However, it is consistent with the lower enthalpy of formation of both ZnO and BaO relative to CaO, since the enthalpy of oxide formation can be connected to the  $T_g$  of a glass as demonstrated by Islam *et al*<sup>(58)</sup> and as such is in line with what would be expected for the replacement of CaO with ZnO and BaO in a silicate system. The raised values of  $T_g$  reported for the ASZ and ASB was connected to the effect of the  $Zn^{2+}$  and  $Ba^{2+}$  cations on the coordination of the silicate network, which was connected to an increase in  $T_g$ . It is possible that this effect was not observed in ASZ1 due to the less polymerised silicate network of the system relative to either intermediate system as demonstrated by FT-IR, which could mitigate the effects caused by  $Zn^{2+}$  and  $Ba^{2+}$  cations on the silicate network. Further insights on the coordination of these species would be required to achieve a firm conclusion.

As with ASZ1, the changes observed in the  $T_g$  and  $T_{liq}$  of the ASZ2 glass can be connected to the combination of the  $T_{liq}$  and  $T_g$  reducing properties of the intermediate glass systems. However, these properties are further complicated by the effect of the removal of alkali oxides from the system. As such, the increased value of  $T_g$  observed in the system can be attributed to removal of the alkali oxides  $Na_2O$  and  $Li_2O$ , both of which possess a low enthalpy of formation, increasing the average enthalpy of formation for the oxide constituent

of the system. Similarly, the removal of alkali oxide phases increases the  $T_{liq}$  of the system due to the loss of their modifying effect on the silicate network, as is consistent with generally held theory<sup>(47)</sup>. The effect of the BaO and ZnO modifications effectively compensate for the increase to the  $T_{liq}$  of the glass allowing the composition to include a lower proportion of alkali oxide species whilst not significantly impairing the  $T_{melt}$  for the glass.

As has been mentioned, FT-IR spectroscopy of the hybrid glasses showed that significant variations in the average  $Q^n$  speciation were present relative to the base glass and intermediate glasses. In the case of the ASZ2 glass, the large increase in average  $Q^n$  speciation of the silicate network, which indicates an increase in the polymerisation of the silicate network, can be directly attributed to the removal of modifying alkali cations from the glass system<sup>(65)</sup>. The decrease in the  $Q^n$  speciation of the ASZ1 glass is most likely to be attributable to the combined effect of the ZnO and BaO additions present in the glass, which have been demonstrated to individually lower the  $Q^n$  speciation. This further indicates that these two modifications do not affect the impact that either has upon the physical properties of the glass to any significant extent.

Mossbauer spectroscopy of the hybrid glass systems indicated that both possessed a small proportion of reduced  $Fe^{2+}$ , although the majority of the iron content was in the  $Fe^{3+}$  oxidation state. Notably, there was no significant difference between the two hybrid systems which indicates that the alkali oxide content of the system does not have an impact upon the extent of iron reduction. It is also notable that the extent of reduction seen in the hybrid systems falls directly between the values seen in the ASB and ASZ intermediate glasses. This implies that increased overall BaO content in the hybrid glasses, relative to the ASZ glass leads to an increase in the extent of reduction in the system. This can be attributed to the slight increase in the acidity of the system which is caused by the replacement of CaO with BaO, as supported by Bingham *et al*<sup>(63)</sup>. This also shows that the charge compensating effect of the ZnO reported previously is only effective to a limited extent.

### 3.2.4 Conclusion

This work has shown that the hybrid compositions explored here, based upon previous studies of an alkali alkaline-earth silicate glass system, demonstrate superior properties for the vitrification of ion exchange resin wastes. In terms of reduced melting temperature, increased density and reduced alkali oxide content these compositions exceed what has previously been achieved in this glass system.

Specifically, the ASZ1 hybrid glass demonstrated a value of  $T_{liq}$  of  $802 \pm 10$  °C, approximately 50 °C below that of the previous low  $T_{liq}$  composition (ASZ) and approximately 160 °C below that of the base glass composition. This represents a significant improvement in that it allows vitrification at lower temperatures, potentially allowing a significant improvement in Cs retention in these types of glass. The  $T_g$  and viscosity of the system remained within acceptable parameters for the vitrification of ion-exchange resin wastes. The ASZ2 hybrid glass demonstrated a value of  $T_{liq}$  close to that of the original system ( $987 \pm 10$  °C) but also contained 40.5% less alkali oxides, which potentially would lead to a significant positive impact upon the chemical durability of the system. The ASZ2 system also demonstrated increased values of  $T_g$  and viscosity, but not exceeding acceptable limits for ion exchange resin vitrification. Both systems demonstrated an increase in density which would allow for a decrease in the volume of material which would need to be held in a repository environment, relative to previous systems. All of these physical effects were linked to changes in the glass forming network and bond enthalpies which have previously been described.

These benefits, in combination with the already known advantages of these alkali alkaline-earth silicate glasses, such as high durability, high anion solubility and known resistance to  $\gamma$ -irradiation at high doses <sup>(35)</sup>, demonstrate that these glass compositions are highly suitable for use in the vitrification of radio-caesium loaded ion exchange resin wastes. It is also highly likely that these hybrid compositions may be applicable to a wide range of other problematic waste streams, where their durability, anion solubility and resistance to reduction would be required.

### Chapter 3.3 - Systematic Development of Alkali Borosilicate and Calcium Aluminosilicate Glass for the purpose of Cs-loaded Ion Exchange Resin Vitrification.

This section addresses the development of two additional glass systems, an alkali borosilicate glass system and a calcium silicate glass system. Both of these systems were subjected to systematic compositional development experiments in order to identify compositions with physical properties which represented improvements over the physical properties of the original system for ion exchange resin vitrification.

The alkali borosilicate glass composition was selected based on previous studies carried out by Bingham *et. al.*<sup>(3,35)</sup>, which indicated that it possessed superior melting properties and due to the similarity of the composition to the MW type glass now used for the vitrification of UK HLW wastes. The calcium aluminosilicate system was selected based on the capacity of the system for the incorporation of unusually high proportions of anionic species, as reported by Schofield *et al.*<sup>(5)</sup>. The compositions of both systems can be found below in Table 3.3.1 and Table 3.3.2. Both of these systems present significant issues in relation to the vitrification of ion exchange resin wastes. The alkali borosilicate system (AB0), while possessing a low melting temperature, low processing temperature and containing Fe as a barrier against reduction, lacks the capacity of other systems for the incorporation of anionic species, limiting the potential waste-loading of the system due to the risk of gall-layer formation. The calcium aluminosilicate system (CA0) however does not possess melting properties which would be desirable for ion exchange resin vitrification, having a melting temperature which is too high for acceptable waste-form processing.

**Table 3.3.1** - Compositions of Alkali Borosilicate system and associated samples.

Sample ID	Component content (mol%)				
	SiO <sub>2</sub>	B <sub>2</sub> O <sub>3</sub>	Fe <sub>2</sub> O <sub>3</sub>	Li <sub>2</sub> O	Na <sub>2</sub> O
Base Glass (AB0)	58.10	17.79	3.94	10.04	10.13
Full Na <sub>2</sub> O	58.10	17.79	3.94	-	20.17
+5 mol% Na <sub>2</sub> O	58.10	17.79	3.94	5.04	15.13
+5 mol% Li <sub>2</sub> O	58.10	17.79	3.94	15.04	5.13
Full Li <sub>2</sub> O	58.10	17.79	3.94	20.17	-

**Table 3.3.2** - Composition of Calcium Alumino-Silicate system and associated samples.

\* Marked samples failed to form a glass.

Sample ID	Component content (mol%)							
	SiO <sub>2</sub>	Al <sub>2</sub> O <sub>3</sub>	CaO	Fe <sub>2</sub> O <sub>3</sub>	Mn <sub>2</sub> O <sub>3</sub>	B <sub>2</sub> O <sub>3</sub>	SrO	ZnO
<b>Base Glass (CA0)</b>	41.43	7.17	51.40	-	-	-	-	-
<b>CF0</b>	41.43	-	51.40	7.17	-	-	-	-
<b>CMn0</b>	41.43	-	51.40	-	7.17	-	-	-
<b>CB0 *</b>	41.43	-	51.40	-	-	7.17	-	-
<b>CAS 0.1</b>	41.43	7.17	46.26	-	-	-	5.14	-
<b>CAS 0.25</b>	41.43	7.17	38.55	-	-	-	12.85	-
<b>CAS 0.5 *</b>	41.43	7.17	25.70	-	-	-	25.70	-
<b>CAZ 0.1</b>	41.43	7.17	46.26	-	-	-	-	5.14
<b>CAZ 0.25 *</b>	41.43	7.17	38.55	-	-	-	-	12.85
<b>CAZ 0.5 *</b>	41.43	7.17	25.70	-	-	-	-	25.70
<b>CFZ *</b>	41.43	-	46.26	7.17	-	-	-	5.14

The following series of experiments are detailed and discussed in this section. The ABO composition underwent one series of compositional experiments in which the ratio of alkali oxides (Na<sub>2</sub>O & Li<sub>2</sub>O) was varied through the full range of compositions from the full alkali content being Li<sub>2</sub>O through to its full replacement with Na<sub>2</sub>O. This series was intended to explore the effect of varying the charge density of the alkali components on the glass network. The CA0 composition underwent two series of compositional development. The first of these series explored the replacement of the Al<sub>2</sub>O<sub>3</sub> component of the composition with an alternative oxide component. The second series explored the replacement of a portion of the Ca content of the system with another divalent oxide. Both of these series were intended to explore the effect of replacing the Al<sub>2</sub>O<sub>3</sub> content on the density, glass transition temperature (T<sub>g</sub>), liquidus temperature (T<sub>liq</sub>) and on the coordination of the Si network.

Compositions from all three series presented reduced values of T<sub>liq</sub> and T<sub>g</sub> and increased values of density. In the first series, significant decreases in T<sub>liq</sub> were apparent at the full Na<sub>2</sub>O extreme of the series, demonstrating a decrease of almost 140 °C from the initial composition. However, this was matched by increases in both the T<sub>g</sub> and the density. The second series demonstrated significant decrease in the T<sub>liq</sub>, T<sub>g</sub> and viscosity and increases in the density of the calcium alumino-silicate glass when the Al<sub>2</sub>O<sub>3</sub> component was fully replaced by either Fe<sub>2</sub>O<sub>3</sub> or Mn<sub>2</sub>O<sub>3</sub>. In addition, the replacement of Al<sub>2</sub>O<sub>3</sub> with multivalent

oxide species potentially increases the capacity of the composition for reduction. The third series demonstrated reduced values of  $T_{liq}$  and  $T_g$ , alongside increases in density, although full replacement of CaO with other divalent oxides was not successful due to phase separation and heterogeneity in the produced samples.

### 3.3.1 Experimental Procedures

Each sample was prepared from its component oxides, as determined by the compositional development series. Sample batches were prepared using oxide and carbonate powders of 99.9% purity or greater. Samples were melted for 3 hours and stirred for the final 2 hours at a rate of 30 rpm before being poured into block moulds, being annealed for 1 hour and then allowed to cool to room temperature at a rate of 1°C per min. The calcium aluminosilicate derived glasses were melted at 1400°C in recrystallised alumina crucibles and annealed at 780°C. The alkali borosilicate derived glasses were melted at 1200°C in Zr-stabilised Pt crucible and annealed at 500 °C.

Sample density was determined through the Archimedes method. Deionised water was used and the data was corrected for the density of water at ambient temperature. The  $T_g$  and  $T_x$  (Crystallisation temperature) for the glasses were determined through the use of DTA (Differential Thermal Analysis). DTA experiments were all performed in air and using Pt crucibles and measurements were taken automatically by a computer operated system (Perkin Elmer DTA 7). The  $T_{liq}$  was determined using a tube furnace in which a fritted sample was heated across a known temperature gradient. By determining the temperature across the length of the sample (inserted in Al<sub>2</sub>O<sub>3</sub> boat of ~10 cm length) the  $T_{liq}$  could be identified by visually locating the point where crystal growth occurs and matching that to the temperature. This technique can produce results accurate to within  $\pm 10^\circ\text{C}$ . In order to discriminate between glass compositions the melting temperature ( $T_{melt}$ ) was defined as being 50 °C above the  $T_{liq}$ . It should be noted that this does not take into account properties such as viscosity which also effect the temperature at which a glass can be melted. The viscosity of the samples was determined using a Viscometer setup (Theta) including a rheometer (Brookfield DV-III-Ultra) and a specially designed vertical muffle furnace (Theta). This setup allows the viscosity of a sample to be determined by measuring the torque experienced by an alumina spindle rotating in a molten sample across a range of temperatures. This produces the viscosity and  $\log \eta$  to be determined as a function of the sample temperature.

Information on the structure and coordination of species in the glass systems was derived from the use of a range of spectroscopic techniques. FTIR (Fourier Transform Infra-red) spectroscopy was applied to investigate the changes in the Si bonding in the structural network of the samples. A Perkin Elmer Spectrum 2000 FT-IR spectrometer was used to collect spectra over the 500 – 1500 nm range. FTIR data was collected using reflectance and as such was corrected utilising a Kramers-Kronig transform. Samples for both techniques were monoliths polished to 1  $\mu\text{m}$ . Sample polishing was achieved utilising a combination of SiC grinding paper and diamond polishing suspension.

$^{57}\text{Fe}$  Mossbauer spectroscopy was utilised to determine the oxidation state and coordination of Fe within the samples. A WissEl  $^{57}\text{Fe}$  Mossbauer spectrometer setup was utilised operating in a constant acceleration mode with a  $^{57}\text{Co}$  source (activity  $\sim 9000 \mu\text{Ci}$ ). The data produced was fitted using single Lorentzian line shapes each set to represent the  $\text{Fe}^{2+}$  and  $\text{Fe}^{3+}$  environments, using the software package Recoil 1.03. The Recoil free fraction was assumed to be equal in the  $\text{Fe}^{2+}$  and  $\text{Fe}^{3+}$  environments. Sample calibration was performed relative to  $\alpha\text{-Fe}$ . More detailed descriptions of these techniques are provided in appendix 8.1.

### 3.3.2 Results

#### 3.3.2.1 Alkali Borosilicate Series - Variation in $\text{Na}_2\text{O} : \text{Li}_2\text{O}$ ratio.

This series comprised 5 glasses, including the original base glass AB0, spanning the range of compositions between the complete alkali content being comprised by Na through to the complete replacement of the Na with Li. X-ray diffraction experiments indicated that all produced glasses were X-ray amorphous, to within the estimated 5 vol% limit of detection, with the exception of the full Li sample which was found to contain the crystalline phase  $\text{Li}_2\text{SiO}_3$ . Density was seen to vary proportionally to the presence of  $\text{Na}_2\text{O}$  in the samples. This observation is in good agreement with the work of Huggins *et al*<sup>(57)</sup> in which increased density is linked to the increasing average relative molecular mass of a system. The  $T_g$  was seen to vary across a range of approximately  $60^\circ\text{C}$  in response to the variation in alkali cation size. The  $T_g$  was highest at the full replacement of  $\text{Li}_2\text{O}$  with  $\text{Na}_2\text{O}$ , and achieved a minimum point between  $\text{Li}_2\text{O} / (\text{Li}_2\text{O} + \text{Na}_2\text{O})$  0.5 and 0.75. The  $T_{\text{liq}}$  was seen to increase relative to the proportion of  $\text{Li}_2\text{O}$  present in the system. This increase was seen to cover a range of

temperatures from 555 °C to 880 °C ( $\pm 10^\circ\text{C}$ ). The full  $\text{Li}_2\text{O}$  sample was not measured due to its inability to form an amorphous solid on cooling. The variation in density,  $T_g$  and  $T_{\text{liq}}$  can be seen in figures 3.3.1, 3.3.2 and 3.3.3 respectively. The viscosity of the samples showed no significant variation across the compositional range explored.

FT-IR spectroscopy was carried out on all samples in the series, and the resultant spectra were fitted based upon the assignments of Serra *et al* and MacDonald *et al* <sup>(68,70)</sup>. A single distribution of mixed  $\text{Q}^n$  Si bands were observed throughout the series, as is typical of alkali-borosilicate type glasses. Across the series only slight variation was apparent in the  $\text{Q}^n$  bands, within statistical limits. On increasing Li content, a small increase in the area of the  $\text{Q}^2$  band was apparent at the expense of the  $\text{Q}^3$  band. The full  $\text{Li}_2\text{O}$  sample presented radically different spectra under FT-IR investigation, presenting a complex signal indicative of increased levels of crystallisation in the sample. Figures 3.3.4 and 3.3.5 show the spectra obtained by FT-IR and the variation in  $\text{Q}^n$  bands as determined by the fitting of spectra from both techniques.

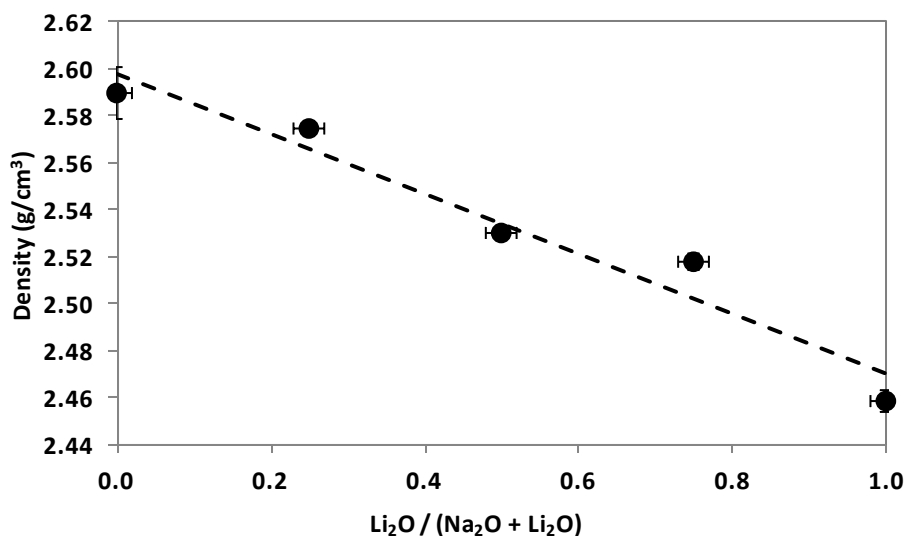


**Figure 3.3.1.** Variation in density across the  $\text{Na}_2\text{O}:\text{Li}_2\text{O}$  variation series. Density error bars determined from deviation of three measurements. Composition error determined from error associated with EDS analysis.

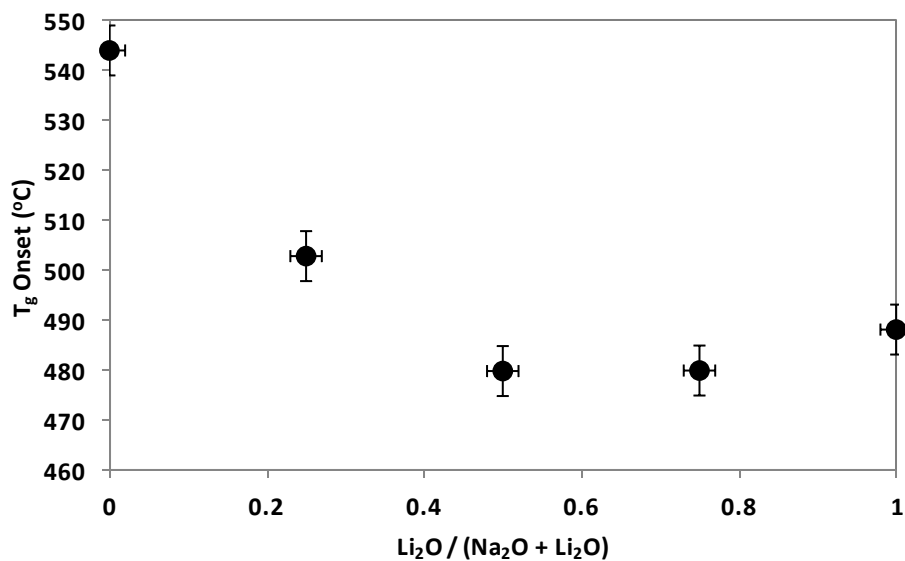


**Figure 3.3.2.** Variation in  $T_g$  across the  $\text{Na}_2\text{O}:\text{Li}_2\text{O}$  variation series.  $T_g$  error bars determined from error associated with experiment. Composition error determined from error associated with EDS analysis.

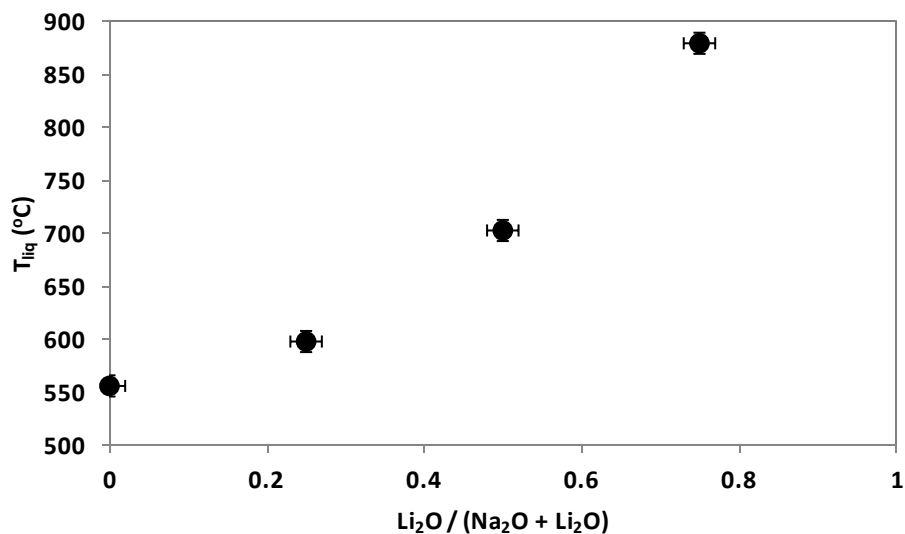


**Figure 3.3.3.** Variation in  $T_{\text{liq}}$  across the  $\text{Na}_2\text{O}:\text{Li}_2\text{O}$  variation series.  $T_{\text{liq}}$  error bars determined from error associated with experiment. Composition error determined from error associated with of EDS analysis. Full  $\text{Li}_2\text{O}$  result is absent due to crystallinity of sample.

### 3.3.2.2 Calcium Alumino-silicate glasses - Replacement of $\text{Al}_2\text{O}_3$

The series comprised 3 glasses, the original base glass CA0 and the two alumina replacement glasses, CF0 and CMn0, in which the alumina content of the base glass was replaced by  $\text{Fe}_2\text{O}_3$  and  $\text{Mn}_2\text{O}_3$  respectively. X-ray diffraction experiments indicated that all the produced glasses were X-ray amorphous, to within the limit estimated 5 vol% limit of detection.

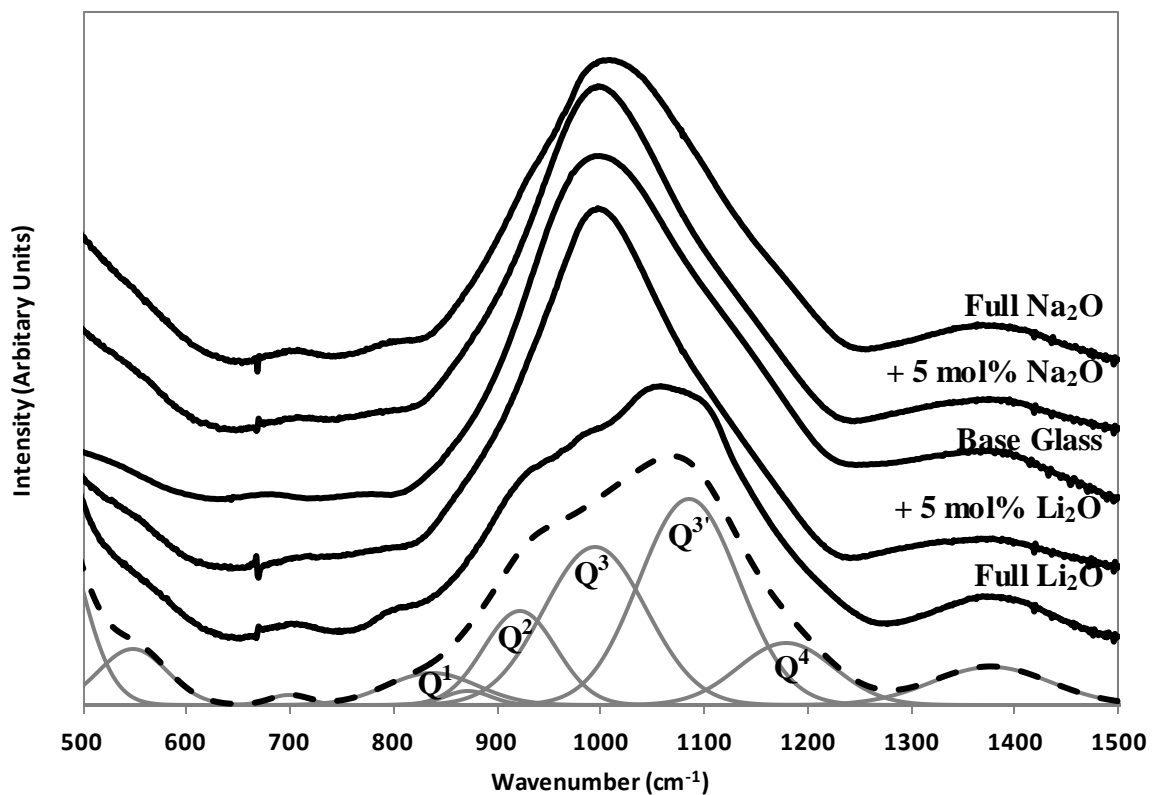


**Figure 3.3.4.** FT-IR spectra of samples from the  $\text{Na}_2\text{O} : \text{Li}_2\text{O}$  variation series. Fitting bands and convolution displayed below spectra.

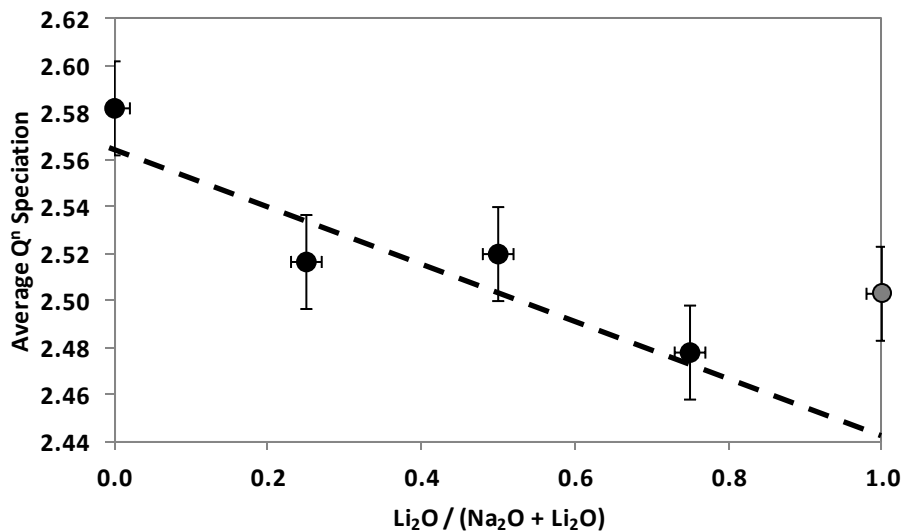


**Figure 3.3.5.** Average Q<sup>n</sup> speciation of samples derived from fitting of FT-IR data for the Na<sub>2</sub>O : Li<sub>2</sub>O variation series. Error derived from errors associated with fitting. Composition error determined from error associated with of EDS analysis. Highlighted data point associated with crystalline full Li<sub>2</sub>O sample.

The density of both the CF0 and CMn0 samples was seen to be higher than that of the base glass. The Fe doped glass CF0 presented the highest density at  $3.14 \pm 0.01 \text{ g cm}^{-3}$ , and the CMn0 glass presented an intermediate density at  $3.05 \pm 0.01 \text{ g cm}^{-3}$ . This again is in good agreement with the work of Huggins *et al*<sup>(57)</sup> in which increased density is linked to the increasing average relative molecular mass of a system. The  $T_g$  was seen to vary over a range of  $\sim 55^\circ\text{C}$  throughout the series. The base glass presented the highest value of  $T_g$  at  $771 \pm 5^\circ\text{C}$  with the CMn0 and CF0 samples presenting  $T_g$  values of  $749 \pm 5^\circ\text{C}$  and  $716 \pm 5^\circ\text{C}$  respectively. The  $T_{liq}$  of the samples was seen to vary over a range of  $\sim 45^\circ\text{C}$ . The base glass and the MnO replacement sample both presented values of  $T_{liq}$  at  $1348 \pm 10^\circ\text{C}$ . However, the CF0 glass presented a value of  $T_{liq}$  lower at  $1302 \pm 10^\circ\text{C}$ . The variation in density,  $T_g$  and  $T_{liq}$  are plotted in figures 3.3.6, 3.3.7 and 3.3.8 respectively.

The viscosity of the samples showed a significant degree of variation between the Al replacement samples and the base glass in terms of the rate of viscosity change over temperature. The  $\log \eta$  of the replacement samples was significantly lower than that of the base glass. At  $1400^\circ\text{C}$ , the  $\log \eta$  of both CF0 and CMn0 was  $0.48 \pm 0.01 \text{ Log P}$ , whereas the  $\log \eta$  of the base glass was higher at  $0.958 \pm 0.01 \text{ Log P}$ . The variation in  $\text{Log } \eta$  can be seen in figure 3.3.9.

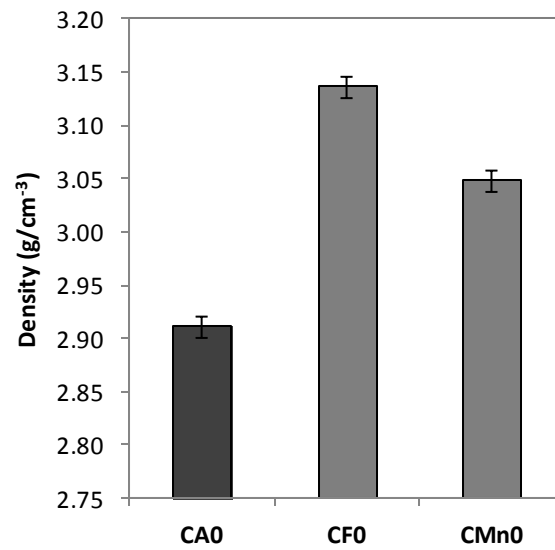


**Figure 3.3.6.** Variation in density across the Al<sub>2</sub>O<sub>3</sub> replacement series. Density error bars are determined from deviation of three measurements.

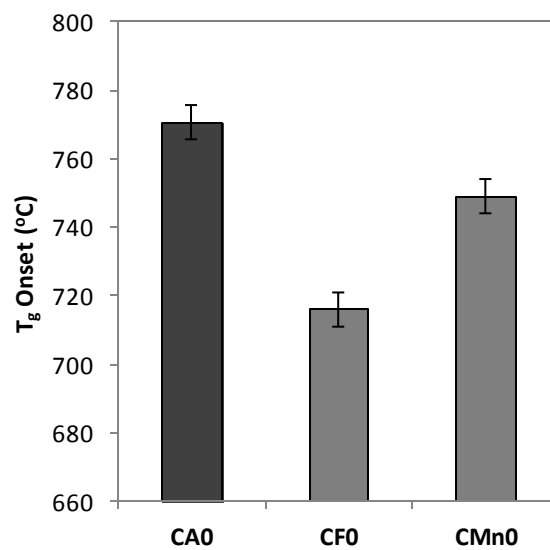


**Figure 3.3.7.** Variation in T<sub>g</sub> across the Al<sub>2</sub>O<sub>3</sub> replacement series. T<sub>g</sub> error bars are determined from error associated with experiment.

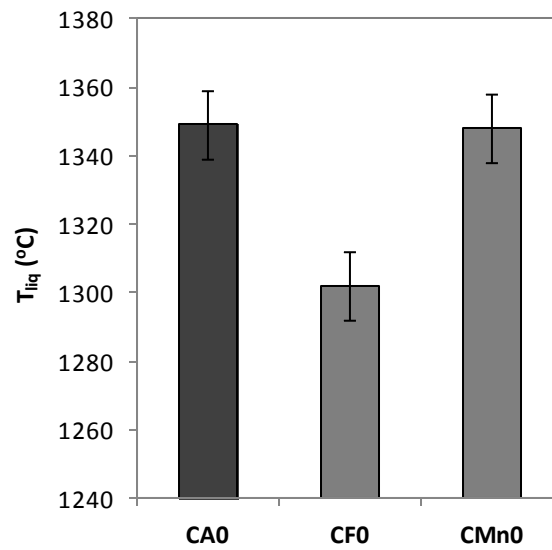


**Figure 3.3.8.** Variation in  $T_{liq}$  across the  $Al_2O_3$  replacement series.  $T_{liq}$  error bars are determined from error associated with experiment.

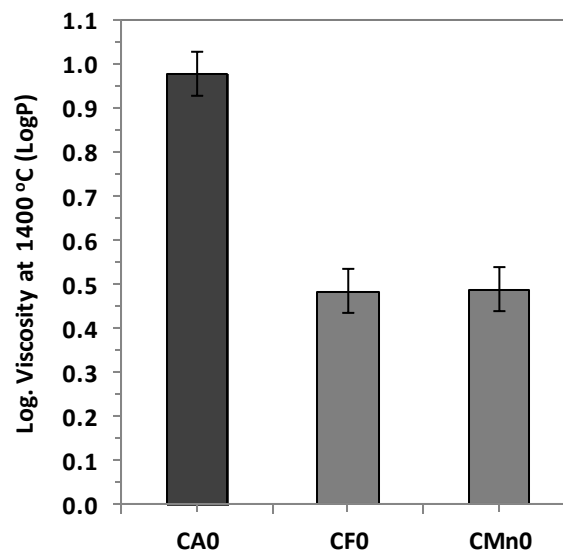


**Figure 3.3.9.** Variation in  $\log \eta$  of the samples at 1400 °C over the  $Al_2O_3$  replacement series. Error determined from experimental errors associated with measurement.

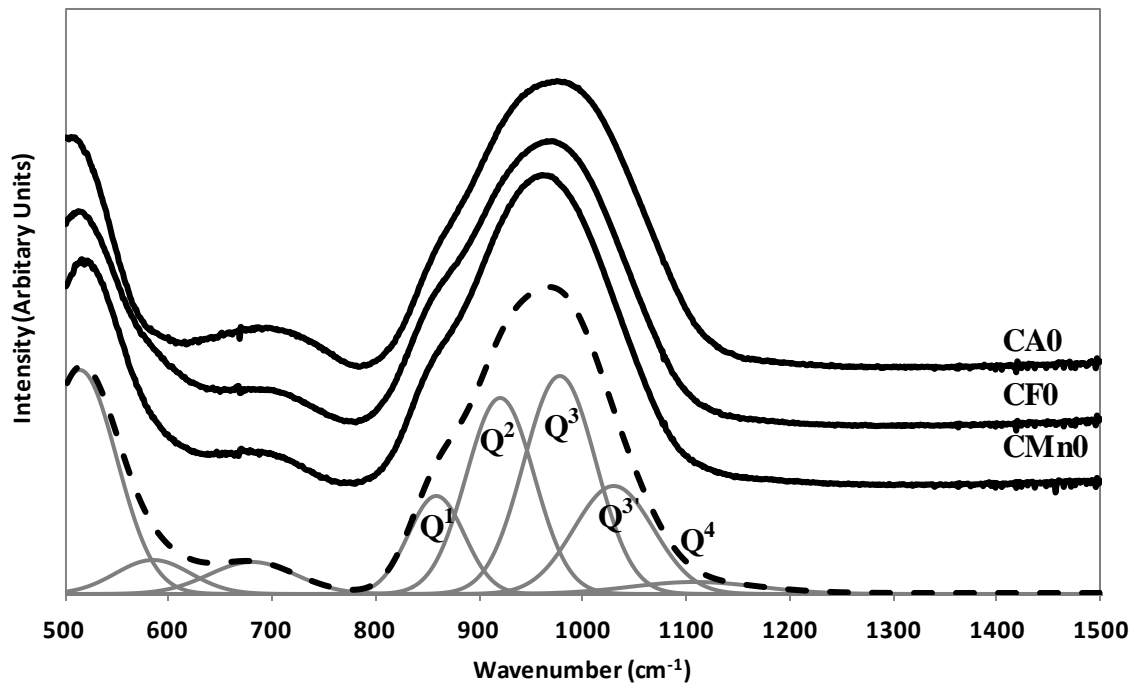


**Figure 3.3.10.** FTIR spectra of samples from the  $\text{Al}_2\text{O}_3$  replacement series. Fitting bands and convolution displayed below spectra.

FT-IR spectroscopy was carried out on all samples in the series and the resultant spectra were again fitted based upon the assignments of Serra *et al* and MacDonald *et al* <sup>(68,70)</sup>. A single distribution of mixed  $\text{Q}^n$  Si bands was observed throughout the series in both spectroscopic techniques. Fitting of the  $\text{Q}^n$  bands indicated that there was no significant variation between the samples in the series in terms of  $\text{Q}^n$  speciation. This indicates the replacement of  $\text{Al}_2\text{O}_3$  with either  $\text{Fe}_2\text{O}_3$  or  $\text{Mn}_2\text{O}_3$  has no significant detectable effect upon the polymerisation of the glass network. Fitting of the FT-IR data presented a small but significant change in a band at  $587\text{ cm}^{-1}$  which can be associated with absorption of  $\text{Fe}^{3+}\text{-O}$  bonds<sup>(49)</sup>. Figure 3.3.10 shows the FT-IR spectra for these samples.

### 3.3.2.3 Calcium Alumino-Silicate glasses - Replacement of CaO

The series comprised 4 glasses, the original base glass CA0 and three Ca replacement glasses, CAS0.1, CAS0.25 and CAZ0.1 which represented the replacement of 10% and 25% of the CaO content with SrO and the replacement of 10% CaO content with ZnO. These glasses showed no evidence of phase separation and were shown to be X-ray amorphous, to within a 5 vol% limit of detection, by XRD. Samples containing higher proportions of CaO

replacement with ZnO and SrO were produced, but were not homogenous, showing a significant degree of phase separation, and so these samples were excluded from further analysis due to their inadequacy for the purpose for which they were produced.

The density of the SrO replacement samples and the ZnO replacement sample was found to be higher than that of the base glass. In the case of the SrO replacement, the increase in density was seen to be in proportion to the amount of CaO replaced by SrO. This would support the analysis of Huggins *et al.*<sup>(57)</sup> in which an increased density can be linked to the increased relative molecular mass of the composition. The ZnO replacement sample presented a density higher than that presented by either of the SrO replacement samples. This is counter to the analysis of Huggins *et al.* and suggests that additional factors contribute to the density of the CAZ0.1 sample. The  $T_g$  of the CaO replacement samples showed significant variation only in the ZnO replacement sample, which demonstrated a 90 °C decrease in  $T_g$  relative to the base glass. The  $T_{liq}$  shows significant variation in all three of the Ca replacement samples, decreasing by as much as 100 °C relative to the original base glass. The CAZ0.1 sample shows the greatest decrease in  $T_{liq}$ , decreasing to  $1250 \pm 5$  °C from the  $1349 \pm 5$  °C of the base glass. The SrO replacement samples present a similar decrease but on a smaller magnitude, decreasing to  $1282 \pm 5$  °C and  $1278 \pm 5$  °C for CAS0.1 and CAS0.25 respectively. The variation in density,  $T_g$  and  $T_{liq}$  are shown in figures 3.3.11, 3.3.12 and 3.3.13 below.

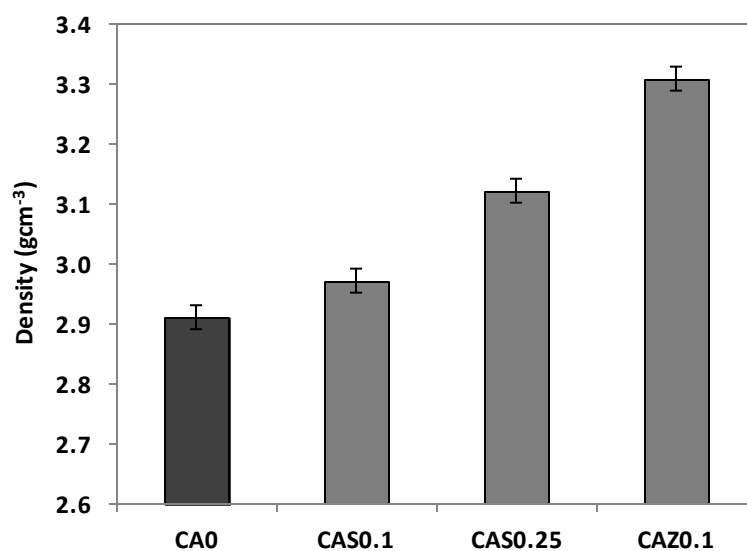


**Figure 3.3.11.** Variation in density across the CaO replacement series. Density error bars are determined from deviation of three measurements.

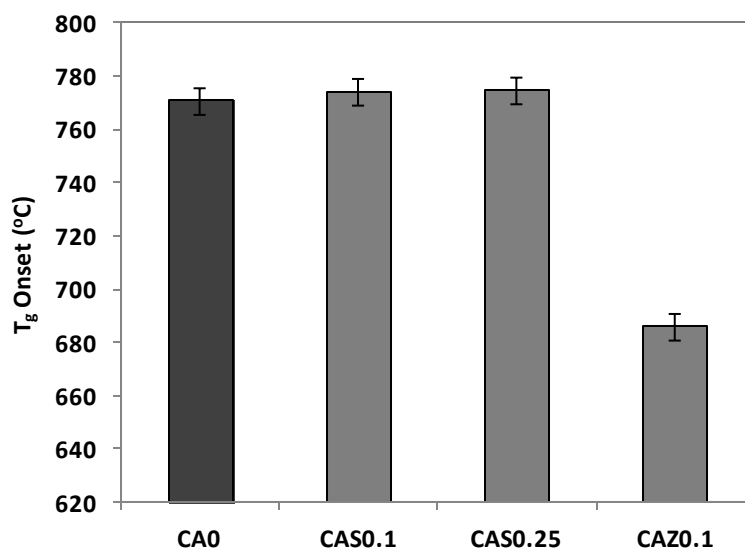


**Figure 3.3.12.** Variation in  $T_g$  across the CaO replacement series.  $T_g$  error bars are determined from error associated with experiment.

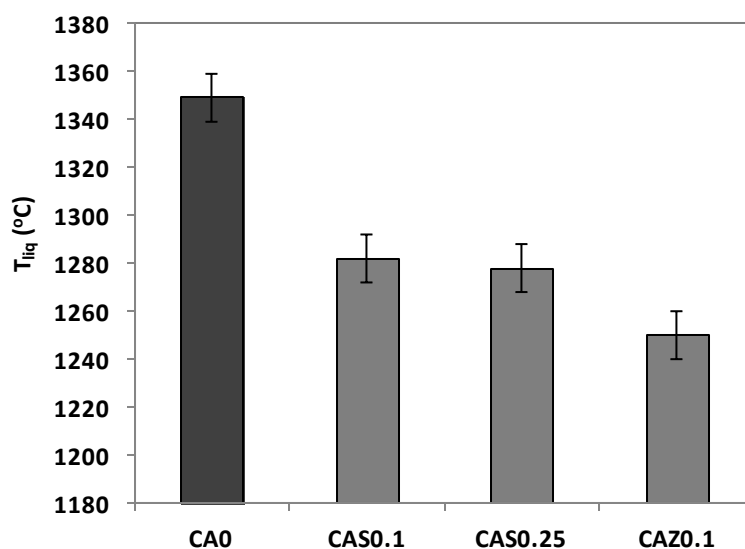


**Figure 3.3.13.** Variation in  $T_{liq}$  across the CaO replacement series.  $T_{liq}$  error bars are determined from error associated with experiment.

FT-IR spectroscopy was carried out on all samples in the series and the resultant spectra were again fitted based upon the assignments of Serra *et al* and McDonald *et al* <sup>(68,70)</sup>.

A single distribution of mixed  $Q^n$  Si bands were observed throughout the series. Fitting of the  $Q^n$  bands from FT-IR data indicated showed a small but significant variation in the  $Q$  speciation of the SrO and ZnO replacement samples relative to the base glass. The SrO replacement samples demonstrated a small decrease in the  $Q^1$  band with a proportional increase in the  $Q^3$  and  $Q^4$  bands. This was observed to a greater extent in the CAS0.25 samples over the CAS0.1 sample indicating that the effect increased in rough proportion to SrO replacement. In the ZnO replacement samples a similar shift in  $Q^n$  speciation was observed. The  $Q^1$  band was again seen to diminish in fitted area and the  $Q^3$  and  $Q^4$  bands increase proportionally. Notably, the shift in  $Q^n$  speciation was seen to be greater than was observed in the SrO replacement samples, despite a lower extent of CaO replacement. Figures 3.3.14 and 3.3.15 show the FT-IR spectra for these samples and the areas of the fitted  $Q^n$  bands for all three samples.

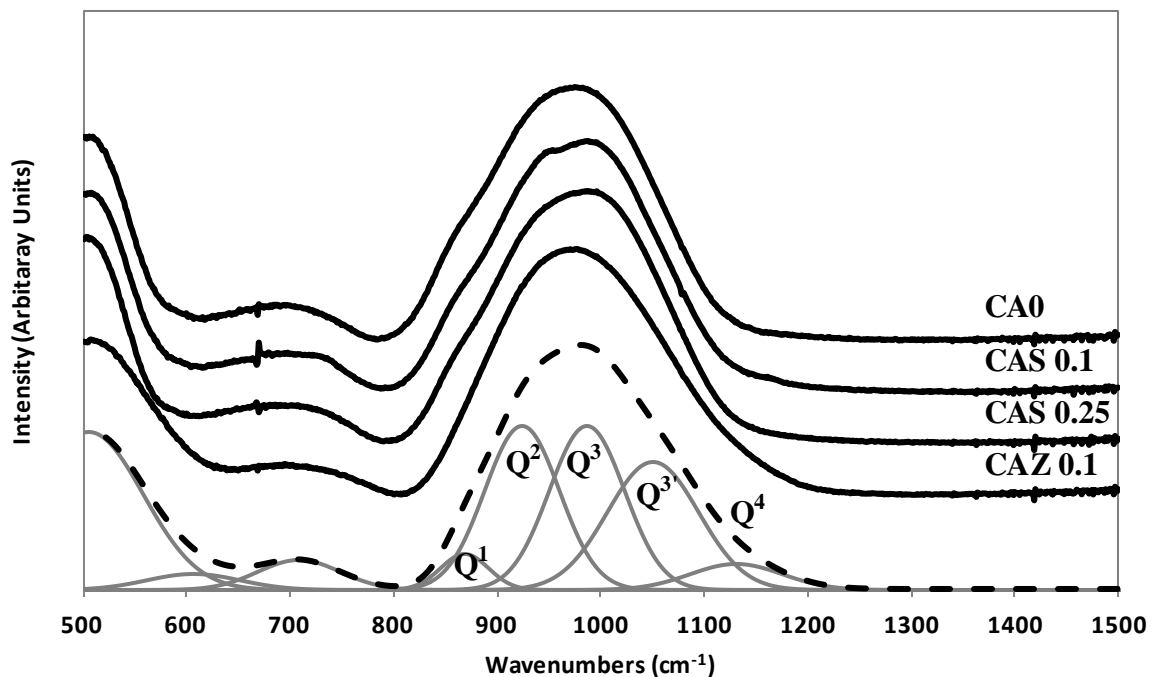


**Figure 3.3.14.** FTIR spectra of samples from the  $Al_2O_3$  replacement series. Fitting bands and convolution displayed below.

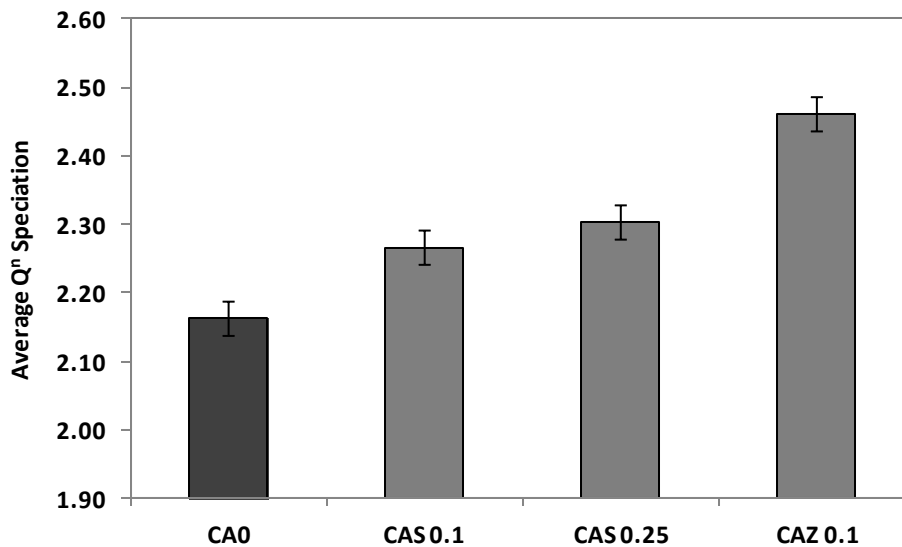


**Figure 3.3.15.** Average Q<sup>n</sup> speciation of samples derived from fitting of FT-IR data for the Al<sub>2</sub>O<sub>3</sub> replacement series. Fitting bands and convolution displayed below. Error derived from errors associated with fitting.

### 3.3.3 Discussion

#### 3.3.3.1 Variation in alkali oxide component of Alkali Borosilicate glass

The alkali oxide variation sample series demonstrated a significant degree of variation across the samples physical properties. The series presented a linear decrease in density and viscosity in response to increase Li<sub>2</sub>O content and non-linear variations in T<sub>g</sub> and T<sub>liq</sub>.

In the context of the vitrification of ion exchange resin, the reduction in melting temperature effected by the increase in Na<sub>2</sub>O content represents a significant improvement for the system, since this could allow vitrification to take place at a much lower temperature without the formation of crystalline phases. However, the increase in T<sub>g</sub> which was also observed in the full Na<sub>2</sub>O sample may in practice prevent low temperature vitrification, since the waste-form produced would be effectively unworkable and therefore higher melting temperatures would still be required for effective vitrification.

The apparent increase in network polymerisation and density would also represent improvements for resin vitrification, since it has favourable implications for the chemical durability of the waste-form and the waste-loading of the waste-form (on a per unit volume

basis). However, despite the apparent increase in network polymerisation, glasses containing high Na<sub>2</sub>O contents are known to possess inferior durability, and as such a waste-form produced using this composition may be unacceptably vulnerable to aqueous attack. Further investigation would be required to confirm this.

The observed decrease in density with the increase in Li<sub>2</sub>O content can be connected to the effect the low relative molecular mass of the Li<sup>+</sup> ion decreasing the average molecular mass of the glass, as is supported by the work of Huggins *et al* and Islam *et al*<sup>(57-58)</sup>. The small but significant variation in Q<sup>n</sup> speciation observed by FT-IR spectroscopy can be linked to the small Li<sup>+</sup> ion, in that the smaller modifying cations would lead to reduction in the average coordination of the alkali species in the glass. This would decrease the extent of polymerisation between network forming units, resulting in the decrease in the average Q<sup>n</sup> speciation of the Si network which was observed. This hypothesis is supported by the work of Vogel *et al*<sup>(72)</sup>, in which Li<sup>+</sup> cations were demonstrated to support lower number of coordinated O atoms than Na. However, further structural data would be required to provide evidence for this hypothesis.

The increase in T<sub>liq</sub> observed in response to the increase of Li<sub>2</sub>O is consistent with information presented in literature about mixed sodium lithium silicate systems<sup>(47,76)</sup> in which the T<sub>liq</sub> is shown to increase in proportion to overall Li<sup>+</sup> content. This is consistent with work in similar systems where the replacement of a modifying species with another smaller species leads to an increase in T<sub>liq</sub>. This can be attributed to the effective reduction in steric effects which impair the coordination of these modifier cations to the network forming species and the increase in the bonding energy between the alkali modifiers and the network forming species. This decrease in steric hindering and increase in bond energies reduces the thermodynamic barrier against crystallisation and increases the T<sub>liq</sub>. The variation between the reported values for T<sub>liq</sub> and the values presented in literature can be attributed to the presence of additional oxide species in the glass system which was studied, since they would similarly affect the thermodynamic barrier against crystallisation.

The T<sub>g</sub> was observed to decrease on Li<sub>2</sub>O addition before levelling off at 0.5 Na<sub>2</sub>O / (Na<sub>2</sub>O +Li<sub>2</sub>O). These variations may be connected to the enthalpy of fusion for the constituent oxides being varied in the composition, as described by Islam *et al*<sup>(74)</sup>. However, the higher enthalpy of fusion for Li<sub>2</sub>O relative to Na<sub>2</sub>O implies that the T<sub>g</sub> should increase with Li<sub>2</sub>O<sup>(73)</sup>, which is not what is seen. As such, the reason for the overall decrease in T<sub>g</sub> remains unclear, although it may be connected to the coordination of Li within the glass and more information would be required to reach a firm conclusion. The levelling off at 0.5 Na<sub>2</sub>O

/ (Na<sub>2</sub>O +Li<sub>2</sub>O) can be attributed to the combination of this decrease in T<sub>g</sub> with increasing Li<sub>2</sub>O content superimposed by the non-linear variation in T<sub>g</sub> associated with the mixed alkali effect <sup>(76)</sup>.

### 3.3.3.2 Replacement of Al<sub>2</sub>O<sub>3</sub> content of Calcium Aluminosilicate glass

The replacement of the Al<sup>3+</sup> content with Fe<sup>3+</sup> and Mn<sup>3+</sup> in the calcium aluminosilicate system was found to have significant effects on the physical properties of the system. Specifically reductions in T<sub>g</sub>, T<sub>liq</sub> and viscosity and increases in density were seen.

Again considering the implications of the observed property changes in the context of ion exchange resin vitrification it can be seen that both the Fe<sub>2</sub>O<sub>3</sub> and Mn<sub>2</sub>O<sub>3</sub> glasses do represent an improvement over the properties of the original system, albeit to a lesser extent in the latter case. The most significant improvement relates to the decrease in T<sub>liq</sub> seen in both replacement systems, which has the potential to allow lower vitrification temperatures and consequentially improved radio-caesium retention. The decreased values of overall viscosity and T<sub>g</sub> are also potentially beneficial in terms of the workability of the vitreous waste-form during production. However, it should be noted that although these improvements in melting temperature and waste-form workability are beneficial, they still fall short of what can be achieved using other candidate glass compositions in chapter 3.1 and chapter 3.2. It should be noted that an additional benefit in replacing the Al<sub>2</sub>O<sub>3</sub> content in this system with Fe<sub>2</sub>O<sub>3</sub> and Mn<sub>2</sub>O<sub>3</sub> is that the Fe<sup>3+</sup> and Mn<sup>3+</sup> cations may act as a buffer against reduction by organic material, which would be of distinct benefit for organic ion exchange resin vitrification.

The increased density observed in both of the Al<sub>2</sub>O<sub>3</sub> replacement samples can be attributed to the replacement of Al<sub>2</sub>O<sub>3</sub> with metal oxides of a higher relative molecular mass and in their metallic form with a higher overall density. As such, these observations are consistent with the observations of Huggins *et al* <sup>(57)</sup>. Similarly, the absence of Al<sub>2</sub>O<sub>3</sub> in the replacement samples provides an explanation for the significantly reduced viscosity which was observed, since Al<sub>2</sub>O<sub>3</sub> is well known to increase the viscosity of silicate glass systems due to the stronger Al-O bonds associated with Al<sup>3+</sup> which is known to increase the activation energy for viscous flow <sup>(52)</sup>.

Both replacement samples demonstrated reduced values of T<sub>g</sub> and T<sub>liq</sub> relative to the base glass. This observation can be connected both to the interaction of transition metals with

the glass network relative to  $\text{Al}^{3+}$  cations. The Al-O bond is known to possess a high strength relative to other cations of similar charge <sup>(53)</sup>, as such the replacement of the  $\text{Al}^{3+}$  cation with transition metal cations, which form weaker M-O bonds, providing some explanation for the lower values of  $T_g$  and  $T_{liq}$  observed in these results. This would occur since the weaker M-O bonds in these elements would present a lower activation energy for viscous flow, reducing the  $T_g$ , and would cause a reduction in the enthalpy of crystallisation for the system reducing the  $T_{liq}$ .

Furthermore, Fe is known to have an additional effect in lowering the  $T_{liq}$  of the system when added to a system at lower levels <sup>(53)</sup>. As such, these results are consistent with explanations found in literature <sup>(75)</sup>.

The lack of any significant change in the  $Q^n$  speciation of the glass network in the replacement samples indicates that  $\text{Fe}_2\text{O}_3$  and  $\text{Mn}_2\text{O}_3$  both perform a similar modifying role in the glass system as  $\text{Al}_2\text{O}_3$ , demonstrating a similar extent of coordination as  $\text{Al}^{3+}$ .

### 3.3.3.3 Replacement of CaO content of Calcium Aluminosilicate glass

As was seen in the previous series the replacement of portions of  $\text{Ca}^{2+}$  in the system with  $\text{Sr}^{2+}$  and  $\text{Zn}^{2+}$  also presented significant changes to the physical properties of the calcium aluminosilicate glass system in terms of the  $T_g$ ,  $T_{liq}$  and density of the system as well as having some effect on the connectivity of the glass forming network.

In relation to the vitrification of ion exchange resin wastes several positive effects upon the physical properties of the system were identified. The decrease in  $T_{liq}$  seen in all of the CaO replacement samples demonstrated that the replacement of CaO with SrO or ZnO can reduce the  $T_{melt}$  of the glass, potentially allowing vitrification at lower melting temperatures and the improved retention of volatile radio-caesium. As with the previous series, decreases in  $T_g$  and increases in density were observed which have potential to improve the workability and waste-loading of a potential waste-form. However, as with the  $\text{Al}_2\text{O}_3$  replacement series, although the decreased  $T_{liq}$  is an improvement for the system for the purpose of ion exchange resin vitrification, the resultant glass still possesses inferior properties in comparison to other possible systems that have been explored.

Considering first the physical property changes observed in the system, it was observed that the density of both the  $\text{Sr}^{2+}$  systems and the  $\text{Zn}^{2+}$  was significantly increased

relative to that of the base glass. In the case of the SrO replacement samples, this can be attributed to the increase in average relative molecular mass, as supported by Huggins *et al*<sup>(57)</sup>, especially since Sr<sup>2+</sup> ions interact with the silicate network in a similar manner to Ca<sup>2+</sup> ions. However, this explanation cannot apply to the ZnO sample, since the average molecular mass of the sample would be lower than that of the SrO sample and, if based on that factor alone, the ZnO sample should be less dense. This implies another effect is impacting the density of the ZnO sample. Zn<sup>2+</sup> is known to act as an intermediate cation in glass networks, with a similar ionic radius to Mg<sup>2+</sup><sup>(59)</sup>, as such it is possible that the increased density observed may be a result of higher coordination of the Zn<sup>2+</sup> cations relative to the Ca<sup>2+</sup> cations since the Zn<sup>2+</sup> cations have a small ionic radius but form stronger bonds with oxygen atoms in the silicate network<sup>(59)</sup>. The increased overall Q<sup>n</sup> speciation of the ZnO sample supports this conclusion in that increased polymerisation observed in the silicate network can be attributed to an increase in the coordination of modifier cations. This is further supported by the work of Islam *et al*<sup>(58)</sup> in which Zn<sup>2+</sup> cations are described creating network forming polyhedra.

Considering the variation in T<sub>g</sub> it was apparent that only the ZnO replacement presented a significant decrease in relation to the base glass. This implies that the decrease in T<sub>g</sub> is connected to the effect of the ZnO specifically and is in line with the understanding of the effect of ZnO on silicate glass systems, in that it is known to improve glass melting and workability<sup>(59)</sup> when added at low levels of concentration (up to approximately 16 mol%). This effect can also be seen in the lower T<sub>liq</sub> associated with the ZnO replacement sample.

The decreases in T<sub>liq</sub> observed in the SrO samples can be attributed to the impact of the Sr<sup>2+</sup> cation on the silicate network. The Sr<sup>2+</sup> cation possess a larger ionic radius than the Ca<sup>2+</sup> cation and as such leads to the decrease in the average coordination of the network modifying components of the system, as has been previously been reported in similar mixed alkaline-earth systems<sup>(47,51,59)</sup>. This effect increases the enthalpy barrier against crystallisation resulting in the observed decrease in the T<sub>liq</sub>. More detailed information on the coordination of the glass network would be necessary to confirm this hypothesis.

### 3.3.4 Conclusion

Through the compositional development series discussed in this work, a number of glass compositions have been identified which represent significant improvements in the calcium-alumino-silicate and alkali borosilicate glass systems in the context of their use for the

vitrification of radio-caesium-containing ion exchange resin wastes. Specifically, in the alkali borosilicate system which was studied it was apparent that the replacement of the  $\text{Li}_2\text{O}$  content with  $\text{Na}_2\text{O}$  has significant positive effects on the liquidus temperature of the system, decreasing it by as much as  $140 \pm 10$  °C, potentially allowing for vitrification of wastes at much lower temperatures, significantly reducing the proportion of volatile species lost during the process. In addition the replacement of  $\text{Li}_2\text{O}$  with  $\text{Na}_2\text{O}$  also showed positive effects on the viscosity and density of the system, potentially improving the systems workability and reducing the volume of any waste-forms produced for a given amount of waste. However, increases in the  $T_g$  and potential issues surrounding the long-term durability of high  $\text{Na}_2\text{O}$  borosilicate glasses potentially impair the composition. The developmental series carried out on the calcium alumino-silicate system also identified compositions which represented significant improvements on the base glass. Specifically the samples in which the full  $\text{Al}_2\text{O}_3$  content as replaced by  $\text{Fe}_2\text{O}_3$  and where 10 mol% of the  $\text{CaO}$  content was replaced by  $\text{ZnO}$  showed the most significant improvements. Both samples demonstrated significant decreases in the  $T_{\text{liq}}$ , reduced by  $50 \pm 10$  °C and  $100 \pm 10$  °C respectively, potentially allowing vitrification at lower temperatures. In addition to this, both of these compositions demonstrated a decreased in  $T_g$  and an increase in density relative to the base glass, indicating potential for improved workability of the samples and an increased waste-loading by volume. The  $\text{Fe}_2\text{O}_3$  replacement sample also demonstrated a significant decrease in the viscosity relative to the base glass, further improving the workability of the system. However, in both cases, despite these improvements, the melting temperature remains higher than would be ideal for the vitrification of ion exchange resins wastes.

It was possible, to a greater extent, to identify the basis for the changes which were observed in the physical samples of the developed glasses. The majority of observed effects were attributable to well-known interactions such as the mixed alkali effect or changes related to the variation of modifier cation size. However, unusual behaviour was seen in relation to the addition of  $\text{Zn}^{2+}$  cations to the calcium alumino-silicate system which supports the notion previously reported by Islam *et al*<sup>(58)</sup> that  $\text{Zn}^{2+}$  acts as an intermediate network former.

Other glass systems which have been reported previously in chapters 3.1 & 3.2 do present superior properties in terms of melting temperature and resistance to oxidation than the glass systems presented here for the purpose of ion exchange resin vitrification. However it is important to note that these systems significantly increase the number of options which could potentially be applied to the vitrification of ion exchange resin wastes. It is worth noting that the compositions which are explored here may have potential for use in applications which range beyond the vitrification of ion exchange resin wastes, with the

vitriification of other waste streams containing volatile components or halogen chemicals such as PCMs<sup>(77-78)</sup> and potentially a wide range of other ILW type waste streams.

## Chapter 4.1 - The Effect of Waste Loading Novel Glass Compositions Developed for the Vitrification of Cs loaded Ion Exchange Resin Wastes

This section explores the impact of loading three base glass compositions and five novel glass compositions, the development of which was discussed in chapter 3, for the vitrification of ion exchange resin wastes contaminated with <sup>137</sup>Cs radio-nuclides. Specifically, this section explores the capacity for each composition to retain Cs, resist the reduction, mitigate sulphate gall layer formation and produce a durable final waste form. In addition, the melt and final physical properties of the waste form are explored in detail.

The compositions of all 8 glasses are given in Table 4.1.1. Glasses CA0, AS0 and AB0 each represent one of the original base glasses which were explored in the original glass development work. Specifically, these glasses were a calcium alumina-silicate composition, an alkali alkaline-earth silicate system and an alkali borosilicate system, and they were selected based upon previous research<sup>(3,5,35)</sup> which identified properties that were potentially useful in the context of IEX resin vitrification. Each of these three base glass systems were initially investigated through a systematic study of ion exchange waste loadings designed to investigate the optimum waste loading that could be obtained in each system, and explore any composition or physical property changes across the range of waste loadings.

**Table 4.1.1.** Composition of base and novel developed host glass compositions.

Composition ID	Component Content (mol%)								
	SiO <sub>2</sub>	Al <sub>2</sub> O <sub>3</sub>	B <sub>2</sub> O <sub>3</sub>	Fe <sub>2</sub> O <sub>3</sub>	BaO	CaO	Na <sub>2</sub> O	Li <sub>2</sub> O	ZnO
<b>AB0 (Base)</b>	58.10	-	17.79	3.94	-	-	10.13	10.04	-
<b>CA0 (Base)</b>	41.43	7.17	-	-	-	51.40	-	-	-
<b>CF0</b>	41.43	-	-	7.17	-	51.40	-	-	-
<b>AS0 (Base)</b>	51.72	0.38	2.23	2.92	18.23	11.08	5.64	7.80	-
<b>ASB</b>	51.72	0.38	2.23	2.92	22.23	7.08	5.64	7.80	-
<b>ASZ</b>	51.72	0.38	2.23	2.92	18.23	6.08	5.64	7.80	5.00
<b>ASZ1</b>	51.72	0.38	2.23	2.92	22.23	2.08	5.64	7.80	5.00
<b>ASZ2</b>	54.97	0.40	2.37	3.10	23.63	2.21	3.36	4.64	5.31

The 5 novel compositions were developed based upon the work presented in Chapter 3. Four compositions are optimisations of alkali alkaline earth silicate glass AS0. The glass ASB and ASZ feature reduced melting temperatures, and in the case of ASZ an increased capacity for reduction by organic species. ASZ1 and ASZ2 are further developments on the

previous two compositions. ASZ1 features a further reduction in melting temperature whereas ASZ2 features an improved resistance to aqueous dissolution by virtue of its decreased alkali content. Finally, CF0 is a development of the calcium alumina silicate glass CA0 where the Al<sub>2</sub>O<sub>3</sub> content is replaced with Fe<sub>2</sub>O<sub>3</sub>, improving the capacity of the system for reducing species and reducing the systems melting temperature. The physical properties of each system are displayed in Table 4.1.2.

**Table 4.1.2.** The physical properties of the base and novel developed host glass compositions (T<sub>g</sub>, T<sub>liq</sub>, and Density)

<b>Composition ID</b>	<b>T<sub>g</sub> (°C)</b>	<b>T<sub>liq</sub> (°C)</b>	<b>Density (g/cm<sup>3</sup>)</b>
<b>AB0 (Base)</b>	480	702	2.530
<b>CA0 (Base)</b>	770	1349	2.911
<b>CF0</b>	715	1302	3.136
<b>AS0 (Base)</b>	491	962	3.422
<b>ASB</b>	494	890	3.542
<b>ASZ</b>	497	852	3.502
<b>ASZ1</b>	474	802	3.598
<b>ASZ2</b>	509	987	3.660

All eight glasses were melted with an optimised amount of inert Cs-loaded IEX resin to produce a final waste-form, which was then subjected to analysis. The calcium silicate glasses were found to demonstrate a low extent of Cs retention and slightly lower extent of sulphur retention. These glasses also demonstrated the formation of secondary phases due to waste-loading. The alkali-borosilicate similarly presented the formations of secondary phases on waste-loading, being sulphate salt phases, but otherwise demonstrated increased levels of sulphur and caesium retention. The alkali alkaline-earth borosilicate glasses explored, as a whole, demonstrated the most favourable properties for IEX resin vitrification, with the highest retention of caesium and sulphur species, negligible changes to the physical properties of the glass, and in the case of the ZnO-containing glasses, no alkali sulphate phase formation.

#### 4.1.1 Experimental Procedures

All glasses were prepared from oxide components, melted and annealed at the temperatures shown in Table 2. They were all fritted to a maximum size of 1mm. In the initial series of experiments, 30g of each base glass frit was mixed with a range of quantities of Cs free ion

exchange resin across equivalent waste loadings from 10 wt% to 50 wt%. The samples were melted in Al crucibles with a diameter of 5 cm and a height of 5 cm, at temperatures as indicated in Table 2. In the second set of experiments, 100 g of each glass frit was combined with Cs-loaded ion exchange-resin and melted at the second set of temperatures shown in Table 2. These melts were conducted in alumina crucibles with a diameter of 7 cm and a height of 12 cm, and the final glasses were cast as blocks and annealed. These blocks and the samples from the initial series were then subject to various experiments in order to determine the physical and spectroscopic properties of the waste-form.

The waste loading used in the experiments was a simulant waste comprised of both unloaded and Cs-enriched Duolite ARC 9359 Ion exchange resin; this is a phenol formaldehyde sulphonated resin. This resin was selected due to its use in the processing of aqueous waste stream from various UK sources. The resin used for the waste loading experiments was pre-dried and either un-loaded or loaded with inert caesium up to the maximum capacity of the resin. The resin was loaded with inert Cs by means of mixing unloaded resin with de-ionised H<sub>2</sub>O containing an excess of dissolved CsCO<sub>3</sub>. This mixture was kept at a constant temperature of 25 °C for 7 days to allow the ion exchange process to reach equilibrium. The resin was subsequently filtered out dried and rinsed in de-ionised H<sub>2</sub>O to eliminate any CsCO<sub>3</sub> on the surface of the resin.

The density of the samples was determined by the Archimedes method and the glass transition temperature ( $T_g$ ) of the samples was determined through differential thermal analysis (DTA). The liquidus temperature ( $T_{liq}$ ) was determined utilising the temperature gradient of a horizontal tube furnace. Fritted glass samples were contained in an Al<sub>2</sub>O<sub>3</sub> boat along a portion of the furnace with a known temperature gradient and were kept at constant temperature for 24 hours. The samples were removed whilst hot and the point at which crystallisation was seen to start was visually identified. By measuring the displacement from the end of the boat to this point, and comparing the result against the known temperature gradient which the sample was subjected to, it was possible to determine the  $T_{liq}$  of the glass.

X-ray diffraction (XRD) was utilised to detect and identify any crystalline phases in the waste form (above 5 vol%) or in separated phases. A Seimans D500 with a Cu source and Philips PSD with a Mo source was used.

Fourier transform infra red (FT-IR) spectroscopy and Raman spectroscopy were applied to investigate the change in glass structure on waste-loading. A Perkin Elmer Spectrum 2000 FT-IR spectrometry was used to collect spectra over the 500 -1500 nm range. FT-IR data was collected using a reflectance technique and data was corrected using a

Kramers-Kronig transform. Raman data was collected directly using 530 nm laser excitation and a Renishaw InVia Raman spectrometer.

<sup>57</sup>Fe Mossbauer spectroscopy was utilised to determine the oxidation state and coordination of Fe within the samples. A WissEl <sup>57</sup>Fe Mossbauer spectrometer setup was utilised operating in a constant acceleration mode with a <sup>57</sup>Co source (activity ~9000 µCi). The data produced were fitted using the software package Recoil 1.03 and the recoil free fraction was assumed to be equal in the Fe<sup>2+</sup> and Fe<sup>3+</sup> environments.

SEM EDS experiments were carried out utilising a Philips D500 SEM equipped with an EDS detector system. Samples were mounted in epoxy resin and carbon coated prior to analysis.

More detailed descriptions of these techniques are provided in appendix 8.1.

## 4.1.2 Results

### 4.1.2.1 Base Glass Waste-Loading and the Determination of Optimum Waste-Loading.

The series of base glass samples loaded over a range of 10 wt% to 50 wt% IEX waste loading were each visually inspected and subjected to experiments to determine density variation and changes in  $T_g$  and  $T_{liq}$ . In addition, SEM EDX was applied to investigate variations in composition, <sup>57</sup>Fe Mossbauer spectroscopy was used to investigate changes in the Fe oxidation state and FTIR and Raman spectroscopy were applied to investigate structural changes caused by waste loading. The non zero value of SO<sub>3</sub> content seen in figure 4.1.3 at 0% waste-loading is attributable to residual sulphate present in glass batch materials.

#### Calcium Alumina-Silicate Glass (CA0)

The waste-loaded CA0 samples were homogenous and showed no indication of phase separation across the range of waste-loadings investigated. XRD indicated that the waste-forms contained no detectable crystalline phases. The density of the waste-loaded series was observed to decrease by a small but statistically significant amount on increased waste-

loading. The glass density decreased  $0.03 \pm 0.01 \text{ gcm}^{-3}$  between the base glass and the 50 wt% loaded sample. The  $T_g$  similarly was observed to decrease on waste-loading, from  $771 \pm 5 \text{ }^\circ\text{C}$  to  $750 \pm 5 \text{ }^\circ\text{C}$  between the base glass and the 50 wt% loaded sample. The variation in density and  $T_g$  can be found in Tables 4.1.3 & 4.1.4 respectively.

EDS investigation of the samples demonstrated that the sulphur content of the glass, where present at trace levels, did not show any statistically significant increase in proportion to waste-loading, indicating the sulphur was not retained by the glass. The  $\text{Al}_2\text{O}_3$  content of the waste-loaded samples was seen to increase across the series from 5.2 mol% to 10 mol% ( $\pm 0.1 \text{ mol}\%$ ). This increase can be attributed to the corrosion of the alumina crucible by the melt. All other species present in the system showed no significant variations, other than a decrease in proportion to the increased  $\text{Al}_2\text{O}_3$  content of the system. The variation in the  $\text{SO}_3$  and  $\text{Al}_2\text{O}_3$  content of the samples can be found in tables 4.1.5 & 4.1.6.

### **Alkali Borosilicate Glass (AB0)**

The waste-loaded AB0 glass samples were homogeneous between 10 wt% and 30 wt% loading. At 40 wt% loading and greater, the produced samples were heterogeneous, consisting of glassy material and carbonised but not incorporated resin material. XRD confirmed that no detectable crystalline phases were present throughout the series. The density of the series was observed to increase on waste-loading by a small but significant amount. Density was seen to increase by  $0.06 \pm 0.01 \text{ gcm}^{-3}$  between the base glass and the 40 wt% loaded sample. At 50 wt% loading the density was observed to decrease significantly (by  $0.15 \pm 0.01 \text{ gcm}^{-3}$ ). This can be attributed to the presence of the unincorporated carbonised resin material. The  $T_g$  similarly was observed to decrease on waste-loading, from  $480 \pm 5 \text{ }^\circ\text{C}$  to  $460 \pm 5 \text{ }^\circ\text{C}$  between the base glass and the 50 wt% loaded sample, which can similarly be attributed to presence of carbonised material. The variation in  $T_g$  and density can be found in tables 4.1.3 & 4.1.4 respectively.

EDS investigation of the waste-loaded samples indicated that on waste-loading, the sulphur content did increase by a small but significant amount. The  $\text{SO}_3$  content was observed to increase from  $0.1 \pm 0.1 \text{ mol}\%$  in the base glass to  $0.4 \pm 0.1 \text{ mol}\%$  at 30 wt% loading, indicating a low level of sulphur uptake. At 40 - 50 wt% loading sulphur content decreased, due to failure to incorporate a proportion of the resin. It should be noted that although the increase in sulphur is significant, it only represents a small proportion of the sulphur inventory, indicating the majority of the sulphur content is still lost. The  $\text{Al}_2\text{O}_3$

content of the waste-loaded samples was seen to increase across the series from 0.4 mol% to 3.4 mol% ( $\pm 0.1$  mol%). This increase can be attributed the corrosion of the alumina crucible by the melt. All other species present in the system showed no significant variation other than a decrease in proportion to the increased  $\text{Al}_2\text{O}_3$  content of the system. The variation in the  $\text{SO}_3$  and  $\text{Al}_2\text{O}_3$  content of the samples can be found in tables 4.1.5 & 4.1.6.

Raman spectroscopy of the 50 wt% loaded sample showed evidence of strong bands at  $\sim 400\text{ cm}^{-1}$  and  $\sim 990\text{ cm}^{-1}$ , which are associated with  $\text{S}^{2-}$  and  $\text{SO}_4^{2-}$  groups respectively, indicating retention of sulphur in both oxidation states in this system. Mossbauer spectroscopy indicated no significant variation in  $\text{Fe}^{3+}$  content between 10 wt% and 30 wt% loading but showed a significant decrease in the proportion of  $\text{Fe}^{3+}$  at 50 wt% loading. The proportion of  $\text{Fe}^{3+}$  was seen to decrease from  $97 (\pm 2)\%$  to  $11 (\pm 2)\%$  with a proportional increase in the proportion of  $\text{Fe}^{2+}$  present which can be attributed to the reducing effect of the significant organic resin waste-loading. This variation is shown in Figure 4.1.7 and the data values are shown in Table 4.1.7.

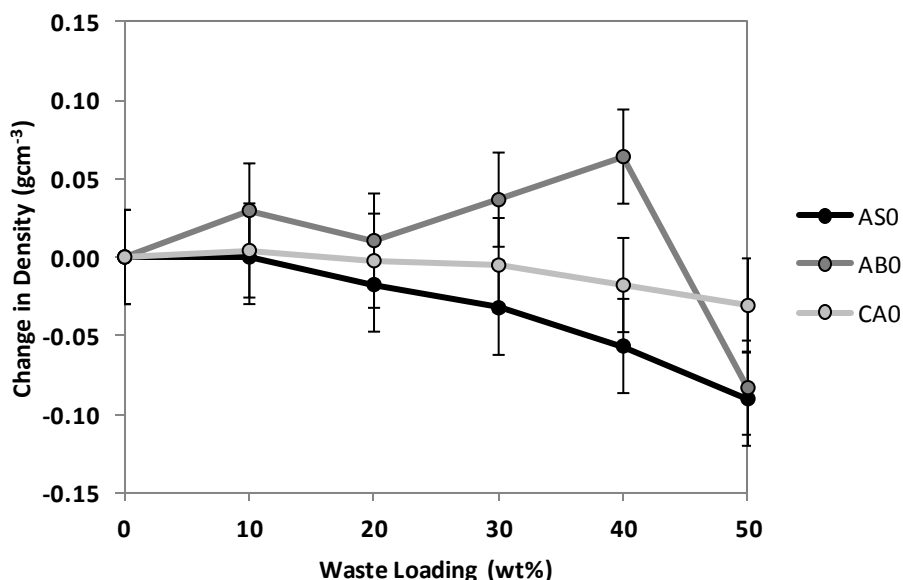
### **Alkali Alkaline-Earth Silicate Glass (AS0)**

The waste-loaded AS0 glass samples were homogeneous between 10 wt% and 30 wt% loading. As with the AB0 samples at 40 wt% loading and above, samples were heterogeneous, consisting of glassy material and carbonised but not incorporated resin material. XRD confirmed that no detectable crystalline phases were present throughout the series. The density of the series was observed to decrease on waste-loading by a significant amount. Density was seen to decrease by  $0.2 \pm 0.01\text{ gcm}^{-3}$  between the base glass and the 50 wt% loaded sample. A large proportion of this overall decrease occurred between 40wt% and 50wt% ( $0.11 \pm 0.01\text{ gcm}^{-3}$ ), indicating that this decrease can be associated with presence of incorporated resin material. The  $T_g$  similarly was observed to decrease on waste-loading, from  $491 \pm 5\text{ }^\circ\text{C}$  to  $465 \pm 5\text{ }^\circ\text{C}$  between the base glass and the 50 wt% loaded sample. The variation in  $T_g$  and density can be found in Tables 4.1.3 & 4.1.4 respectively.

EDS investigation of the waste-loaded AS0 samples revealed a significant increase in the sulphur content of the samples. The  $\text{SO}_3$  content of the waste-form increased from  $0.3 \pm 0.1$  mol% in the base glass to  $2.10 \pm 0.1$  mol% at 40 wt % and 50 wt%. The sulphur content can be seen to increase linearly up to 30 wt%, above which the sulphur content is essentially constant. This is likely due to the failure to incorporate resin at waste-loadings of 40 wt% and above. It is likely that up to the 30 wt% loading a high proportion of the resin sulphur content

was incorporated into the glass and hence sulphur loss was minimal. The  $\text{Al}_2\text{O}_3$  content of the waste-loaded samples was seen to increase across the series from 0.5 mol% to 3.7 mol% ( $\pm 0.1$  mol%). This increase can be attributed to the corrosion of the alumina crucible by the melt. All other species present in the system showed no significant variation other than a decrease in proportion to the increased  $\text{Al}_2\text{O}_3$  content of the system. The variation in the  $\text{SO}_3$  and  $\text{Al}_2\text{O}_3$  content of the samples can be found in Tables 4.1.5 & 4.1.6.

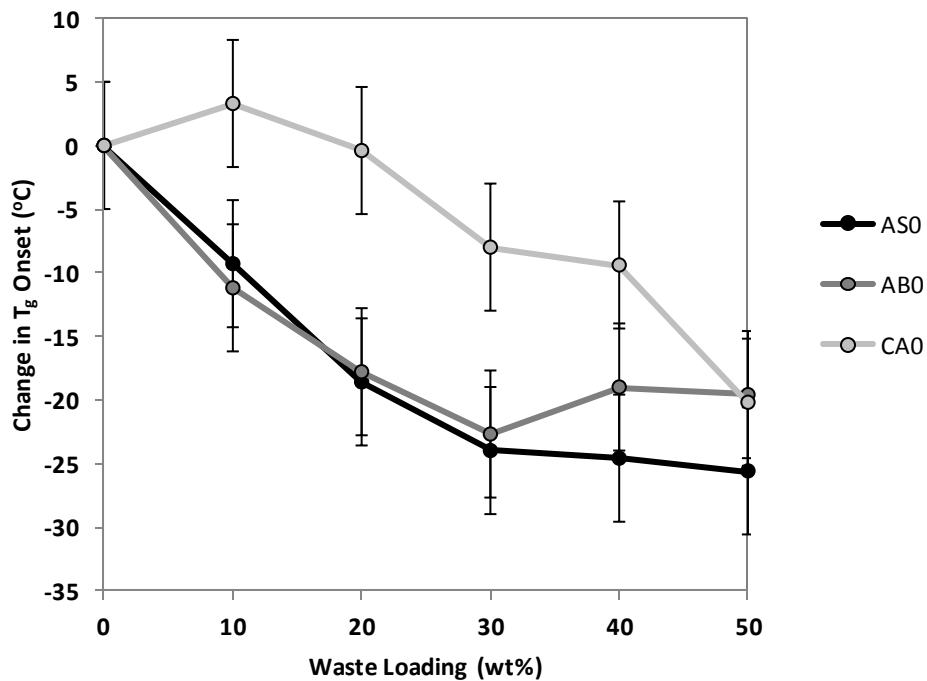
Raman spectroscopy of all waste loaded samples revealed the presence of strong bands at  $400\text{ cm}^{-1}$  and  $990\text{ cm}^{-1}$  as associated with  $\text{S}^{2-}$  and  $\text{SO}_4^{2-}$  respectively<sup>(79-80)</sup>. Between 10wt% and 30wt%, the  $990\text{ cm}^{-1}$  band increases in intensity in rough proportion to loading. This band then diminishes at 40wt% to 50wt% loading and the band at  $400\text{ cm}^{-1}$  appears. This variation in  $\text{S}^{2-}$  and  $\text{SO}_4^{2-}$  bands is displayed in Figure 4.1.6. Mossbauer spectroscopy showed a significant decrease in the proportion of  $\text{Fe}^{3+}$  in the system between 10 wt% and 30 wt% loading, decreasing from  $96 (\pm 2) \%$  to  $39 (\pm 2) \%$ . However at 50 wt% loading the proportion of  $\text{Fe}^{3+}$  was seen to increase by a small but significant amount, from  $39 (\pm 2) \%$  to  $51 (\pm 2) \%$ . This variation is shown in Figure 7 and the data is presented in Table 4.1.7.



**Figure 4.1.1.** Variation in density relative to the density of the base glass for CA0, AB0 and AS0 glasses across range of IEX waste-loadings. Error determined from standard deviation of three individual measurements.

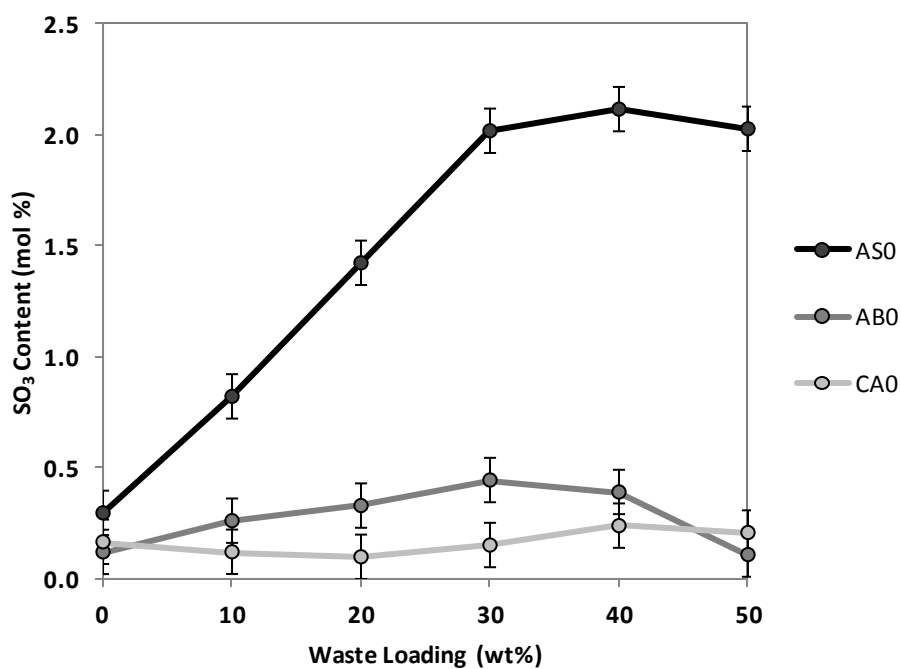
**Table 4.1.3.** Variation in density across initial waste-loading series.

Waste-Loading (wt%)	Density (gcm <sup>-3</sup> )		
	AS0	AB0	CA0
Base Glass	3.42	2.53	2.91
10	3.4	2.56	2.92
20	3.39	2.54	2.91
30	3.37	2.57	2.91
40	3.33	2.59	2.89
50	3.23	2.45	2.88

**Figure 4.1.2.** Variation in T<sub>g</sub> relative to the T<sub>g</sub> of the base glass for CA0, AB0 and AS0 glasses across range of IEX waste-loadings. Error based on standard error of technique.

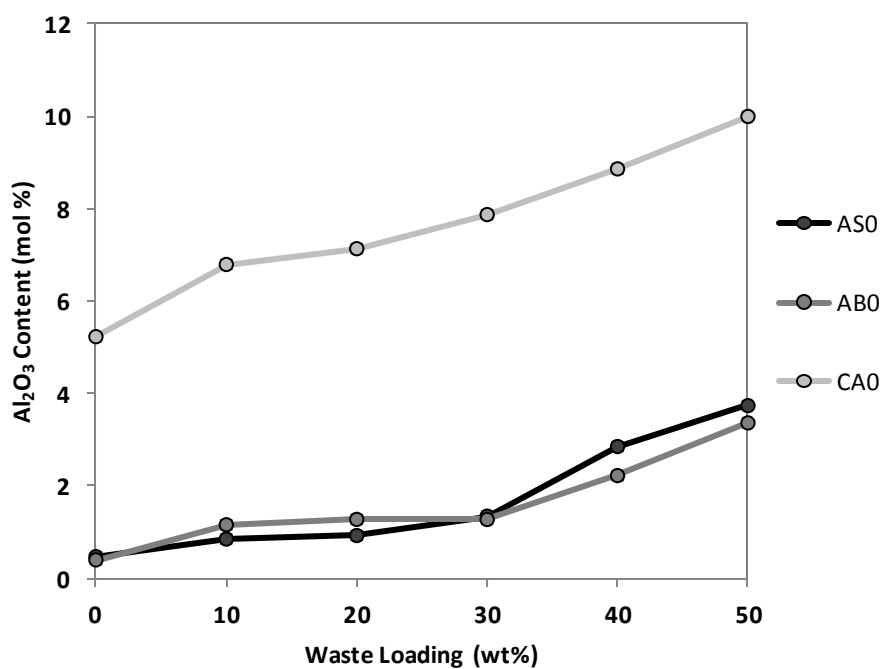
**Table 4.1.4.** Variation in  $T_g$  onset across initial waste-loading series.

Waste-Loading (wt%)	$T_g$ Onset ( $^{\circ}\text{C}$ )		
	AS0	AB0	CA0
Base Glass	491	480	770.6
10	481.7	468.8	773.9
20	472.4	462.2	770.2
30	467	457.3	762.6
40	466.4	461	761.2
50	465.4	460.4	750.4

**Figure 4.1.3.** Variation in  $\text{SO}_3$  content as analysed by EDX spectroscopy across range of IEX waste-loadings. Error based on standard error of technique.

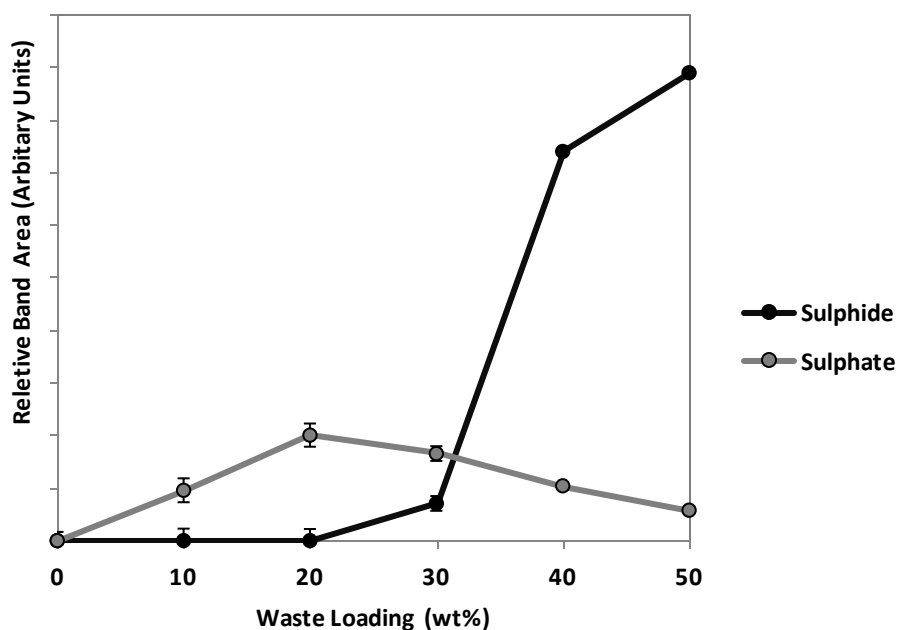
**Table 4.1.5.** Variation in SO<sub>3</sub> content across initial waste-loading series.

Waste-Loading (wt%)	SO <sub>3</sub> Content (mol%)		
	AS0	AB0	CA0
Base Glass	0.29	0.12	0.16
10	0.82	0.26	0.12
20	1.42	0.33	0.10
30	2.02	0.44	0.15
40	2.11	0.39	0.24
50	2.02	0.11	0.21

**Figure 4.1.4.** Increase in Al<sub>2</sub>O<sub>3</sub> content in each glass as analysed by EDX spectroscopy across a range of IEX waste-loadings. Error based on standard error of technique.

**Table 4.1.6.** Variation in Al<sub>2</sub>O<sub>3</sub> content across initial waste-loading series.

Waste-Loading (wt%)	Al <sub>2</sub> O <sub>3</sub> Content (mol%)		
	AS0	AB0	CA0
Base Glass	0.47	0.40	5.22
10	0.85	1.16	6.78
20	0.92	1.27	7.13
30	1.34	1.27	7.86
40	2.85	2.22	8.85
50	3.73	3.36	9.99

**Figure 4.1.6.** Variation in intensity of Raman spectroscopy bands related to S<sup>2-</sup> and SO<sub>4</sub><sup>2-</sup> in glass AS0 across a range of IEX resin waste-loadings. Error determined from accuracy of fit.

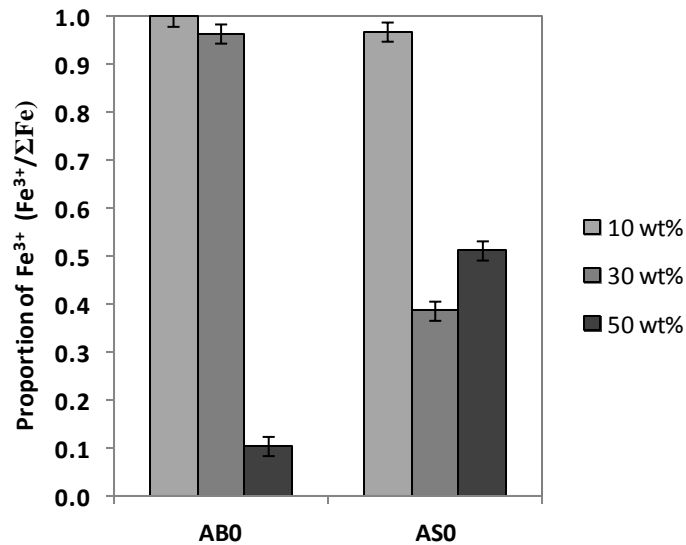


**Figure 4.1.7.** Variation in proportion of  $\text{Fe}^{3+}$  in glasses AS0 and AB0 across a range of IEX resin waste loadings. Error determined from standard error associated with fitting.

**Table 4.1.7.** Variation  $\text{Fe}^{3+}$  in glasses AS0 and AB0 across initial waste-loading series.

Waste-Loading (wt%)	Proportion of $\text{Fe}^{3+}$ ( $\text{Fe}^{3+}/\Sigma\text{Fe}$ )	
	AS0	AB0
10	0.969	1.000
30	0.387	0.965
50	0.513	0.105

### Base Glass Loading Summary

It is apparent from the results that neither the AB0 or AS0 glass produced a homogenous waste form with a waste loading of 30 wt%. All waste-forms loaded with 30 wt% or less IEX resin were homogenous products with no evidence of heterogeneity, phase separation or the presence of a salt gall layer. The observed changes in  $T_g$ , density and  $Q^n$  speciation can largely be attributed to the addition of  $\text{Al}_2\text{O}_3$  into the system from the crucible utilised in fabricating the waste-form. Sulphur retention in both  $\text{SO}_4^{2-}$  and  $\text{S}^{2-}$  forms was detected in both AB0 and AS0 glass waste-forms, however, the AS0 glass demonstrated a far greater capacity for sulphur than either of the other base glass compositions studied. Raman

spectroscopy revealed a variation in the ratio of sulphur oxidation states with waste-loading, with more reduced S<sup>2-</sup> becoming more prominent at higher waste-loadings. This could be attributed to reduction of the sulphur species by action of the increased organic content from the IEX resin waste at higher waste-loadings.

#### **4.1.2.2 Waste Loading of Developed Waste-Forms**

Based on the results of the initial loading experiments detailed above, all eight glasses (three original compositions plus the five additional developed compositions) were loaded to a maximum loading of 30 wt% and an intermediate loading of 15 wt%.

#### **Initial Observations**

At 30 wt% loading of IEX simulant the waste-forms produced from glasses AS0, AB0 and ASB presented evidence of some extent of phase separation and gall-layer formation, which was most apparent in the AB0 sample which also presented evidence of unincorporated resin material. The waste form produced from glass CA0 was observed to possess inclusions and striations, indicative of the presence of phase separated material. The waste-form produced from the glass CF0 was found to contain phase separated metallic iron, despite being otherwise free from additional phase separation or gall layer formation. Waste-forms formed from ASZ, ASZ1 and ASZ2 formed homogeneous products, however, a crystalline phase was formed above the surface of all three melts. This crystalline phase was analyzed through XRD and determined to be dominated by ZnO. All produced waste-forms were found to be amorphous under XRD analysis indicating that any crystalline material present occupied less than 5 vol%.

At 15wt% loading, no evidence of phase separation was observed in any of the waste-forms produced. No surface gall layer was formed and no evidence of crystallisation or metallic inclusions was apparent. All waste-forms were found to be amorphous under XRD analysis indicating that any crystalline material present occupied less than 5 vol%.

### Physical Property Variation on Waste-loading

Seven waste loaded glasses presented a decrease in density on loading ranging from a decrease of  $0.02 \pm 0.01 \text{ gcm}^{-3}$  in ASZ1 to  $0.13 \pm 0.01 \text{ gcm}^{-3}$  in the CF0 waste-form. In contrast, the AB0 waste form which showed an increase in density of  $0.03 \pm 0.01 \text{ gcm}^{-3}$ . These results are consistent with the initial loading experiments carried out on the base glasses. The significant decrease in density apparent in the 30 wt% waste loaded CF0 sample can be directly attributed to the loss of Fe content to the metallic inclusion which was found in that sample. The change in density for the waste forms is shown in figure 4.1.8. Density values for all glasses are shown in Table 4.1.8.

The  $T_{\text{liq}}$  of the alkali alkaline-earth silicate and alkali borosilicate based waste-forms was seen to increase approximately in proportion to the waste-loading of each waste-form. The most significant increases in  $T_{\text{liq}}$  were apparent in the ASZ and ASZ1 waste-forms which at the highest waste-loading demonstrated an increase in  $T_{\text{liq}}$  of  $178 \pm 10 \text{ }^{\circ}\text{C}$  and  $246 \pm 10 \text{ }^{\circ}\text{C}$  respectively. The AS0 and ASB glasses demonstrated a lower increase in  $T_{\text{liq}}$  on waste-loading. The alkali borosilicate waste-form demonstrated an increase of  $108 \pm 10 \text{ }^{\circ}\text{C}$  in its  $T_{\text{liq}}$  at 30 wt% loading. Notably, calcium silicate glasses did not demonstrate an increase in  $T_{\text{liq}}$  on waste-loading, but actually demonstrated a decrease. This is most apparent in the CA0 waste-form where the  $T_{\text{liq}}$  was seen to be reduced by  $92 \pm 10 \text{ }^{\circ}\text{C}$ , but is also apparent in CF0 at lower waste-loadings. CF0 at 30 wt% loading demonstrated a  $33 \pm 10 \text{ }^{\circ}\text{C}$  increase in  $T_{\text{liq}}$ . The variation in  $T_{\text{liq}}$  can be seen in figure 4.1.9.  $T_{\text{liq}}$  values for all glasses are shown in Table 4.1.9.

The  $T_{\text{g}}$  of the waste-loaded glasses was seen to decrease by a significant extent in six of the eight waste-loaded glass systems. No significant change in  $T_{\text{g}}$  was apparent at either 15 wt% or 30 wt% waste-loading in either the AB0 or ASZ1 glass system. The most substantial reduction was observed for the ASZ2 system, in which a decrease in  $T_{\text{g}}$  of  $38 \pm 5 \text{ }^{\circ}\text{C}$  was apparent at 30 wt% loading. The remaining three alkali alkaline-earth silicate waste-forms demonstrated fairly consistent decreases in  $T_{\text{g}}$  of approximately  $15 \text{ }^{\circ}\text{C}$ , showing no significant variation between the 15 wt% and 30 wt% loaded samples. Both of the calcium silicate glasses showed a similar decrease  $T_{\text{g}}$  which averaged approximately  $10 \text{ }^{\circ}\text{C}$ , however between the two waste-forms the CF0 waste-form showed a larger decrease than was seen in the CA0 waste-form. The variation in  $T_{\text{g}}$  can be seen in figure 4.1.10.  $T_{\text{g}}$  values for all glasses are shown in Table 4.1.10.

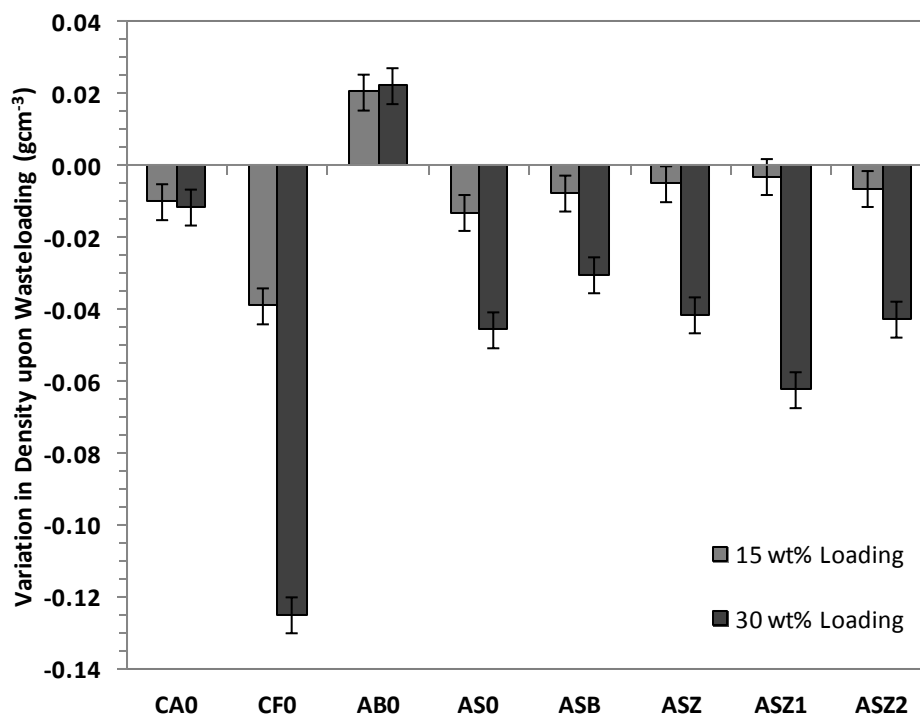


**Figure 4.1.8.** The Variation in Density upon the waste-loading of all eight novel glass compositions. Error bars determined from standard measurement error.

**Table 4.1.8.** Variation in density upon waste-loading with 15 wt% and 30 wt%.

Composition	Density (gcm <sup>-3</sup> )		
	Base	15 wt%	30 wt%
<b>AB0</b>	2.53 ± 0.01	3.51 ± 0.01	2.55 ± 0.01
<b>CA0</b>	2.91 ± 0.01	3.50 ± 0.01	2.90 ± 0.01
<b>CF0</b>	3.14 ± 0.01	3.54 ± 0.01	3.01 ± 0.01
<b>AS0</b>	3.42 ± 0.01	3.62 ± 0.01	3.41 ± 0.01
<b>ASB</b>	3.54 ± 0.01	3.55 ± 0.01	3.53 ± 0.01
<b>ASZ</b>	3.50 ± 0.01	2.92 ± 0.01	3.46 ± 0.01
<b>ASZ1</b>	3.60 ± 0.01	3.10 ± 0.01	3.60 ± 0.01
<b>ASZ2</b>	3.66 ± 0.01	3.38 ± 0.01	3.63 ± 0.01

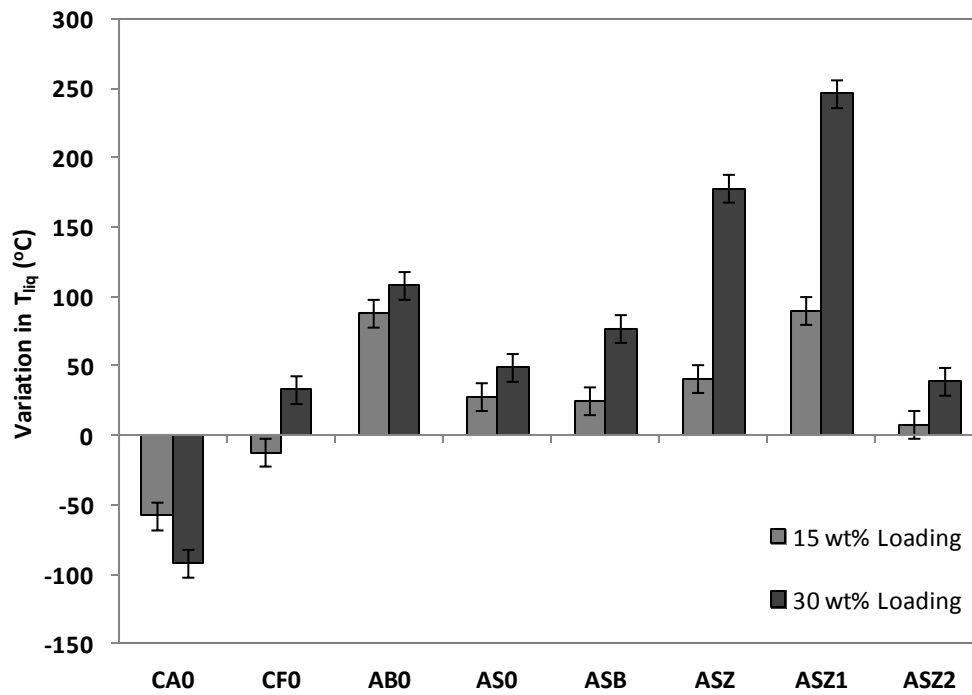


**Figure 4.1.9.** The Variation in  $T_{liq}$  upon the waste-loading of all eight novel glass compositions. Error bars determined from standard measurement error.

**Table 4.1.9.** Variation in  $T_{liq}$  upon waste-loading at 15 wt% and 30 wt%.

Composition	$T_{liq}$ (°C)		
	Base	15 wt%	30 wt%
<b>AB0</b>	702 ± 10	790 ± 10	810 ± 10
<b>CA0</b>	1349 ± 10	1291 ± 10	1257 ± 10
<b>CF0</b>	1302 ± 10	1290 ± 10	1335 ± 10
<b>AS0</b>	962 ± 10	990 ± 10	1011 ± 10
<b>ASB</b>	890 ± 10	915 ± 10	967 ± 10
<b>ASZ</b>	852 ± 10	893 ± 10	1030 ± 10
<b>ASZ1</b>	802 ± 10	892 ± 10	1048 ± 10
<b>ASZ2</b>	987 ± 10	995 ± 10	1026 ± 10

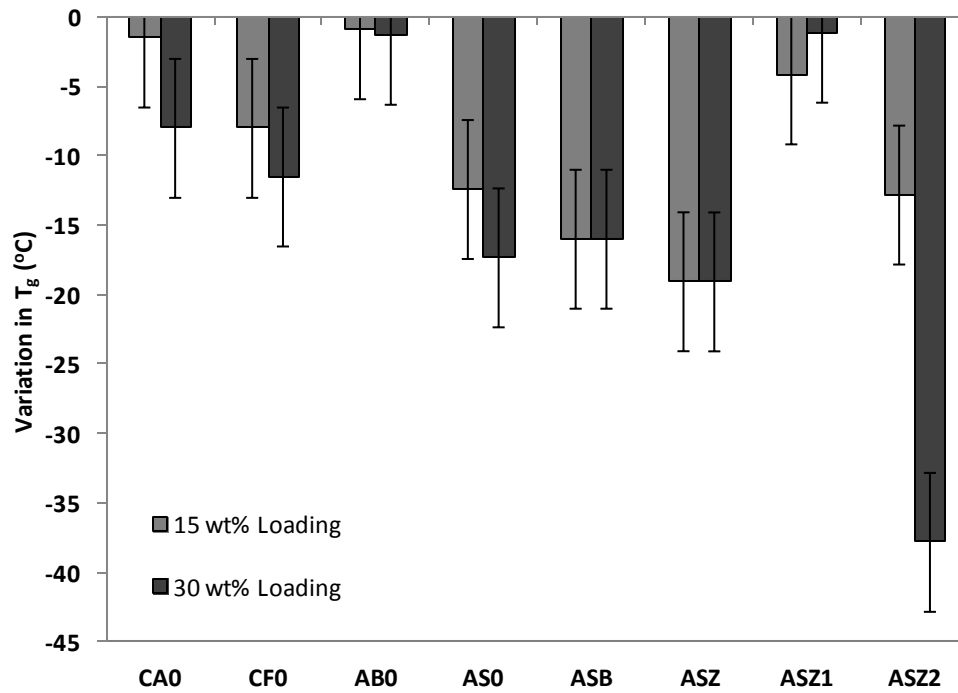


**Figure 4.1.10.** The Variation in  $T_g$  upon the waste-loading of all eight novel glass compositions. Error bars determined from standard measurement error.

**Table 4.1.10.** Variation in  $T_g$  onset upon waste-loading at 15 wt% and 30 wt%.

Composition	$T_g$ Onset ( $^{\circ}\text{C}$ )		
	Base	15 wt%	30 wt%
<b>AB0</b>	$480 \pm 5$	$479 \pm 5$	$479 \pm 5$
<b>CA0</b>	$770 \pm 5$	$769 \pm 5$	$762 \pm 5$
<b>CF0</b>	$715 \pm 5$	$707 \pm 5$	$705 \pm 5$
<b>AS0</b>	$491 \pm 5$	$479 \pm 5$	$474 \pm 5$
<b>ASB</b>	$494 \pm 5$	$478 \pm 5$	$478 \pm 5$
<b>ASZ</b>	$497 \pm 5$	$478 \pm 5$	$478 \pm 5$
<b>ASZ1</b>	$474 \pm 5$	$470 \pm 5$	$473 \pm 5$
<b>ASZ2</b>	$509 \pm 5$	$496 \pm 5$	$471 \pm 5$

## Composition Variation

XRF analysis of the base glass samples and the waste-loaded samples allowed the composition changes which occurred as a consequence of waste-loading to be investigated. No significant variation in SiO<sub>2</sub>, Fe<sub>2</sub>O<sub>3</sub>, BaO and CaO was determined, however variations were observed in the Na<sub>2</sub>O, Al<sub>2</sub>O<sub>3</sub> and ZnO content of some or all of the waste-loaded glasses. The composition of the base glass samples as well as the waste-loaded samples may be found below in table 4.1.11, 4.1.12 and 4.1.13 below.

The Na<sub>2</sub>O content in the AB0, AS0 and ASB samples was observed to decrease on waste-loading by a significant extent. The largest decrease was apparent in the AB0 sample which demonstrated a decrease of  $4.1 \pm 0.4$  mol% between the base glass and the 30 wt% loaded sample. A similar decrease was apparent in the AS0 and ASB waste-loaded samples. However, the Na<sub>2</sub>O loss was of lower magnitude at  $\sim 0.6 \pm 0.3$  mol% for both glasses. The ASZ, ASZ1 and ASZ2 samples did not present any evidence of significant Na<sub>2</sub>O loss from their XRF results. This implies that sulphur and sodium loss are not directly connected. Also this shows that the decrease in  $T_{liq}$  seen in these glasses cannot be attributed to the loss of Na<sub>2</sub>O from the glass composition. The variation in Na<sub>2</sub>O content for these glasses can be found below in Figure 4.1.11.

The proportion of Al<sub>2</sub>O<sub>3</sub> present in the glasses was seen to increase upon waste-loading in all eight glasses. The most significant increase in Al<sub>2</sub>O<sub>3</sub> content as apparent in the CF0 glass, which demonstrated an increase in Al<sub>2</sub>O<sub>3</sub> content of  $7.1 \pm 0.5$  mol% at 30 wt% waste loading. The AB0 glass also demonstrated a significant increase in Al<sub>2</sub>O<sub>3</sub> content, showing an increase of  $3.06 \pm 0.2$  mol% at 30 wt% waste loading. The alkali alkaline-earth silicate glasses generally presented the lowest increases in Al<sub>2</sub>O<sub>3</sub> content, averaging an increase of approximately 1.5 mol%. The variation in Al<sub>2</sub>O<sub>3</sub> content for these glasses can be found below in Figure 4.1.12.

**Table 4.1.11.** Analysed composition of all glass compositions explored prior to waste-loading, as determined by XRF.

Composition	Sample Composition (mol%)									
	SiO <sub>2</sub>	Al <sub>2</sub> O <sub>3</sub>	Fe <sub>2</sub> O <sub>3</sub>	Na <sub>2</sub> O	BaO	CaO	ZnO	SO <sub>3</sub>	Cs <sub>2</sub> O	
AB0	80.4±4.0	0.1±0.1	5.5±0.3	14.0±0.7	0.0±0.1	0.0±0.1	0.0±0.1	0.1±0.1	0.0±0.1	
CA0	41.5±2.1	7.2±0.4	0.2±0.1	0.0±0.1	0.0±0.1	51.1±2.6	0.0±0.1	0.1±0.1	0.0±0.1	
CF0	41.4±2.1	0.1±0.1	7.1±0.4	0.0±0.1	0.0±0.1	51.2±2.6	0.0±0.1	0.1±0.1	0.0±0.1	
AS0	57.6±2.9	0.2±0.1	3.4±0.2	6.1±0.3	20.4±0.4	12.3±0.6	0.0±0.1	0.1±0.1	0.0±0.1	
ASB	57.3±2.9	0.5±0.1	3.4±0.2	6.4±0.3	24.6±0.4	7.8±0.4	0.0±0.1	0.0±0.1	0.0±0.1	
ASZ	57.3±2.9	0.5±0.1	3.3±0.2	6.2±0.3	20.0±0.4	6.8±0.4	5.7±0.2	0.1±0.1	0.0±0.1	
ASZ1	57.8±2.9	0.5±0.1	3.1±0.2	6.3±0.3	24.5±0.4	2.0±0.1	5.7±0.2	0.1±0.1	0.0±0.1	
ASZ2	60.4±3.0	0.5±0.1	3.3±0.2	2.5±0.1	25.4±0.4	2.2±0.1	5.6±0.2	0.1±0.1	0.0±0.1	

**Table 4.1.12.** Analysed composition of all glass compositions explored at 15 wt% waste-loading, as determined by XRF.

Composition	Sample Composition (mol%)									
	SiO <sub>2</sub>	Al <sub>2</sub> O <sub>3</sub>	Fe <sub>2</sub> O <sub>3</sub>	Na <sub>2</sub> O	BaO	CaO	ZnO	SO <sub>3</sub>	Cs <sub>2</sub> O	
AB0	79.0±4.0	3.1±0.2	5.7±0.3	11.0±0.5	0.2±0.1	0.3±0.1	0.0±0.1	0.1±0.1	0.6±0.1	
CA0	44.5±2.2	8.2±0.4	0.0±0.1	0.1±0.1	0.1±0.1	46.5±2.2	0.0±0.1	0.0±0.1	0.5±0.1	
CF0	42.8±2.1	7.2±0.4	6.3±0.3	0.1±0.1	0.1±0.1	43.0±2.2	0.0±0.1	0.0±0.1	0.5±0.1	
AS0	58.8±2.9	1.7±0.1	3.0±0.2	5.9±0.3	18.2±0.9	11.0±0.6	0.0±0.1	0.5±0.1	0.7±0.1	
ASB	58.0±2.9	1.2±0.1	3.2±0.2	5.8±0.3	23.2±1.2	7.1±0.3	0.0±0.1	0.7±0.1	0.7±0.1	
ASZ	57.6±2.9	1.4±0.1	3.1±0.2	6.4±0.3	18.6±0.9	6.0±0.3	5.3±0.3	1.0±0.1	0.7±0.1	
ASZ1	57.7±2.9	2.4±0.1	2.8±0.2	6.4±0.3	22.1±1.1	2.2±0.1	5.1±0.3	0.7±0.1	0.6±0.1	
ASZ2	59.3±3.0	0.9±0.1	3.2±0.2	4.8±0.2	23.7±1.2	2.4±0.1	4.6±0.3	0.3±0.1	0.8±0.1	

**Table 4.1.13.** Analysed composition of all glass compositions explored at 30 wt% waste-loading waste-loading, as determined by XRF.

Composition	Sample Composition (mol%)									
	SiO <sub>2</sub>	Al <sub>2</sub> O <sub>3</sub>	Fe <sub>2</sub> O <sub>3</sub>	Na <sub>2</sub> O	BaO	CaO	ZnO	SO <sub>3</sub>	Cs <sub>2</sub> O	
AB0	77.1±3.9	0.7±0.1	6.5±0.3	11.5±0.6	0.4±0.1	0.3±0.1	0.1±0.1	1.8±0.1	1.6±0.1	
CA0	47.7±2.3	8.2±0.3	0.0±0.1	0.0±0.1	0.0±0.2	42.2±2.1	0.0±0.1	1.0±0.1	0.5±0.1	
CF0	45.4±2.3	3.9±0.2	1.1±0.1	0.1±0.1	0.1±0.1	47.9±2.4	0.0±0.1	0.3±0.1	1.2±0.1	
AS0	57.9±2.9	0.8±0.1	3.2±0.2	5.9±0.3	18.9±0.3	10.6±0.5	0.0±0.1	1.4±0.1	1.3±0.1	
ASB	56.6±2.8	0.9±0.1	3.0±0.2	6.0±0.3	23.2±0.3	7.2±0.4	0.0±0.1	1.9±0.1	1.2±0.1	
ASZ	58.3±2.9	0.7±0.1	3.2±0.2	6.4±0.3	18.6±0.2	6.2±0.3	3.5±0.2	1.9±0.1	1.2±0.1	
ASZ1	56.1±2.8	0.7±0.1	2.7±0.1	6.6±0.3	22.4±0.3	2.3±0.1	4.1±0.2	3.0±0.2	2.0±0.1	
ASZ2	59.4±3.0	0.7±0.1	3.3±0.2	2.7±0.1	24.7±0.3	2.7±0.1	3.8±0.2	1.2±0.1	1.4±0.1	

**Table 4.1.14.** Theoretical composition for 30 wt% waste-forms assuming full retention of Cs and S, and total loss of organic component.

Composition	Sample Composition (mol%)									
	SiO <sub>2</sub>	Al <sub>2</sub> O <sub>3</sub>	Fe <sub>2</sub> O <sub>3</sub>	Na <sub>2</sub> O	BaO	CaO	ZnO	SO <sub>3</sub>	Cs <sub>2</sub> O	
AB0	76.81	0.04	5.27	13.30	0.11	0.02	0.01	2.85	1.57	
CA0	39.85	6.91	0.16	0.01	0.10	48.85	0.01	2.64	1.47	
CF0	39.74	0.11	6.80	0.02	0.11	48.84	0.01	2.81	1.56	
AS0	54.50	0.18	3.22	5.72	19.30	11.62	0.02	3.49	1.94	
ASB	54.09	0.49	3.21	6.01	23.23	7.31	0.02	3.60	2.04	
ASZ	54.23	0.48	3.16	5.86	18.93	6.46	5.37	3.54	1.97	
ASZ1	54.48	0.44	2.94	5.96	23.15	1.89	5.40	3.69	2.06	
ASZ2	56.94	0.45	3.15	2.35	23.97	2.09	5.23	3.76	2.08	

The ZnO content of glasses ASZ, ASZ1 and ASZ2, was found to vary significantly in proportion to waste loading. All three glasses demonstrated a similar decrease in ZnO content on waste-loading, showing an average decrease of 1.8 mol% at 30 wt% loading. The ZnO content of the 30 wt% loaded ASZ1 and ASZ2 sample were seen to be higher than the ASZ sample by a small but significant margin after waste-loading, indicating a larger proportion of ZnO was lost from the ASZ glass at 30 wt% loading. However, in contrast, the proportion of ZnO present in the ASZ2 sample at 15 wt% loading was seen to be significantly lower than the ZnO content of the ASZ1 and ASZ glasses, indicating that a greater proportion of ZnO was lost from ASZ2 at 15 wt% loading. These ZnO losses can be attributed to the formation of the Zn-rich crystalline phase observed on waste-loading of these glasses. The variation in ZnO content in these three glasses can be seen in Figure 4.1.13.

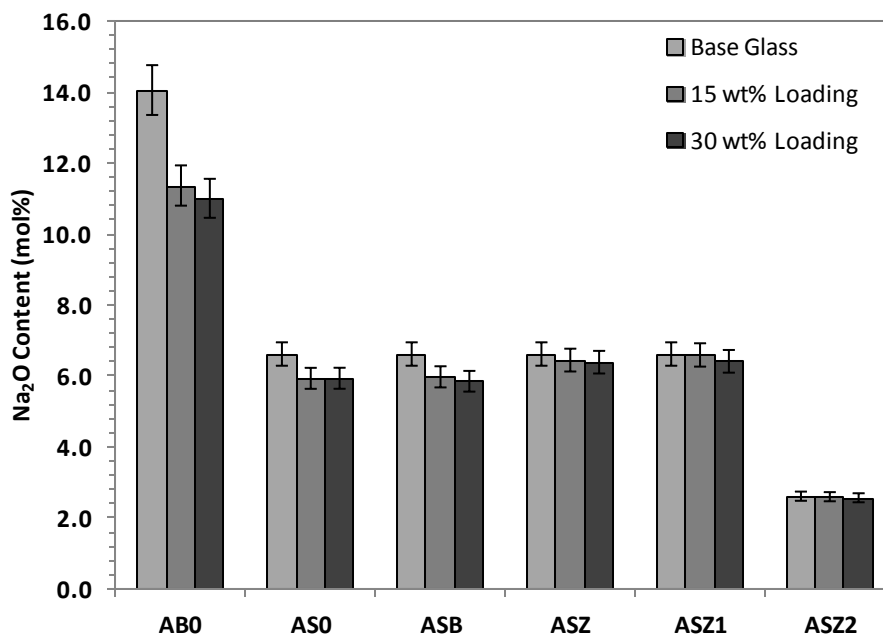


**Figure 4.1.11.** The Na<sub>2</sub>O content in the base glass sample and waste-loaded samples for the alkali borosilicate and alkali alkaline earth silicate glasses. Error bars determined from percentage experimental error associated with XRF measurement.

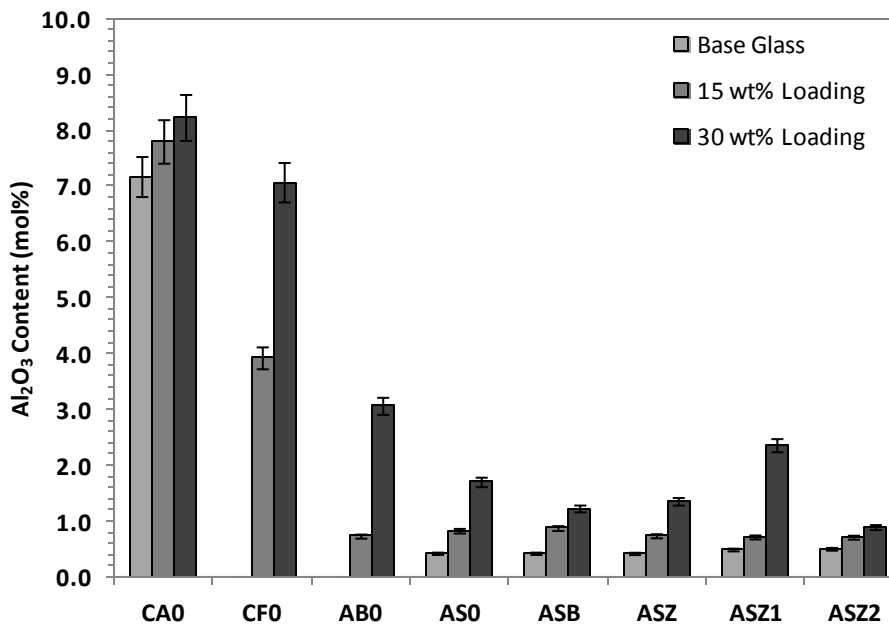


**Figure 4.1.12.** The Al<sub>2</sub>O<sub>3</sub> content in the base glass sample and waste-loaded samples for all glasses. Error bars determined from percentage experimental error associated with XRF measurement.

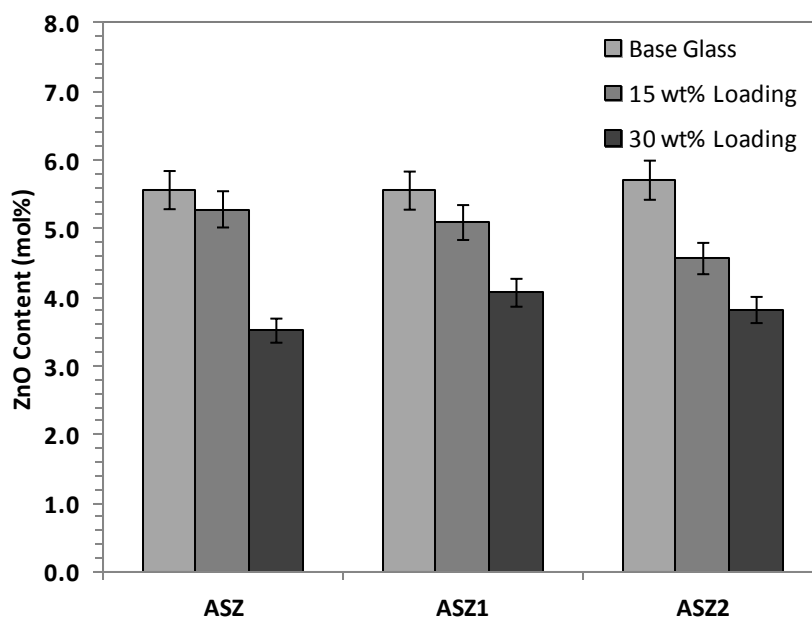


**Figure 4.1.13.** The ZnO content in the base glass sample and waste-loaded samples for the ASZ, ASZ1 and ASZ2 glasses. Error bars determined from percentage experimental error associated with XRF measurement.

XRF analysis was also able to quantify the proportion of species from the IEX resin waste-loading present in the samples, in terms of  $\text{SO}_3$  and  $\text{Cs}_2\text{O}$  content. Considering the proportion of  $\text{SO}_3$  in the glasses, it can be seen in Figure 4.1.14 that all eight glasses demonstrated some level of  $\text{SO}_3$  retention. However, it is important to note that the levels of  $\text{SO}_3$  presented by XRF analysis does not necessarily indicate sulphur which has been incorporated into the waste-form, but could be associated with phase-separated salt material that either has not volatilised or has been encapsulated within the glass as is discussed by Manara *et al* <sup>(32)</sup>. The results of the 15 wt% loading samples, which were found to be free of heterogeneity, are more beneficial as a comparable demonstration of sulphur incorporation by the glass systems investigated. At 15 wt% loading, the calcium silicate and alkali borosilicate glass samples demonstrate only a negligible  $\text{SO}_3$  content, in the order of 0.07 mol%. All five of the alkali alkaline-earth silicate waste-forms demonstrate a significant  $\text{SO}_3$  content at 15 wt% waste-loading, demonstrating their higher capacity for anionic species and sulphur in particular. At 30 wt% loading all samples display a significant retention of  $\text{SO}_3$ . The lowest retention of sulphur is demonstrated by the calcium silicate host glasses, which is potentially attributable to the higher  $T_{\text{melt}}$  of these glasses. At both 15 wt% and 30 wt% loading, the highest retention of sulphur was seen in the ZnO-containing alkali alkaline-earth silicate glasses, demonstrating that the presence of ZnO in these glasses directly benefits  $\text{SO}_3$  retention. The alkali borosilicate AB0 glass demonstrated a similar level of  $\text{SO}_3$  content to the alkali alkaline-earth silicate glass waste-forms, but as has been mentioned this may be due to the retention of phase separate sulphate salt material.

The Cs content of the samples, as determined through XRF, is similarly affected by the heterogeneity of the 30 wt% waste loaded samples since the caesium content detected may either be present in the vitreous waste-form itself or in any phase separated regions present in the waste-forms. The XRF results demonstrated that no significant  $\text{Cs}_2\text{O}$  content was present in any of the base glass samples, confirming the purity of the batch materials. At 15 wt% waste-loading, all eight samples demonstrated a proportion of  $\text{Cs}_2\text{O}$  content varying between 0.53 and 0.78 ( $\pm 0.04$ ) mol%. The highest proportions of  $\text{Cs}_2\text{O}$  were found in the ASZ and ASZ2 samples, where proportions of 0.75 and 0.78 ( $\pm 0.04$ ) mol% respectively were found. The CA0 glasses were seen to demonstrate the lowest levels of  $\text{Cs}_2\text{O}$  at 15 wt% loading with retention of 0.50 and 0.53 ( $\pm 0.03$ ) mol% respectively. At 30 wt% loading, the proportion of  $\text{Cs}_2\text{O}$  was found to be significantly higher in all samples with the exception of the CA0 sample. The highest proportions of  $\text{Cs}_2\text{O}$  were found again in the AB0 sample and in the ASZ1 sample, which were seen to possess 1.64 and 1.99 ( $\pm 0.1$ ) mol%  $\text{Cs}_2\text{O}$  respectively. The alkali alkaline-earth silicate sample, excluding ASZ1, demonstrated  $\text{Cs}_2\text{O}$

values of approximately 1.3 mol%, close also to the value demonstrated by the CF0 sample. The proportion of Cs<sub>2</sub>O in the samples can be seen in Figure 4.1.15.

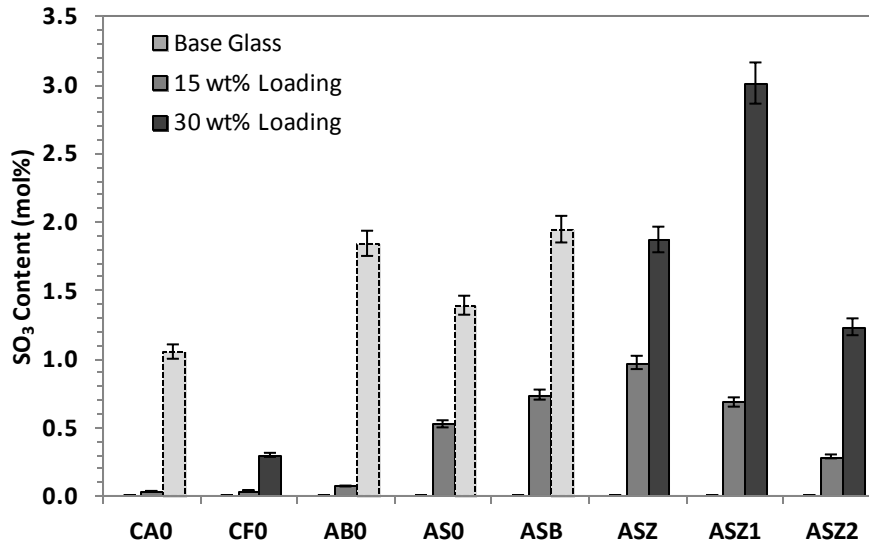


**Figure 4.1.14.** The SO<sub>3</sub> content in the base glass sample and waste-loaded samples for all glasses. Error bars determined from percentage experimental error associated with XRF measurement. Bars with dotted border indicates samples known to contain heterogeneous phases.

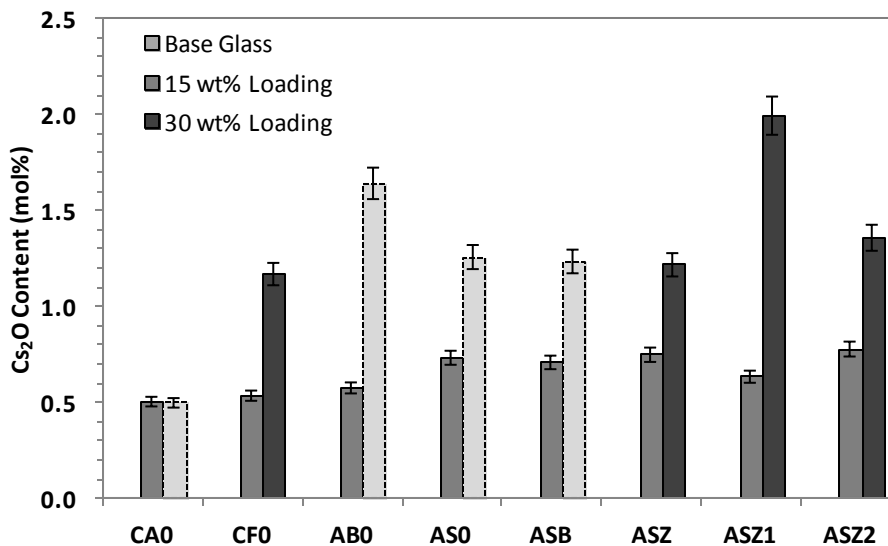


**Figure 4.1.15.** The Cs<sub>2</sub>O content in the base glass sample and waste-loaded samples for all glasses. Error bars determined from percentage experimental error associated with XRF measurement. Bars with dotted boarder indicates samples known to contain heterogeneous phases.

From this information it is possible to calculate the overall retention of sulphur and caesium that was achieved by the vitrification process. These values may be found in Table 4.1.15 below. Figures 4.1.16 and 4.1.17 below show the percentage retention for sulphur and caesium and allow variations between the waste-loadings to be discerned more clearly in both cases. Considering the sulphur percentage retention it is apparent that unlike the ASZ waste-form at 15 wt% and 30 wt% waste-loading, which displays a consistent retention of sulphur at both waste loadings, the CF0, ASZ1 and ASZ2 waste-forms demonstrate an increase in sulphur retention at higher waste-loadings, showing a two-fold increase in their respective sulphur retention between 15 wt% loading and 30 wt% loading. In considering the caesium retention, similar observations can be made where the CF0 and ASZ1 waste-forms demonstrate increased caesium retention at 30 wt% relative to that which was achieved in the 15 wt% loaded waste-forms for these glasses. It can also be seen that the ASZ and ASZ2 waste-forms demonstrate a decrease in caesium retention at 30 wt% loading relative to that which was observed at 15 wt%. However, more significantly, a fairly uniform retention of caesium is demonstrated by all eight development glass waste-forms at 15 wt% loading at between approximately 70% and 80%. In the 30 wt% waste-loaded waste-form from the ABO and ASZ1 host glasses a near total retention of caesium is demonstrated, although this may be limited in the case of the ABO waste-form by the presence of a phase separated gall layer.

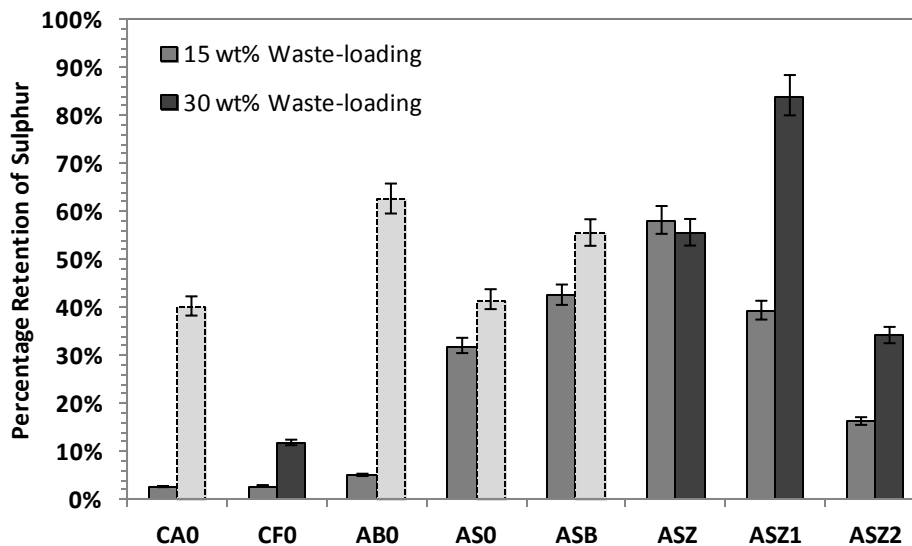


**Figure 4.1.16.** The percentage of sulphur retained in the waste-loaded samples for all glasses. Error bars determined from percentage experimental error associated with XRF measurement. Bars with dotted border indicates samples known to contain heterogeneous phases.

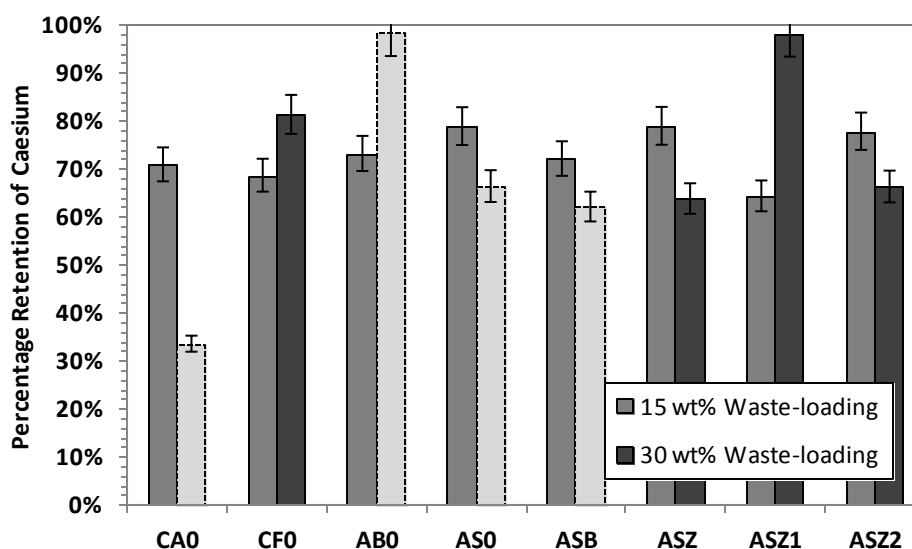


**Figure 4.1.17.** The percentage of caesium retained in the waste-loaded samples for all glasses. Error bars determined from percentage experimental error associated with XRF measurement. Light grey bars with dotted border correspond to samples known to contain heterogeneous phases.

**Table 4.1.15.** Calculated retention of Cs and S in all waste-loaded samples. Italic values indicate values were samples were contaminated with phase separated material.

Composition	SO <sub>3</sub> Retention (Retained SO <sub>3</sub> / Loaded SO <sub>3</sub> )		Cs <sub>2</sub> O Retention (Retained Cs <sub>2</sub> O / Loaded Cs <sub>2</sub> O)	
	15 wt% Load	30 wt% Load	15 wt% Load	30 wt% Load
<b>AB0</b>	4.9 ± 0.2 %	62.5 ± 3.1 %	73.2 ± 3.7 %	98.4 ± 4.9 %
<b>CA0</b>	2.4 ± 0.1 %	40.1 ± 2.0 %	70.9 ± 3.5 %	33.5 ± 1.7 %
<b>CF0</b>	2.6 ± 0.1 %	11.6 ± 0.6 %	68.6 ± 3.4 %	81.3 ± 4.1 %
<b>AS0</b>	31.9 ± 1.6 %	41.5 ± 2.0 %	78.9 ± 3.9 %	66.3 ± 3.3 %
<b>ASB</b>	42.4 ± 2.1 %	55.4 ± 2.8 %	72.1 ± 3.6 %	62.1 ± 3.1 %
<b>ASZ</b>	58.0 ± 2.9 %	55.5 ± 2.8 %	78.9 ± 3.9 %	63.7 ± 3.2 %
<b>ASZ1</b>	39.2 ± 2.0 %	84.0 ± 4.2 %	64.3 ± 3.2 %	98.2 ± 4.9 %
<b>ASZ2</b>	16.1 ± 0.8 %	34.0 ± 1.7 %	77.8 ± 3.9 %	66.3 ± 3.3 %

### Spectroscopy of Waste-Loaded samples

FT-IR spectroscopy of the loaded glasses showed an increase in  $Q^n$  speciation between the initial base glasses and the loaded waste-forms in all eight samples, although to varying extents between the samples. The  $Q^n$  speciation was seen to increase by between 0.05 and 0.1, in terms of average  $Q^n$  speciation, upon waste-loading in all samples with the exception of CA0. This indicates an increase in the extent of glass forming network polymerisation in the waste-forms as a result of waste-loading. The  $Q^n$  speciation was also seen to increase by  $0.25 \pm 0.05$  in the CA0 waste-forms, showing that the increase in network polymerisation was larger in these waste-forms. The variation in  $Q^n$  speciation is shown in figure 4.1.18 below.

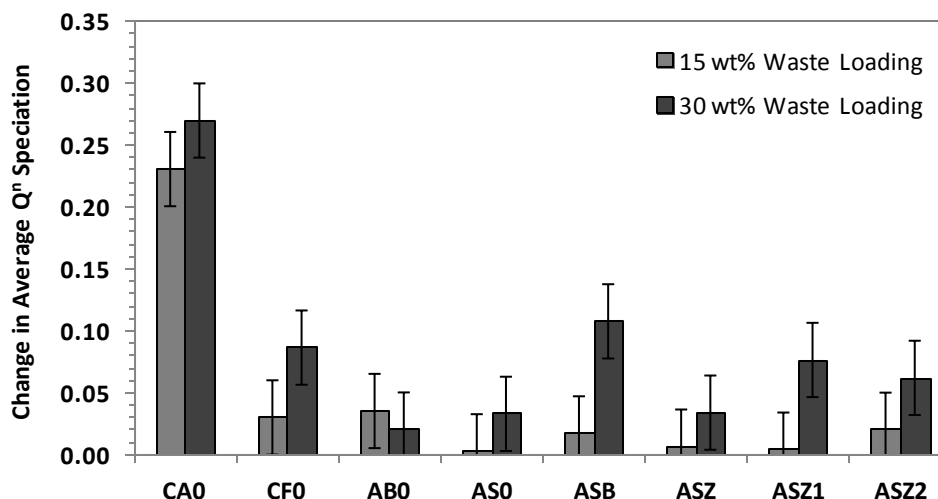


**Figure 4.1.18.** Change in  $Q^n$  speciation on waste-loading as determined by FT-IR spectroscopy. Error determined from fitting accuracy.

Raman spectroscopy showed the appearance of additional bands on waste-loading at  $400\text{ cm}^{-1}$  and  $990\text{ cm}^{-1}$ . All waste-loaded samples, excluding the CA0 waste-form, show a strong peak at  $400\text{ cm}^{-1}$  which has been connected to the presence of the  $S^{2-}$  anion, possibly in association with  $Fe^{3+}$  in the form of the amber chromophore  $Fe^{3+}-S^{2-}$  (79). In addition to this all samples, excluding CA0, CF0 and AB0, presented a weaker band at  $990\text{ cm}^{-1}$  which is associated with  $SO_4^{2-}$  content (80-81), although this band was considerably weaker than the  $400\text{ cm}^{-1}$ . Although it should be noted that the relative intensities of these two bands cannot be used to directly quantify the ratio of sulphur oxidation states in the samples, it can be utilised

to provide a certain amount of qualitative information about the oxidation state of the sulphur present in the waste-forms. Figures 4.1.19 and 4.1.20 show the relative intensities of the 400  $\text{cm}^{-1}$  and 990  $\text{cm}^{-1}$  Raman bands in association with the waste-form and the waste-forms waste loading. A pattern is clearly discernible in the alkali alkaline-earth silicate glass waste-forms in that at 15 wt% loading the 990  $\text{cm}^{-1}$  band is apparent in all five samples. However at 30 wt% loading this band is either no longer present or is diminished and the 400  $\text{cm}^{-1}$  band is now present, or has significantly increased in intensity. This trend is consistent with what was seen in the initial waste-loading experiments previously discussed. This trend is partially apparent in the CF0 and AB0 waste-forms in that a significant 400  $\text{cm}^{-1}$  band is apparent in both samples at 30 wt% waste loading but no 990  $\text{cm}^{-1}$  band is apparent at any waste loading in either sample.

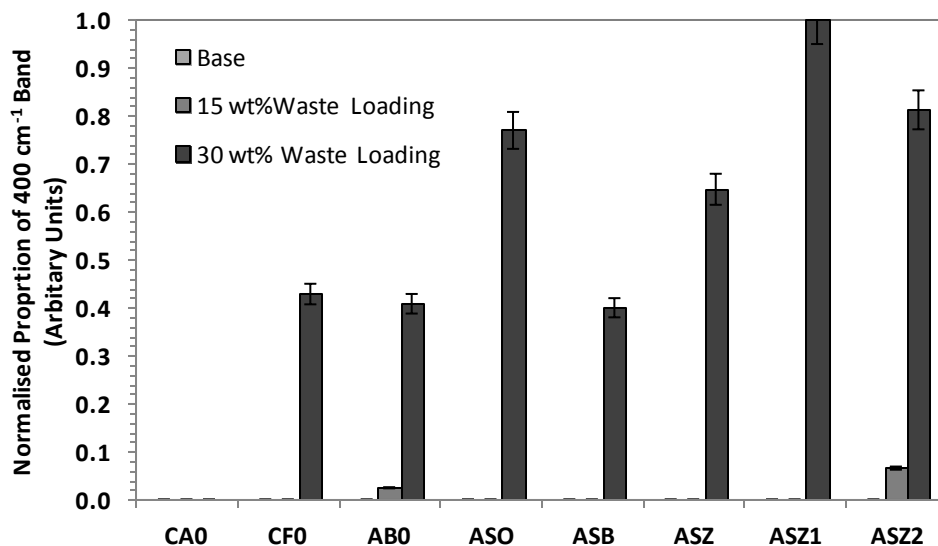


**Figure 4.1.19.** Variation in 400  $\text{cm}^{-1}$  Raman band across all 8 samples as determined by the fitting of Raman spectra. Error bars determined upon percentage fitting error.

Mossbauer spectroscopy results show clear variations in the oxidation state of Fe in all (Fe containing) waste-forms on waste-loading. The smallest variation was apparent in the AB0 waste-form which demonstrated a small but statistically significant decrease in oxidation state on waste-loading. The largest decrease was apparent in the CF0 waste-loaded sample, which is consistent with the formation of phase separated metallic Fe from that sample at 30 wt% waste-loading. The ASO derived samples all demonstrated a similar extent of reduction on waste-loading with the largest decreases in  $\text{Fe}^{3+}$  content being seen in the ASZ1 and ASZ2

waste-forms at 30 wt% loading. The variation in the proportion of Fe<sup>3+</sup> in the glass samples is shown below in Figure 4.1.21.

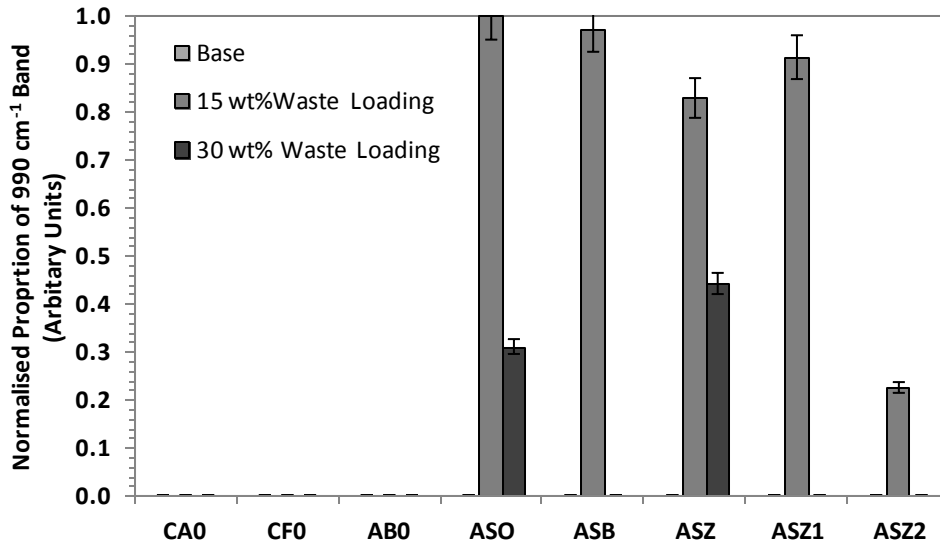


**Figure 4.1.20.** Variation in 990 cm<sup>-1</sup> Raman band across all 8 samples as determined by the fitting of Raman spectra. Error bars determined upon percentage fitting error.

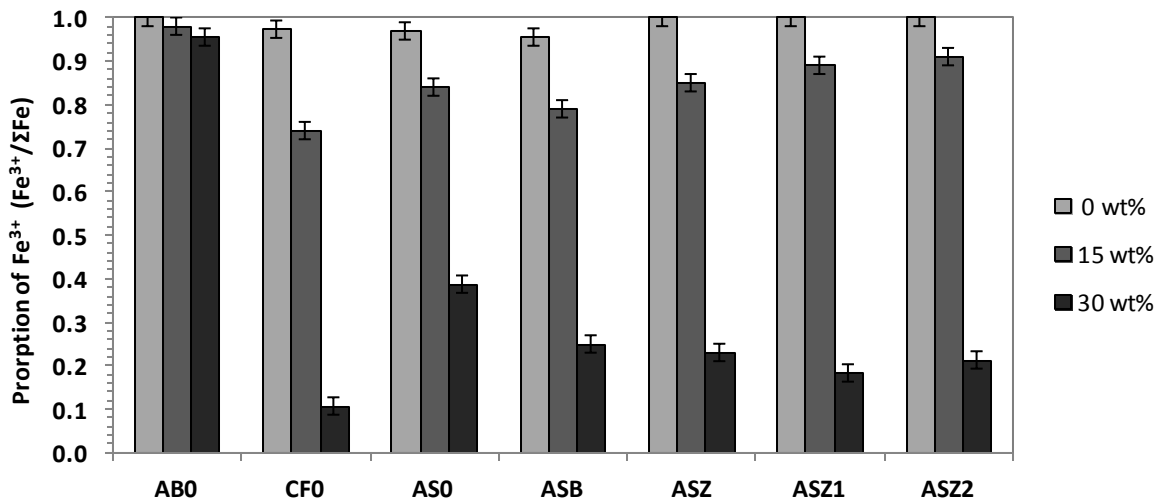


**Figure 4.1.21.** Variation in proportion of Fe<sup>3+</sup> on waste-loading for all 7 samples which contain Fe, as determined through the fitting of Mossbauer spectra. Error bars determined from experimental error associated with fitting.

### 4.1.3 Discussion

#### 4.1.3.1 Initial Waste-loading Experiments

The initial waste-loading experiments carried out on a small scale with the base glasses CA0, AB0 and AS0 demonstrated a number of significant results which provide insight into the larger waste-loading experiments carried out on the development glass compositions. The primary outcome of the initial study was the identification of maximum resin loading for the melts at 30 wt% IEX resin loading, since this limit defined the maximum loading that was applied in the development glass waste-loading experiments. At high waste-loading it was found that resin was not incorporated into the melt but instead combusted and failed to react. This effect has been previously described in the work of Herman *et al* and Hutson *et al* <sup>(1,29)</sup> in which resin, and other similar low density waste-forms, form a cold-cap on the melt surface which acts as barrier preventing the further incorporation of waste into the glass melt. It has been demonstrated by Hutson *et al* <sup>(29)</sup> that this effect can be avoided through the physical disruption of the melt surface through stirring or some other process.

On waste-loading it was found that the  $T_g$  and density of the waste-loaded glasses decreased in approximate proportion to waste-loading, with the exception of the AB0 glass which demonstrated an increase in density up to 40 wt% waste-loadings where the presence of the IEX resin cold cap caused a significant decrease in density. Both of these effects can be directly attributed to the effect of  $Al_2O_3$  addition to the glass composition through the corrosion of the re-crystallised alumina crucibles used in the waste-loading experiments. This can be seen through the relatively low enthalpy of fusion for  $Al_2O_3$ , which has been connected by Islam *et al* and Micoulaut *et al* <sup>(58,82)</sup> to the glass  $T_g$ , decreasing the average enthalpy of fusion for the oxide constituent of the glass and so reducing the  $T_g$ . Similarly, the presence of increased proportion of  $Al_2O_3$  decreases the average molar mass of the glass, leading to a decrease in density, except in the case of AB0 where the  $Al_2O_3$  addition increases the average molar mass of the glass increasing the glass density as is consistent with Huggins *et al* <sup>(57)</sup>.

Raman spectroscopy of the AS0 and AB0 waste-loaded base glasses demonstrated the presence of Raman bands at  $400\text{ cm}^{-1}$  and  $990\text{ cm}^{-1}$ . These bands have been previously associated with the presence of  $S^{2-}$ , in conjunction with  $Fe^{3+}$  and  $SO_4^{2-}$ , in conjunction with  $Na^+$ , in silicate glasses <sup>(79,80)</sup>. As such, they provide a limited insight into the oxidation state of the sulphur content of the waste-forms. These bands were most apparent in the AS0 glass

waste-forms, which were found to retain the largest proportion of sulphur, supporting the link between these bands and the sulphur species described in literature. The absence of these bands in the waste loaded CA0 samples can be connected to the relatively low concentration of sulphur retained in those samples. The variation in the intensity of these Raman bands in the AS0 glass, as shown in Figure 4.1.6, indicates that there is a relationship between the extent of IEX resin waste-loading and the apparent oxidation state of the sulphur species in the sample waste-forms. Specifically, at low waste loadings the 990  $\text{cm}^{-1}$  band supporting sulphur in the  $\text{S}^{6+}$  oxidation state ( $\text{SO}_4^{2-}$ ) is prevalent. However at 30 wt% loading this is seen to diminish in favour of the 400  $\text{cm}^{-1}$  band associated with sulphur in the reduced ( $\text{S}^{2-}$ ) oxidation state. This change in sulphur oxidation state, tending towards more reduced species on increased waste-loading, demonstrates that the reducing effect of the organic species from the resin directly impacts upon the oxidation state of the sulphur retained by the waste-form at high waste-loadings. These conclusions are further supported by the Mossbauer results from the AB0 and AS0 glasses which both displayed a clear decrease in the proportion of oxidised  $\text{Fe}^{3+}$  and increase in reduced  $\text{Fe}^{2+}$  as a function of waste loading from waste-loadings of 30 wt% and upwards. This demonstrates the significant reductive effect of the organic content of the ion exchange resin upon the iron content of the host glass material, with further implications for other species present in the glass system vulnerable to reduction.

In terms of sulphur retention it can be seen in Figure 4.1.3 that only the AS0 waste-loaded samples demonstrated a significant degree of  $\text{SO}_3$  retention from the IEX resin waste-loading. The AB0 samples also demonstrated a degree of  $\text{SO}_3$  retention. However, the CA0 sample showed no significant retention of  $\text{SO}_3$ . The low levels of sulphur present in the AB0 samples is consistent with expectations due to the low solubility of sulphur species in alkali borosilicate glass compositions. The failure of the CA0 samples to retain sulphur can be attributed to the high temperatures required to melt the host glass, due to its high  $T_{\text{liq}}$ , which would lead to the oxidation of the sulphur content of the resin before it could be incorporated in the glass to any significant extent. The high levels of sulphur retention by the AS0 glass demonstrates that the alkali alkaline-earth glass system has significant potential for sulphur retention. This can be connected to the high cation field index of the glass composition, which has been connected by Bingham and Hand *et al* to the retention of sulphate species in glass systems<sup>(31)</sup>. A clear correlation can be seen between the cation field index of the AB0 and AS0 glasses and their respective sulphur retention, as shown in Figure 4.1.22. The data also closely matches the trend between cation field index and sulphur content as reported by Bingham *et al*<sup>(31)</sup>. Notably, the CA0 glass does not fit the trend in cation field index, indicating that factors not relating to the glass composition itself, such as the processing conditions, lead to the low sulphur content reported. No gall layer was found in retention to

any of the waste-loading experiments despite the loss of significant proportions of sulphur in the majority of samples. This can be attributed to the volatilisation of the gall layers produced due to the relatively small scale of the melts and the large surface area of the melt exposed to atmosphere.

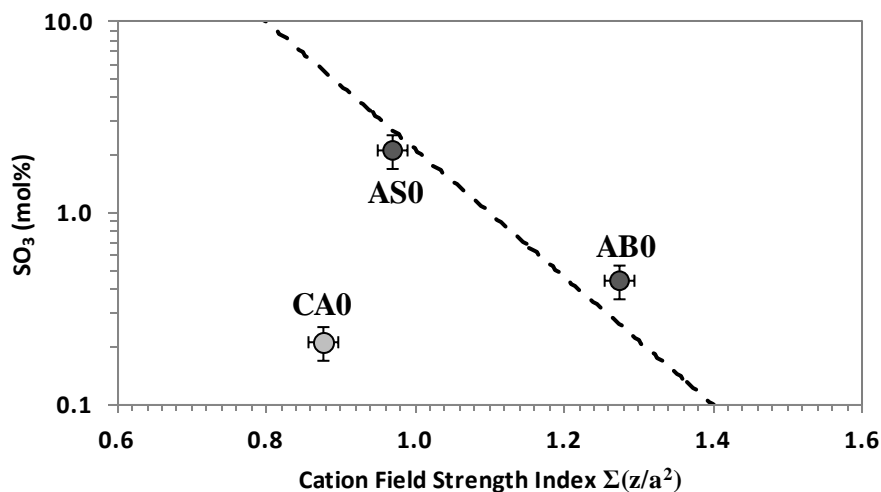


**Figure 4.1.22.** Sulphate content in initial experimental series as a function of cation field strength index. Dotted line marks trend reported by Bingham *et al*<sup>(31)</sup>.

#### 4.1.3.2 Effects of Waste-loading on Developed Host Glasses

The waste-loading of the developed host glasses, carried out on a larger scale than the initial tests, supported many of the observations which had been previously made in the initial experiments. The density was found to decrease in all glasses, apart from the AB0 glass waste form, and the  $T_g$  of the glasses was observed to decrease by a small but significant factor. Finally, the results of Mossbauer spectroscopy and Raman spectroscopy presented evidence for the reduction of both Fe and S species in the waste-forms occurring as a function of waste-loading, as had been observed in the initial experiments discussed above. Notably, however, the variation observed in  $T_g$  and density are all of a smaller magnitude in the waste-forms produced from the developed host glass experiments than were observed in the initial experimental series. The smaller magnitude of change observed in  $T_g$  and density can be attributed to the increase in glass melt mass relative to the surface area of the re-crystallised alumina crucible which was vulnerable to attack. This would reduce the amount of  $Al_2O_3$

input into the waste-forms through the corrosion of the crucibles. The variations seen in S and Fe oxidation state as a function of waste-loading can be attributed to the reducing effect of the organic component of the IEX resin waste, as was discussed with regards to the initial experimental series above.

#### 4.1.3.2.1 Physical Property Changes

A number of dissimilarities were seen between the initial experimental series and the observations made of the waste-forms produced from the developed host glasses. The main disparity can be seen in the formation of glass layers and phase separated regions which occurred in the all three base glass compositions at 30 wt% loading, despite not having been observed in the previous initial experiment series. The formation of this gall layer can be attributed to the larger scale of the melts carried out for the waste-loading of the development glasses (100 g melts) in comparison to the melts carried out in the initial series (30 g). The larger-scale melts therefore produced a larger volume of molten material but due to the fixed size of the crucibles used possessed a similar exposed area at the surface of the melt. As a result the larger melts produced a proportionally higher amount of phase separated material, but due to the unchanged surface area of the melt this was not fully volatilised in the course of the experiment, resulting in the retained phase separated material observed.

Gall layers were found to be present at 30 wt% waste loading in the glasses AB0, AS0 and ASB0 corresponding to all three alkali containing melts which did not possess a significant zinc content. The decrease in Na<sub>2</sub>O content seen in the XRF results for these glasses indicates that the gall layer, and volatilised material, is primarily Na<sub>2</sub>SO<sub>4</sub>, although it is possible that it is mixed with other alkali and alkaline-earth sulphate salts, including Cs<sub>2</sub>SO<sub>4</sub>. This is consistent with the gall layers which have been reported to be formed in similar melts with IEX resin wastes as reported by Herman *et al*<sup>(1)</sup> and Bingham *et al*<sup>(3)</sup>. The phase separated material found in the CA0 glass waste-form did not form a gall layer as was seen in the AB0, AS0 and ASB glasses, but rather formed inclusions within the waste-form itself. This is likely to be due to the higher viscosity of the CA0 glass, preventing the flow of the phase separated material to the surface of the melt, and due to the higher density of the phase separated material, which due to the composition of the CA0 glass is likely to be CaSO<sub>4</sub>.

As reported above, the ASZ, ASZ1 and ASZ2 glasses did not show any evidence of gall layer formation or the presence of inclusion as was seen in the other waste-forms at 30 wt% waste

loading, but instead, a significant volume of structured crystalline material was formed at the surface of the glass melt. These crystals are shown in Figure 4.1.23. These crystals were analysed through XRD and found to be ZnO crystals. The formation of these crystals is novel and clearly associated with the presence of Zn in the glass composition.

The mechanism for the formation of these ZnO crystals is not immediately apparent, although it can be seen that, as previously stated, they occur in the absence of a Na<sub>2</sub>SO<sub>4</sub> gall layer. It can also be inferred from their crystalline form that they have grown in situ above the melt surface as opposed to having been formed as a phase separated material from the glass melt itself. This implies that these crystals are the result of an unseen intermediate phase which was lost either through volatilisation or through dissolution into the glass melt resulting in the formation of the ZnO crystalline phase. In addition the apparent difference in the magnitude of the crystals seen between the ASZ1, where large crystals were formed, and the ASZ2 waste-forms, where smaller crystals formed, indicates that the alkali content of the glass was involved in the formation of these crystalline phases. From these facts it is possible to present a mechanism by which the ZnO crystalline phase may have been formed. A mixed alkali sulphate phase, of comparatively smaller volume than those seen in the other glass systems (due to the effect of the Zn<sup>2+</sup> cation) may have formed, which contained a quantity of Zn<sup>2+</sup> cations. This phase was then lost through volatilisation of SO<sub>3</sub>, resulting in the formation of a ZnO crystalline phase as the salt phase was lost. This would explain the formation of the ZnO phase and the variation seen in the size of the ZnO crystals in relation to the alkali content of the glass since the size of the intermediate alkali sulphate phase would be determined by the alkali content of the glass. However, the high degree of sulphur retention in the ASZ1 waste-form in particular would appear to contradict this mechanism since no significant proportion of sulphur could have been lost through volatilisation in that waste-form.

This unusual formation of ZnO crystals has both positive and negative implications for the vitrification of IEX resin wastes, since it is likely that preferential formation of these ZnSO<sub>4</sub> crystalline phases limits or prevents the formation of more conventional alkali sulphate phases, it is plausible that it may have the effect of limiting the proportion of radio-caesium lost to off-gases. However, the formation of these phases is also likely to be problematic for industrial scale vitrification processes.

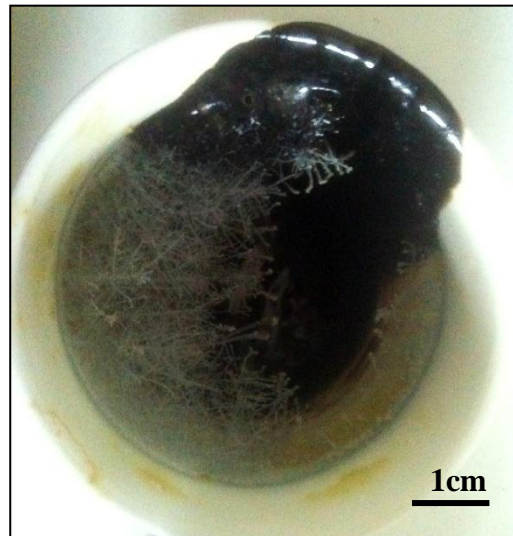


**Figure 4.1.23.** ZnO crystal formation retained in crucible after pouring of glass monolith.

None of the alkali borosilicate or alkali alkaline-earth silicate glass waste-forms presented any evidence of inclusions or of the presence of metallic sulphide inclusions, such as have been reported in past publications<sup>(83)</sup>. However, in the case of both calcium silicate glass composition, CA0 and CF0, inclusions were present. In the case of the CA0 glass, the inclusions are phase separated sulphate salts and have been discussed above. However, in the case of the CF0 waste-form at 30wt% loading, a metallic inclusion was formed. This inclusion was determined to be primarily metallic Fe, although some extent of impurities was also present. The formation of this metallic inclusion can be attributed to the effect of the reducing organic content of the IEX resin waste, which has caused a proportion of the Fe<sub>2</sub>O<sub>3</sub> content of the glass to be fully reduced to metallic Fe. This is supported by the Mössbauer results for this sample, which showed the largest extent of reduction. The increased extent of reduction in the sample can be attributed to the increased waste-loading at the higher temperatures involved in the vitrification process for the CF0 composition. The presence of unincorporated resin in the AB0 glass melt at 30 wt% waste-loading, most probably in the form of a cold-cap, can be attributed to the relatively low values of T<sub>liq</sub> and T<sub>g</sub> for the AB0 host glass composition. As the AB0 host glass frit becomes fluid at a lower temperature, the less dense IEX resin material is able to float to the top of the melt to form a cold cap, whereas in other melts the higher values of T<sub>liq</sub> and T<sub>g</sub> would cause the resin to break down prior to this separation. The presence of un-incorporated resin in the AB0 30 wt% waste-loaded sample also provides an explanation for the high proportion of Fe<sup>3+</sup> found to be present in that sample, since the reduced volume of resin present in the glass results in a reduced proportion of organic material available to cause the reduction of the Fe<sup>3+</sup> content of the host glass.

The  $T_{liq}$  of these development glass waste-forms was seen to vary significantly from the values of the host glass compositions. Increases in  $T_{liq}$  were apparent in all alkali alkaline-earth silicate glass waste-forms and in the alkali borosilicate AB0 glass waste-form. These increases can be attributed to the loss of species from the glass compositions which had a negative effect upon the  $T_{liq}$  of the base glasses. The loss of  $Na^+$  cations from the AB0, AS0 and ASB glass waste-forms through the production of the alkali sulphate gall layer and the loss of  $Zn^{2+}$  cations in the ASZ, ASZ1 and ASZ2 compositions removes two cations which have been shown previously in Chapter 3.1 & 3.2 to have negative effects of the  $T_{liq}$  of the glass compositions being explored, and so the  $T_{liq}$  of the waste-forms produced increases. The largest increases in  $T_{liq}$  are apparent in the waste-forms produced from ASZ and ASZ1. This can be attributed to the relatively large content of BaO in these compositions, which in absence of ZnO has been shown to lead to greater increases in  $T_{liq}$  than the reduction of alkali content. Furthermore, a greater overall proportion of the ZnO content is lost than is the case for the  $Na_2O$ . This being the case, it is unclear why the ASZ2 composition does not demonstrate a more significant increase in  $T_{liq}$ . This may be associated with the low alkali content and relatively high  $T_{liq}$  of the ASZ2 base glass. The CA0 waste-forms, and the CF0 15 wt% loaded waste-form, demonstrate a decrease in the overall  $T_{liq}$  of the waste-forms. This can again be attributed to the loss of glass species to the formation of sulphur salt phases. However, in this instance the loss of  $Ca^{2+}$  cation has a positive effect on the  $T_{liq}$  since the presence of CaO has been shown to increase the  $T_{liq}$  of these systems<sup>(60)</sup>. The apparently anomalous increase in  $T_{liq}$  seen in the CF0 30 wt% waste loaded sample may be attributed to the loss of  $Fe_2O_3$  from the composition due the reduction of the metallic Fe phase, again since Fe has been shown to have a positive effect on the  $T_{liq}$  of silicate glasses<sup>(59)</sup>.

#### 4.1.3.2.2 Caesium Retention

Considering the retention of Cs by the waste-forms produced using the developed host glass compositions, it can be seen that all eight glass achieved some level of caesium retention. However the ASZ1 waste-form demonstrated the highest levels of caesium retention, presenting near-complete retention of caesium from the waste-loading. It is plausible that this high caesium retention is associated with the low  $T_{liq}$  of the host glass, allowing incorporation of caesium at lower temperature during the melting process, thereby increasing retention.

Considering the different compositions, it is apparent that the calcium silicate glass waste-forms demonstrate an inferior ability to retain the caesium from the IEX resin waste-loading. This is in line with expectations due to the higher temperature necessary for the vitrification of wastes material using these host glasses due to their high  $T_{liq}$ , since the higher

temperatures lead to a larger proportion of caesium being lost through volatilisation. The alkali alkaline-earth silicate glasses all demonstrated a similar level of caesium retention, with the exception of the ASZ1 host glass, which was superior to that of the calcium silicate glasses. This is primarily attributable to the lower melting temperature required for the vitrification of IEX resin waste with these host glasses. The percentage retention of caesium at 30 wt% loading, as shown in figure 4.1.17, shows that the ASZ and ASZ2 demonstrate a small but significant decrease in caesium retention. This is consistent with expectations related to the increased volume of waste present at higher waste-loadings, since with the formation of a temporary cold-cap, such as have been described in static IEX resin vitrification experiments previously <sup>(29)</sup> would provide increased opportunity for the volatilisation of caesium before it can be incorporated in to the glass melt. The CF0 and ASZ1 30wt% waste-forms demonstrated an increase in caesium retention at the higher waste-loading. This can be connected to the increased capacity of the waste-forms for sulphur, which potentially would reduce the proportion of caesium volatilised in combination to sulphur species. The increased retention demonstrated in ASZ1 may also be connected to the increased capacity of the system to retain sulphur species.

#### 4.1.3.2.3 Sulphur Retention

Considering the extent of sulphur retained by the developed glass at 15 wt% loading, it can be seen that the trends which were previously noted in the initial waste-loading experiments are reflected in the results. This can be seen in the calcium silicate glass waste-forms which demonstrate a low extent of sulphur retention and the alkali borosilicate glass waste-form which demonstrates slightly increased sulphur retention relative to the calcium silicate glasses. As with the initial series, the alkali alkaline-earth silicate glass waste forms demonstrate significant retention of sulphur, averaging 0.8 mol% which is equivalent to an approximate 45 % retention of sulphur by the glass. The low extent of sulphur retention seen in the alkali borosilicate waste-form AB0 can be linked to the known low solubility for sulphur in this type of glass composition <sup>(29)</sup>. The further reduced retention seen in the calcium silicate glass waste-forms is less easily explained since they are known to have a high capacity for anionic species, as has been demonstrated by the work of Schofield *et al.* <sup>(5)</sup> However in these waste-forms it is possible that the low retention may be linked either to the higher temperatures required for the vitrification with these glasses, due to their high value of  $T_{liq}$ , or due to the absence of alkali species in the system. The high sulphur retention demonstrated by the alkali alkaline-earth silicate glass waste-forms can be linked to the low cation field index of the glasses, as defined by Bingham and Hand <sup>(31)</sup>. Figure 4.1.24 & 4.1.25 (below) demonstrate the correlation between cation field index for the investigated

glass systems loaded with 30 wt% resin and 15 wt% resin respectively. Figure 4.1.24 shows that the alkali alkaline-earth silicate glasses roughly follow the trend described by Bingham *et al*, but the alkali borosilicate glass deviates from this trend. It is probable that this can be attributed to an overestimation of sulphur content due to the presence of a separate sulphate phase. Figure 4.1.25 shows that sulphur content of the alkali borosilicate glass is consistent with the model of Bingham *et al* where no phase-separated material is present. The systematic shift to lower sulphur values seen in Figure 4.1.25 can be attributed to the lower waste-loading of the glasses. As was seen with the initial series, the observation that calcium silicate glasses show results inconstant with the model of Bingham *et al* is most probably due to sulphur lost through the vitrification process as stated above. These results show that, where not complicated by secondary factors, the sulphur retention achieved in the glasses investigated is consistent with the trend described by Bingham *et al* <sup>(83)</sup>. It should be noted that the trend line presented in figure 4.1.24, derived from the work of Bingham *et al* <sup>(33)</sup>, is specifically related to sulphur containing phosphate glasses. As such where these results do demonstrate a relationship between sulphur incorporation and cation field strength index in the borosilicate glass systems explored they cannot be expected to directly match the trend reported by Bingham *et al* <sup>(33)</sup>.

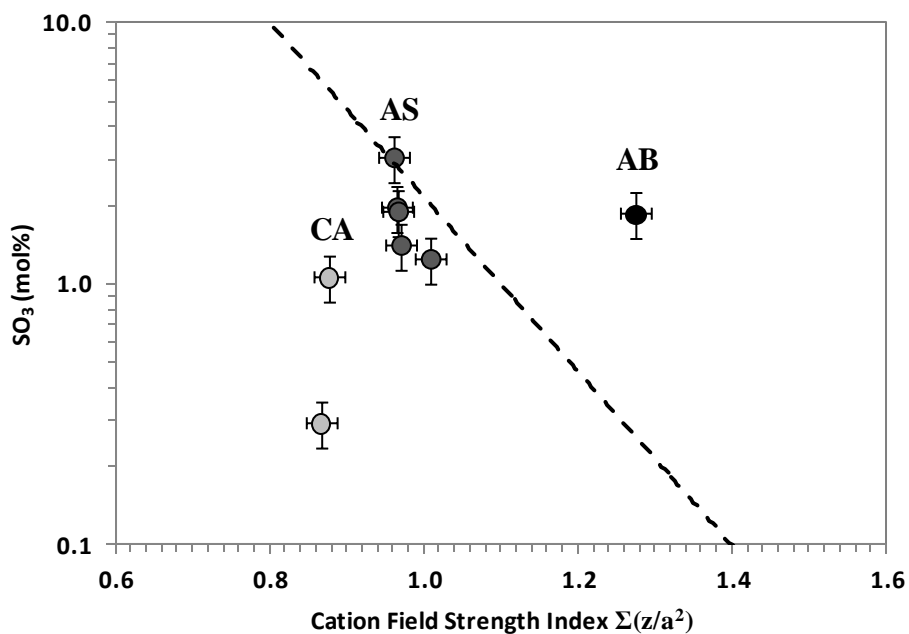


**Figure 4.1.24.** Sulphate content 30 wt% loaded waste-forms as a function of cation field strength index. Dotted line marks trend reported by Bingham *et al* <sup>(31)</sup>. AB = Alkali Borosilicate type glasses, AS = Alkali Alkaline-Earth Silicate type glasses and CA = Calcium Silicate type glasses.

Raman spectroscopy provides further insight into the interactions of sulphur with the host glass systems. Raman spectroscopy results from the 15 wt% loaded waste-forms demonstrate that in the alkali alkaline-earth silicate waste-forms, the sulphur content appears to be coordinated in bonds analogous to  $\text{Na}_2\text{SO}_4$  <sup>(80-81)</sup>. This seems to imply that in these waste-forms, the  $\text{S}^{6+}$  cations exist in an oxidised state coordinated to oxygen atoms and to the glass forming network through monovalent interaction analogous to alkali species. The results at 30 wt% loading demonstrate that when the sulphur content of the glass systems is reduced to  $\text{S}^{2-}$  the sulphur species preferentially interact with  $\text{Fe}^{3+}$ , where it is present, to form the  $\text{Fe}^{3+}\text{-S}^{2-}$  complex termed the 'amber chromophore' for its use in packaging glasses. This is supported by the observation of a  $400\text{ cm}^{-1}$  band in the CF0 glass 30 wt% loaded waste-form, in which a significant sulphur content was also determined by XRF despite the absence of sulphur containing heterogeneity. This is evidence for the presence of a significant sulphur content incorporated with the host glass by means of the  $\text{Fe}^{3+}\text{-S}^{2-}$  complex. The assignment of this  $400\text{ cm}^{-1}$  is supported by the work of Baert *et al* <sup>(79)</sup> who has linked the  $400\text{ cm}^{-1}$  band to  $\text{S}^{2-}$  in Fe containing glasses. In addition the lack of a  $400\text{ cm}^{-1}$  band in the (Fe free) CA0 waste-form, despite the presence of sulphur, demonstrates that its occurrence is dependent on the presence of Fe, further supporting the connection of the  $400\text{ cm}^{-1}$  band to the  $\text{Fe}^{3+}\text{-S}^{2-}$  complex.

At 30 wt% loading several glass systems were not affected by the formation of phase separated gall layers either due to the volatilisation of the sulphate gall layer, as in the CF0 glass waste-forms, or due to the formation of a ZnO crystalline phase which could be separated from the waste-form, as was the case for the ASZ, ASZ1 and ASZ2 waste-forms. The high levels of sulphur retention seen at 30 wt% waste-loading in the ZnO containing alkali alkaline-earth borosilicate glass waste-forms demonstrates the high affinity of the  $\text{Zn}^{2+}$  cation for sulphur species. The relatively large variations seen between the three 30 wt% waste loaded waste-forms, ASZ, ASZ1 and ASZ2 can be attributed to the varying cation field strength indices of the glass systems <sup>(31)</sup>, where ASZ1 possesses a higher cation field strength index relative to ASZ due to the increased proportion of  $\text{Ba}^{2+}$  in its composition, and ASZ2 possess a lower cation field strength index due to the depletion of alkali species in the composition of the ASZ2 host glass. The apparent high retention of sulphur demonstrated by the AB0, AS0 and ASB samples similarly may be governed by their relative cation field indices. However this cannot be confirmed, due to the presence of the sulphate gall layer in these samples which prevents accurate determination of the sulphate content of the glass.

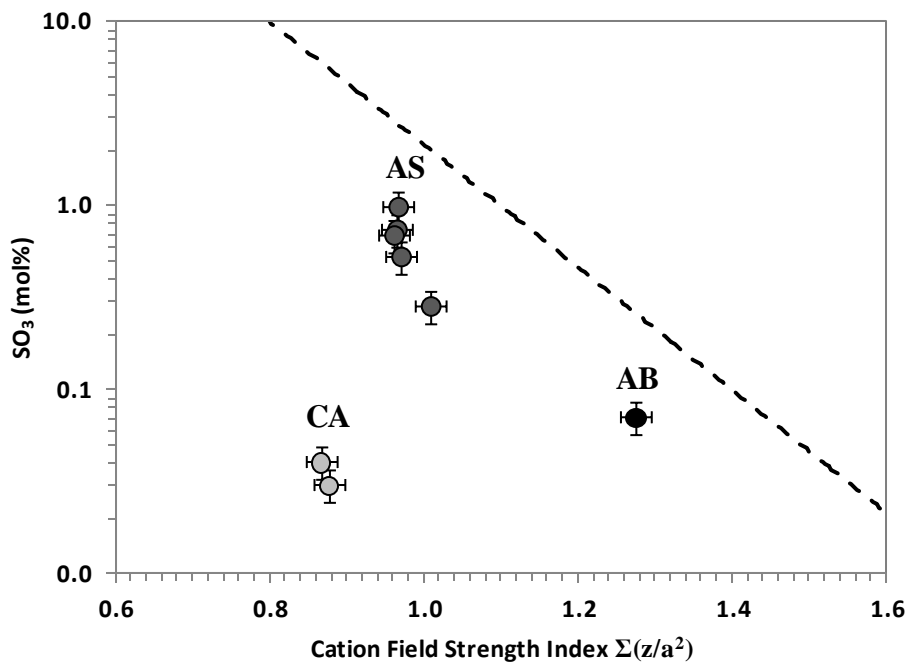


**Figure 4.1.25.** Sulphate content in 15 wt% loaded waste-forms as a function of cation field strength index. Dotted line marks trend reported by Bingham *et al*<sup>(31)</sup>.

#### 4.1.3.2.4 Changes to Silicate Network

The  $Q^n$  speciation of the waste-loaded development glasses displayed an increase in value in a similar manner to that which had been seen in the initial waste-loading experiment series, and could potentially be explained as the effect of the increased  $Al_2O_3$  content of the glasses due to the corrosion of the re-crystallised alumina crucibles used for the waste-loading experiments. This explanation would be supported by the smaller increase in  $Q^n$  speciation displayed in the waste-loaded development glasses relative to the initial series, which could be linked to the decreased proportion of  $Al_2O_3$  taken in during the melting process as with the  $T_g$  and density. However, on closer analysis, specifically of the CA0 waste-form, this cause seems less likely since a large change in  $Q^n$  speciation is apparent in the CA0 waste-loaded samples despite the significant (7.18 mol%) presence of  $Al_2O_3$  in the composition already and due to the relatively low increase in  $Al_2O_3$  from the corrosion of the crucible. Given the unique absence of  $Fe_2O_3$  from the composition of the CA0 host glass in comparison with the other compositions explored, it is possible that this large increase in the  $Q^n$  speciation of the

waste-form may be related to this absence of  $\text{Fe}_2\text{O}_3$ .  $\text{Fe}_2\text{O}_3$  is present in the other host glass compositions and was explored primarily for its capacity to act as a buffer against reduction which has been described by other researchers<sup>(3,35)</sup> and is therefore useful in limiting the reductive effects caused by the organic content of the IEX resin waste. It is possible that the lack of this buffer against reduction by the organic content of the resin waste is the reason why a large increase in  $\text{Q}^{\text{n}}$  speciation is seen uniquely in the waste-loaded CA0 development glass.

#### 4.1.3.2.5 Suitability of Developed Glass Compositions

Each of the waste-forms developed from the novel developed host glasses demonstrate attributes which may be beneficial in the context of ion exchange resin waste vitrification. Unfortunately, however, there are also a number of attributes associated with these waste-forms which may prove to be prohibitive. By comparing the results of the waste-loading of these potential host glasses it may be possible to determine the potential of these glass compositions for use in the vitrification of IEX resin wastes.

#### Calcium Silicate Glasses

Considering first the calcium silicate glass derived waste-forms, it is apparent that these glasses do not meet the required standard for use in the vitrification of IEX resin waste glasses. The low retention of sulphur demonstrated by both of the glass systems is undesirable since it indicates that the emission of  $\text{SO}_x$  compounds would occur during the vitrification process. However, this is not a critical issue since  $\text{SO}_x$  emissions from off-gas is a relatively common industrial problem that may be resolved. Only 70% of the caesium from the resin is retained by the waste-form at 15 wt% loading demonstrating that an unacceptably large proportion of the caesium is lost to volatilisation. At 30 wt% waste-loading, additional issues become apparent in both the CA0 and CF0 glass waste-forms, with formation of phase separated materials in both waste-forms. The phase-separated salt and metallic phases identified in the waste-forms would represent a significant risk to a melt vessel for large scale vitrification and in the case of the salt phases may impair the durability of the waste-form due to the aqueous solubility of the salt phase. Furthermore, at 30 wt% waste-loading the CA0 waste-form demonstrates a significant decrease in caesium retention, losing the majority to volatilisation. However, the CF0 waste-form does demonstrate an increased level of caesium

retention at 30 wt% waste-loading and does not produce water soluble salt phases, thereby demonstrating the relative superiority of the CF0 glass in comparison to the CA0 base glass. The observed changes in density,  $T_g$  and  $T_{liq}$  are relatively minor with variable waste-loading although the significant decrease in density demonstrated by the CF0 waste-forms would not be desirable. Finally, the shift in  $Q^n$  speciation seen in the CA0 waste-forms demonstrates the effect  $Fe_2O_3$  content has in silicate glass systems as a buffer against reduction, highlighting the need for  $Fe_2O_3$  content in host glasses intended for IEX resin vitrification. Neither of the calcium silicate glasses studied presented properties that would be desirable for IEX resin vitrification due to their capacity to form secondary phases detrimental to the vitrification process, such as metallic inclusions, and to the formation of a durable waste-form, such as the presence of sulphate salts. However, as have been reported previously they may be appropriate for use with other waste streams <sup>(5)</sup>.

### **Alkali Borosilicate Glass**

Considering the alkali borosilicate glass composition (AB0), it can be seen that despite the presence of  $Fe_2O_3$ , the glass system displays many of the same issues previously identified as problematic for alkali borosilicate type glasses when used for IEX resin vitrification <sup>(11)</sup>. The AB0 waste-form demonstrated a low capacity for sulphate species at both of the investigated waste-loadings, and at 30 wt% waste-loading a significant volume of gall layer material was formed due to this low capacity for sulphur species. As has been described previously, the presence of this gall layer is undesirable due its capacity to contain caesium species and due to its aqueous solubility. The changes seen in the  $T_g$  and density of the waste-forms on waste-loading are relatively minor, with limited impact upon the processability of the waste-form, and maybe avoided through the use of a vessel less susceptible to corrosion. However the increase in  $T_{liq}$  due to the loss of sodium through the formation of the gall layer is undesirable. The lack of significant change in the polymerisation of the silicate network as determined from the change in speciation, and the extent of reduction observed in the iron content of the glass, as determined through Mössbauer spectroscopy, indicate that the presence of  $Fe_2O_3$  on the glass system does act as an adequate buffer against reduction by the organic content of the IEX resin waste-loading. Considering the caesium however, it is apparent that as with the calcium silicate glass samples and most of the alkali alkaline-earth silicate host glasses the AB0 waste-form at 15 wt% loading does not achieve a caesium retention of greater than 70%, indicating the potential for the loss of a significant proportion of caesium to off-gases. At 30 wt% waste-loading it is apparent that a higher caesium

retention is achieved, approaching the full retention of caesium by the waste-form. However due to the presence of the sulphate salt gall layer, it is not possible to determine if this caesium content is present within the waste-form or in the water soluble salt phase. Overall it can be seen that the alkali borosilicate AB0 host glass system does not possess the necessary properties to be used for the vitrification of IEX resin wastes.

### **ZnO-Free Alkali Alkaline-Earth Silicate Glasses**

Finally in considering the alkali alkaline-earth borosilicate glass systems it is apparent that the various developed glass compositions display a wide range of effects in response to waste-loading with IEX resin materials. It is possibly more helpful to consider the system in two separate sets: those containing ZnO and those not containing ZnO.

The ZnO-free development glass waste-forms AS0 and ASB displayed generally similar properties with regards to sulphur and caesium retention and with regards to their physical property changes. Both glass systems demonstrated the retention of a significant proportion of the sulphur content of the resin at both 15 wt% waste-loading and at 30 wt% waste-loading. However, as with the AB0 glass waste-forms a gall layer, determined to be primarily Na<sub>2</sub>SO<sub>4</sub>, was found to form in both glass melts at 30 wt% loading with clear implication due to the known interaction of these phases with melting vessel<sup>(83)</sup> and due to their solubility in aqueous solutions. Waste-forms produced from both host glasses demonstrated small variations in T<sub>g</sub> and density consistent with the effect of the addition of Al<sub>2</sub>O<sub>3</sub> to their compositions through the corrosion. In addition, waste-forms formed from both compositions demonstrated significant reductions in T<sub>liq</sub> as is consistent with the loss of alkali species from their composition due to the formation of sulphate salt phases. This is potentially problematic since it may prevent the successful vitrification of the IEX resin wastes at lower temperatures such as maybe necessary to increase the retention of caesium. With regards to the variation in Q<sup>n</sup> speciation it is apparent that although the AS0 glass demonstrates no significant variation, the ASB glass demonstrates an increase in Q<sup>n</sup> speciation in proportion to the increase in waste-loading. This increase is also apparent in the ASZ1 and ASZ2 glasses which implies that this increase may be related to the higher proportion of BaO relative to CaO in these glass systems. It was shown in Chapter 3.1 that the Fe<sub>2</sub>O<sub>3</sub> constituents of these alkali alkaline-earth silicate glasses are partially reduced to Fe<sup>2+</sup> due to the relative acidity of the alkaline-earth and optical basicity of the alkaline-earth oxide phases present in the glass composition. As such, in combination with the lower overall proportion of Fe<sub>2</sub>O<sub>3</sub> in the alkali alkaline-earth glass compositions it is possible that

the increased proportion of BaO in these glass systems increase the optical basicity of the glass systems, as is supported by the work of Mysen *et al* <sup>(62-63)</sup>, and so leads to the further reduction of the iron content, effectively impairing the capacity of the Fe to act as a buffer against the reducing effects of the organic content of the resin waste. As a consequence of this the durability of the ASB waste-forms alongside the ASZ1 and ASZ2 waste-forms may be impaired relative to the other waste-forms produced from developed alkali alkaline-earth silicate glasses. The AS0 and ASB glasses demonstrate a similar extent of caesium retention at both 15wt% waste-loading and at 30wt% waste loading, showing no significant difference within the limits of error. In comparison to the AB0 glass waste forms and the calcium silicate glass waste-forms, it can be seen that waste-forms produced from these two waste glasses retain between 5% to 10% more caesium. However, this still indicates that more than 20% of the caesium content of the waste is lost to off-gas. Overall, these two glasses can be seen to produce superior waste-forms to those shown to be produced from either of the calcium silicate glasses or the AB0 glass in so far that they retain a greater proportion of the caesium content of the waste. However, due to the formation of the sulphur salt gall layer at higher waste-loadings these glasses could not be considered optimal for the vitrification of ion-exchange resin wastes since reduced waste-loading would be necessary to ensure a homogenous product waste-form.

### **ZnO-Containing Alkali Alkaline-Earth Silicate Glasses**

Considering the alkali alkaline-earth silicate glass waste-forms which contained ZnO, it is apparent that in terms of density variation on waste-loading, all three waste-forms demonstrate similar changes in density that are attributable to the increase in the Al<sub>2</sub>O<sub>3</sub> content of the glass due to corrosion the melt vessel. However in considering the variation in the T<sub>g</sub> and the T<sub>liq</sub> there are significant variations in comparison to the ZnO free composition waste-forms. In the case of the T<sub>liq</sub> variation, most notably seen in the ASZ and ASZ1 composition waste-forms, this can be attributed to the loss of ZnO from the glass system due to the formation of the ZnO crystalline phase. In general these variations in physical properties are not significantly problematic for the processability of the waste-form. However the increase in T<sub>liq</sub> seen in the ASZ and ASZ1 compositions may prevent the use of these host glass compositions at lower temperatures with higher waste-loadings. The results demonstrate that these glasses possess the highest capacity for sulphur species and demonstrate the highest values of sulphur retention. Furthermore, uniquely amongst the developed host glasses explored in this work, the ZnO-containing alkali-alkaline earth silicate glass waste-forms did

not demonstrate the formation of a phase separated gall layer, or reduced metallic phase inclusions, but instead it was found that these waste-forms developed ZnO crystal formations, as shown above in figure 4.1.23. The preferential formation of the ZnO phase over the Na<sub>2</sub>SO<sub>4</sub> phase seen in the other alkali borosilicate and alkali alkaline-earth silicate glass waste-forms is advantageous for the purpose of IEX resin vitrification for two primary reasons. Firstly, as it formed preferentially it prevents the formation of the water soluble alkali sulphate phases which may include Cs<sub>2</sub>SO<sub>4</sub> and secondly because ZnO is known to have a low aqueous solubility, preventing the dissolution of any Cs<sub>2</sub>SO<sub>4</sub> salt that may be mixed with the ZnO phase. However, it is important to note that, as with the formation of any heterogeneous phases during vitrification, the formation of this zinc sulphate phase presents a number of issues. The most apparent of this is the potential that the crystalline ZnO phase may have for disrupting the vitrification process or for forming cold-caps on the surface of the melt, since these issues have the potential to prevent effective vitrification on an industrial scale. It may be possible to disrupt the ZnO crystalline phase to avoid these issues and possibly even re-input the material into the glass melt, since ZnO will then be reincorporated by the melt. However, it is possible that if this is done, inclusions of ZnO will instead be formed within the melt which would be retained by the waste-form, such as have been reported by Mosel *et al* <sup>(84)</sup>. Considering the retention of caesium by the ZnO-containing alkali alkaline-earth silicate glasses, it is apparent that at 15 wt% waste-loading the ZnO containing waste-forms demonstrate levels of caesium retention equal to the best observed from the ZnO free alkali alkaline-earth silicate glass waste-forms. However, at this level of Cs retention approximately 20% of the Cs content of the IEX resin waste-loading is lost through volatilisation, which is undesirable. At 30 wt% waste-loading the ASZ and ASZ2 waste-forms demonstrate a reduction in caesium content but are free of the sulphate gall layer. Furthermore the ASZ1 glass waste-form demonstrated a significant increase in caesium retention, demonstrating a retention of caesium up to 100%, within the limits of error. This is clearly a highly desirable outcome which alongside the relatively high caesium retention of the ASZ and ASZ2 waste-forms can be attributed to the effect of the ZnO content of the glass in retaining the sulphur content and preventing the formation of an alkaline sulphate gall layer by which caesium content may be lost. Overall, it can be seen from these results that the ZnO containing alkali alkaline-earth silicate glasses possess significant potential for use in the vitrification of IEX resin wastes if the issues surrounding the formation of ZnO crystalline phases prove not to be problematic or can be overcome through the modification of current vitrification practices. The presence of Zn<sup>2+</sup> cations has been shown to have a significant positive effect on the prevention of alkali sulphate gall layer formation and on the retention of sulphur species, and by connection, caesium species, achieving high levels of caesium retention. Specifically, it can be seen that the waste-forms

produced from the ASZ1 host glass demonstrate extents of caesium retention that are close to total, despite the presence of organic and anionic phase in the waste. As a consequence the ASZ1 host glass can be seen to be the most promising of the developed host glasses studied here for the purpose of vitrifying IEX resin wastes from the nuclear fuel cycle.

#### 4.1.4 Conclusion

The experimental series described in this work have explored the potential of three glass systems, an alkali borosilicate system, a calcium silicate system and an alkali alkaline-earth silicate system, for the purpose of the vitrification of IEX resin wastes. Initial experiments carried out on a small scale identified that the alkali alkaline-earth silicate glass system possessed the greatest capacity for the retention of anionic species and showed that beyond 30 wt% waste-loading in the alkali alkaline-earth silicate and in the alkali borosilicate glass system, a cold cap of resin formed which prevented the creation of a satisfactory waste-form and the full incorporation of the waste into the glass. In addition, it was found that the corrosion of the re-crystallised alumina crucible used in these experiments, due to the corrosive nature of the melt, resulted in changes in density,  $T_g$  and in the extent of the polymerisation in the silicate network which were portioned to the waste-loading of the IEX resin waste. These results provided the parameters for a series of waste-loading experiments carried out on a larger scale where glass compositions which had been previously developed for the purpose of IEX resin waste loading were loaded with 15 wt% and 30 wt% waste-loadings of simulant IEX resin waste. These experiments identified that amongst the compositions explored the AS0, ASZ, ASZ2 and in particular the ASZ1 host glass composition demonstrated properties that would allow them to be a particularly suitable for the vitrification of IEX resin wastes. The ASZ2 glass demonstrated a high capacity for sulphur anions, the capacity to resist the reductive effects of organic material and demonstrated a near total retention of volatile caesium at the highest waste-loading explored. However, at the highest waste-loadings these compositions, including the ASZ1 composition, were found to suffer issues due to the formation of phase separated or crystalline material to varying extents in all waste-forms at 30 wt%. In the ASZ1, ASZ and ASZ2 glass waste-forms these heterogeneous phases were found to be comprised primarily ZnO crystals, which are less corrosive and less likely to contain waste radionuclides than the alkali sulphate phases that may be problematic for current vitrification technologies without modification.

In addition to these general observations a number of specific observations were made. Investigation of the two calcium silicate glass waste-forms through FT-IR

spectroscopy demonstrated that the extent of polymerisation in the silicate network of the Fe-free CA0 waste-form was significantly affected by the IEX resin waste-loading, whereas the network of the Fe-containing CF0 waste-form demonstrated no significant variation. This provides a clear demonstration of the effectiveness of Fe<sub>2</sub>O<sub>3</sub> content as a buffer against reduction by organic species, such as these present in the IEX resin, a feature which may be pertinent to the vitrification of other problematic wastes. Also, Raman spectroscopy of the waste-loaded alkali alkaline-earth silicate waste-forms demonstrated evidence for a link between Raman bands at 400 cm<sup>-1</sup> and 990 cm<sup>-1</sup> and the Fe<sup>3+</sup>-S<sup>2-</sup> amber chromophore and SO<sub>4</sub><sup>2-</sup> species coordinated with monovalent species respectively, as has been previously suggested by Beart *et al*, McKeown *et al* and Konijnendijk *et al* <sup>(79-81)</sup>. These bands demonstrated variation which provide evidence for the reduction of sulphur species incorporated into the glass by the organic content of the IEX resin, and provided a valuable insight into the oxidation state and environment of sulphur species within the waste-forms, and so presents a possible method for the determination of sulphur oxidation state and environment in similar glass compositions without the need for techniques such as X-ray absorption spectroscopy. Finally, as is effectively demonstrated in the ASZ1 glass waste-forms, a link was determined to exist between the Zn<sup>2+</sup> cation and increased sulphur retention by the waste-forms, which supports the work of Volf *et al* <sup>(59)</sup> in which the Zn<sup>2+</sup> is shown to have a strong affinity for sulphur species. This demonstrates the potential the ZnO containing host glasses may possess for the vitrification of IEX resin wastes.

Overall it has been demonstrated that from the eight developed glass compositions explored in this chapter, three compositions demonstrated properties on waste-loading which represented significant improvements over compositions which have previously been explored for the vitrification of IEX resin wastes. The ASZ1 glass composition in particular demonstrated a near total retention of caesium during a vitrification process at 1200 °C. Although the glass did form a ZnO crystalline phase at high waste-loadings, which may be problematic on an industrial scale, the high retention of sulphur species and its demonstrated resistance to reduction by organics, as well as its low T<sub>liq</sub>, which gives it the potential for use in vitrification at lower temperatures, shows that the composition possesses many favourable qualities. The glass composition is therefore close to optimal for the purposes of IEX resin vitrification. Only the ZnO crystalline phase which was formed at higher waste-loadings may limit the usefulness of the composition.

## **Chapter 4.2 - Investigation of the Off-Gas Released from the Vitrification of Ion-Exchange Resin Wastes in Alkali Borosilicate and Alkali Alkaline-Earth Silicate Glass Compositions.**

It is well known that the primary route by which radionuclides species, as well as other components of the ion exchange resin waste, are lost is through the off-gases output during the vitrification process<sup>(1,2)</sup>. As such, the off-gases, and the conditions on which they are released during the melting process, are of vital importance for the development of a composition capable of successfully vitrifying radio-caesium loaded ion exchange resin waste. The aim of this work was to investigate the off-gas produced during the vitrification of an ion exchange resin waste using two glass systems previously developed in Chapter 3. Specifically, the intention was to perform analysis of the off-gas produced from the vitrification process in both developed glass compositions across the full range of temperatures and time scales involved in the vitrification process. This would allow the loss of caesium and other components of the resin to be quantified over time, and would allow the identification of phases critical in the volatilisation process. The two glass compositions investigated were previously developed glass compositions intended for ion exchange resin vitrification. The compositions for these glasses may be found in Table 4.2.1, and further information on their development can be found in the following literature by Bingham *et al*<sup>(3,35)</sup> and in Chapter 3. The relevant physical properties of these glasses are given in Table 4.2.2.

The investigation determined that during the vitrification process, a significant proportion of sulphur was released. Sulphur release was found to peak twice during the course of the vitrification experiment for each of the compositions investigated. Both compositions demonstrated sulphur release at ~180 minutes and a subsequent release at between ~ 260 and 320 minutes. These were connected to two separate sulphur releasing processes, namely the thermal degradation of the resin and the volatilisation of phases separated sulphate salts. In addition to this, a very low level of boron volatilisation was also detected.

**Table 4.2.1.** The compositions for the host glasses investigated.

Composition	Component Content (mol%)								
	SiO <sub>2</sub>	Al <sub>2</sub> O <sub>3</sub>	B <sub>2</sub> O <sub>3</sub>	Fe <sub>2</sub> O <sub>3</sub>	BaO	CaO	Na <sub>2</sub> O	Li <sub>2</sub> O	ZnO
AB0	58.10	-	17.79	3.94	-	-	10.13	10.04	-
AS0	51.72	0.38	2.23	2.92	18.23	11.08	5.64	7.80	-

**Table 4.2.2.** The T<sub>g</sub>, T<sub>liq</sub>, density and viscosity at 1200 °C of the host glasses.

Composition	T <sub>g</sub> (°C)	T <sub>liq</sub> (°C)	Density (g/cm <sup>3</sup> )	Log. Viscosity at 1200 °C (Log(η/dpa.s))
AB0	480	702	2.530	1.305
AS0	491	962	3.422	1.044

## 4.2.1 Experimental Procedures

The off-gas experiments were performed utilising a simulant waste-loaded ion exchange resin waste mixed with pre-prepared glass frit material. The glass frit was prepared from a monolithic sample prepared to a high degree of precision utilising batch ingredients with a purity of 99.9%. The block was fritted by means of a percussion mortar, screened for contamination and sieved to a sub 1mm size fraction. The resin used was a Duolite ARC 9359 ion exchange resin material which was loaded with caesium by means of a reaction with a caesium enriched aqueous solution. The resin was dried prior to vitrification. The composition, and caesium loading, of the resin and glass material were quantified by means of X-ray fluorescence spectroscopy. The batches used for the off-gas experiments consisted of 80 g of glass frit mixed with 30 wt% (24g) of ion exchange resin material.

Off-gas experiments were conducted using a specially designed furnace and off-gas collection apparatus. A diagram of this apparatus is presented in figure 4.2.1. The resin vitrification was conducted in a re-crystallised alumina crucible mounted in a vertically mounted tube furnace. The top of the crucible was sealed with a re-crystallised alumina lid which was cemented into position with refractory alumina cement. The crucible lid was penetrated by two fused silica pipes which ran from a position approximately 2 cm above the melt surface to a position above the top of the tube furnace. The open top of the tube furnace was blocked up with refractory materials to prevent heat loss. These two fused silica pipes

acted as an input and an output for the flow of atmosphere into the crucible and the low of off-gasses out of the crucible. The input end was exposed to atmosphere. The output end was connected to a dreschel bottle filled with UHQ de-ionised water. This allowed water soluble off-gas species to be collected by their dissolution into the solution. The output from the dreschel bottle was connected to a vacuum pump which was used to draw the off-gasses from the crucible through the dreschel bottle and to draw air in through the input silica tube. The output gases from the pump were then directed to safe extraction.

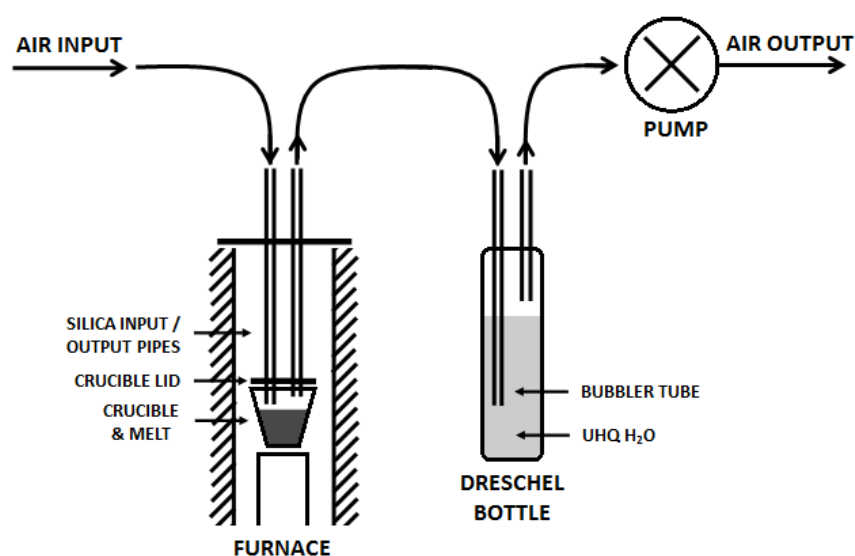


**Figure 4.2.1.** Diagram of Off-gas collection experiment set-up.

Experiments were performed using the setup using a constant airflow. The samples were heated to 1200 °C at a rate of 5 °C per minute and then held at temperature for 3 hours, giving an overall experimental duration of 7 hours. Off-gas sampling was achieved by sampling from the solution in the dreschel bottle and then replacing the sample solution with fresh de-ionised water at discrete intervals over the duration of the experiment. From 300 °C to 1200 °C, the sample solution was sampled and replaced at intervals of 10 minutes (50 °C steps) and after the experiment had achieved melt temperature, the sample solution was sampled every 20 minutes. The samples were analysed by inductively coupled plasma atomic emission spectroscopy (ICP-AES) and inductively coupled plasma mass spectroscopy (ICP-MS) in order to quantify the species captured from the off-gases. It is important to note that due to the sampling system and analysis techniques utilised organic species and insoluble

species present in the off-gases from vitrification were not detected. However, since the primary problematic species encountered in the off-gases emitted from IEX resin vitrification are SO<sub>x</sub>, sulphur salt and caesium species, all of which are water soluble, this was not viewed as a significant impairment to the intended goal. The only significant species omitted by this route for analysis are organic species such as furans and dioxins, which are known to be produced at low levels <sup>(29)</sup>.

ICP-AES and ICP-MS experiments were carried out at the Elemental Analysis service in the Department of Chemistry at Sheffield University. XRF experiments were performed at the Manchester University XRF facility at the School of Earth, Atmospheric and Environmental Sciences.

More detailed descriptions of these techniques are provided in appendix 8.1.

#### 4.2.2 Results

The results of the ICP-AES and ICP-MS analysis of the solutions captured during the off-gas run revealed that above all other components present in the waste and the host glass composition, sulphur was released in the off-gases in the greatest concentration. The release of sulphur was found to be 5 orders of magnitude greater than the release of any other component captured in solution and analysed in terms of ppm released per minute. The apparent lack of any other species being released indicates that the sulphur content is released in the form of SO<sub>x</sub> as opposed to any other possible soluble species. It is possible that sulphur may also be released in partially combusted organic sulphur species, but this is considered unlikely in the view of the evidence presented in literature <sup>(12)</sup>. These observations are consistent with previous studies <sup>(22,29)</sup>.

Considering first the sulphur release from the two host-glass systems as a function of temperature during the vitrification process, it is apparent that from the initial temperature up to approximately 420 °C there is no evidence of sulphur emission from either the AB0 or AS0 waste melt. However, from 420 °C upwards both melts demonstrated significant emission of sulphur with up to 1000 ppm being captured in solution per minute. Slight differences were apparent between the two glass melts at this stage. The AS0 glass melt demonstrated significant sulphur loss over the temperature range 460 °C to 720 °C with a peak sulphur loss being apparent at 520 °C. In comparison the AB0 glass melt demonstrated sulphur loss over a larger range of temperatures, demonstrating loss of sulphur from 420 °C to 920 °C with a

peak value occurring at 620 °C. The sulphur loss per unit temperature can be seen in Figure 4.2.2. It is important to note however that a large proportion of sulphur loss occurred once the melt had achieved the dwell temperature of 1200 °C. To investigate this, the loss of sulphur from the melt over time for both glass melts was plotted. This can be seen in Figure 4.2.3. In considering the release of sulphur over time, it is apparent that subsequent to the initial sulphur loss in both glass compositions a second peak in sulphur release occurs once the melts have achieved 1200 °C. This second sulphur peak occurred at different times in the two melts investigated. In the AS0 glass melt, the second peak in sulphur release was seen to occur between 220 and 280 minutes, corresponding to the first 40 minutes after the melting temperature had been achieved, whereas in the AB0 glass melt, the second peak of sulphur release was seen to occur from approximately 300 to 340 minutes, between 60 and 100 minutes after the maximum melt temperature had been achieved. Finally, in considering the overall loss of sulphur demonstrated by both the AS0 and AB0 glass melts over the duration of the experiment, it can be seen that the AB0 glass melt demonstrated a much larger overall loss of sulphur than was demonstrated by the AS0 glass melt. The AB0 glass lost 95% of the sulphur inventory present in the resin, whereas the AS0 glass melt lost 68%. This is consistent with the results of chapter 4.1 (in the absence of gall layer formation) and with previous studies of these glass systems since the AS0 host glass is known to have a significantly greater capacity for sulphur retention than the AB0 host glass.

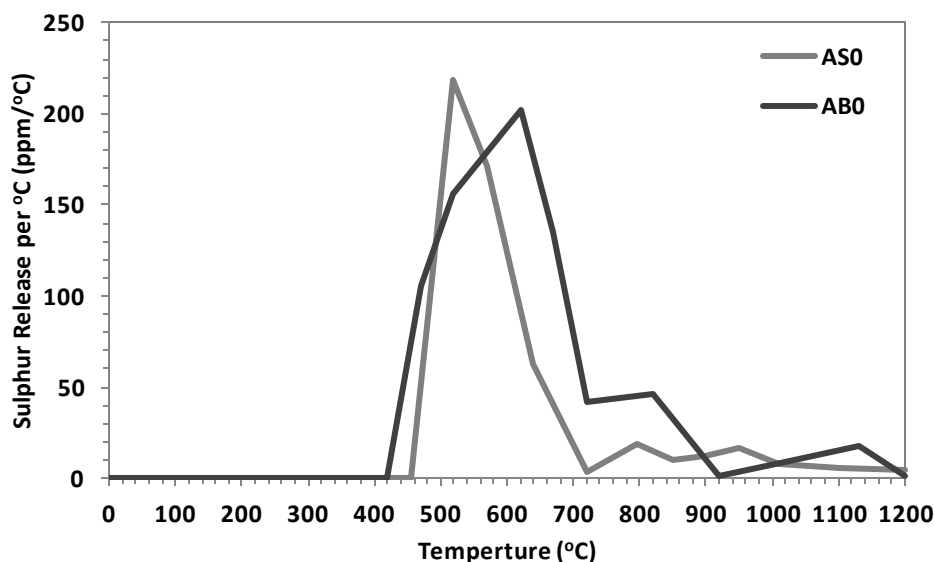


**Figure 4.2.2** Sulphur release from both AS0 and AB0 glass melts over temperature for the initial heating range.

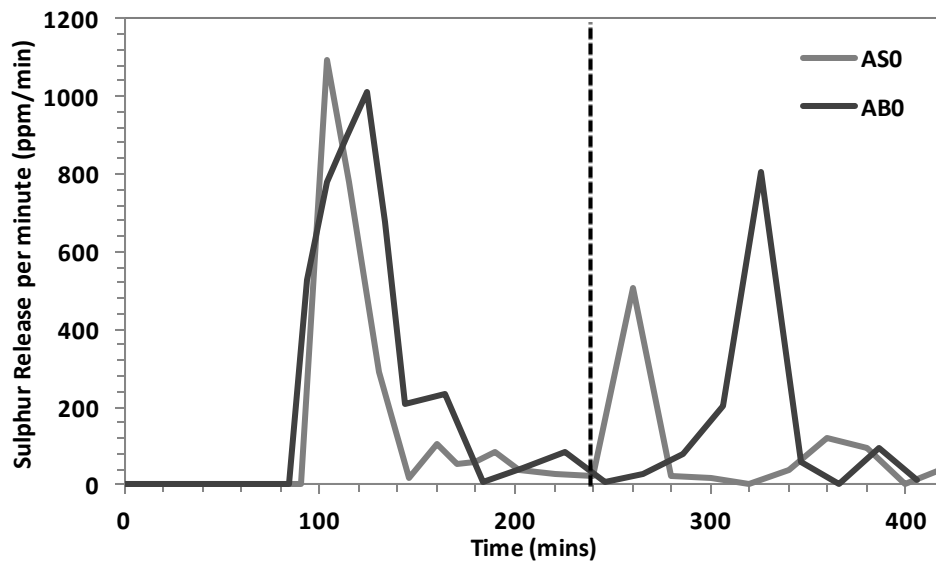


**Figure 4.2.3** Sulphur release from both AS0 and AB0 glass melts over time for the full duration of the off-gas experiment. Dotted line indicates point at which dwell temperature of 1200 °C was achieved.

In considering the release of other species from the glasses over the duration of the melt, it can be seen in Figure 4.2.4 and Figure 4.2.5 that where other species were released from the melt in the off-gases, they were released at much lower levels than were observed for the release of sulphur. In both AS0 and AB0 glass melts the next highest release was observed in boron, followed by Si in the AS0 glass melt and Si, Na and Al in the AB0 glass melt. As can be seen from the figures the release of boron recorded was in the order of 4 times greater than the release of any other species, and furthermore the boron release was seen to occur only at temperatures above 1000 °C. From 1000 °C / 200 minutes the boron release was seen to increase and reach a maximum at 260 minutes for both glass melts. Subsequent to achieving this maximum, the boron release rate diminished to near zero at around 400 minutes, after 3 hours at 1200 °C. Concurrently with this observed release of boron, the proportion of release for all other species present in both glass systems were seen to decrease. Considering the other species, apart from Cs, present in the glass melts, it was apparent that in both the AS0 and AB0 melts that Si was released at low levels from 500 °C to 1000 °C. However, in comparing the two melts it was apparent that in terms of B and Si release the proportion of material released was significantly larger from the AS0 glass melt, which demonstrated release for B and Si approximately twice as large as those seen in AB0. Both glass melts also demonstrated a small release of Na and Al, of roughly the same proportion in both melts, which peaked at temperatures between 400 °C and 700 °C. Notably the release of Na and Al seen in both AS0 and AB0 melts roughly corresponds to the

temperatures over which the initial release of sulphur was seen to occur. The release for these species can be seen in figures 4.2.6 and 4.2.7.

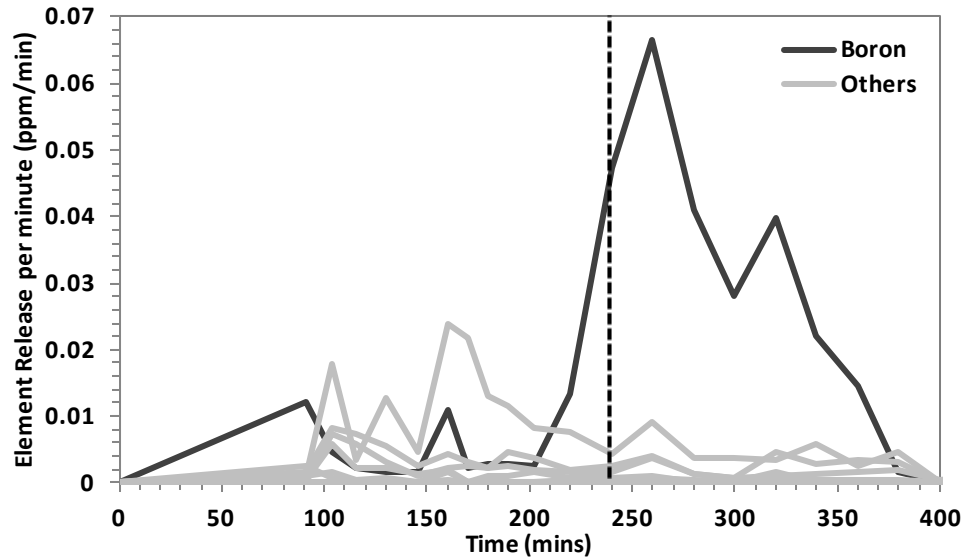


**Figure 4.2.4** Boron release from the AS0 glass melt over time for the full duration of the off-gas experiment. Dotted line indicates point at which a dwell temperature of 1200 °C was achieved.

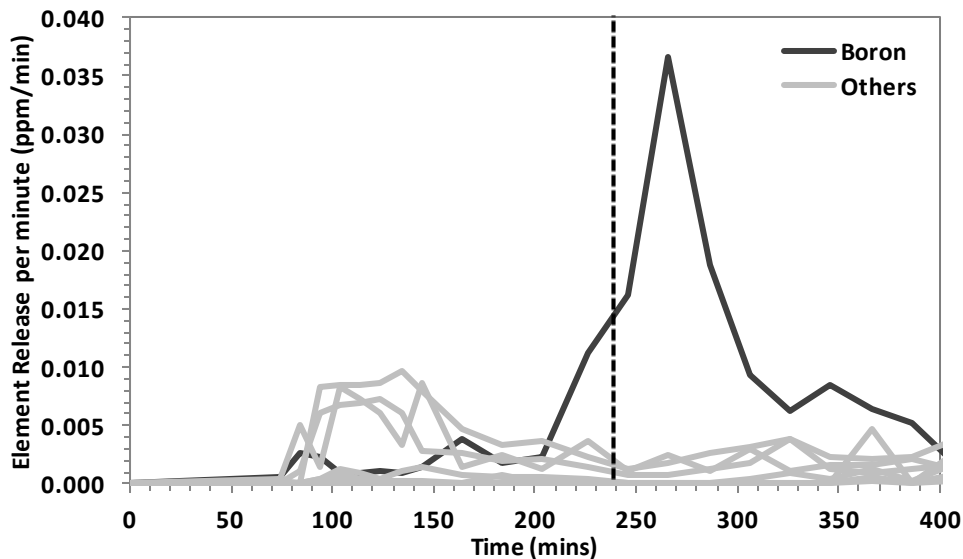


**Figure 4.2.5** Boron release from the AB0 glass melt over time for the full duration of the off-gas experiment. Dotted line indicates point at which a dwell temperature of 1200 °C was achieved.

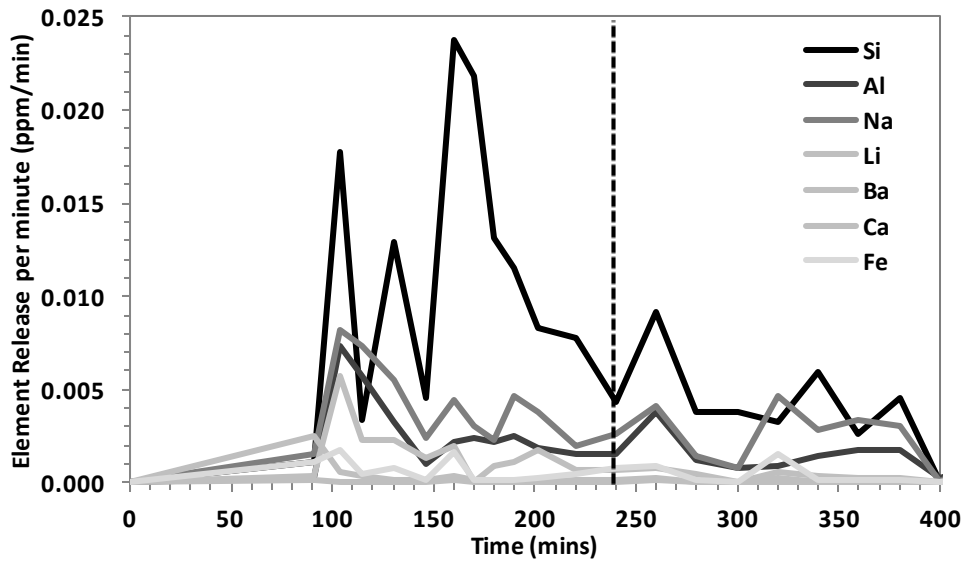


**Figure 4.2.6** Na, Al, Si, Li, Ba, Ca and Fe release from the AS0 glass melt over time for the full duration of the off-gas experiment. Dotted line indicates point at which a dwell temperature of 1200 °C was achieved.

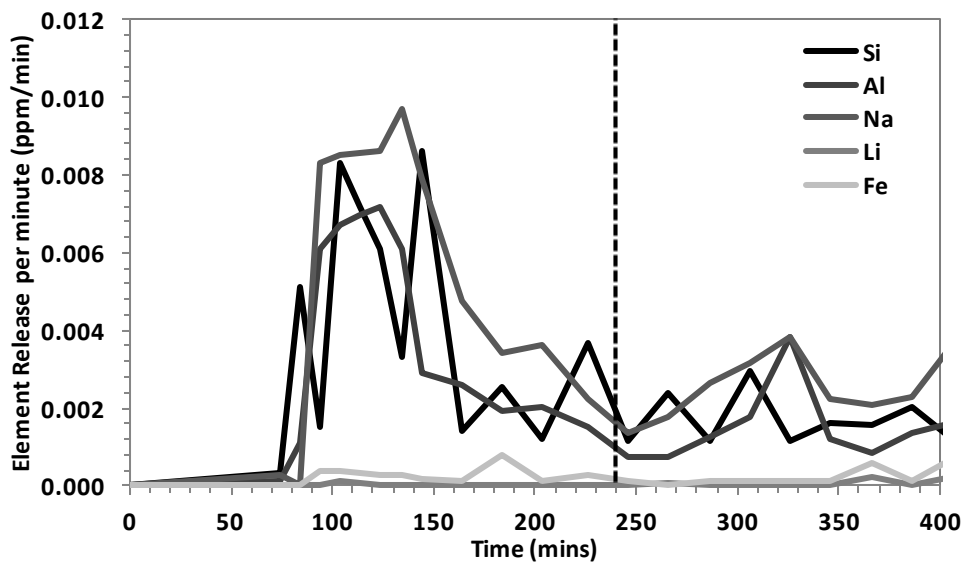


**Figure 4.2.7** Na, Al, Si, Li and Fe release from the AB0 glass melt over time for the full duration of the off-gas experiment. Dotted line indicates point at which a dwell temperature of 1200 °C was achieved.

Finally, considering the release of caesium from the glass melt, a pattern or release with distinct parallels to the boron release was observed in both glass melts. In both glass melts Cs release was observed to increase to significant levels from 200 minutes into the glass melt, corresponding to 1000 °C. This increased to a peak value in both glass melts at 260 minutes into the experiment, corresponding to 20 minutes after the maximum temperature was achieved. Subsequent to this peak release value the level of Cs release diminishes over time to achieve a steady state at approximately 360 minutes into the experiment. The AS0 glass demonstrates a second minor peak in Cs release at 320 minutes which was not apparent in the AB0 glass melt. This further reflects the release of B in the glass melt since a similar peak was observed in B release at the same point. In comparing the overall Cs release from the two glass melts, it is apparent that the overall Cs release demonstrated by the AS0 glass melt was seen to be approximately twice the magnitude of the Cs release demonstrated by the AB0 glass melt over the duration of the experiment. These results indicate at 83 % retention of Cs by the AB0 glass melt in comparison to a 66% retention by the AS0 glass melt. The Cs release from both glass melts is shown in figure 4.2.8.

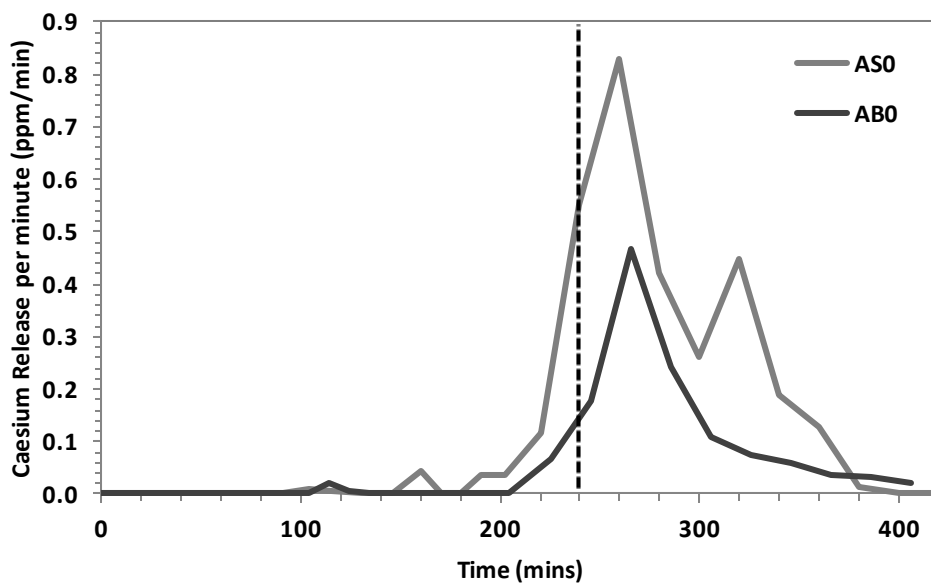


**Figure 4.2.8.** Caesium release from both AS0 and AB0 glass melts over time for the full duration of the off-gas experiment. Dotted line indicates point at which dwell temperature of 1200 °C was achieved.

### 4.2.3 Discussion

In considering the loss of sulphur as demonstrated by both glass melts, it is plausible that the two peaks in sulphur loss which were observed are attributable to two different stages in the vitrification processes. From the work of Hamodi *et al* <sup>(12)</sup> it can be seen that the temperature range over which the initial peak for sulphur release was observed is consistent with the temperatures associated with the thermal breakdown of the IEX resin waste itself and the decomposition of the organic and sulphur-containing portions of the resin. As such, it is likely that this first peak in sulphur release can be attributed to the decomposition of resin which has not been incorporated at this stage into the glass melt. This is further supported when this first peak is compared to the second peak which displays a greater extent of variation in timing and in the proportion of sulphur released, which implies that this second peak is affected by the properties of the host glass, whereas the first sulphur release peak is not. The small increase in the duration / temperature range of the first sulphur release seen in the AB0 glass composition can be attributed to the lower values of  $T_{liq}$  and  $T_g$  for the host glass frit, which would have resulted in the softening and flow of the host glass to be further advanced, providing a greater physical barrier against the release of the IEX resin combustion products.

As has been mentioned, the second sulphur release peaks seen in both glass melts demonstrate variations in the timing and size of the release which imply that they are influenced by the properties of the host glass, and therefore likely to be connected with the release of sulphur from IEX resin material which has been incorporated into the glass melt. As has been described in the work of Sobolev *et al* <sup>(22,33)</sup>, it is known that the sulphur material present in the glass melt during IEX resin vitrification is either incorporated into the glass matrix or forms a phase-separated alkali sulphate salt which forms in discrete regions and eventually forms an insoluble gall layer on the surface of the glass melt or is volatilised. It is plausible therefore that this second peak observed in sulphur can be associated with sulphur loss due to the formation and release of these sulphate salt species which subsequent to peaking decline rapidly due to either the partial pressure of the melting environment into which the sulphur material is released or due to the quantity of sulphate salt remaining in the melt. The variations seen in the timing and size of the sulphur release further support this possibility in two ways. Firstly, the AS0 glass melt demonstrated the occurrence of the second sulphur release peak significantly earlier in the course of the experiment than was seen in the AB0 glass melt. This can be attributed to the higher density and lower viscosity of the AS0 glass relative to the AB0 glass which would, due to the low density of the alkali sulphate salt phase, allow the separation of the immiscible sulphate salt phase to the surface

of the glass melt to occur more rapidly in the AS0 glass melt than in the AB0 glass melt. As such, this supports the association of the second sulphur release peak being attributable to the volatilisation of an alkali sulphate salt phase. Secondly, the size of the second peak, which was seen to be smaller in the AS0 glass melt than in the AB0 glass melt, indicates that this second sulphate release peak is connected to the formation of alkali sulphate salt phases, since the sulphur species are known<sup>(3)</sup> to have a higher solubility in the AS0 glass than in the AB0 glass and as such a smaller proportion of sulphur species are available for the formation of sulphur salts, which is concurrent with the smaller size of the second sulphur release in the AS0 glass melt. The melting and boiling temperatures for the sulphate salts present do not have an effect upon the sulphur release, since the mechanism for SO<sub>3</sub> dissociation is dependent upon oxygen partial pressure and temperature as shown by the work of Kim *et al*<sup>(85)</sup>.

Considering the release of other species from the glass melt it can be seen from the results that only boron demonstrated a significant proportion of release from the melt. The release of other elements, which is apparent in the results from both melts up to ~ 160 - 200 minutes or 800 - 1000 °C can be attributed to the capture and dissolution of glass particles carried by combustion gasses from the IEX resin into the collection solution. This can be seen firstly from the fact that the majority of the release observed occurred at timings concurrent with the first sulphate release peak, which is known to be associated with the thermal degradation of the resin, and secondly due to the decrease in release seen beyond 800 °C in the AB0 melt and 1000 °C in the AS0 melt which are concurrent with the T<sub>melt</sub> for both host glasses. The release of boron however occurs in both glass melts at roughly the same timing in the duration of the experiment, and seems to occur from temperatures of 1000 °C and upwards. This is consistent with previous work undertaken by Snyder *et al*<sup>(86)</sup> in which boron has been shown to be volatilised from glass melts, especially in environments with high partial pressures of water vapour such as would be present in IEX resin vitrification. This has been shown to have impacts upon the density and T<sub>g</sub> of the glasses studied. However it is unlikely to have a significant impact upon the waste-forms produced in this study since the levels of boron loss are low.

The loss of caesium from both glass melts was seen to closely correspond to the trend which was observed for the release of boron, in terms of timing, duration and in terms of the comparative intensity of the release between the two host glass compositions, in that as with boron, the AS0 glass melt demonstrated a larger overall release of caesium than was observed in the AB0 glass. These similarities indicate that the release of caesium and boron from the glass melts is likely to be governed by similar mechanisms, which are most likely associated

with the direct volatilisation of species due to thermal effects. It is unlikely that a direct connection exists between the loss of caesium and boron from the glass melt, such as the volatilisation of a caesium borate phase, since the higher caesium release was observed in the AS0 glass melt which possess a lower boron content, showing any such mechanism to be unlikely. As reported by Snyder *et al* <sup>(86)</sup> in connection to boron volatilisation it is known that the rate and proportion of volatilisation of boron, and by connection caesium, is affected primarily by the temperature of the melt but also by the partial pressure of water vapour present in the melt environment and the relative viscosity and density of the melt. This being the case, it is possible that the higher caesium releases observed in the AS0 glass melt may be associated with the lower viscosity and higher density of the glass, since these properties would increase the rate of convection which occurs in the melting process, increasing the proportion of species which are exposed to the atmosphere above the glass melt and as such increasing the proportion of these species which are lost to volatilisation. It is also significant to note that these results show no connection between the release of sulphur species and the release of caesium species in either of the glass melts. This has significant implications for the process utilised in the vitrification of IEX resin wastes.

#### 4.2.3.1 Implications for IEX Resin Vitrification

These results, in particular the observations made of sulphur release, have significant implications for the processes and host glasses used in the vitrification of IEX resin wastes. The results demonstrate that in these experiments, a large proportion of the sulphur content of the IEX resin waste is lost through the thermal degradation of the resin before it has the opportunity of being incorporated into the host glass matrix. This is undesirable due to the toxic nature of SO<sub>x</sub> emissions and highlights the need both for glasses with lower values of T<sub>liq</sub>, which may be able to incorporate the resin at low temperatures and so reduce the proportion of sulphur lost before the resin is incorporated, but also highlights the importance of the rate of heating used in vitrification, since a quicker heating rate or process by which waste is input directly to the molten host glass would eliminate the period where IEX resin is exposed to temperatures which are high enough to cause the resin to degrade but not high enough to allow the resin to be incorporate into the glass melt. With regard to the second peak in sulphate release, these results clearly show the importance of the physical properties of the host glass system for the mechanism for the formation and separation of alkali sulphate salt phases formed in the vitrification process.

However it is important to note that the release of caesium, the greater issue in the context of radionuclide contaminated IEX resin vitrification, was shown not to be directly linked to the emission of sulphur from the glass melt, but rather it was shown to be affected by the temperature of glass melt as well as the physical properties of the host glass melts. The fact that significant caesium release was not demonstrated below 1000 °C clearly underlines the importance of achieving the vitrification of these wastes at lower temperatures, since a reduction in melting temperature from 1200 °C to 1000 °C or less could significantly reduce the proportion of caesium species released from the glass melt. The variations observed between the overall caesium loss of the two glass systems explored demonstrates how properties which ordinarily would be seen as beneficial for waste vitrification, a high density and low viscosity, have the effect of exacerbating caesium release, although if vitrification can be achieved at a suitably low temperature, with the result of significant caesium volatility being avoided, then the effect of these properties will not significantly impact the caesium retention of the host glass. Furthermore, the connection made by Snyder *et al* <sup>(86)</sup> between boron volatilisation and H<sub>2</sub>O partial pressure may have further implication for the IEX resin vitrification process, since if the same applies to caesium release then it may be possible to retard caesium volatilisation through the control of the H<sub>2</sub>O partial pressure in the atmosphere present during vitrification.

#### 4.2.4 Conclusion

In summary, this work has demonstrated that in the process of vitrifying IEX resin wastes under the parameters described above using either the alkali alkaline-earth silicate (AS0) glass composition or the alkali borosilicate (AB0) glass composition, a significant proportion of sulphur is lost to off-gas in the form of SO<sub>x</sub>. The release of sulphur species was found to occur with two distinct peaks. The first was seen to occur at ~600 °C (120 minutes into the experiment) which was attributable to the thermal degradation of IEX resin material which had not been incorporated into the glass, since the T<sub>liq</sub> for both glasses was 800 °C or higher. The second peak was seen to occur once the melt had achieved its maximum temperature and after period of time had elapsed which differed between the two glass compositions explored. This second release was attributed to the release of sulphur through the volatilisation of an alkali sulphate salt gall layer produced due to the relatively low solubility of sulphur in silicate glass compositions. Variations were observed in timing and amount of sulphur species released due to the differing viscosity and density of the two glass melts and due to the higher capacity for retaining sulphur species attributed to the AS0 host glass. In addition

to this, above 1000 °C the volatilisation of boron was detected in both melts which was found to be consistent with literature expectations <sup>(86)</sup> and of little impact for the purpose of IEX resin vitrification.

Caesium release was determined to occur at much lower levels than was observed for sulphur, and did not match the release profile for the sulphur species, indicating that caesium release was unaffected by release of sulphur from the glass melts. This showed that caesium is not lost during the initial degradation of the IEX resin or alongside sulphur species at later stages of the melting process. However, a connection between caesium release and boron release was demonstrated, which was taken as an indication that both species were affected by the same thermally driven release mechanism described by the work of Snyder *et al* <sup>(86)</sup>. This connection shows that a significant improvement in caesium retention could be achieved by limiting the temperatures which are achieved during the IEX resin vitrification process. If vitrification can be achieved at no more than 1000 °C then caesium retention may be significantly improved. Variation in the extent of the overall caesium release between the two glass melts demonstrated the impact of the density and viscosity of the host glasses upon the release of volatile species from the glass melts.

These results have implications for the process of IEX resin vitrification in that they demonstrate that, under the conditions explored, a large proportion of the caesium content of the resin is lost to volatilisation processes which only occur above 1000 °C and that a significant proportion of sulphur release occurs due to the thermal degradation of the IEX resin, at temperatures lower than the melting temperature of the glass frit. This underlines the importance in both optimising the vitrification process in order to prevent the thermal decomposition of the resin, but more importantly the use of host glasses with lower values of  $T_{\text{melt}}$ . The results also demonstrate the importance of the density and viscosity of the host glasses to the loss of volatile species and the separation of the sulphate salt gall layer.

## **Chapter 5.1 - The effects of $\gamma$ -radiation on model vitreous wasteforms intended for the disposal of intermediate and high level radioactive wastes in the United Kingdom.\***

Vitrification is the currently accepted technology for the immobilisation of the high level radioactive wastes arising from the reprocessing of nuclear fuels and has been deployed on an industrial scale since at least 1977<sup>(87)</sup>. Radioactive waste vitrification has been applied by the USA, UK, Russia, France and Germany<sup>(11,29,88)</sup>, and to date has been used in the production of at least 11,000 canisters of vitrified waste<sup>(27)</sup>. The purpose of these vitrified waste-forms is to function as the primary barrier to the release of radionuclides to the environment, within a multi-barrier geological disposal facility. A vitrified waste-form must therefore be expected to withstand a range of adverse conditions over periods of  $10^2 - 10^6$  years with a minimal and quantifiable deterioration in chemical or mechanical integrity which could result in the release of radionuclides to the environment<sup>(28,43,78)</sup>.

The decay of fission products and actinides in radioactive waste glasses results in the emission of ionising radiation which may interact with the vitreous material through several mechanisms, potentially leading to an adverse impact on the long term physical and chemical stability of the material<sup>(89,90)</sup>. Ionising radiation has been linked to changes to the coordination of the species comprising the glass network, in alkali-borosilicate glasses, which typically results in a small increase in density, with a concomitant effect on mechanical properties<sup>(91)</sup>. The interaction of ionizing radiation with alkali-borosilicate glasses has also been linked to the formation of oxygen bubbles, the formation of various defect centres<sup>(91)</sup>, and at very high radiation doses even phase separation<sup>(92)</sup>. Such  $\gamma$ -radiation induced changes in structure and composition may adversely affect the long term mechanical integrity and chemical durability of the waste-form<sup>(92)</sup>. These ionization interactions are commonly associated with  $\beta$ - and  $\gamma$ -radiation;  $\alpha$  particles and neutrons typically interact with glasses through ballistic processes which result in atomic displacements<sup>(91)</sup>. As such, these ballistic processes result in stronger effects at equivalent doses, and can even produce cracking and crazing in glasses, as well as significant densification<sup>(91)</sup>, however, these effects are not generally observed in response to  $\gamma$ -radiation.

---

\*This chapter is presented in a modified version of a published paper; O. J. McGann, P. A. Bingham, R. J. Hand, A. S. Gandy, M. Kavcic, M. Zitnik, K. Bucar, R. Edge and N. C. Hyatt, "The effects of  $\gamma$ -radiation on model vitreous waste-forms intended for the disposal on intermediate and high level wastes in the United Kingdom," J. Nuc. Mater., 429 353-367 (2012).

$\beta$ -decay of fission products leads to the emission of  $\gamma$ -ray photons which interact with the glass matrix primarily through Compton Scattering and the photoelectric effect <sup>(89)</sup>. Absorption of  $\gamma$ -ray photons results in the formation of mobile electron and hole pairs which can lead to metastable defects associated with a change in element valence state and coordination. These effects are comparable to some extent with the effects of electron irradiation <sup>(93)</sup>. Furthermore, as  $\gamma$ -radiation is more penetrating than other forms of ionising radiation its effects typically permeate the entirety of a glass waste-form instead of being limited to structural regions local to the radiation source. The impact of  $\gamma$ -irradiation on the properties of a glass can be diverse and depend heavily upon the composition of the glass in question.

Experiments involving ion beam irradiation of amorphous silica, analogous in effects to  $\gamma$ -irradiation, revealed that ionising radiation resulted in the formation of crystalline regions and resulted in an overall increase in density as result of bond modification in the amorphous silica network. <sup>(94)</sup> These effects were noted to be strongly dependent upon the chemistry associated with the elements present <sup>(95)</sup>. Therefore it can be seen that the ionising effects of radiation, including  $\gamma$ -irradiation, vary considerably depending on the composition of the affected amorphous material.

In borosilicate glass compositions similar to those used for radioactive waste vitrification, it was observed that  $\gamma$ -radiation induced the formation of boron-oxygen hole centre (BOHC) defect sites which were detectable by electron paramagnetic resonance (EPR) spectroscopy <sup>(96)</sup>. However, the  $\gamma$ -irradiation effects are not limited to defect formation and typically in borosilicate glasses a range of effects have been reported to occur: the formation of colour centres occurs at low doses of  $\gamma$ -radiation (0.018 MGy) <sup>(98)</sup>; and at larger doses (>1 MGy) increases in silicate network polymerisation, the formation of free oxygen gas, decreases in average Si-O-Si bond angle and increases in glass density which have been connected with an increase in mechanical strength <sup>(97,99)</sup>.  $\gamma$ -radiation might therefore be expected to cause a range of detectable effects on borosilicate glasses due to the induced defects and changes in bonding of the borate and silicate networks caused by electron and hole pairs.

Research has demonstrated that the presence of transition metal species in silicate glasses, such as Fe, Cr, Zr and some actinides such as U, may inhibit the accumulation of  $\beta$ -radiation induced defects, similar to those noted above <sup>(95-96)</sup>. The mechanism of this effect, proposed by Debnath *et al.* <sup>(6)</sup>, is linked to the ability of these elements to effectively ‘trap’ the excitons (electron and hole pairs) produced by the irradiation via changes in oxidation

states, such as the ferrous and ferric oxidation states of iron <sup>(93)</sup>. As the different oxidation states of these elements usually coexist in oxide glasses the excitons produced by the incident radiation are prevented from forming structural defects because they are removed from the system by altering the oxidation state of these elements. <sup>(93)</sup>. Whilst electron beam and  $\beta$ -radiation effects cannot be directly compared to the effects of  $\gamma$ -radiation due to difference in the path of ionisation, the effects on materials fall into the category of ‘ionizing interactions’, which allows comparison between inhibiting mechanisms which occur in materials irradiated by either form of radiation. Indeed, it has been shown that in the case of iron containing glasses irradiated with  $\gamma$ -radiation, iron can act as an absorber of both electrons and electron holes depending on iron content and on radiation dose <sup>(6,89)</sup>.

### 5.1.1 Experimental Procedures

Irradiation experiments employed a selection of glass compositions which are either in consideration for use in the vitrification UK ILW (Intermediate level wastes), namely glasses AB1, AS0 and AB0, or are already used for UK HLW (High level waste vitrification) namely glass MW-25%. All of the glasses were loaded with appropriate inactive simulated wastes. The nominal compositions of these waste-forms and key preparation details are listed in Table 5.1.1.

Glasses AB1 and AB0 are similar to several of the mixed alkali borosilicate glasses, including the “MW” base glass developed and used for vitrification of UK HLW (Marples *et al.* <sup>(101)</sup>). In contrast Glass AS0 is distinct as it is an alkali-alkaline earth borosilicate. These three glass compositions were designed for ILW waste vitrification <sup>(102,103)</sup>, and all contain quantities of  $\text{Fe}_2\text{O}_3$  in their compositions for improved compatibility with a potential intended waste stream through control of glass redox. These three glasses were loaded with simulated ILW waste (an ion exchange resin) with high organic and sulphur contents. MW-25% is an inactive simulant UK HLW glass, the composition of this material corresponds to 25% of HLW waste oxides from spent Magnox fuel, incorporated within an alkali borosilicate (MW) base glass.

Glasses were melted in recrystallised alumina crucibles using an electrical muffle furnace. Melting temperatures ranged from 1060 °C to 1200 °C depending on glass composition. Glasses were melted for 2 hours before pouring into a steel mould and annealed in a muffle furnace, set close to the glass transition temperature ( $T_g$ ) for the glass composition. The melting and annealing temperatures are given in Table 5.1.1.

**Table 5.1.1.** Nominal Glass compositions (mol%) and glass melting temperatures.

<b>Component</b>	<b>AB1</b>	<b>AS0</b>	<b>AB0</b>	<b>MW-25%</b>
SiO <sub>2</sub>	58.2	50.2	58.8	48.4
B <sub>2</sub> O <sub>3</sub>	9.1	2.2	17.8	17.2
Al <sub>2</sub> O <sub>3</sub>	2.5	0.4	-	5.1
Fe <sub>2</sub> O <sub>3</sub>	5.2	2.9	3.9	3.4
CaO	-	10.7	-	-
BaO	-	17.6	-	-
Li <sub>2</sub> O	10.6	7.6	10.4	4.2
Na <sub>2</sub> O	13.3	3.0	8.0	8.7
SO <sub>3</sub>	1.1	5.4	1.1	-
MgO	-	-	-	8.4
Other waste oxides	-	-	-	4.6
Melting Temperature	1200°C	1200°C	1200°C	1060 °C
Annealing Temperature	450°C	480°C	480°C	500°C

Annealed glass prisms, measuring approximately 10mm x 10mm x (100 – 200) mm, were subsequently exposed to a  $\gamma$ -radiation dose of 4 or 8 MGy, a control specimen (0 MGy) was retained for each composition. The  $\gamma$ -radiation source was <sup>60</sup>Co (2.824 MeV) and irradiation was carried out at the UK AEA Harwell Site.

The  $\gamma$ -radiation doses represented levels of radiation up to what would be expected for a 8.7 year dose for the waste-forms AB1, AS0 and AB0 (8 MGy) and approximately 0.13 years for the waste-form MW-25%. The estimates for AB1, AS0 and AB0 are based on the  $\gamma$ -irradiation produced by the decay of 0.1 wt% <sup>137</sup>Cs, which is the proportion expected in the optimum (35 wt%) waste-loading of ILW simulated waste (Cs loaded, sulphonated ion exchange resin). The estimate for MW-25% is based on values published by Marples *et al.* <sup>(101)</sup> for this type of waste-form (loaded with a HLW simulated waste loading of 25wt%). Post irradiation, the samples were stored in a dark and refrigerated environment (approximately –15 °C) to reduce the potential for the thermal and optical healing of radiation induced defects.

A wide selection of experimental techniques was implemented to determine the effect of  $\gamma$ -irradiation upon the glasses, for the purpose of this chapter they are divided into two broad categories: mechanical techniques and spectroscopic techniques.

### 5.1.1.1 Mechanical Techniques

A resonant frequency technique was applied to determine the effect of  $\gamma$ -radiation on Young's modulus, shear modulus and Poisson's ratio. Vickers indentation, utilising a diamond tipped indenter, was applied to determine the effect of  $\gamma$ -radiation on glass hardness and fracture toughness.

Davis *et al* <sup>(104)</sup>, demonstrated that the shear and Young's modulus of a material can be determined non-destructively by measuring the resonant frequency of an internal standing acoustic wave, generated by mechanical excitation using an electrostatic drive. The resonant frequency can be connected to the elastic constants of the material through the Equations 5.1.1 and 5.1.2.

$$E = 4 \times 10^{-6} f_0^2 l^2 \rho \times \left[ \frac{1}{\left[ 1 - \frac{(\pi v)^2 (h^2 + b^2)}{2l^2 z l} \right]^2} \right] \quad (\text{Equation 5.1.1})$$

and

$$G = 4 \times 10^{-6} f_0^2 l^2 \rho \times \left[ \frac{\left(\frac{h}{b}\right) + \left(\frac{b}{h}\right)}{4\left(\frac{h}{b}\right) - 2.52\left(\frac{h}{b}\right)^2 + 0.21\left(\frac{h}{b}\right)^6} \right] \quad (\text{Equation 5.1.2})$$

with

$$v = \frac{E}{2G} - 1 \quad (\text{Equation 5.1.3})$$

where E is Young's modulus, G is shear modulus,  $f_0$  the resonant frequency, l the length of the sample,  $\rho$  the material density, v is the Poisson's Ratio, h is the height of the sample and b is the width of the sample; assuming the sample is a regular prism. By finding the resonant frequency of the material both in the longitudinal mode (i.e. the resonant frequency of a first order standing wave parallel to the length of a prism) and the flexural mode (i.e. the resonant frequency of a first order standing wave passing diagonally across the length of a prism) the Young's modulus and shear modulus can be experimentally determined; a comprehensive experimental description has been published elsewhere <sup>(104)</sup>. Poisson's ratio can be determined from the resulting shear and Young's modulus results (Equation 5.1.3).

Micro-indentation experiments were performed based upon the work of Connelly *et al* <sup>(107)</sup> using a Mitutoyo HM hardness testing machine. Experiments were performed on sample surface polished and finished with 0.25  $\mu\text{m}$  diamond paste. Polishing was undertaken after the irradiation process. Indentations were created across a range of forces 1 – 50 N with a minimum of 5 measurements taken at each value of force. Force was applied for a period of 20 s. The size of the resultant indentation was measured and used to calculate the hardness,  $H$ , using Equation 5.1.4. The lengths of the fractures radiating from the indentation were utilized to calculate the indentation fracture toughness,  $K_{Ic}$  using Equation 5.1.5.

$$H = \frac{1.854mg}{d^2} \quad (\text{Equation 5.1.4})$$

$$K_{Ic} = \frac{0.0824m}{\frac{3}{c^2}} \quad (\text{Equation 5.1.5})$$

where  $m$  is the applied mass,  $d$  is the size of the indentation, measured from the central point to the furthest point and  $c$  is the size of the fractures, measured from the central point to their furthest extent. A total of 25 indentations were made per sample, over the range of force. The indentation fracture toughness is not necessarily equal to fracture toughness measured by more conventional techniques, however the indentation fracture toughness can be used successfully to rank the toughness of materials within a class or the effect of specific treatments on the toughness of a given material.

### 5.1.1.2 Spectroscopic Techniques

Spectroscopic techniques were implemented to determine the effect of  $\gamma$ -irradiation upon glass structure and redox. Optical absorption spectroscopy was utilised to identify the colour generating absorption bands in the glasses. A Perkin Elmer Lambda 900 optical absorption spectrometer collected spectra over a range of 300 – 3300 nm. Experiments were performed on thin (30–100  $\mu\text{m}$ ), optically transparent glass slides which were polished to 1  $\mu\text{m}$ . Differences in sample thickness were accounted for utilising the Beer-Lambert law.

FTIR (Fourier Transform Infra-Red) spectroscopy and Raman spectroscopy were used to quantify changes to the silicate network in response to  $\gamma$ -irradiation. A Perkin Elmer Spectrum 2000 FT-IR spectrometer was used with spectra being collected over 500 – 1500 nm. Experiments were performed via reflectance off sample surfaces which had been polished to 1  $\mu\text{m}$ . The subsequent results were then corrected through a

Kronig-Kramers transform. A Renishaw InVia Raman microscope was used to collect spectra over a range of 0 – 1800  $\text{cm}^{-1}$ . Results were acquired utilising laser (514 nm) excitation of samples polished to 1  $\mu\text{m}$ .

Room temperature  $^{57}\text{Fe}$  Mössbauer spectroscopy was applied to probe changes in Fe valence and coordination in response to  $\gamma$ -irradiation. A WissEl  $^{57}\text{Fe}$  Mössbauer Spectrometer was used, operating in a constant acceleration mode and a  $^{57}\text{Co}$  source (activity 9000  $\mu\text{Ci}$ , accounting for the decay of the source at time of experiment) was used as a radiation source. Samples were mixed with graphite to prevent excess absorption, and mounted in a perspex holder suitable for transmission, perpendicular to the incident radiation and the detector. Mössbauer spectra were fitted using two Lorentzian doublets, one each to represent the  $\text{Fe}^{2+}$  and  $\text{Fe}^{3+}$  environments, using the software package Recoil 1.03. The recoil free fraction was assumed to be equal in the  $\text{Fe}^{2+}$  and  $\text{Fe}^{3+}$  environments. Consequently, the area of the Lorentzian line shapes could be equated to the relative abundance of these oxidation states.

EPR spectroscopy was applied to characterise potential defect sites formed by  $\gamma$ -irradiation. An X-band Brüker EPR spectrometer with a field sweep of 0 to 800 mT at room temperature ( $\sim 291$  K) was used. Additional scans were performed over a field sweep of 330-350 mT at higher resolution in some samples. EPR experiments were performed on samples which were powdered to 75  $\mu\text{m}$ . Samples were contained within a high purity silica tube during the experiment.

XAS (X-ray absorption spectroscopy) at the S K-edge and XES (X-ray emission spectroscopy) utilising S  $\text{K}\alpha$  emission was utilised to determine changes in sulphur valence and coordination within samples with a high sulphur content. These experiments were carried out at the ID26 beam line at the European Synchrotron Radiation Facility (ESRF), Grenoble. Samples were powdered to 75  $\mu\text{m}$  and mounted on to an Al plate using acetone. The incident energy was controlled on the beamline utilising a fixed-exit double Si ( $^{53}$ ) crystal monochromator. Collimating and harmonic rejection mirrors were used to remove higher order harmonics. The theoretical resolution of the XAS experiment was 0.36 eV at the S K-edge. The energy was calibrated by using the absorption edge of natural S at 2472.0 eV. For XAS experiments the data was collected utilising a fluorescence detector mounted at  $45^\circ$  from the incident X-ray beam. The incident X-ray energy was varied over a range of 2450 – 2550 eV. XES experiments were carried out utilising a Johansson type crystal spectrometer employing a Si crystal which was curved cylindrically to meet a 500 mm Rowland circle radius, and a

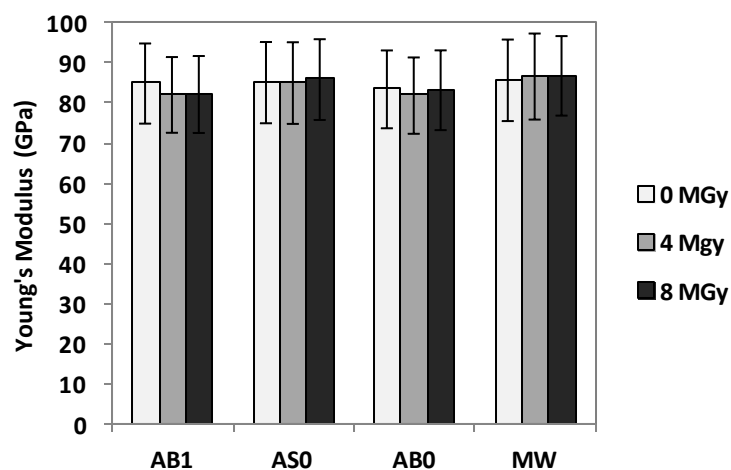
thermoelectrically cooled CCD detector (pixel size  $22.5 \times 22.5 \mu\text{m}^2$ )<sup>(106-107)</sup>. The incident photon energy was tuned to 2.52 keV. The sample surface was mounted at  $45^\circ$ , and the target X-ray fluorescence was collected at  $90^\circ$  with respect to the incident beam direction. The energy calibration was performed relative to the  $K\alpha$  line of native S (2307.89 eV) which was used as a reference. The overall experimental energy resolution was  $\sim 0.4$  eV, which was high enough to separate clearly between the  $\text{S}^{2-}$  and  $\text{S}^{6+}$  emission lines and quantitatively determine the proportion of reduced sulphur species in the sample. The latter was performed by fitting the measured XES spectra with a combination of two individual Lorentzian line shape doublets, corresponding to the emission lines associated with  $\text{S}^{2-}$  and  $\text{S}^{6+}$ , respectively<sup>(108-109)</sup>.

Further details for these techniques are provided in appendix 8.1.

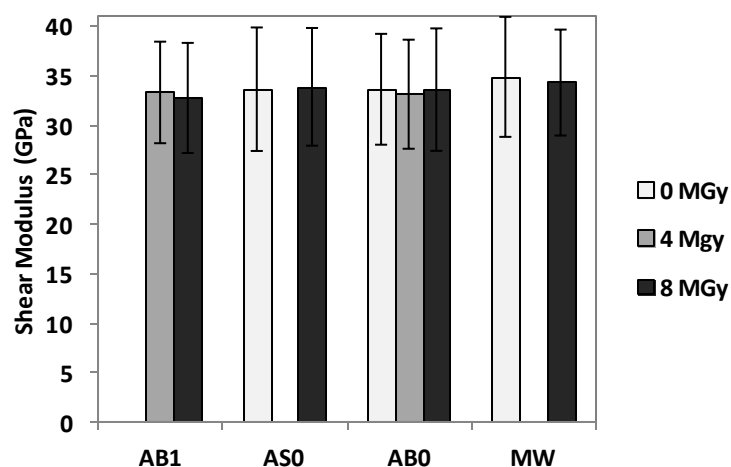
## 5.1.2 Results

### 5.1.2.1 Mechanical Techniques

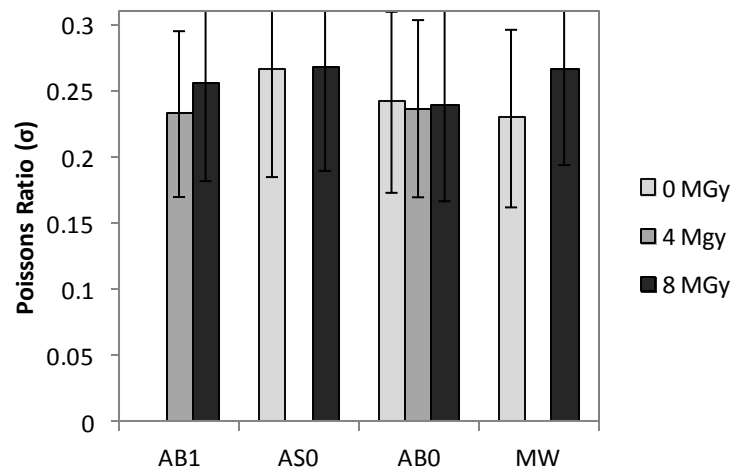
Figures 5.1.1 and 5.1.2 show the Young's and shear moduli of the sample prisms as determined by the resonant frequency method described previously. The values of both moduli determined for the control samples (0 MGy) are in good agreement with previous research<sup>(105)</sup>, in which values of 78 – 81 GPa and 31 – 32 GPa respectively were reported for similar waste loaded compositions. The  $\gamma$ -irradiated specimens when compared with the un-irradiated control specimens show no significant change, within the precision of the measurements. In contrast, previous  $\gamma$ -irradiation studies of alkali-borosilicate glasses reported a significant increase in density and hence Young's and shear modulus, due to increased network polymerisation<sup>(106)</sup>, as discussed further in Section 5.1.3.1. The error bars shown in Figures 5.1.1 and 5.1.2 represent the propagated errors associated with measurement of the dimensions, density and resonant frequency of the glass prisms, based on at least three independent measurements.



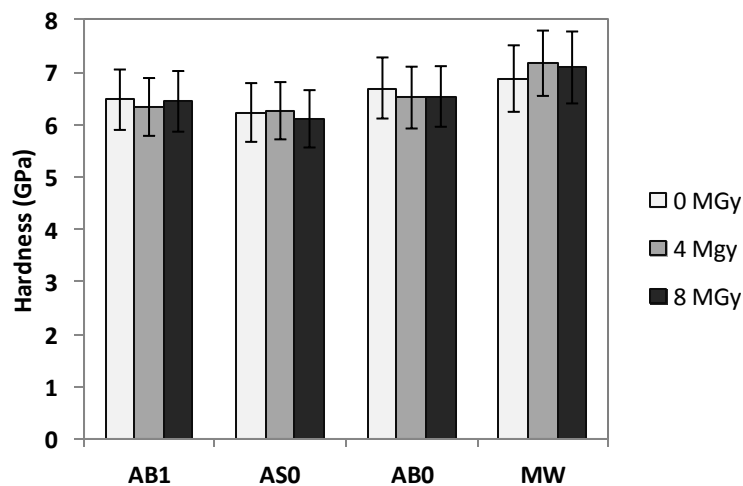
**Figure 5.1.1.** Comparison of Young's modulus of control (0 MGy) and  $\gamma$ -irradiated (4 and 8 MGy) glasses. Determined by the resonant frequency technique. Error bars correspond to three standard deviations, as described in text.



**Figure 5.1.2.** Comparison of shear modulus of control (0 MGy) and  $\gamma$ -irradiated (4 and 8 MGy) glasses. Determined by the resonant frequency technique. Data for AS0 and MW-25% 4 MGy could not be obtained due to the dimensions of specimens for which a reliable standing wave could not be measured. Error bars correspond to three standard deviations as described in text.



**Figure 5.1.3.** Comparison of Poisson's ratio in control (0 MGy) and  $\gamma$ -irradiated (4 and 8 MGy) glasses. Derived from the Young's and shear modulus using Equation 3. Data for ASO and MW-25% 4 MGy results are not shown due to absence of satisfactory shear modulus data. Error bars correspond to three standard deviations, as described in text.



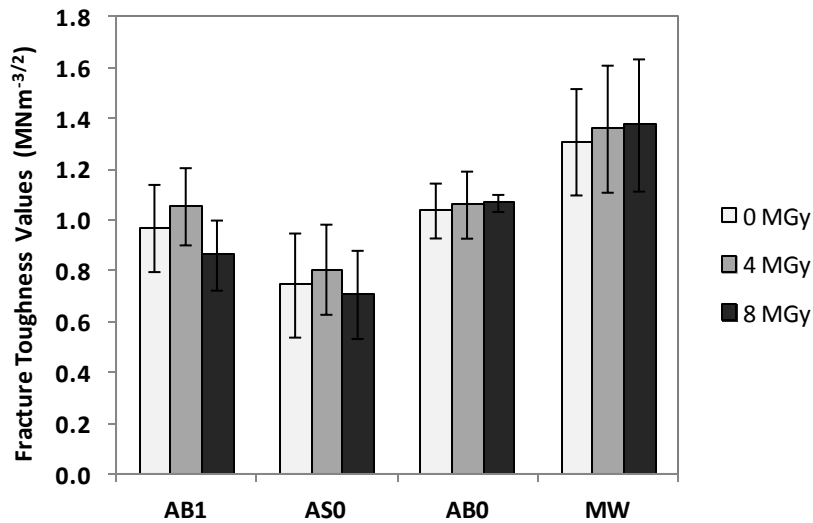
**Figure 5.1.4.** Comparison of hardness values in control (0 MGy) and  $\gamma$ -irradiated (4 and 8 MGy) glasses. Determined through Vicker's indentation experiments across a range of indentation forces. Error bars represent three standard deviations

Figure 5.1.3 shows Poisson's ratio, as determined from the Young's and shear moduli utilising Equation 3. Given the agreement between the values of Young's and shear moduli

for the current work and previous work it is not surprising that the values of Poisson's ratio determined for the control glass samples are in good agreement with values previously reported for glasses of similar compositions for which  $\nu \approx 0.25$  <sup>(105)</sup>. In addition, it is not surprising that there is no significant change in the value of Poisson's ratio, within the precision of the measurements, for the  $\gamma$ -irradiated samples from the values for the control (0 MGy) samples. The error bars quoted in Figure 5.1.3 represent the propagated errors associated with measurement of the Young's modulus and the shear modulus of the prism.

Figure 5.1.4 shows the hardness values as determined from micro-indentation of the glass surfaces. The hardness values which were determined for the control samples were in good agreement with results from previous research <sup>(107)</sup> which reported values of 5.9 – 7.1 GPa for similar compositions. The hardness values determined for the  $\gamma$ -irradiated glass samples showed no significant variation from the values obtained for the control samples (0 MGy) within the estimated precision of the measurements. These results are consistent with past observations of alkali-borosilicate glasses, albeit at lower doses (1 MGy) <sup>(89,106)</sup>. The errors bars reported in Figure 5.1.4 were derived from the standard deviation of the 30 – 50 results obtained for each sample.

Figure 5.1.5 shows the indentation fracture toughness of the samples as determined through micro-indentation of the glass surface. The samples were not annealed prior to the measurement of fracture toughness which would otherwise heal any defects induced by  $\gamma$ -irradiation. Therefore, although the absolute values of indentation fracture toughness may be subject to systematic error, relative changes in indentation fracture toughness are considered meaningful. The indentation fracture toughness values obtained for the control glass samples (0 MGy) are in good agreement with previous research <sup>(107)</sup> in which values of 0.81 – 1.06  $\text{Nm}^{-3/2}$  were reported. Within the estimated precision of the measurements, the  $\gamma$ -irradiated glass samples presented no significant variation in fracture toughness when compared with the results determined from the control samples. These results are broadly consistent with previous studies of alkali-borosilicate glasses, albeit at lower doses (1 MGy) <sup>(89,106)</sup>. The errors bars reported in Figure 5.1.5 were derived from the standard deviation of the 30 – 50 results obtained for each sample.



**Figure 5.1.5.** Comparison of fracture toughness values in control (0 MGy) and  $\gamma$ -irradiated (4 and 8 MGy) glasses. Determined through Vicker's indentation experiments across a range of indentation forces. Error bars represent three standard deviations, as described in the text.

### 5.1.2.2 Spectroscopic Techniques

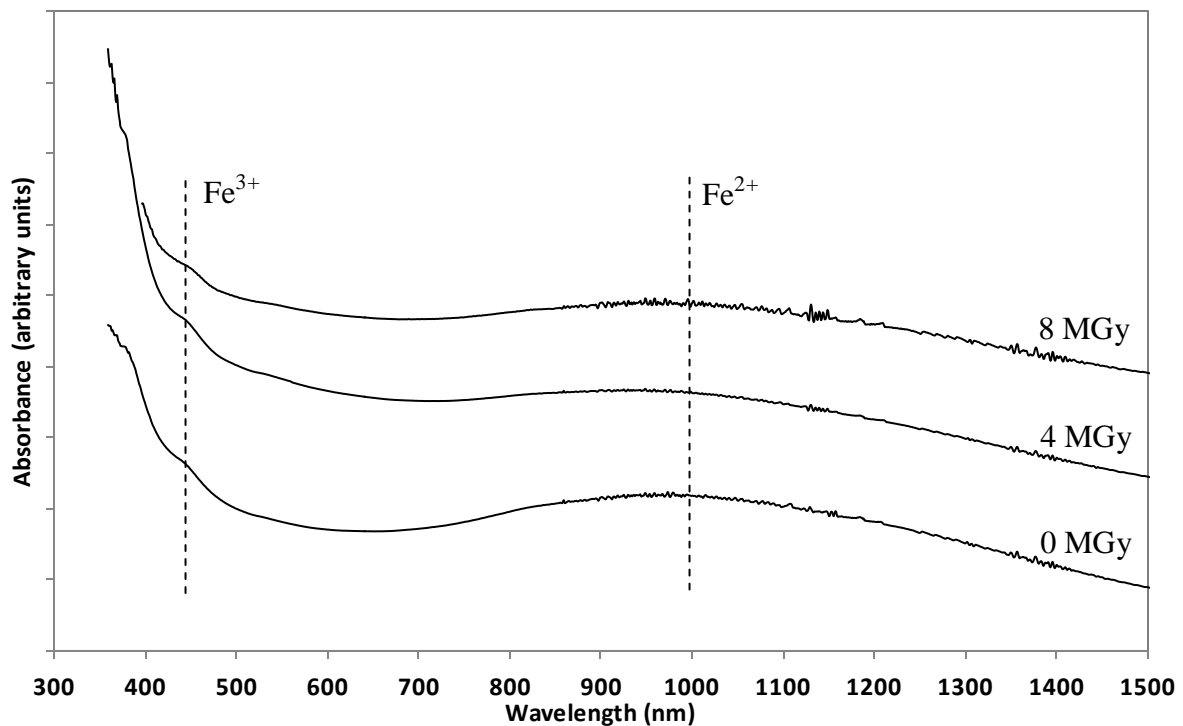
#### 5.1.2.2.1 Optical Absorption Spectroscopy

A clear non-linear variation in colour was observed in the samples MW-25% and AS0, in response to increased radiation dose. In glass AS0 the shade increased in darkness in the order 8 MGy < 0 MGy < 4 MGy, and in the order 0 MGy < 4 MGy = 8 MGy in the MW-25% glass sample. The variation in glass AS0 is displayed in Figure 5.1.6.



**Figure 5.1.6** Photographic image of 75  $\mu$ m powder samples of glass AS0 (0, 4 and 8 MGy). Variation in colour induced by  $\gamma$ -irradiation is clearly observed.

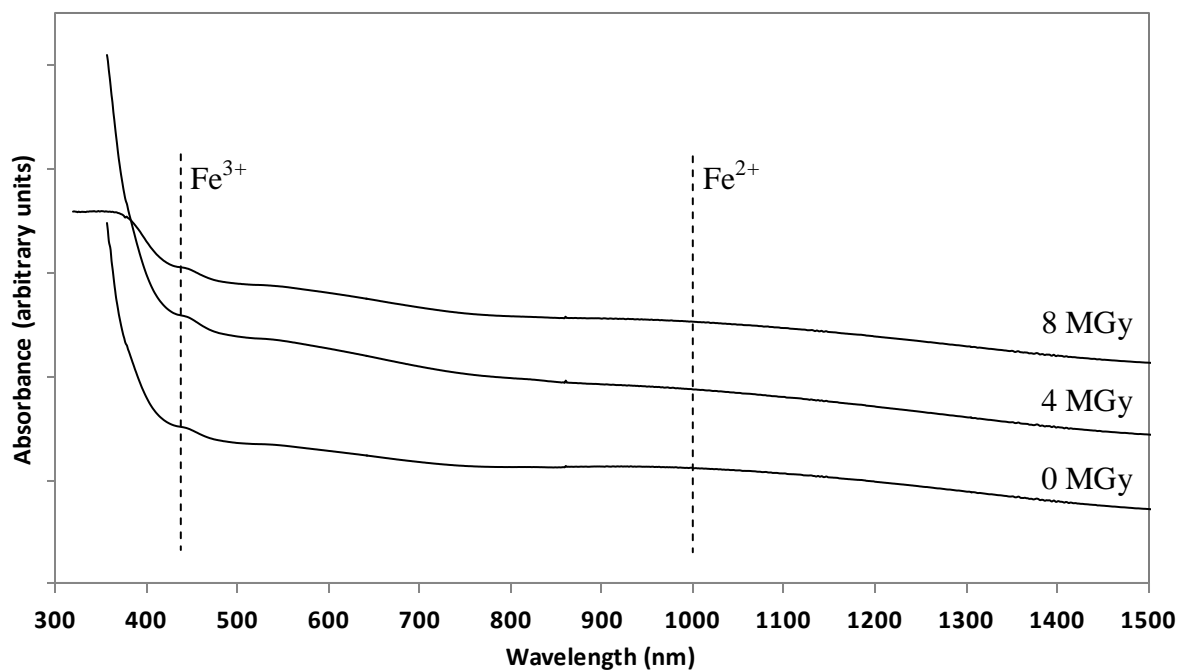
Optical absorption spectroscopy was applied to identify  $\gamma$ -radiation induced changes in absorbing species. Figures 5.1.7 and 5.1.8 show the optical absorption spectra for glasses AB1 and AB0. Two absorption bands are apparent in the spectra of both glasses; a broad band centred at ca. 1000 nm and a comparatively narrow absorption band at ca. 450 nm. Both of these bands can be attributed to absorption from Fe species within the glass, the former to  $\text{Fe}^{2+}$  species, specifically those in distorted octahedral coordination environments, and the latter to  $\text{Fe}^{3+}$  species<sup>(63)</sup>. The UV edge in these glasses, visible at the lower extreme of wavelengths, is prominent at a higher wavelength than is typical in alkali-borosilicate glasses. This can be attributed to the high Fe content of these glasses, which is known to bring the UV edge to longer wavelengths<sup>(63)</sup>. The bands identified are in good agreement with those reported to be present in similar high Fe content alkali-borosilicate glasses, where bands related to  $\text{Fe}^{2+}$  have been identified at 1075 nm and at 2000 nm, and  $\text{Fe}^{3+}$  bands have been identified at 380 nm, 415 nm, 435 nm, and 445 nm<sup>(63,110-111)</sup>. Overall, inspection of Figures 5.1.7 and 5.1.8 demonstrates that the optical absorption spectra do not show any significant change as a consequence of  $\gamma$ -irradiation.



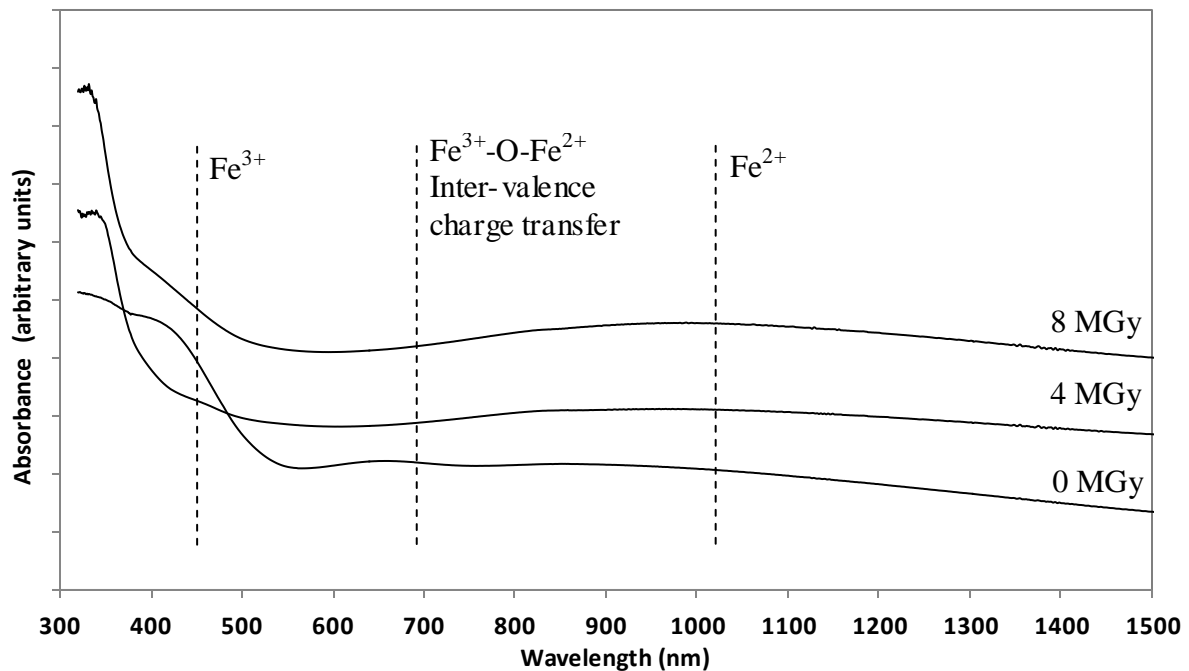
**Figure 5.1.7** Comparison of optical absorption spectra in control (0 MGy) and  $\gamma$ -irradiated (4 and 8 MGy) samples from glass AB1. Data are the sum of three averaged optical absorption spectra taken from different areas of a transparent section; for clarity data are offset on the y-axis.

Figure 5.1.9 displays the optical absorption spectra for the glass AS0. Three absorption bands are apparent in the spectra of the control sample (0 MGy); one broad band centred at approximately 1000 nm, which can be attributed to  $\text{Fe}^{2+}$  in a distorted octahedral coordination, another at 450 nm which can be attributed to  $\text{Fe}^{3+}$  species<sup>(111)</sup>, and a third at approximately 650 nm. This third band is attributable to inter-valence charge transfer between  $\text{Fe}^{3+}$  and  $\text{Fe}^{2+}$  across a bridging oxygen ( $\text{Fe}^{2+}\text{-O-Fe}^{3+}$ )<sup>(63)</sup>. This band has been observed in Fe rich alkali-borosilicate glasses in previous studies<sup>(63)</sup>.

The  $\gamma$ -irradiated AS0 samples present only two significant absorption bands, those at 1000 nm and 450 nm which have been attributed to  $\text{Fe}^{2+}$  and  $\text{Fe}^{3+}$  respectively<sup>(111)</sup>. The inter-valence transfer band is absent from these samples. In this respect, the optical absorption spectra of the  $\gamma$ -irradiated AS0 samples are in good agreement with the AB1 and AB0 samples as well as the majority of comparable reduced high Fe alkali-borosilicate glasses, such as those reported in<sup>(63,110-111)</sup>. Notably the UV edge is also at longer wavelengths apparent in the un-irradiated AS0 glass samples.



**Figure 5.1.8** Comparison of optical absorption spectra in control (0 MGy) and  $\gamma$ -irradiated (4 and 8 MGy) samples from glass AB0. Data are the sum of three optical absorption spectra taken from different areas of a transparent section; for clarity data are offset on the y-axis.



**Figure 5.1.9** Comparison of optical absorption spectra in control (0 MGy) and  $\gamma$ -irradiated (4 and 8 MGy) samples from glass AS0. Data are the sum of three optical absorption spectra taken from different areas of a transparent section; for clarity data are offset on the y-axis.

Figure 5.1.10 shows the optical absorption spectra of the glass MW-25%. One strong absorption band is present at approximately 450 nm, and three weaker absorption bands at 580 nm, 745 nm and 805 nm. As in the glasses AB1, AS0 and AB0, the band at 450 nm can be attributed to  $\text{Fe}^{3+}$ . The three weaker bands are consistent with absorption by  $\text{Nd}^{3+}$  ions<sup>(112)</sup>. Notably the absorption band related to  $\text{Fe}^{2+}$  at 1000 nm was absent. These results show, in general, good agreement with published literature relating to high Fe content alkali-borosilicate glasses as has been primarily reported in<sup>(63,110-111)</sup>. The notable features of this glass, namely the absence of the  $\text{Fe}^{2+}$  optical absorption band and the presence of  $\text{Nd}^{3+}$  optical absorption bands, can be attributed to the HLW simulant waste loading, which lacks the high organic content of the ILW simulant waste, that acts as a carbonaceous reductant, but instead contains rare earth elements, such as Nd. Overall, inspection of Figure 5.1.10 demonstrates that the optical absorption spectra do not present any significant change as a consequence of  $\gamma$ -irradiation.

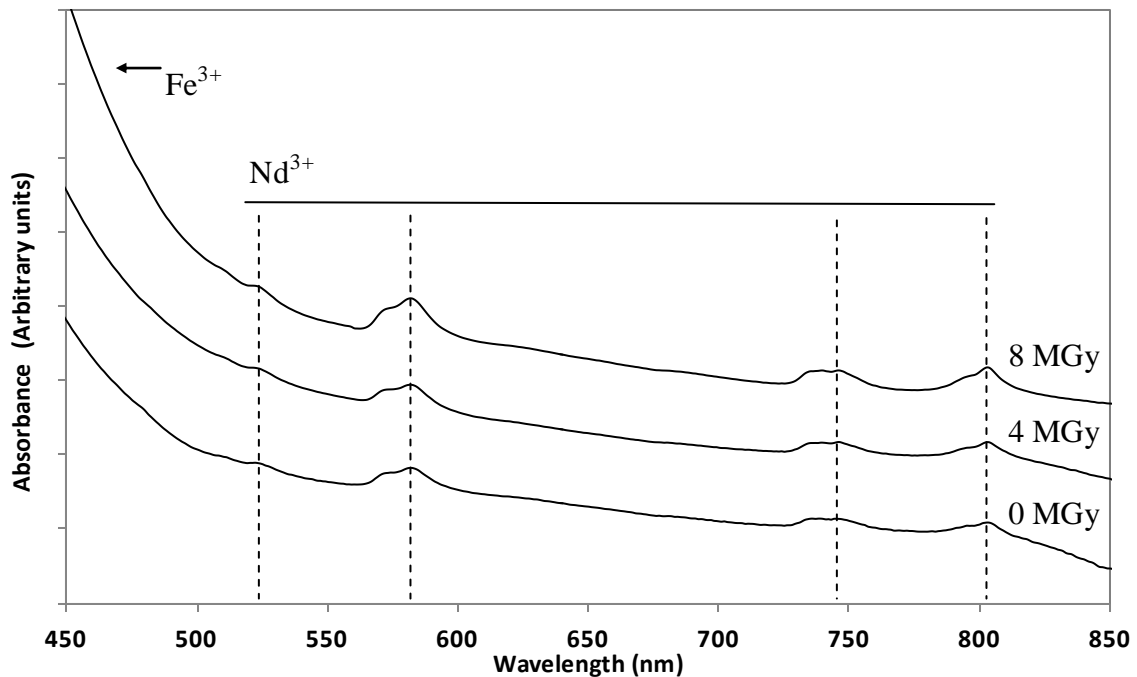
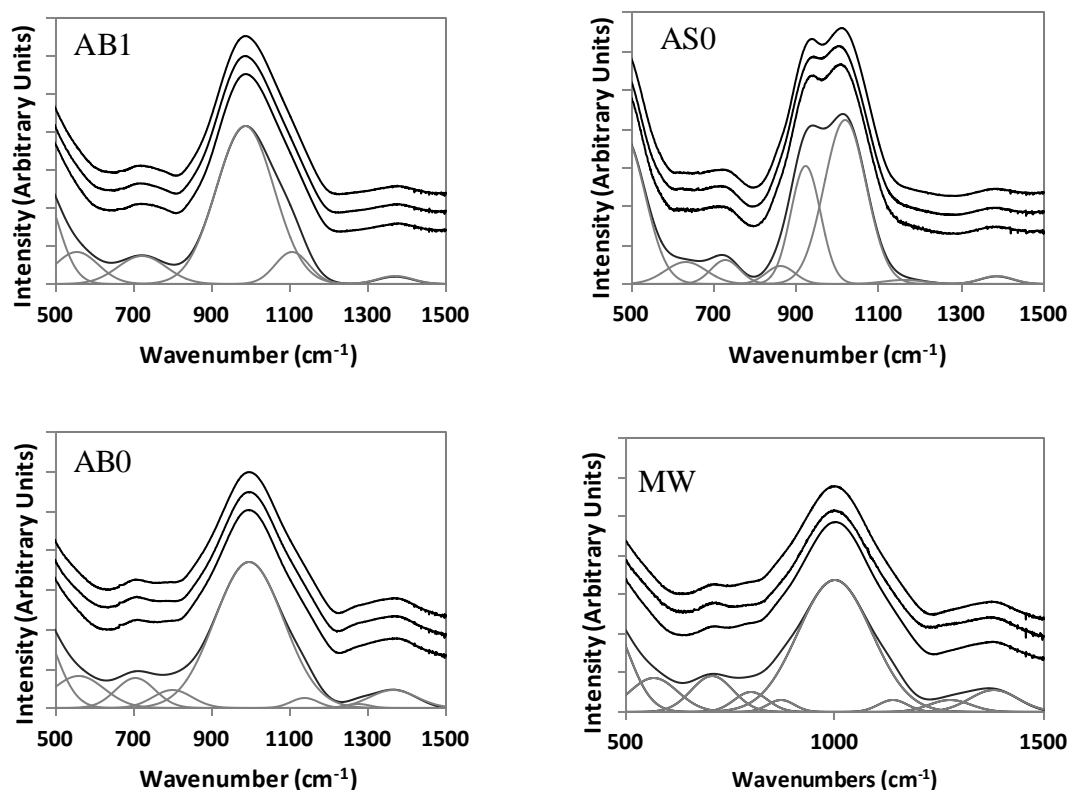


**Figure 5.1.10** Comparison of optical absorption spectra in control (0 MGy) and  $\gamma$ -irradiated (4 and 8 MGy) samples from glass MW-25%. Data are the sum of three optical absorption spectra taken from different areas of a transparent section; for clarity data are offset on the y-axis.

### 5.1.2.2.2 FTIR Spectroscopy

FTIR spectroscopy was applied to probe potential changes in glass structure induced by  $\gamma$ -irradiation. FTIR spectra were fitted using Gaussian line-shapes assigned to well established IR absorption bands, as summarised in Table 5.1.2. Figures 5.1.11 a-d shows the FTIR spectra of the samples and the associated fits, based on assigned bands. The primary absorption bands were associated with Si-O-Si bending and stretching modes ( $\sim 455\text{ cm}^{-1}$  and  $\sim 1000\text{ cm}^{-1}$ ), B-O-B bending and stretching modes associated with  $\text{BO}_3$  units ( $\sim 720\text{ cm}^{-1}$  and  $\sim 1370\text{ cm}^{-1}$ ) and Fe-O bending modes ( $\sim 550\text{ cm}^{-1}$ ). These assignments are in good agreement with previous investigations of alkali-borosilicate glasses<sup>(48-49,70,113-114,117)</sup>, and specifically Fe-rich alkali-borosilicates<sup>(116)</sup>. Additional bands were present in the AB0 and MW-25% glass samples at  $800\text{ cm}^{-1}$  and  $1275\text{ cm}^{-1}$  respectively; these were fitted to B-O-B bending and stretching modes in  $\text{BO}_4$  units<sup>(49,114-115)</sup>. The intensity of this band was observed to be strongly correlated to higher boron content and the presence of  $\text{BO}_4$  units.



**Figures 5.1.11 a-d** Comparison of FTIR spectra in control (0 MGy) and  $\gamma$ -irradiated (4 and 8 MGy) samples. Data are the sum of three FTIR spectra from each sample; for clarity data are offset on the y-axis in order of increasing dose (from 0 to 8 MGy). Bold line corresponds to sum of fitted Gaussian contributions in grey.

**Table 5.1.2** FTIR Band Assignments

Band Position (cm <sup>-1</sup> )	Band Assignment	References
450 - 480	Si-O-Si Bending	(63,110-113)
555 - 560	Fe <sup>3+</sup> -O Stretch	(112-113)
705 - 730	B-O-B (BO <sub>3</sub> ) Bending	(112-114)
798 - 800	B-O-B (BO <sub>4</sub> ) Bending	(112,114)
860 - 870	Si-O-NB Q <sub>0</sub> Stretching	(49)
920	Si-O-NB Q <sub>1</sub> Stretching	(63,115)
985-1020	Si-O-Si Stretching	(49,63,113-115)
1135 - 1160	Si-O-NB Q <sub>3</sub> Stretching	(108,112)
1275	B-O-B (BO <sub>4</sub> ) Stretching	(112-114)
1365 - 1385	B-O-B (BO <sub>3</sub> ) Stretching	(112-114)

The position of the broad Si-O-Si stretching mode of the AB1, AB0 and MW-25% was always within  $7\text{ cm}^{-1}$  of  $992\text{ cm}^{-1}$ , in reasonable agreement with the typical range of  $950\text{--}970\text{ cm}^{-1}$  expected for high Fe alkali-borosilicate glasses<sup>(49,116)</sup>. The appearance of this band is characteristic of a distribution of unresolved  $Q^n$  species. In contrast, glass AS0 presented two well resolved Si-O-Si stretching modes centred at  $921\text{ cm}^{-1}$  and  $1017\text{ cm}^{-1}$ . This implies that the Q speciation of glass AS0 is strongly affected by the alkaline-earth content of the glass, which produces a high proportion of  $Q^2$  units that can be distinguished from the distribution otherwise dominated by the (alkali-associated)  $Q^3$  units typically present in alkali-borosilicate glasses. This conclusion is consistent with available data for related Ba-rich borosilicate glasses<sup>(4)</sup>, in which clearly resolved Si-O-Si stretching modes attributed to  $Q^2$  and  $Q^3$  species were apparent.

Across all four glasses, no significant variation in the distribution of IR bands was apparent between the control (0 MGy) and the  $\gamma$ -irradiated samples. As discussed in Section 5.1.3.2, previous FTIR studies of  $\gamma$ -irradiated alkali borosilicate glasses pointed to a marked change in  $Q^n$  speciation and hence network polymerisation<sup>(106)</sup>. In the present study, however, the lack of detectable change in  $Q^n$  speciation, as a consequence of  $\gamma$ -irradiation, is wholly consistent with the observed invariance in mechanical properties presented in Section 5.1.2.

### 5.1.2.2.3 Raman Spectroscopy

Raman spectroscopy was also applied to probe potential changes in glass structure induced by  $\gamma$ -irradiation. Raman spectra were fitted using Gaussian line-shapes assigned to well established Raman modes, as summarised in Table 5.1.3. Figures 5.1.12 a-d show the Raman spectra of the samples and the associated fits. The most significant Raman bands were related to Si-O-Si stretching modes assigned to specific Q units ( $\sim 871\text{--}1140\text{ cm}^{-1}$ ), Si-O-Si bending modes ( $490\text{ cm}^{-1}$ ), B-O-B stretching modes ( $\sim 1390\text{ cm}^{-1}$ ), to borosilicate ring breathing modes ( $\sim 570\text{ cm}^{-1}$  and  $\sim 650\text{ cm}^{-1}$ ), and  $\text{Fe}^{3+}$ -O stretching modes ( $\sim 920\text{--}945\text{ cm}^{-1}$ )<sup>(79,126-127)</sup>. These band assignments are in good agreement with Raman observations of alkali-borosilicate glasses, and Fe-rich alkali borosilicate glasses<sup>(79,119,121-128)</sup>. In addition to the aforementioned bands, a strong band located at  $990\text{ cm}^{-1}$  was detected in glasses AB1 and AS0, and fitting of data from glass AB0 also indicated a contribution from a band at  $\sim 990\text{ cm}^{-1}$ ; however, this band was absent from the glass MW-25%. The  $990\text{ cm}^{-1}$  band is

attributed to the S-O stretching mode in the  $\text{SO}_4^{2-}$  oxyanion, typically when associated with alkali species such as Na, based on previous reports<sup>(79,118-120,129)</sup>. An additional Raman band was apparent at  $\sim 400\text{ cm}^{-1}$  in the spectra of glasses AB1, AS0, and AB0, which was attributed to the  $\text{Fe}^{3+}\text{-S}^{2-}$  stretch, based on the analysis of Klimm *et al*<sup>(131)</sup> and several mineralogical examples of metal sulphides<sup>(132-134)</sup>. Figure 5.1.13 shows the variation in intensity of the fitted  $400\text{ cm}^{-1}$  band. The absence of the 900 and  $400\text{ cm}^{-1}$  bands in the Raman spectra of MW-25% glass, is consistent with the negligible sulphur content of this composition.

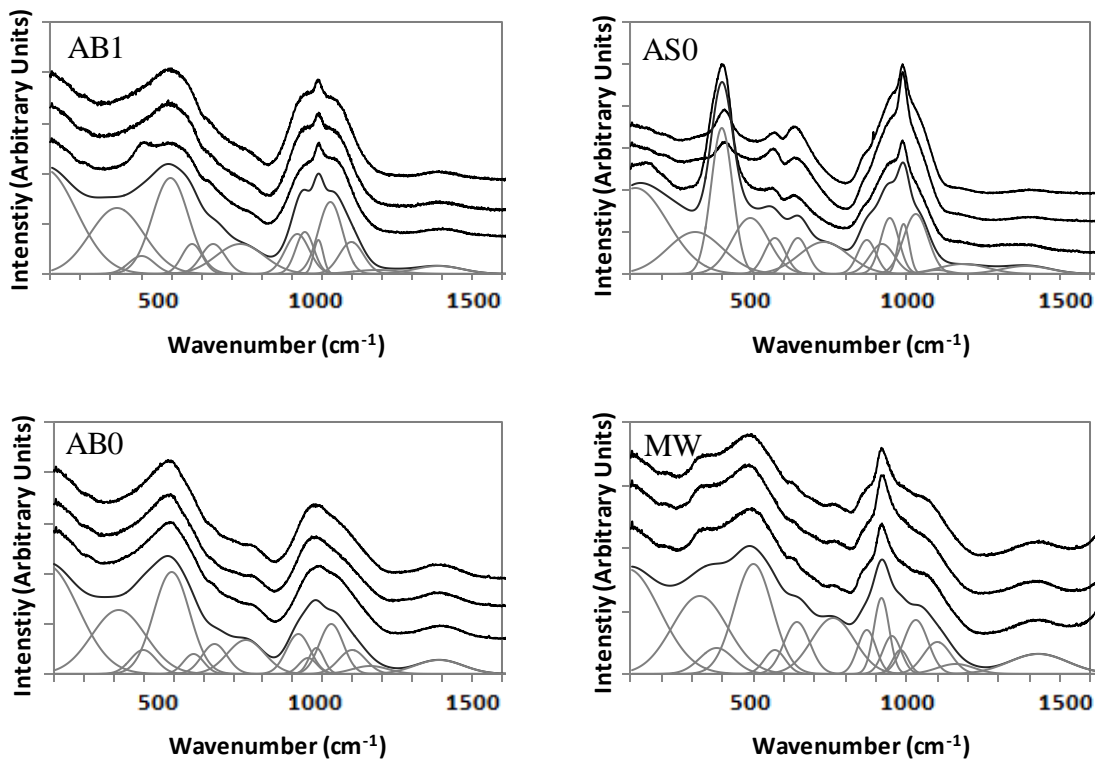


**Figure 5.1.12 a-d** Comparison of Raman spectra in control (0 MGy) and  $\gamma$ -irradiated (4 and 8 MGy) samples. Increasing radiation dose ascending up graph. Data are the sum of three Raman spectra from each sample; for clarity data are offset on the y-axis in order of increasing dose (from 0 to 8 MGy). Bold line corresponds to sum of fitted Gaussian contributions in grey.

**Table 5.1.3** Raman band assignments

Band Position (cm <sup>-1</sup> )	Band Assignment	Reference
400 – 420	Sulphide (Fe <sup>3+</sup> -S <sup>2-</sup> )	(4,48,70,117)
480 – 500	Si-O-Si Bending Mode	(4,79,117,119-122)
570 – 650	Borosilicate Ring Breathing Mode	(4,117,120)
860 – 880	Si-O-Si Stretching Q <sub>1</sub>	(70,119-124)
910 – 930	Si-O-Si Stretching Q <sub>2</sub>	(70,79,119,121-123,125-126)
940 – 950	Fe <sup>3+</sup> -O Stretching	(4,124-125)
990	S-O Stretching (S <sup>6+</sup> )	(48,70,116,124)
1020 – 1040	Si-O-Si Stretching Q <sub>3</sub>	(4,79,117,119-124,126)
1090 – 1110	Si-O-Si Stretching Q <sub>3</sub> '	(4,70,79,117,119,121-124)
1160 – 1180	Si-O-Si Stretching Q <sub>4</sub>	(4,70,79,120-124,126)
1380 – 1400	B-O-B Stretching	(4,79,120)

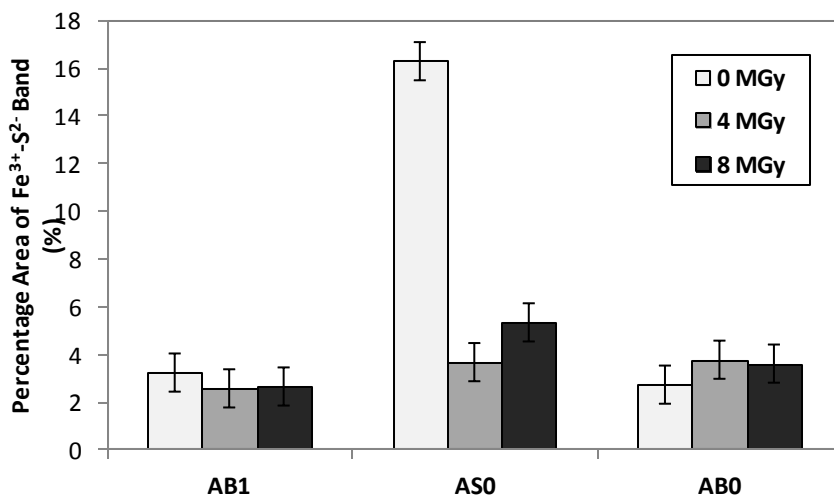


**Figure 5.1.13** Variation in 400cm<sup>-1</sup> band area relative to total fitted area of spectra, between control (0 MGy) samples and  $\gamma$ -irradiated (4 and 8) MGy samples, in glasses AB1, AS0 and AB0. Error bars based on estimated precision of fit.

Comparison between the control glass samples (0 MGy) and the  $\gamma$ -irradiated samples showed no significant variation between the bands associated with Si or B derived modes, associated with the glass network, consistent with the results of FTIR analysis. Comparison of the AS0 control samples and the  $\gamma$ -irradiated samples show significant band variations at 400 cm<sup>-1</sup>. This is clearly reduced in intensity post  $\gamma$ -irradiation, most significantly in glass AS0. This reduction points to a decrease in the volume fraction of the Fe<sup>3+</sup>-S<sup>2-</sup> species as a consequence of  $\gamma$ -irradiation.

#### 5.1.2.2.4 <sup>57</sup>Fe Mössbauer Spectroscopy

<sup>57</sup>Fe Mössbauer spectroscopy was used to quantify any variation in Fe oxidation state in the glasses induced by  $\gamma$ -irradiation. In addition, examination of the dipole and quadrupole splitting associated with the fitted Mössbauer spectra was used to determine the potential change in average Fe coordination induced by  $\gamma$ -irradiation.

Figures 5.1.15 a-d show the Mössbauer spectra for the glasses AB1, AS0 and AB0. The spectra show two convoluted doublet signals, indicating the presence of Fe in mixed valence state in these glasses. Figure 5.1.15 d shows the Mössbauer spectra for the MW-25% glasses, a single doublet was apparent, showing only Fe<sup>3+</sup> is present in these materials. Figure 5.1.14 shows the relative quantity of Fe<sup>2+</sup> relative to the overall Fe content of the glasses, as derived from the areas of the fitted Lorentzian line-shapes, which can be assigned to Fe<sup>2+</sup> or Fe<sup>3+</sup> species. Comparison of the three glasses shows that glass AS0 has a volume fraction of Fe<sup>2+</sup> that is 25% greater than AB1 or AB0. These results are in line with prior expectation, as glasses loaded with highly reducing organic waste (AB1, AS0 and AB0) contain partially reduced Fe, whereas Fe in the MW-25% glass is fully oxidised due to the absence of organic reducing agents in the simulant HLW. The higher extent of Fe reduction in AS0 can be linked to the lower content of Fe in this glass compared to AB1 or AB0, relative to the waste loading which was equivalent across all three glasses.

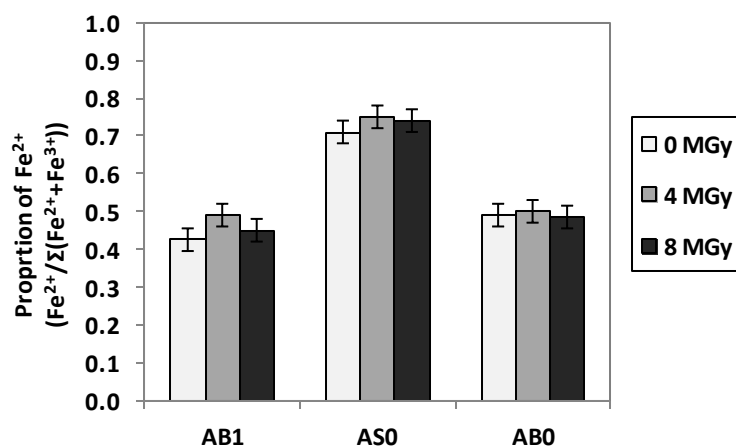
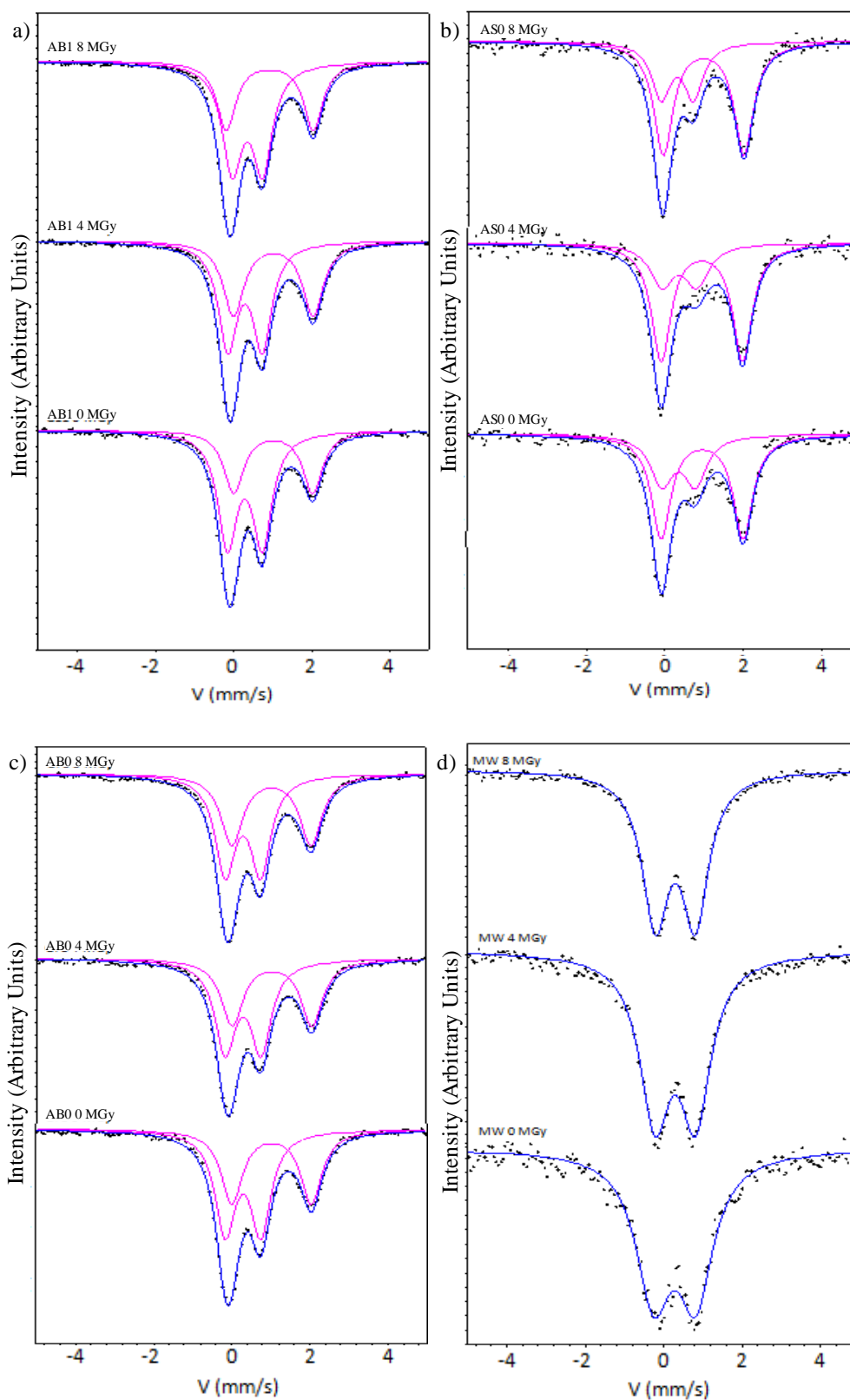


**Figure 5.1.14** Comparison of Fe oxidation state in control (0 MGy) and  $\gamma$ -irradiated (4 and 8 MGy) glasses. Derived from Lorentzian fitting of Mössbauer spectra. Error bar represents three standard deviations, derived from three independent measurements.



**Figures 5.1.15 a-d** Comparison of  $^{57}\text{Fe}$  Mossbauer data (solid points) in control (0 MGy) and  $\gamma$ -irradiated (4 and 8 MGy) samples fitted with Lorentzian line-shapes (lines).

Figure 5.1.14 also shows a comparison of the extent of Fe reduction in the control samples (0 MGy) against the  $\gamma$ -irradiated samples. There was no significant change in the Fe oxidation state between the control and the  $\gamma$ -irradiated samples, within the estimated limits of error, consistent with a previous Mössbauer study of the effect of  $\gamma$ -irradiation on Fe redox in borosilicate glasses<sup>(100)</sup>. The errors described were determined from the standard deviation of the peak areas of three independent measurements.

Figure 5.1.16 shows the average dipole ( $\delta$ ) and quadrupole ( $\Delta$ ) splitting of the  $\text{Fe}^{2+}$  and  $\text{Fe}^{3+}$  species present in the samples, based upon the Lorentzian fitting of the spectra. The splitting values for the  $\text{Fe}^{2+}$  environment in all samples shows there is no significant change within the estimated error across the range of  $\gamma$ -radiation doses. The splitting values for  $\text{Fe}^{3+}$  sites in the glasses AB1 and AB0 also show no measurable change within the estimated errors across the range of  $\gamma$ -irradiation doses.  $\text{Fe}^{3+}$  environments within the MW-25% glass present a statistically significant decrease in quadrupole splitting ( $0.10 \pm 0.02$  mm/s) with  $\gamma$ -irradiation between 0 MGy and 4 MGy, no subsequent variation is apparent, within the limits of precision.  $\text{Fe}^{3+}$  environments in glass AS0 present no significant variation in coordination between 0 MGy and 4 MGy, within the estimated errors, however a significant decrease in quadrupole splitting is apparent between 4 MGy and 8 MGy ( $0.11 \pm 0.02$  mm/s). The results in AS0 and MW-25% results are consistent with investigation of Eissa *et al.*<sup>(100)</sup>, which reported comparable changes in  $\text{Fe}^{3+}$  quadrupole splitting in Fe rich Na-borosilicate glasses as a consequence of  $\gamma$ -irradiation.

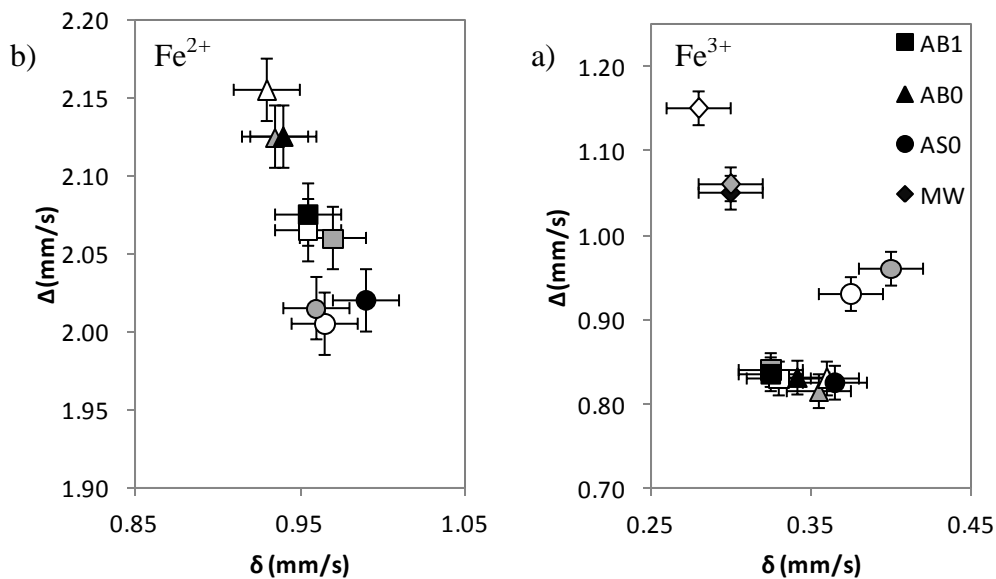


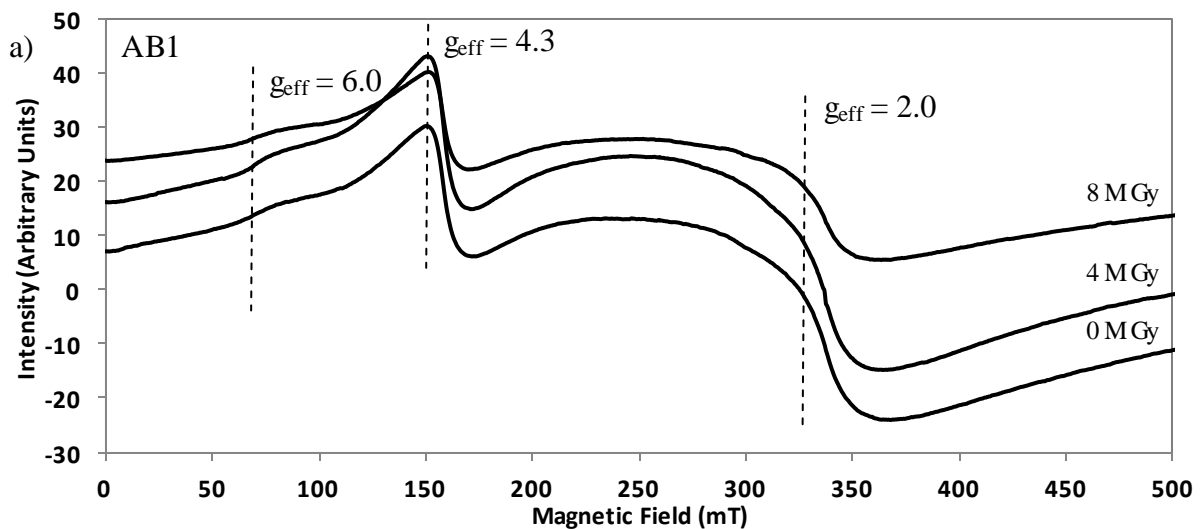
**Figure 5.1.16 a,b** Comparison of Fe dipole ( $\delta$ ) and quadrupole ( $\Delta$ ) splitting in control (0 MGy) and  $\gamma$ -irradiated (4 and 8 MGy) glasses; open, grey and black symbols correspond to

dose of 0, 4, and 8 MGy, respectively. Errors derived from the standard deviation of results associated with the fitting of three individual experiments

### 5.1.2.2.5 EPR Spectroscopy

EPR spectroscopy was used to probe defects produced by the process of  $\gamma$ -irradiation within the glasses. In addition EPR spectroscopy allowed the  $\text{Fe}^{3+}$  environment to be studied, and other paramagnetic species to be detected.

Figure 5.1.17 shows the EPR spectra for the glasses AB1, AS0 and AB0 unirradiated (0 MGy) and  $\gamma$ -irradiated (4 and 8 MGy). Previous studies of  $\gamma$ -irradiated alkali-borosilicate<sup>(135)</sup> reported the presence of boron based oxygen hole centres (BOHCs) identified by a strong and sharp EPR signal near  $g_{\text{eff}} \approx 2.0$ , these signals are absent from the EPR spectra of the  $\gamma$ -irradiated glasses reported here, in both the broad scans shown in Figure 5.1.17 and in high resolution scans of the  $g_{\text{eff}} \approx 2.0$  region. Olivier *et al.* reported that EPR signals associated with BOHCs, generated by ionising  $\beta$  radiation, decrease in intensity in proportion to increasing Fe content<sup>(136)</sup>. Thus, the absence of sharp signals at  $g_{\text{eff}} \approx 2$  in the plots displayed in Figure 5.1.17 may be a consequence of the Fe mediated healing of such defects, as discussed in Section 5.1.3.3.



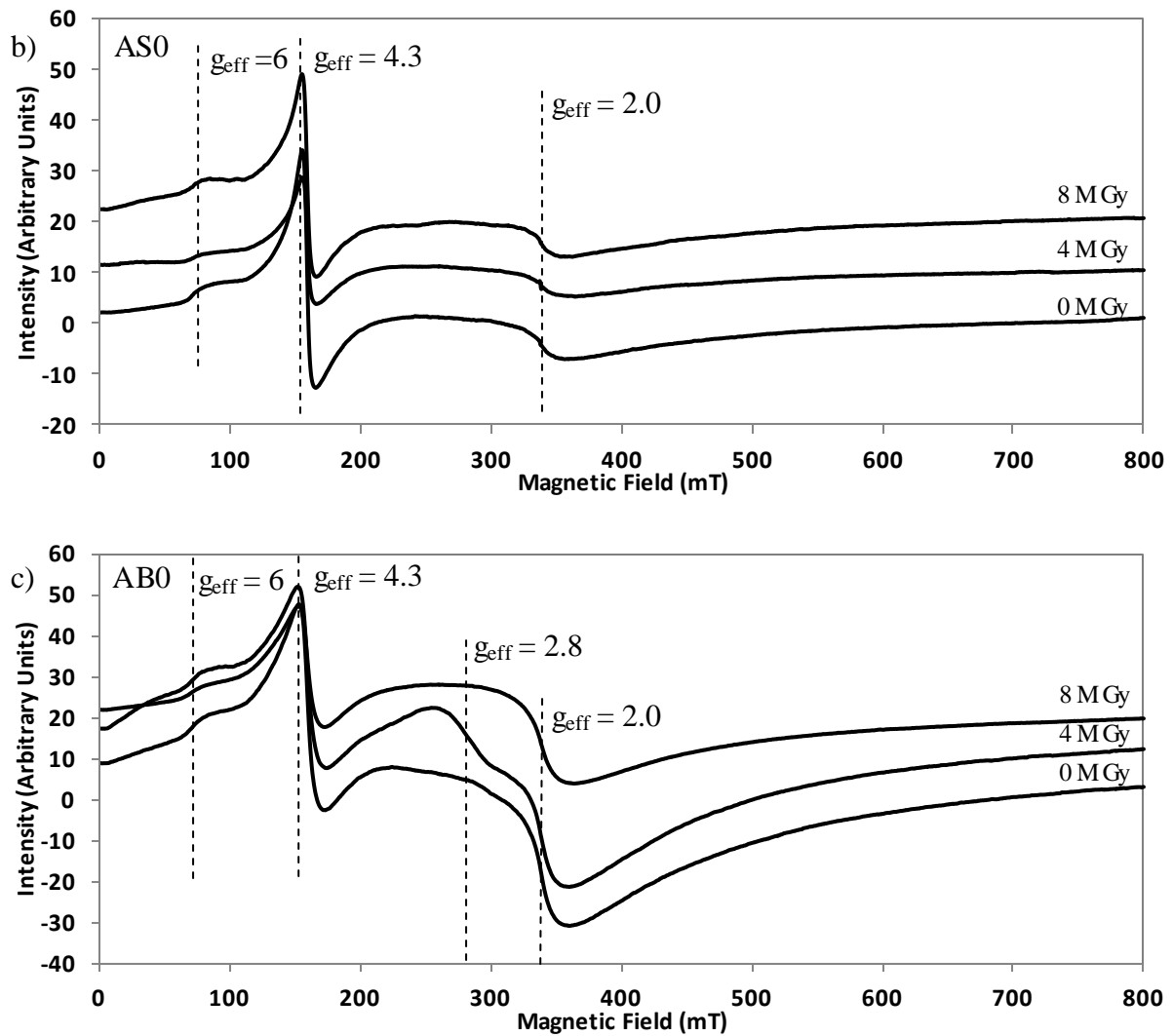


**Figure 5.1.17 a-c** Comparison of EPR spectra in control (0 MGy) and  $\gamma$ -irradiated (4 and 8 MGy) samples from glass AB1, AS0 and AB0.

Two intense but broad EPR signals were detected from all samples at  $g_{\text{eff}} \approx 2.0$  and  $g_{\text{eff}} \approx 4.3$ . The signal at  $g_{\text{eff}} \approx 2.0$  was unrelated to the signature signal of BOHCs. These signals have been attributed to the  $\text{Fe}^{3+}$  species, specifically to  $\text{Fe}^{3+}$  in clustered regions in which  $\text{Fe}^{3+}$  atoms are in close enough proximity for exchange interactions to dominate, or to regions in which  $\text{Fe}^{3+}$  is in isolated distorted tetrahedral or octahedral sites for  $g_{\text{eff}} \approx 2.0$  and  $g_{\text{eff}} \approx 4.3$  respectively. A further signal was evident in the glasses at approximately  $g_{\text{eff}} \approx 6.3$  which has also been attributed to  $\text{Fe}^{3+}$  environments, ostensibly in which one or more coordinating anion is not  $\text{O}^{2-}$ . Therefore, this signal may be associated with the  $\text{Fe}^{3+}\text{-S}^{2-}$  species, although a definite connection has not been proven<sup>(63)</sup>. The presence of these signals is in general agreement with established knowledge for Fe containing borosilicate glasses<sup>(133-137)</sup>.

Table 5.1.4 shows the intensity ratio of the  $g_{\text{eff}} \approx 2.0$   $\text{Fe}^{3+}$  signal against the  $\text{Fe}^{3+}$   $g_{\text{eff}} \approx 4.3$ , for each EPR spectrum, determined based upon the assumption that there is no significant change in the width of the observed EPR peaks. By analysing the peak to peak intensity ( $I_{\text{p-p}}$ ) of the  $\text{Fe}^{3+}$  signal the variation in  $\text{Fe}^{3+}$  environment and distribution of  $\text{Fe}^{3+}$  environments can be quantified for each sample. The reported variations in  $I_{\text{p-p}}$  between the three glasses are in good agreement with work conducted by Bingham *et al.* <sup>(139)</sup> and can be attributed to the quantity and ionic radius of alkali and alkaline-earth species which are present in glass compositions. The presence of alkali ions in the glass can be linked to the increase in the prevalence of  $\text{Fe}^{3+}$  in clustered sites, increasing the signal at  $g_{\text{eff}} \approx 2.0$ . This correlates with the known compositions of the AB1 and AB0 samples, where increased Na content in AB1 leads to an increase in  $g_{\text{eff}} \approx 2.0$  relative to  $g_{\text{eff}} \approx 4.3$ . The AS0 results show a weak  $g_{\text{eff}} \approx 2.0$  signal relative to  $g_{\text{eff}} \approx 4.3$ , this is attributable to the high Ba content of this glass, since large alkaline-earth ions have been identified as being less effective at causing  $\text{Fe}^{3+}$  cluster formation (63).

In comparing the  $I_{\text{p-p}}$  results, which are presented in Table 4, for the control glass (0 MGy) and the  $\gamma$ -irradiated glasses (4 and 8 MGy) it can be seen that there is no significant variation in  $I_{\text{p-p}}$  in response to  $\gamma$ -radiation. A unique signal was noted in the 4 MGy sample of AB0 at  $g_{\text{eff}} \approx 2.8$ . Possible explanations for this signal are that it is related to ferro-magnetic inclusions present in the glass <sup>(140)</sup>, the presence of anti-ferromagnetic coupling between  $\text{Fe}^{3+}$  and  $\text{Fe}^{2+}$  <sup>(138)</sup>, both of which are present in these glasses, or the presence of a high symmetry  $\text{Fe}^{3+}$  resonant centre <sup>(141)</sup>.

**Table 5.1.4** Peak to peak intensity ratio variation across radiation doses. Derived from EPR spectra. Errors derived from systematic errors based on estimation of peak intensity.

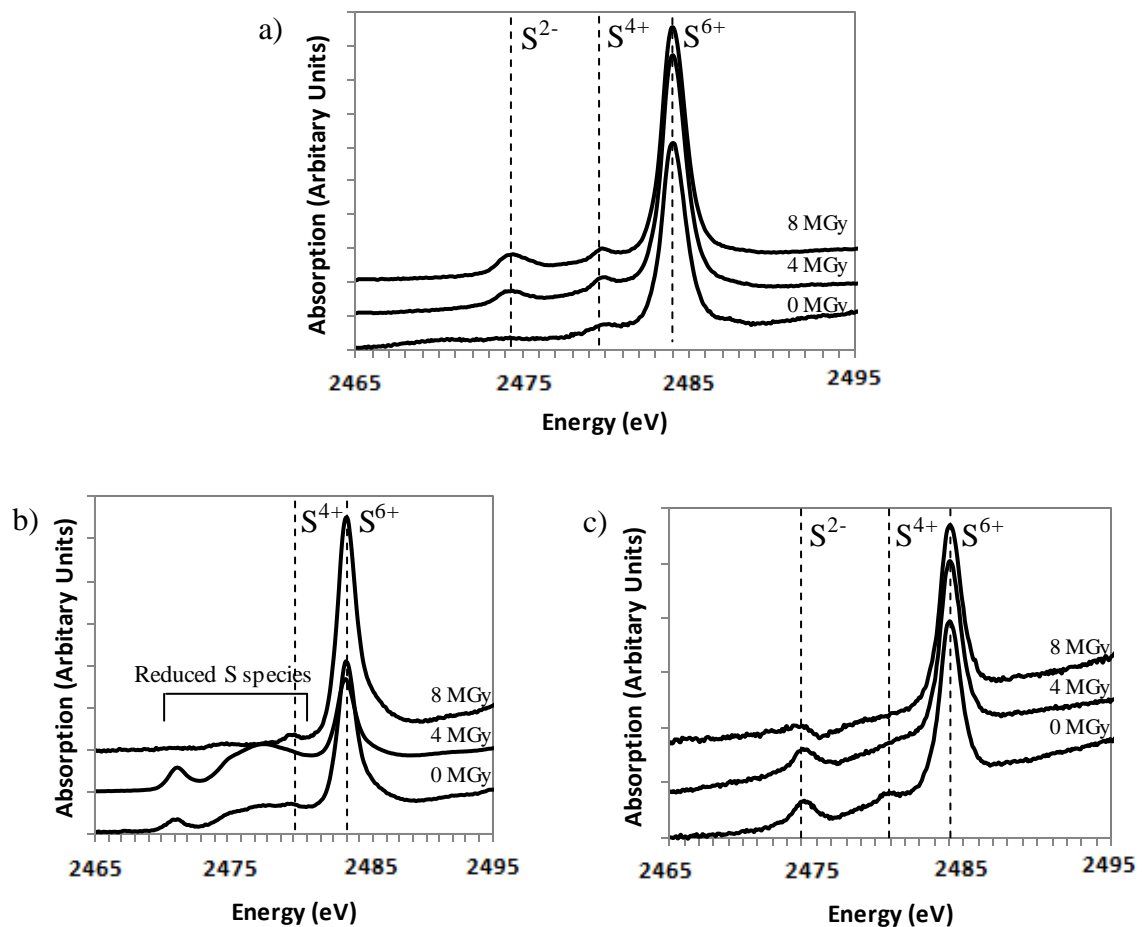
Glass	Intensity Ratio $I_{\text{p-p}}$ ( $g_{\text{eff}} \approx 2$ / $g_{\text{eff}} \approx 4.3$ )		
	0 MGy	4 MGy	8MGy
<b>AB1</b>	$1.54 \pm 0.10$	$1.40 \pm 0.10$	$1.24 \pm 0.10$
<b>AS0</b>	$0.18 \pm 0.10$	$0.23 \pm 0.10$	$0.15 \pm 0.10$
<b>AB0</b>	$0.77 \pm 0.10$	$0.99 \pm 0.10$	$0.82 \pm 0.10$

### 5.1.2.2.6 X-ray absorption spectroscopy

X-ray absorption spectroscopy and X-ray emission spectroscopy at the sulphur K-edge were applied in order to determine the oxidation state and environment of sulphur within the glasses AB1, AS0 and AB0. The MW-25% set was excluded as it contained a negligible quantity of sulphur.

Figure 5.1.18 shows the X-ray absorption spectra for the three glasses over the XANES (X-ray Absorption Near Edge Structure) region. The spectra are the result of a convolution of two or more absorption spectra relating to sulphur in different oxidation states. The strong feature present in all spectra at 2482 eV is related to sulphur in the S<sup>6+</sup> oxidation state in good agreement with both sulphate standards and with the work of Bingham *et al.*<sup>(139)</sup>. The features present from 2468 – 2472 eV are associated with sulphur in a more reduced environment matching closely to spectra of sulphide (S<sup>2-</sup>) standards reported by Bingham *et al.*<sup>(139)</sup>. It is probable the intermediate oxidation states of sulphur are present in these spectra, such as sulphite (S<sup>4+</sup>) which can be attributed to the weak feature present at ~2478 eV<sup>(139)</sup>. The pre-edge and edge region of the X-ray absorption spectra were fitted to a range of sulphur standards in an effort to identify a chemical analogue for the interaction of the reduced sulphur with the glass. However, fitting was inadequate for the quantification of the sulphur oxidation state due to strong post-edge features seen with the sulphur standards, which were absent in the glass spectra.

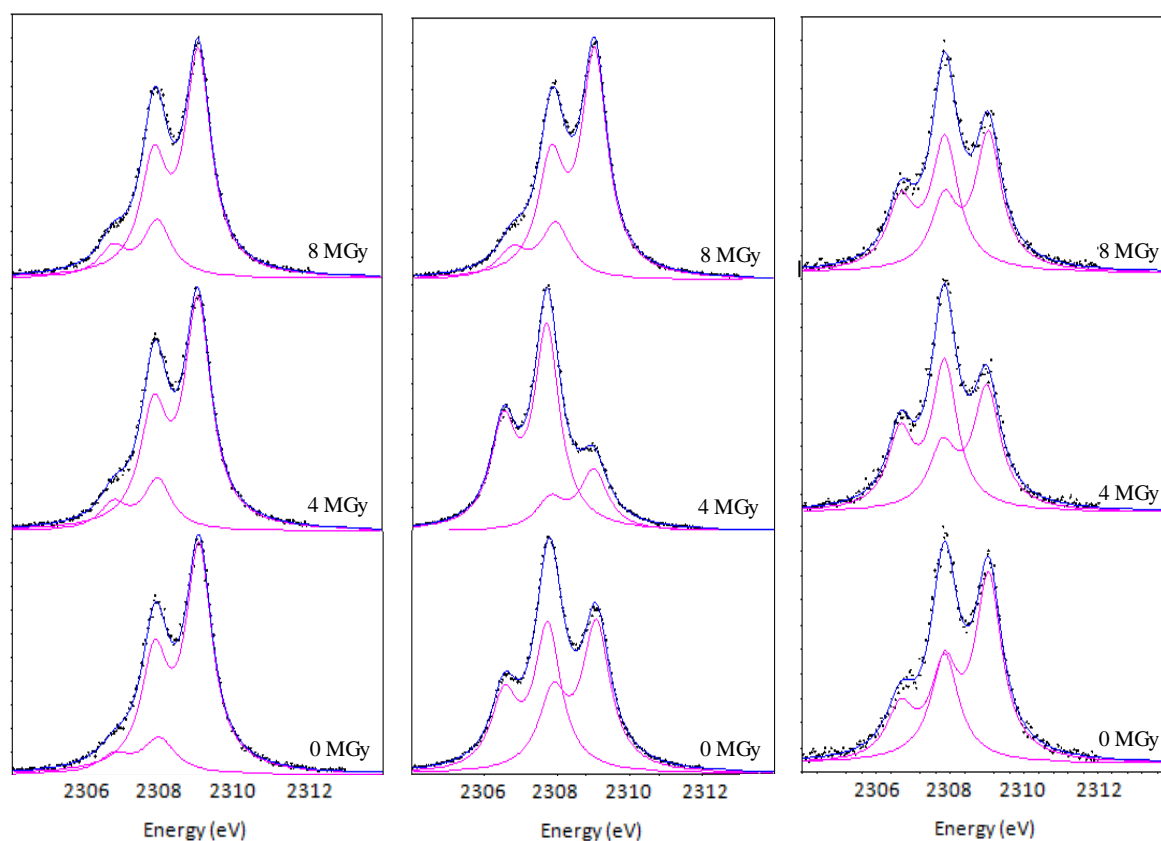
The features associated with reduced sulphate species in glass AS0 are notably different to those observed in AB1 and AB0. The features associated with reduced sulphur species in AB1 and AB0 approximately match those of As<sub>2</sub>S<sub>3</sub>, implying the presence of sulphide (S<sup>2-</sup>)<sup>(139)</sup>. The features associated with reduced sulphur species in glass AS0 approximately match the spectra of the CuFeS<sub>2</sub> and CuFeS<sub>4</sub><sup>(139)</sup>. The features observed in the case of the AS0 glass show good agreement with observations made by Backnaes *et al.*<sup>(142)</sup> which proposed sulphur coordination to transition metals. This suggests that the reduced sulphur species present in the AS0 glass may be coordinated to the glass network via a transition metal atom, most probably Fe, and that they are in the sulphide oxidation state (S<sup>2-</sup>). This is consistent with Raman spectroscopy results discussed in Section 5.1.4.2.



**Figure 5.1.18 a-c** Comparison of S K-edge XANES spectra in control (0 MGy) and  $\gamma$ -irradiated (4 and 8 MGy) samples from glass AB1, AS0 and AB0.

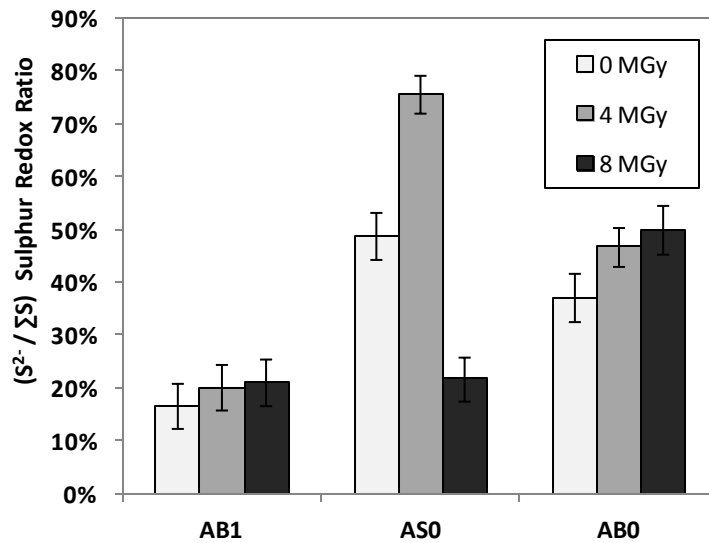
#### 5.1.2.2.7 X-ray emission spectroscopy

Figure 5.1.19 a-c shows the XES data collected for the control (0 MGy) samples compared with those from the  $\gamma$ -irradiated (4 and 8 MGy) samples. The proportion of reduced sulphur species can be seen to vary in all three glasses in response to  $\gamma$ -irradiation. This variation cannot be quantified by fitting of the XANES region which is more sensitive to the local co-ordination environment, in contrast to XES<sup>(108-109)</sup>. Figure 5.1.19 shows the X-ray emission spectra for the three glasses and the fitted Lorentzian line shapes. The intensity ratio of the  $K\alpha_{1,2}$  doublets fitted to the spectra was constrained to be constant.



**Figure 5.1.19 a-c** Comparison of XES spectra in control (0 MGy) and  $\gamma$ -irradiated (4 and 8 MGy) samples fitted with Lorentzian line-shapes.

Figure 5.1.20 shows the proportion of  $S^{2-}$  relative to the overall proportion of sulphur in the glasses AB1, AS0 and AB0 across all  $\gamma$ -irradiation doses. In the glass AB1 no variation is apparent within the estimated limits of error, whereas in glass AS0 and AB0 a clear variation in the sulphur oxidation state is apparent, which is consistent with the qualitative XAS observations. Glass AB0 shows a linear increase in the proportion of  $S^{2-}$  with respect to the applied radiation dose, whereas glass AS0 shows a non-linear trend with an increase in  $S^{2-}$  from 45 % to 71 % at 4 MGy, with a decrease to 13 % at 8 MGy (estimated precision of  $\pm 5\%$ ). This trend parallels the observed variation in colour observed in the powdered samples, increasing in the order 8MGy < 0 MGy < 4MGy. Variations in sulphur oxidation state induced by  $\gamma$ -irradiation have not been previously reported to the best of our knowledge.



**Figure 5.1.20** Comparison of S oxidation state in control (0 MGy) and  $\gamma$ -irradiated (4 and 8 MGy) glasses. Derived from Lorentzian fitting of XES spectra. Error values determined from standard deviations of three fitted spectra.

## 5.1.3 Discussion

### 5.1.3.1 Mechanical property variation.

Comparison of the mechanical properties of the control glass samples (0 MGy) against the  $\gamma$ -irradiated samples, Section 5.1.2, showed that there is no significant change in Young's modulus, shear modulus, hardness or fracture toughness. This behaviour is not typically observed in simplified alkali-borosilicate compositions, where  $\gamma$ -irradiation typically results in increased density with concomitant change in the mechanical properties<sup>(106)</sup>. According to Shelby *et al.*<sup>(106)</sup>, such an increase in density arises from an increase in the degree of network polymerisation induced by  $\gamma$ -irradiation, although the mechanism has not been fully elucidated. Boizot has linked similar effects observed as a result of  $\beta$ -radiation to the migration and clustering of alkali species within the glass<sup>(143)</sup>. Such changes in network polymerisation would be expected to be apparent in both FTIR and Raman spectra, however, as discussed in Section 5.1.3, the FTIR and Raman spectra present no evidence for a change

in network polymerisation induced by  $\gamma$ -irradiation, consistent with the invariance in mechanical properties.

### 5.1.3.2 Glass structure variation as detected by Raman and FTIR spectroscopy.

Fitting of FTIR and Raman spectra revealed no significant change between the control and  $\gamma$ -irradiated glass samples. Therefore it can be concluded that  $\gamma$ -irradiation does not induce a significant change in Q speciation up to a dose of 8 MGy. Fe has previously been linked to negating the deleterious effect of  $\gamma$ -irradiation<sup>(98,134,136)</sup>, consistent with the mechanical property results, which are determined by the silicate network polymerisation in the glass.

In considering Raman bands associated with  $\text{Fe}^{3+}\text{-S}^{2-}$  bonds in AS0 glass, a marked decrease in the  $400\text{ cm}^{-1}$  band was observed with increasing dose applied to AS0 glass, implying a decrease in the volume fraction of the  $\text{Fe}^{3+}\text{-S}^{2-}$  species. Klimm *et al.*<sup>(131)</sup> indicate that this Raman band is uniquely associated with the  $\text{Fe}^{3+}\text{-S}^{2-}$  species. Consequently, this result does not necessarily indicate a decrease in the overall proportion of  $\text{S}^{2-}$  species, for which there is no evidence from S XES data. This is further supported by the invariant relative intensity of the stretching mode at  $990\text{ cm}^{-1}$  band, characteristic of  $\text{SO}_4^{2-}$  species, which is inconsistent with significant oxidation of  $\text{S}^{2-}$  species.

### 5.1.3.3 Fe analysis by optical absorption, EPR and Mössbauer spectroscopy.

As shown in section 5.1.2.2 no evidence of paramagnetic defects, such as boron oxygen hole centres, were detected by EPR spectroscopy. However, EPR experiments did provide information about  $\text{Fe}^{3+}$  species in the control glasses, through variation in the intensity ratio of the  $g_{\text{eff}} = 2.0$  and  $g_{\text{eff}} = 4.3$  signals. This variation was attributable to the glass compositions, and is in good agreement with Bingham *et al.*<sup>(63)</sup>. However, no significant variation in the intensity ratios in relation to radiation could be ascertained.

Figure 5.1.15 shows that there is no significant variation in the overall Fe oxidation state, in response to  $\gamma$ -irradiation, within the estimated errors, in agreement with the study of Eissa *et al.*<sup>(100)</sup>.

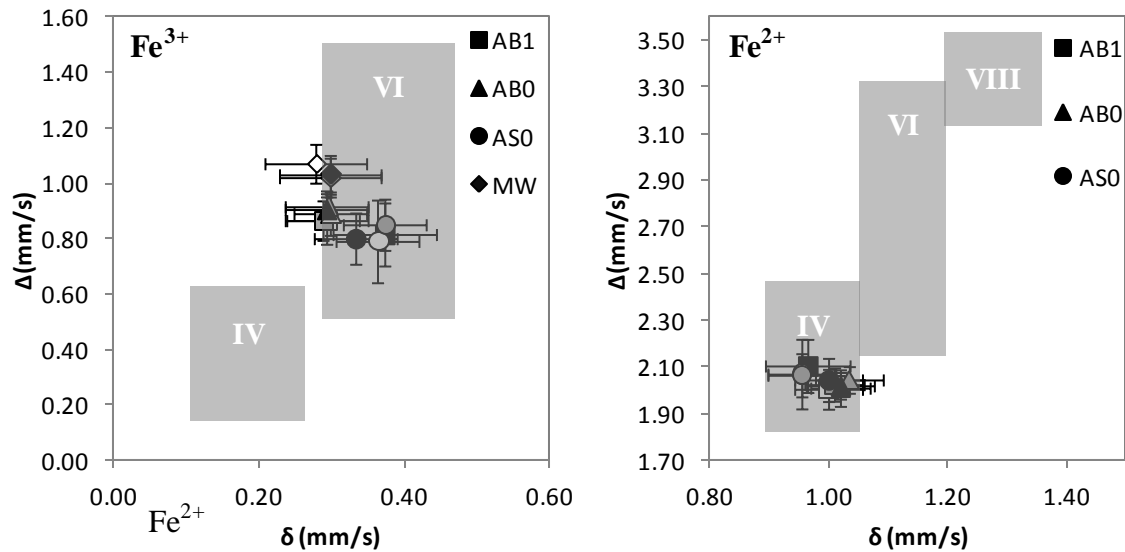


**Figure 5.1.21 a-b** Comparison of Fe dipole ( $\delta$ ) and quadrupole ( $\Delta$ ) splitting in control (0 MGy) and  $\gamma$ -irradiated (4 and 8 MGy) glasses; open, grey and black symbols correspond to dose of 0, 4, and 8 MGy, respectively. Errors derived from the standard deviation of results associated with the fitting of three individual experiments

Figure 5.1.21 shows the dipole and quadrupole splitting values for the fits of the  $\text{Fe}^{2+}$  and  $\text{Fe}^{3+}$  environments superimposed onto the speciation plot devised by Dyar<sup>(71)</sup>, highlighting the features associated with the tetrahedral and octahedral coordination environments. In all glasses it is apparent that  $\text{Fe}^{2+}$  is present in 4-fold coordination sites and  $\text{Fe}^{3+}$  species are present in 6-fold coordination sites.  $\text{Fe}^{2+}$  splitting parameters were unaffected by  $\gamma$ -irradiation, however  $\text{Fe}^{3+}$  quadrupole splitting results glasses for AS0 and MW-25% glasses showed a decrease in quadrupole splitting in proportion to increasing  $\gamma$ -irradiation. This suggests a decrease in the average population of  $\text{Fe}^{3+}$  in 6-fold coordination in these glasses, and an increased average population of  $\text{Fe}^{3+}$  in 4-fold coordination.

Furthermore, in comparing the magnitude of the change in the S oxidation state against the Fe content, per unit S, of the AB1, AS0 and AB0 glasses it can be seen that there is a strong correlation between the Fe content of the glass and the extent of sulphur reduction. This is shown in figure 5.1.22. This implies that the presence of Fe reduces the extent of S reduction in these glasses.

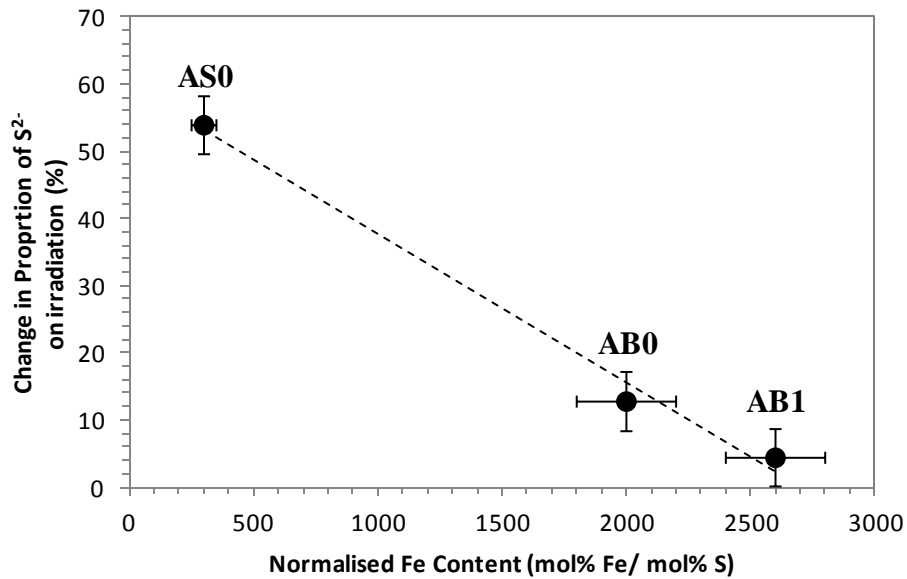
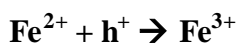
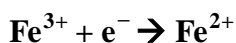


Figure 5.1.22 Variation in S oxidation state change across normalised Fe content in AS0, AB0 and AB1.

Overall, the combined mechanical property and spectroscopic data support the mechanism first suggested by Debnath *et al.* <sup>(6)</sup> for the remediation of  $\gamma$ -radiation induced defects by the capture of excitons between Fe oxidation states. In this mechanism, effective annihilation of the excitons, i.e. holes and electrons generated by  $\gamma$  irradiation, is achieved by the following redox couple.



Assuming this mechanism to operate in the present study would explain the absence of significant induced changes in glass structure and hence physical properties, preventing the accumulation of radiation induced defects. The mechanism enables the coordination environment of the Fe to undergo a relaxation, for which evidence has been gleaned from the decreased quadrupole splitting observed by Mössbauer spectroscopy, and which has been previously reported <sup>(100)</sup>.

Optical absorption spectroscopy identified the presence of Fe related absorption bands in all four glasses, including a band associated with  $\text{Fe}^{2+}$ -O- $\text{Fe}^{3+}$  inter-valence interactions.

Note that the invariance of these absorption bands and Fe redox determined by Mössbauer spectroscopy cannot provide an explanation for the observed variation in colour in glass AS0. However, a correlation between the proportion of  $S^{2-}$ , as determined by XES, and the observed variation in colour of AS0 glasses was apparent. The  $Fe^{3+}-S^{2-}$  species (the amber chromophore) is known to be optically absorbing at wavelengths of  $415\text{ cm}^{-1}$  and provides a possible explanation for the observed colouration<sup>(139)</sup>. However, further evidence is required to support the presence of this species in the glass AS0.

#### 5.1.3.4 X-ray absorption and X-ray emission spectroscopy at the S K-edge.

The X-ray absorption and X-ray emission experiments conducted on glass AB1 showed no significant change in sulphur oxidation within the estimated error. However, glasses AB0 and AS0 both exhibited a variation in sulphur oxidation, most strongly in AS0. The glass MW-25% was not included in these experiments due to its negligible sulphur content. The changes can be attributed to the capture of electrons and holes generated by the  $\gamma$ -radiation, based on the mechanism that has been proposed by Debnath *et al.*<sup>(6)</sup>. The  $S^{2-}$ ,  $S^{4+}$  and  $S^{6+}$  oxidation states have been identified in the glasses by the comparison of XANES results to sulphur reference standards, but other sulphur oxidation states may also be present. The variation in sulphur reduction in the glasses can be related to the compositional variations present in the glasses. The Fe content of these three waste-forms decreases in the order AB1 > AB0 > AS0, whereas the sulphur content increases in the order AB1 = AB0 < AS0. Therefore it is possible that the greater change in sulphur oxidation state observed in AS0, and to a lesser extent AB0 are the result of the sulphur being exposed to a higher proportion of  $\gamma$ -radiation derived excitons which are otherwise annihilated by the more abundant Fe species in glass AB1. S is preferentially reduced by the  $\gamma$ -radiation induced excitons over Fe as it is known to be more susceptible to chemical reduction, according to the work of Schreiber *et al.*<sup>(144)</sup>.

The atypical results observed in glass AS0 can be explained by the increased incidence of reduced glass components occurring in AS0 control sample (0 MGy) in which both  $S^{2-}$  and  $Fe^{2+}$  are more populous than in the other control samples. This explains the increased extent of sulphur reduction, as the extent of sulphur reduction appears to correlate with the Fe content of the glass. The oxidative step seen at 8 MGy in glass AS0, which is atypical of the observations made of the other glasses, provides evidence of two competing processes occurring with regards to sulphur oxidation state in response to  $\gamma$ -irradiation. This may be linked to either the environment in which the samples were irradiated or phase

separation occurring at high  $\gamma$ -radiation doses. However, there is insufficient evidence to suggest a likely cause in the reported results, and further work is required.

#### 5.1.4 Conclusion

This work has shown that  $\gamma$ -radiation produces no significant change in mechanical properties of the waste-form materials studied, up to 8 MGy, within the precision of the techniques applied. Similarly,  $\gamma$ -irradiation was found to have no significant effect on the glass network as detected through Raman and FTIR spectroscopy, within the precision of the techniques. This has been attributed to the presence of a significant proportion of iron within the glass compositions, which has been identified as providing a mechanism to heal radiation induced defects in glasses of similar compositions <sup>(6,135,137)</sup>. Mossbauer and EPR spectroscopies provided evidence for a small degree of change in Fe coordination environments within the glasses. This supports the mechanism proposed by Debnath *et al.* <sup>(6)</sup> by which excitons produced by the incident  $\gamma$ -radiation are trapped or annihilated by the capture of electrons and holes by individual Fe<sup>2+</sup> and Fe<sup>3+</sup> sites. This produces no net change in Fe oxidation state due to the equal oxidation and reduction of the Fe, but causes minor variations in Fe environment.

Variation in sulphur oxidation state was observed in glasses AS0 and AB0. This was attributed to  $\gamma$ -radiation induced reduction or oxidation of coordinated sulphur. A dependence on redox state was observed to influence the variations observed and was most apparent in glass AS0. The presence of the Fe<sup>3+</sup>-S<sup>2-</sup> species was implied by Raman and optical absorption spectroscopy result in glass AB1, AS0 and AB0. Raman spectroscopy showed that this species was eliminated by incident  $\gamma$ -radiation in glass AS0, which can be connected to the effect of  $\gamma$ -radiation upon S and Fe species within the glass.

These results support past observations of Fe rich alkali-borosilicate exposed to  $\gamma$ -irradiation <sup>(96-97,100,137)</sup> and parallel observation made in  $\beta$ -radiation experiments <sup>(136)</sup>. However, the data differs from observations of alkali-borosilicate glasses with low Fe contents, such as Pyrex and the MW-25% base glass, in which a correlation exists between  $\gamma$ -radiation dose and changes of mechanical properties and defect formation <sup>(97)</sup>. This indicates that the presence of Fe in these glasses, which is present due either to waste loading or for waste compatibility reasons, has a significant and positive effect on the resistance of the waste-form to  $\gamma$ -irradiation. Finally it may be concluded that  $\gamma$ -radiation does not have a significant deleterious effect on the mechanical stability or composition of simulant inactive UK ILW and HLW glasses, up to the dose of 8 MGy.

## **Chapter 5.2 - Investigation of the Durability of Novel Glass Compositions Developed for the Purpose of Cs loaded Ion Exchange Resin Vitrification.**

This section considers a number of glass compositions that have been developed for the vitrification of IEX resins wastes, which were discussed in chapter 3. These compositions have the capacity to better withstand the detrimental effects of reduction and retain a larger proportion of the anionic species from the IEX resin waste <sup>(1-2,11-12,17)</sup>. If implemented, the vitreous waste-forms produced through the immobilisation process would need to be sufficiently resistant to physical and chemical attack to prevent the release of their inventory of radioactive material for a sufficient period of time, which in the case of the main caesium radio-isotope, <sup>137</sup>Cs, is approximately 300 years. This work applies the ASTM PCT technique in order to determine the relative durability of the samples in comparison to currently used waste glass compositions. It also investigates a selection of the developed glasses which have been waste-loaded in order to determine the impact of the ion exchange resin loading upon the durability of the waste forms produced.

A total of nine different compositions were explored using PCT experiments derived from work presented in chapter 3. These compositions form three distinct compositional groupings; alkali borosilicate glasses (AB), alkali alkaline-earth silicate glasses (AS) and calcium silicate (CS) glasses. These systems have all demonstrated the potential suitability in the context of ion exchange resin waste vitrification. The composition of each of the nine different compositions can be found in Table 5.2.1. The samples AS0, ASB, ASZ1 and ASZ2 were subjected to waste-loading with simulant <sup>133</sup>Cs-loaded ion exchange resin. PCT experiments showed significant variation in the dissolution behaviour between the three glass systems investigated and some variation between most samples studied. Samples from the alkali alkaline-earth silicate and calcium silicate systems were found to possess low normalised mass loss values over the course of the test period. These values were found to be significantly lower than those associated with glass compositions currently utilised for nuclear waste vitrification. The alkali borosilicate glass system demonstrated mass loss values which were significantly higher than those demonstrated by the other glass systems, and close to those associated with current waste glass compositions. The ASZ and ASZ2 glasses were found to demonstrate the lowest values of normalised mass loss in the alkali alkaline-earth silicate series. The AB base glass and CF0 samples demonstrated the lowest values for normalised mass loss in the alkali borosilicate and calcium silicate systems respectively.

**Table 5.2.1.** Composition of investigated glass systems.

Composition ID	Component Content (mol%)								
	SiO <sub>2</sub>	Al <sub>2</sub> O <sub>3</sub>	B <sub>2</sub> O <sub>3</sub>	Fe <sub>2</sub> O <sub>3</sub>	BaO	CaO	Na <sub>2</sub> O	Li <sub>2</sub> O	ZnO
<b>AB0 (Base)</b>	58.10	-	17.79	3.94	-	-	10.13	10.04	-
<b>ABM</b>	59.97	-	18.36	4.06	-	-	11.72	5.88	-
<b>CA0 (Base)</b>	41.43	7.17	-	-	-	51.40	-	-	-
<b>CF0</b>	41.43	-	-	7.17	-	51.40	-	-	-
<b>AS0 (Base)</b>	51.72	0.38	2.23	2.92	18.23	11.08	5.64	7.80	-
<b>ASB</b>	51.72	0.38	2.23	2.92	22.23	7.08	5.64	7.80	-
<b>ASZ</b>	51.72	0.38	2.23	2.92	18.23	6.08	5.64	7.80	5.00
<b>ASZ1</b>	51.72	0.38	2.23	2.92	22.23	2.08	5.64	7.80	5.00
<b>ASZ2</b>	54.97	0.40	2.37	3.10	23.63	2.21	3.36	4.64	5.31

## 5.2.1 Experimental Procedures

### 5.2.1.1 Sample Preparation

The glasses were prepared from their component oxides according to the compositions in Table 5.2.1. A mixture of carbonates and oxides was used in the initial batches, and all batch chemicals had a purity of 99.9% or greater. Alkali Borosilicate and Alkali Alkaline-Earth Silicate glasses were melted at 1200 °C in Zr-stabilised Pt crucibles and annealed at 500 °C for 1 hour. Calcium Silicate glasses were melted at 1400 °C in recrystallised Al<sub>2</sub>O<sub>3</sub> crucibles and were annealed at 780 °C for 1 hour. All glasses were melted for three hours and were stirred for the latter two hours. All glasses were allowed to cool to room temperature after annealing at a rate of 1 °C per minute. Each glass was prepared as a monolith.

The waste-loaded samples were produced by melting glass frit with a pre-prepared simulant caesium-loaded ion exchange resin. Glass frit material was produced from the glass monoliths by means of pulverising the material using a percussion mortar. The material was sieved to a sub 1 mm size fraction and screened for contamination from the percussion mortar. The resin used was a Duolite ARC-9359 resin which had been loaded with caesium by means of reaction with a caesium rich solution. The loaded resin was mixed with the glass frit at a waste-loading of 15 wt%. The mixed batches were then melted at 1200 °C in recrystallised alumina crucibles for a duration of three hours. The waste-forms produced were then annealed at 500 °C for one hour and then allowed to cool to room temperature at a rate of 1 °C per minute. Each glass was prepared as a monolith.

### 5.2.1.2 Durability Experiments

The ASTM product consistency test (PCT) was used to determine the aqueous durability of the samples and was carried out according to the protocol detailed<sup>(145)</sup>. The protocol is described in more detail in appendix 8.1. The PCT test involves the immersion of glass particles ranging in size from 75 - 120  $\mu\text{m}$  in ASTM Type 1 water for between 3 and 28 days whilst being held at a temperature of 90 °C. 10 ml of leachant solution and 1 g of sample material was used in each individual test. Due to the range of densities being explored, this resulted in a range of surface area of volume ratios being explored (1280 - 1930  $\text{m}^{-1}$ ). The leachants were analysed for pH and for the concentration of elemental species, for which Inductively Coupled Plasma-Atomic Emission spectroscopy (ICP-AES) was used to analyse the solutions. ICP-AES experiments were carried out at the Elemental Analysis service in the Department of Chemistry at Sheffield University. The pH of the leachant solution was measured using a calibrated pH probe. The analysed elemental content of the leachant solutions was used to calculate the leach rate of normalised loss for each element as discussed below according to the PCT ASTM standard<sup>(145)</sup>. These results were compared against the results of earlier studies on borosilicate glasses<sup>(146-148)</sup>.

X-ray Fluorescence Spectroscopy (XRF) was used to determine the composition of the glass samples and waste-forms. XRF experiments were performed at the Manchester University XRF facility at the School of Earth, Atmospheric and Environmental Sciences.

## 5.2.2 Results

### 5.2.2.1 Alkali Alkaline-Earth Silicate glasses

The glass compositions derived from the Alkali Alkaline-Earth Silicate glass system demonstrated a narrow range of variation in normalised elemental mass losses. The pH of the leachant solutions was found to increase from 10.2 ( $\pm 0.1$ ) to 10.6 ( $\pm 0.1$ ) over the period of the durability experiments in all alkali alkaline-earth silicate glass samples. The AS0 glass demonstrated values for  $NL_{\text{Si}}$  which approached a steady state of release after 21 days, reaching a maximum release of  $0.165 \pm 0.010 \text{ gm}^{-2}$  at 28 days. This was closely matched by the ASB glass. In comparison with this, the glass ASZ demonstrated the overall lower values of  $NL_{\text{Si}}$  after 28 days, giving values of  $0.148 \pm 0.007 \text{ gm}^{-2}$ . However as can be seen from Figure 5.2.1, the rate of dissolution has not achieved a steady state for this glass. This

can also be seen to be the case for the ASZ1 and ASZ2 glasses at 28 days, and both glasses show  $NL_{Si}$  values close to or exceeding those of the AS0 glass at  $0.187 \pm 0.010 \text{ gm}^{-2}$  and  $0.167 \pm 0.010 \text{ gm}^{-2}$  respectively. In considering the values of  $NL_B$  in Figure 5.2.2, it can be seen that although the same trends are apparent in terms of the rate of mass loss in all five glasses, the overall levels of mass loss for B are significantly different, with the greatest release of B being seen in the AS0 glass ( $0.357 \pm 0.010 \text{ gm}^{-2}$ ) and ASB ( $0.261 \pm 0.010 \text{ gm}^{-2}$ ) glasses respectively, with ASZ, ASZ1 and ASZ2 demonstrating lower values of  $NL_B$  after 28 days ( $0.177 \pm 0.010 \text{ gm}^{-2}$  for ASZ2 at 28 days).

In considering the alkali content of the systems, a similar pattern can be seen in the normalised mass loss for the AS0 and ASB glasses, reaching an apparent steady state (within error) after 21 days and the ASZ, whereas ASZ1 and ASZ2 glasses continue to increase in mass loss for Na & Li. Also, as with  $NL_B$  ASZ, ASZ1 and ASZ2 demonstrate lower values of normalised mass loss for the elements Na and Li throughout the 28 day experiment. This can be seen in Figures 5.2.3 & 5.2.4. Considering the normalised mass loss of the alkaline-earth components (Figures 5.2.5 & 5.2.6) of the glasses, it is apparent that for both Ca & Ba a steady state of release is achieved within the first 7-14 days of the experiment (within error), whereas ASZ and ASZ2 both show a marked increase in mass loss throughout the 28 days. In comparing the values of  $NL_{Ca}$  and  $NL_{Ba}$  for the AS0 and ASB it can be seen that the mass loss values are similar for both elements. ASZ also demonstrates similar overall values of mass loss for both elements. However, the glasses ASZ2 and more markedly ASZ1 show increases in  $NL_{Ca}$  throughout the 28 day period. The  $NL_{Ca}$  of ASZ1 rises to  $0.401 \pm 0.023 \text{ gm}^{-2}$  over the 28 day course of the experiment, where as the value of  $NL_{Ba}$  reaches a steady state  $0.077 \pm 0.008 \text{ gm}^{-2}$  after 14 days for the same glass. The values of  $NL_{Zn}$  in the ASZ, ASZ1 and ASZ2 (figure 5.2.7) glasses demonstrated that the ASZ1 and ASZ2 glasses achieved a steady state of Zn release after 7 days (within limits of error) and demonstrated lower values of  $NL_{Zn}$  overall relative to ASZ which showed a constant increase in  $NL_{Zn}$  over 28 days up to a value of  $0.0019 \pm 0.0005 \text{ gm}^{-2}$ . The normalised mass loss values for both Al and Fe demonstrated no significant variation (within error) due to their low overall mass loss values, which were close to or below detection limits and so are not discussed. Figures 5.2.1 - 5.2.7 show the normalised mass loss for Si, B, Na, Li, Ca, Ba, and Zn respectively from the alkali alkaline-earth glasses.

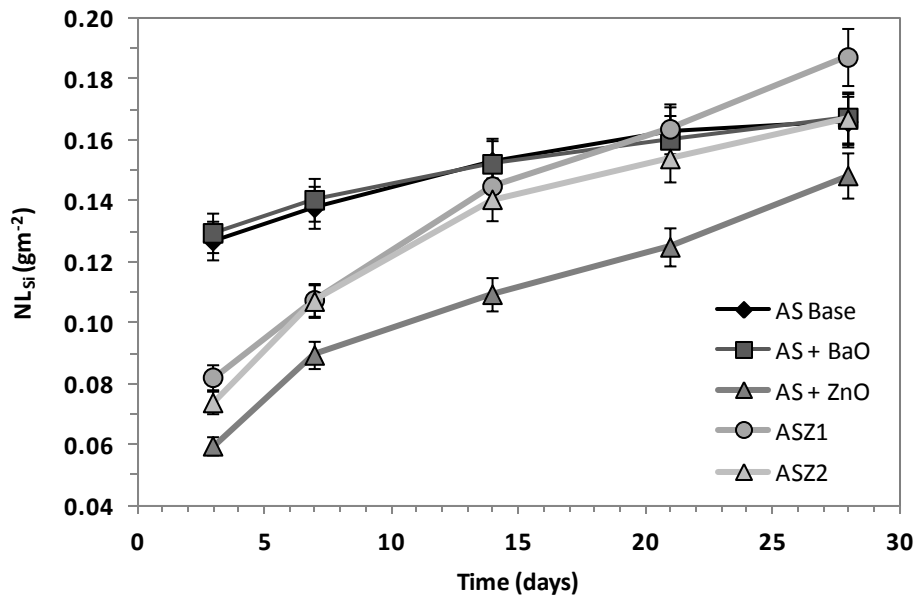


**Figure 5.2.1.** Normalised Si mass loss against time over 28 days of glass alteration under static leach conditions at 90 °C for all five alkali alkaline-earth silicate glass samples.

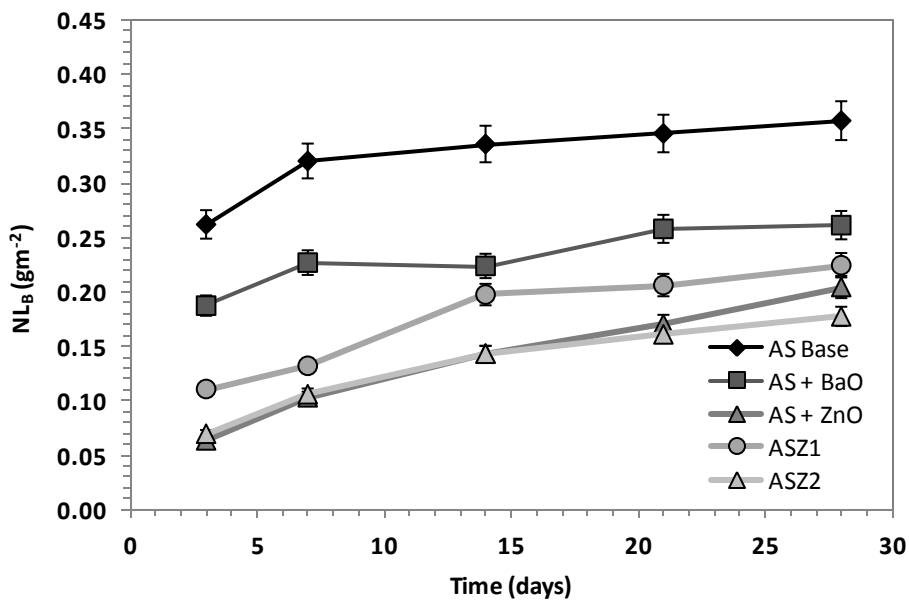


**Figure 5.2.2.** Normalised B mass loss against time over 28 days of glass alteration under static leach conditions at 90 °C for all five alkali alkaline-earth silicate glass samples.

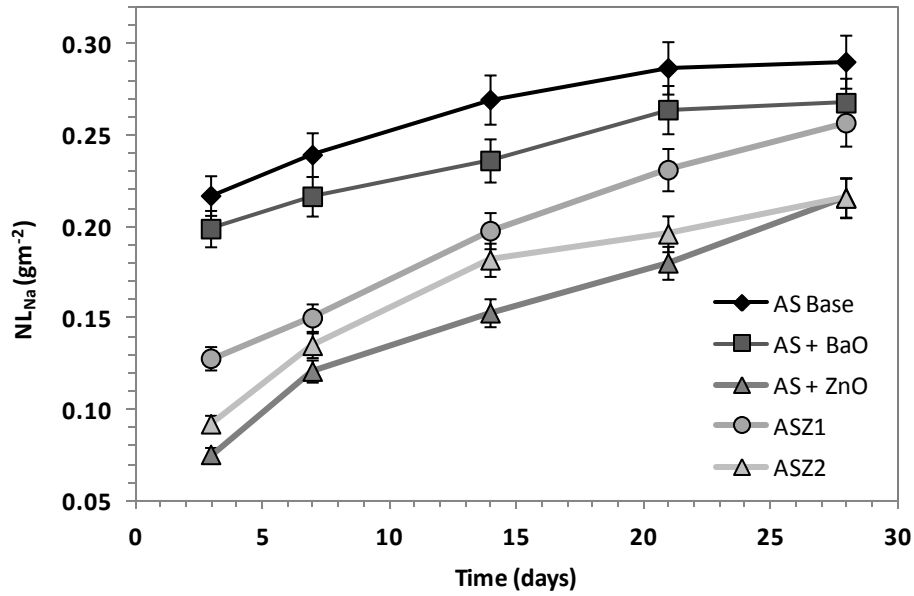


**Figure 5.2.3.** Normalised Na mass loss against time over 28 days of glass alteration under static leach conditions at 90 °C for all five alkali alkaline-earth silicate glass samples.

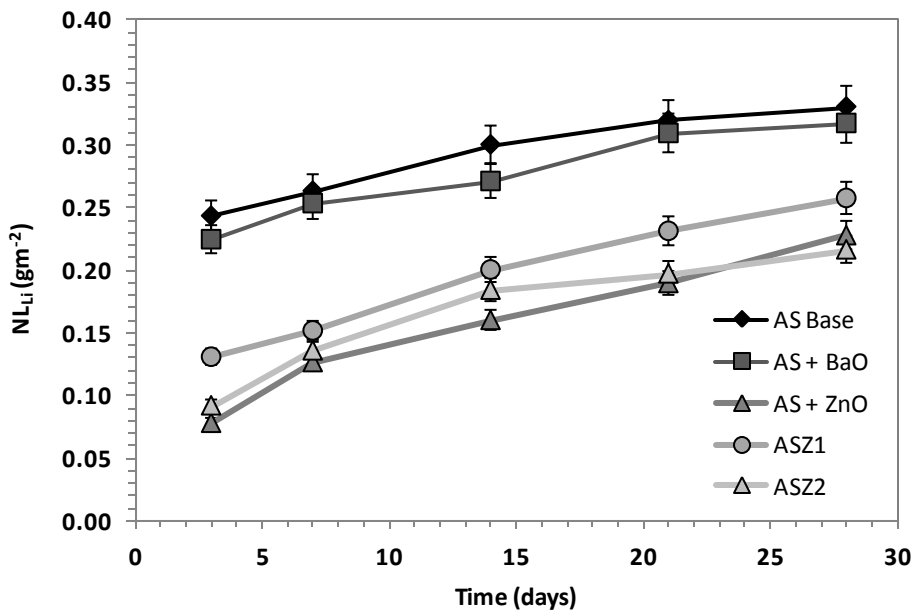


**Figure 5.2.4.** Normalised Li mass loss against time over 28 days of glass alteration under static leach conditions at 90 °C for all five alkali alkaline-earth silicate glass samples.

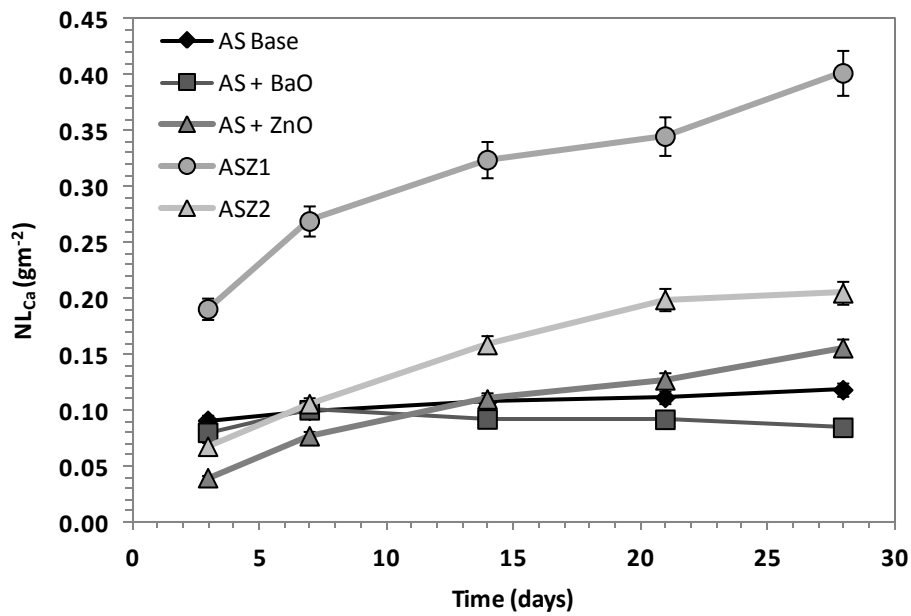


**Figure 5.2.5.** Normalised Ca mass loss against time over 28 days of glass alteration under static leach conditions at 90 °C for all five alkali alkaline-earth silicate glass samples.

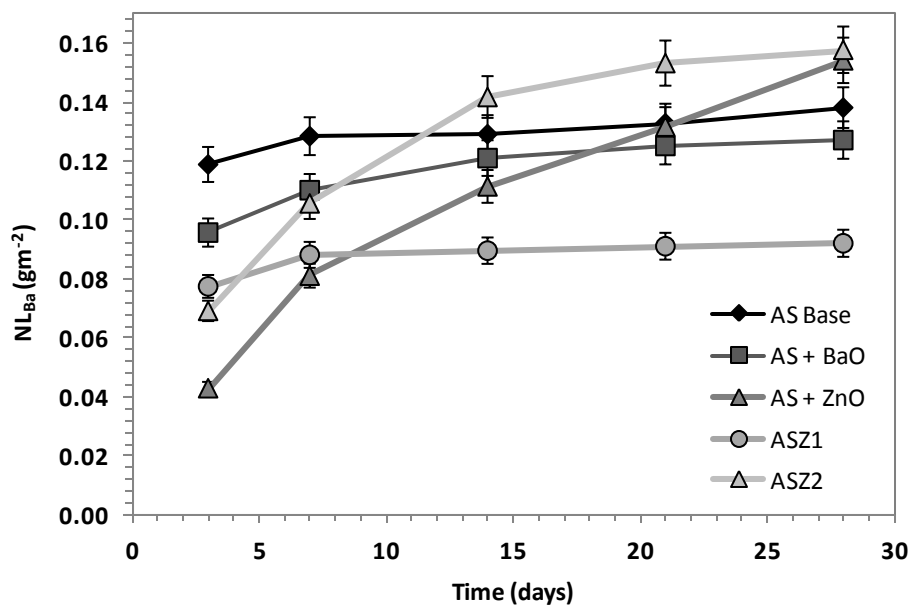


**Figure 5.2.6.** Normalised Ba mass loss against time over 28 days of glass alteration under static leach conditions at 90 °C for all five alkali alkaline-earth silicate glass samples.

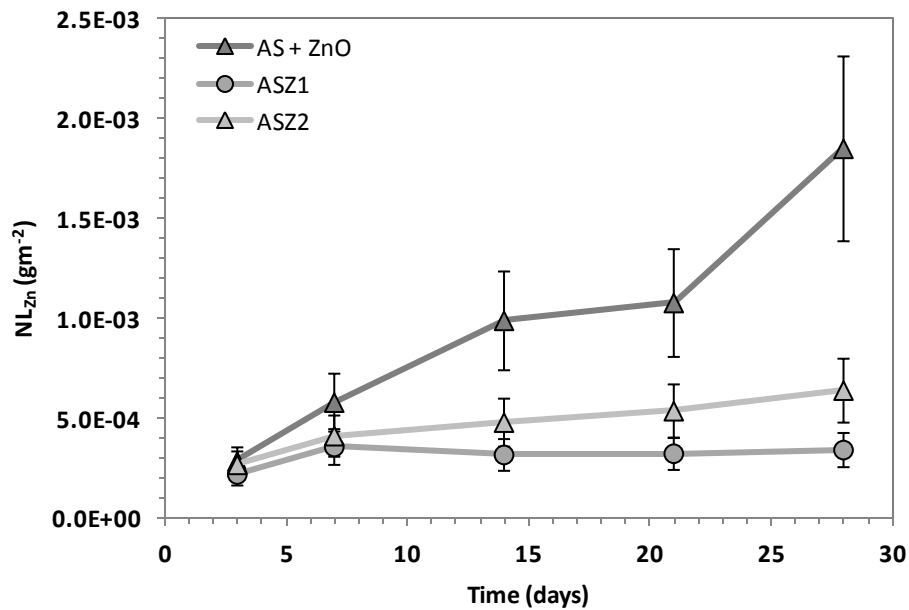


**Figure 5.2.7.** Normalised Zn mass loss against time over 28 days of glass alteration under static leach conditions at 90 °C for all 3 Zn containing alkali alkaline-earth silicate glass samples.

### 5.2.2.2 Alkali Borosilicate Glasses

The two glass compositions derived from the Alkali Borosilicate glass system demonstrated a small degree of variation between them. The pH of the leachant solutions was found to increase from 10.1 ( $\pm 0.1$ ) to 10.8 ( $\pm 0.1$ ) over the period of the durability experiments in both alkali borosilicate glass samples. In general, however, the normalised mass losses found were an order of magnitude higher than those which were found for the glass from the alkali alkaline-earth borosilicate glass system.

In considering the values of  $NL_{Si}$  for both glasses, it is apparent that both glasses achieve a steady-state of mass loss after 14 days after rising to mass loss values of  $1.29 \pm 0.05$  gm<sup>-2</sup> and  $1.27 \pm 0.05$  gm<sup>-2</sup> for AB base and ABM respectively. However, at 28 days, the AB base glass demonstrated a further increase to  $1.44 \pm 0.05$  gm<sup>-2</sup>, possibly indicating an interruption to the steady-state achieved after 14 days. The values of  $NL_B$  presented by both glasses over 28 days show no significant difference in behaviour between the two glasses, with both demonstrating a steadily increasing mass loss increasing to  $8.0 \pm 0.5$  gm<sup>-2</sup> for both glasses. This can be seen in Figures 5.2.8 & 5.2.9 respectively. In considering the normalised mass loss for the alkali species present in the system, it can be seen that as with

NL<sub>B</sub>, there is no indication of the establishment of steady state being achieved within the 28 day time-scale of the experiment. It is also apparent that the ABM composition presents higher values of NL<sub>Na</sub> and NL<sub>Li</sub> throughout the 28 day period of the experiment. This can be seen in Figures 5.2.10 & 5.2.11 respectively. The values of NL<sub>Fe</sub> as shown in Figure 5.2.12 show the establishment of a steady state (with error bars) after 21 days in both alkali borosilicate glasses. The NL<sub>Fe</sub> value for the AB base glass can be seen to be consistently higher than the ABM glass throughout the 28 day experimental period.

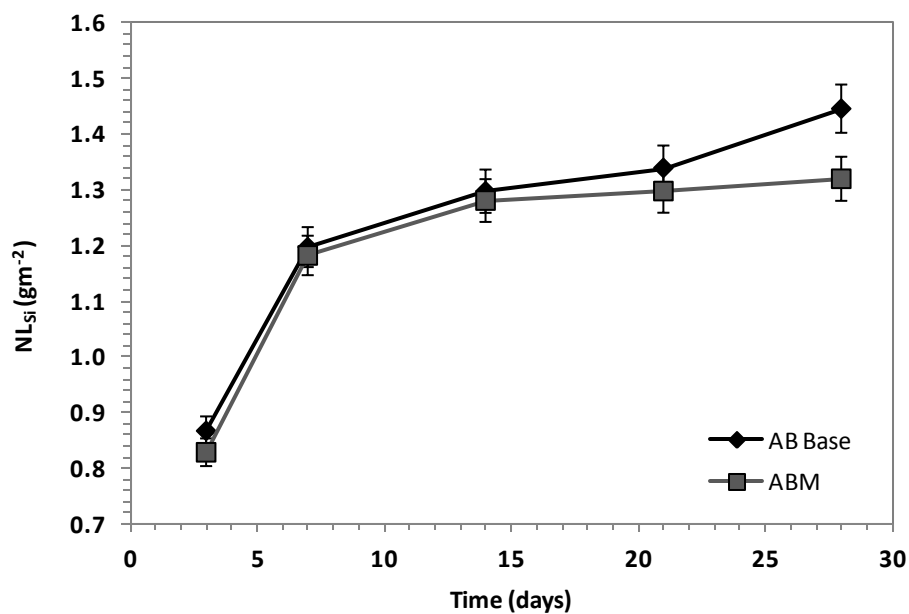


**Figure 5.2.8.** Normalised Si mass loss against time over 28 days of glass alteration under static leach conditions at 90 °C for both alkali borosilicate glass samples.

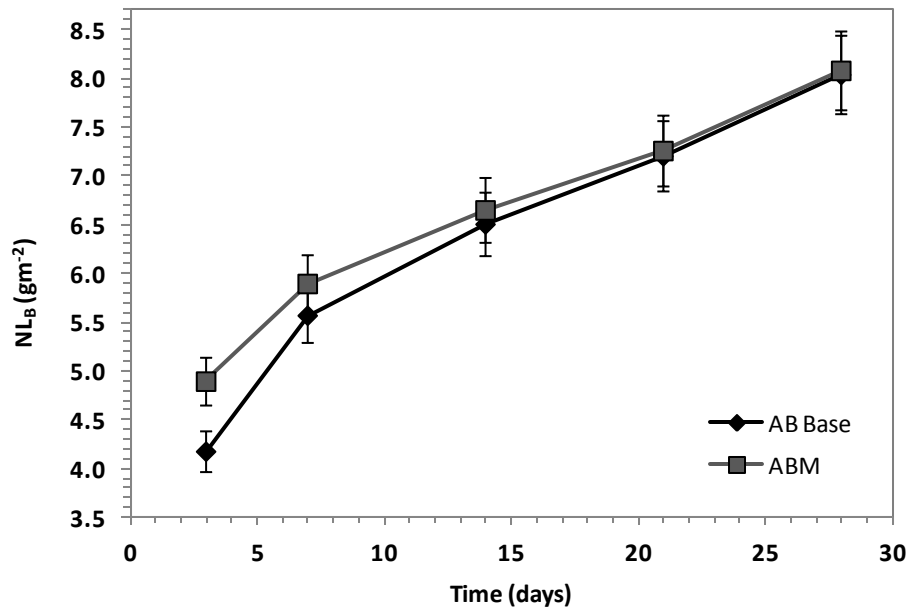


**Figure 5.2.9.** Normalised B mass loss against time over 28 days of glass alteration under static leach conditions at 90 °C for both alkali borosilicate glass samples.

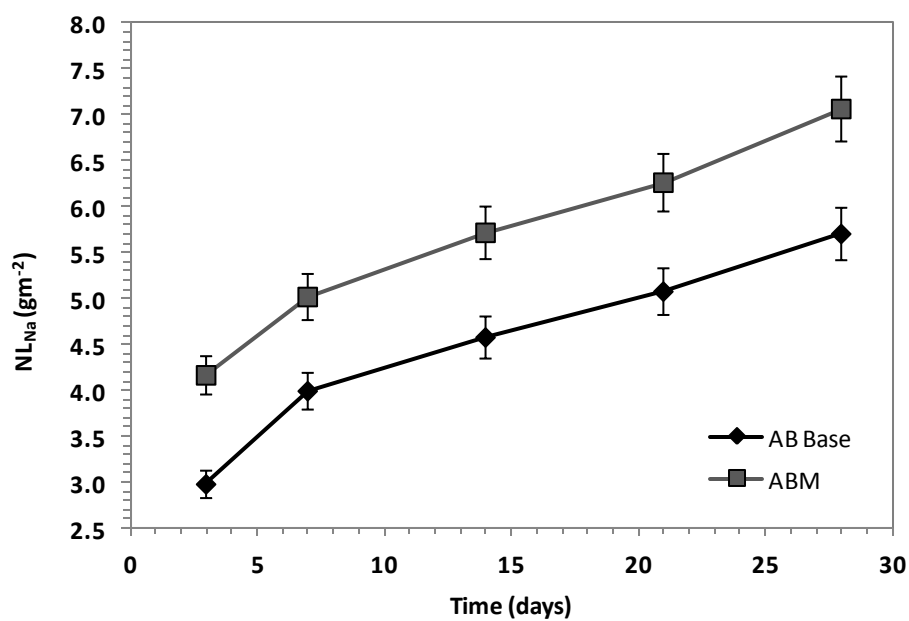


**Figure 5.2.10.** Normalised Na mass loss against time over 28 days of glass alteration under static leach conditions at 90 °C for both alkali borosilicate glass samples.

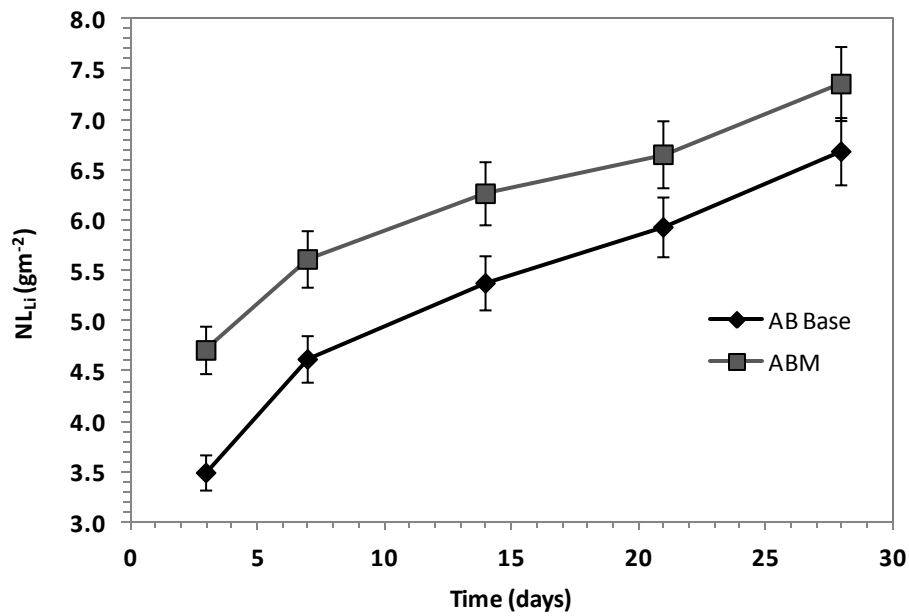


**Figure 5.2.11.** Normalised Li mass loss against time over 28 days of glass alteration under static leach conditions at 90 °C for both alkali borosilicate glass samples.

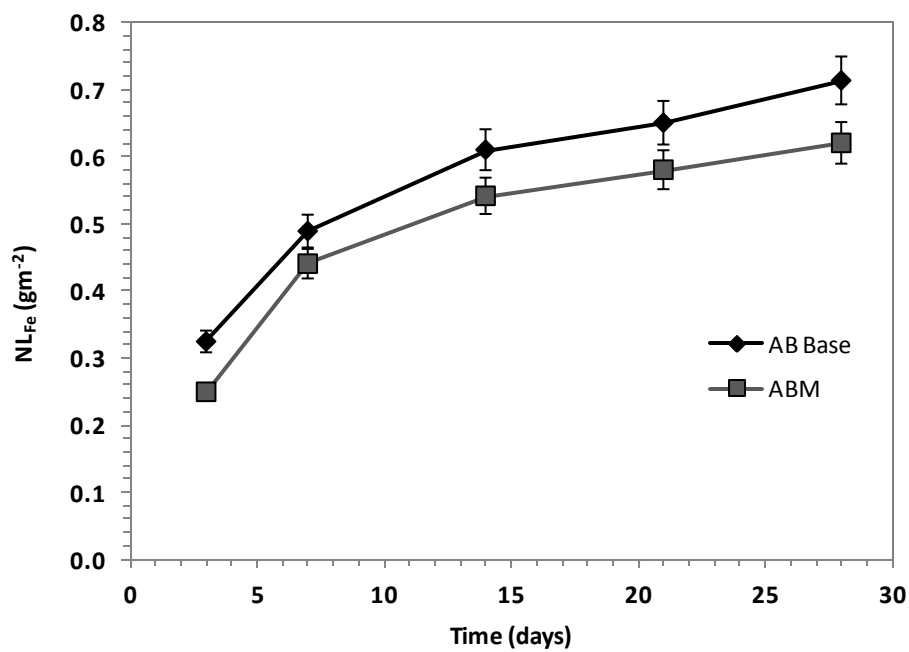


**Figure 5.2.12.** Normalised Fe mass loss against time over 28 days of glass alteration under static leach conditions at 90 °C for both alkali borosilicate glass samples.

### 5.2.2.3. Calcium Silicate Glasses

The normalised mass loss for the calcium silicates glasses in general showed a significant degree of difference between the two compositions explored. The pH of the leachant solutions was found to increase from 9.8 ( $\pm 0.1$ ) to 10.5 ( $\pm 0.1$ ) over the period of the durability experiments in both calcium silicate glass samples.

The values for  $NL_{Si}$  for these glasses (shown in figure 5.2.13) demonstrate significant difference between the CF0 and CA0 glasses. Where CA0 appears to achieve a steady state of  $NL_{Si}$  within 3 days of the start of the experiment the CF0 glass achieves a steady state (within error) after 21 days. There was also significant difference between the values of  $NL_{Si}$  once steady state was achieved in both glasses.  $NL_{Si}$  for CA0 was found to be  $0.063 \pm 0.003 \text{ gm}^{-2}$  after 28 days in comparison to  $0.059 \pm 0.002 \text{ gm}^{-2}$  for CF0. These contrasting trends in  $NL_{Si}$  are reflected in the values of  $NL_{Al}$  in the CA0 glass and  $NL_{Fe}$  in CF0 (Figures 5.2.15 and 5.2.16 respectively), in that  $NL_{Al}$  for CA0 achieves a steady state within 3 days of the start of the experiment, whereas  $NL_{Fe}$  in the CF0 glass increases over the first 21 days after which it achieves a steady state.

The values for  $NL_{Ca}$  do not however show any similarity to the mass loss values for other component in these glasses, with  $NL_{Ca}$  values for both glasses increasing steadily over the course of the 28 day experiment. Notably the  $NL_{Ca}$  value for CA0 was consistently almost twice the value seen in CF0, reaching a value of  $0.054 \pm 0.005 \text{ gm}^{-2}$  after 28 days, whereas the  $NL_{Ca}$  for the CF0 glass reached  $0.039 \pm 0.005 \text{ gm}^{-2}$  after 28 days. The values of  $NL_{Ca}$  can be seen in Figure 5.2.14.

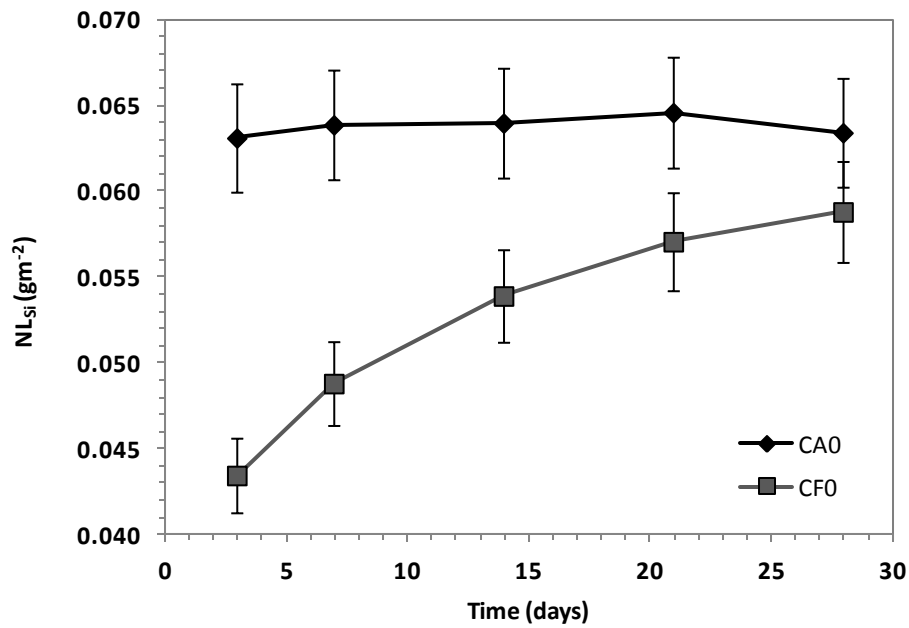


**Figure 5.2.13.** Normalised Si mass loss against time over 28 days of glass alteration under static leach conditions at 90 °C for both calcium silicate glass samples.

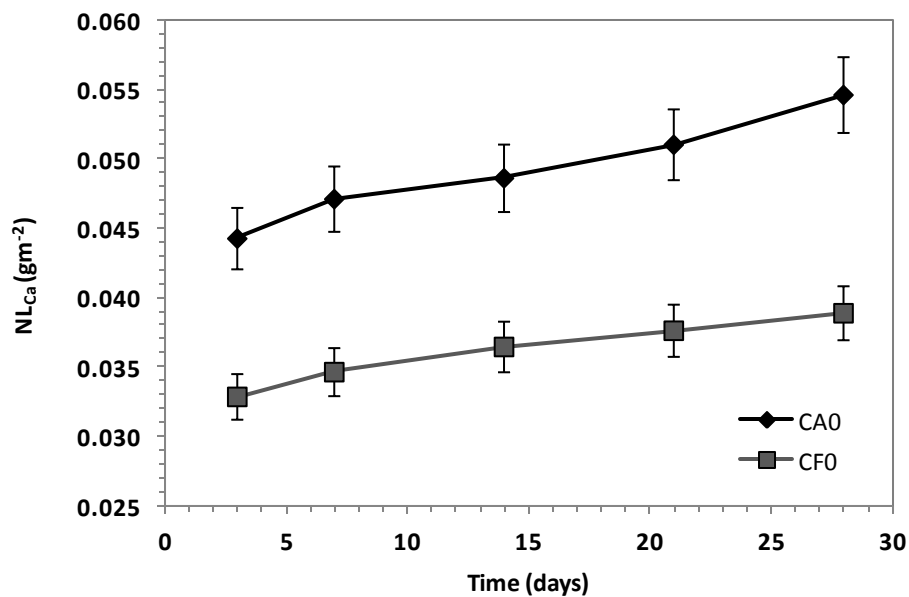


**Figure 5.2.14.** Normalised Ca mass loss against time over 28 days of glass alteration under static leach conditions at 90 °C for both calcium silicate glass samples.

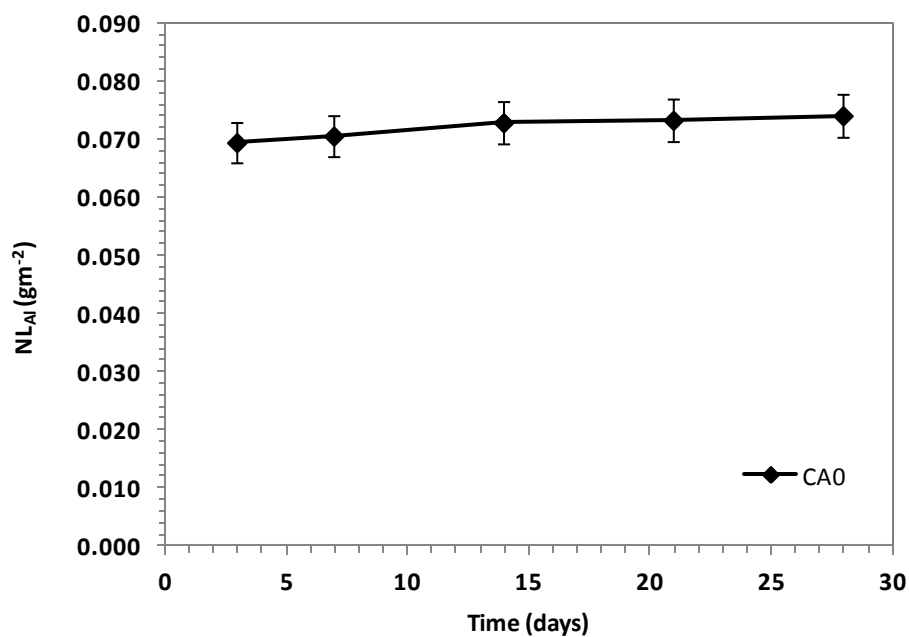


**Figure 5.2.15.** Normalised Al mass loss against time over 28 days of glass alteration under static leach conditions at 90 °C for the calcium silicate base glass CA0.

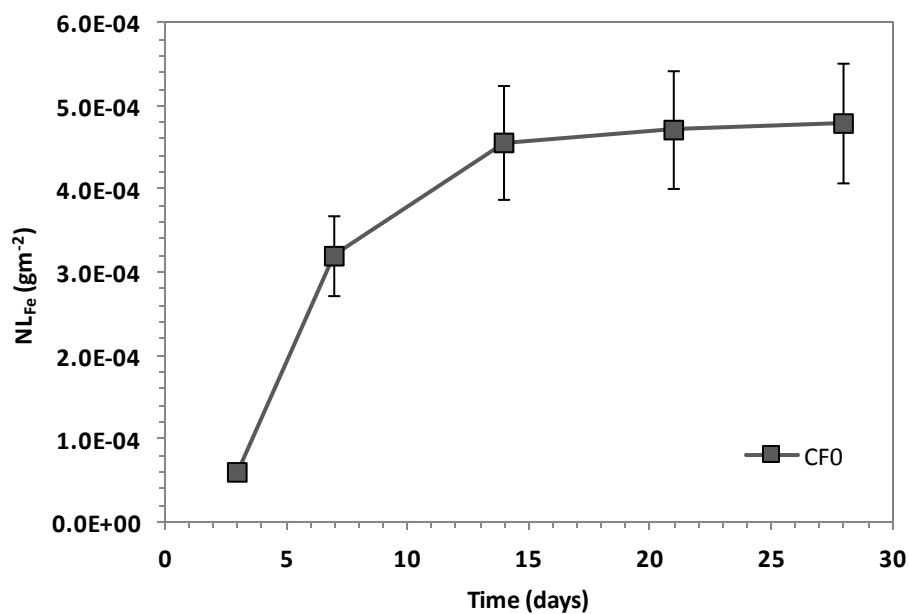


**Figure 5.2.16.** Normalised Fe mass loss against time over 28 days of glass alteration under static leach conditions at 90 °C for the CF0 glass.

#### 5.2.2.4 Waste-loaded Glasses

In considering the four waste-loaded glass samples, it is apparent that there is a significant amount of variation between the waste-loaded samples and the unloaded base glass samples. Considering the normalised mass loss associated with Si, B, Na, Li and Ba (Figures 5.2.17, 5.2.18, 5.2.19, 5.2.20 and 5.2.22 respectively), it can be seen that for all four waste-loaded glasses the values of normalised mass loss has decreased by a statistically significant amount. This is most apparent in the values of  $NL_{Si}$ , where in all glasses a steady state of mass loss is achieved with the first 7 -14 days of the experiment (within error). This decrease is most significant in the values of  $NL_{Si}$  and  $NL_B$  and less so in the values of  $NL_{Na}$ ,  $NL_{Li}$  and  $NL_{Ba}$ , implying that the reduction is most strongly linked with the network-forming elements Si and B.

However, it is important to note that this trend was not apparent across all elements present in the waste-loaded glasses. It was found in the ASB and ASZ1 waste-loaded samples that the normalised mass loss for Ca in the glasses was substantially increased relative to the values present in the unloaded base glass samples. For the ASZ1 glass, this decrease in  $NL_{Ca}$  values also leads to the establishment of steady state mass loss after 7 days. The values of  $NL_{Ca}$  for the waste-loaded glasses can be seen in Figure 5.2.21.

A notable increase in normalised mass loss on waste-loading also occurs for the ASZ1 glass in the values of  $NL_{Zn}$  shown in figure 5.2.23. The values of  $NL_{Zn}$  for ASZ1 after waste-loading shows a significant increase after 7 days, increasing from  $0.0004 \pm 0.0001 \text{ gm}^{-2}$  to  $0.0011 \pm 0.0002 \text{ gm}^{-2}$  and then achieving a steady state (within error), where as ASZ2 demonstrates significantly a significant decrease in  $NL_{Zn}$  after waste-loading.

In terms of the normalised mass loss for sulphur, which was incorporated into the glass samples through the waste-loading, it was apparent from the data (shown in Figure 5.2.24) that both the AS0 and ASB waste-forms achieved a steady-state of mass loss within the first 3 days of the experiment, where as the ASZ2 waste-form reached a steady state after 21 days (within limits of error). The ASZ1 waste-form demonstrated a significant increase in  $NL_S$  at 7 days rising from  $0.122 \pm 0.10 \text{ gm}^{-2}$  to  $0.178 \pm 0.14 \text{ gm}^{-2}$ , subsequent to which a steady state is achieved. It is worth noting that the normalised mass loss for Na, Zn and S for the ASZ1 demonstrated an anomalous increase at 7 days into the experiment, indicating a possible link between the effect seen in the normalised mass loss for S in the ASZ1 waste-form and the release of Zn and Na. Throughout the 28 days of the experiment the glass ASB demonstrated lower overall values of S release, where as the highest values were seen in the ASZ1 and ASZ2 waste-forms.

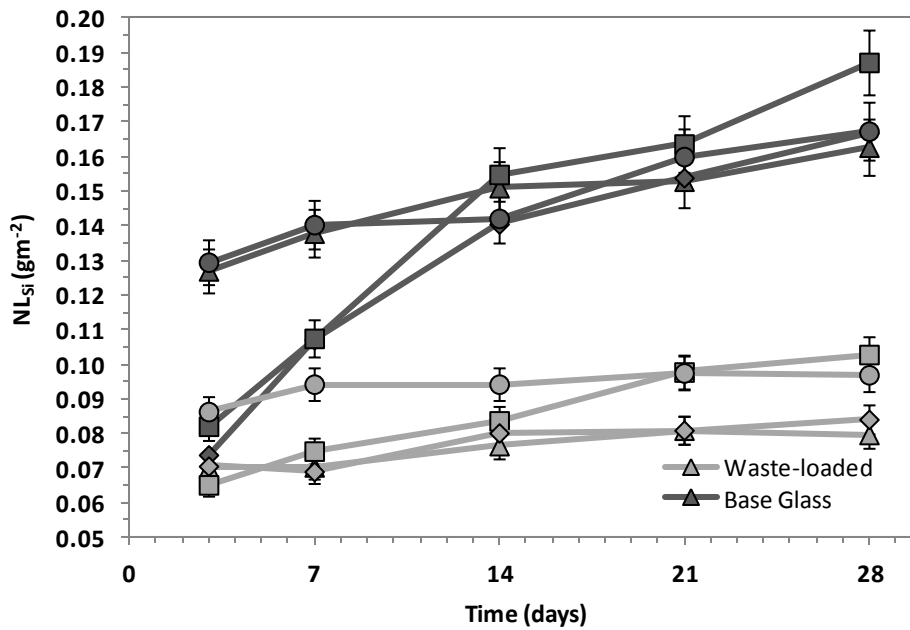


**Figure 5.2.17.** The normalised mass loss (Si) against time over 28 days of glass alteration under static leach conditions at 90 °C for both waste-loaded samples and base glass samples. Triangle - AS0, Circle - ASB, Diamond - ASZ1 and Square - ASZ2.

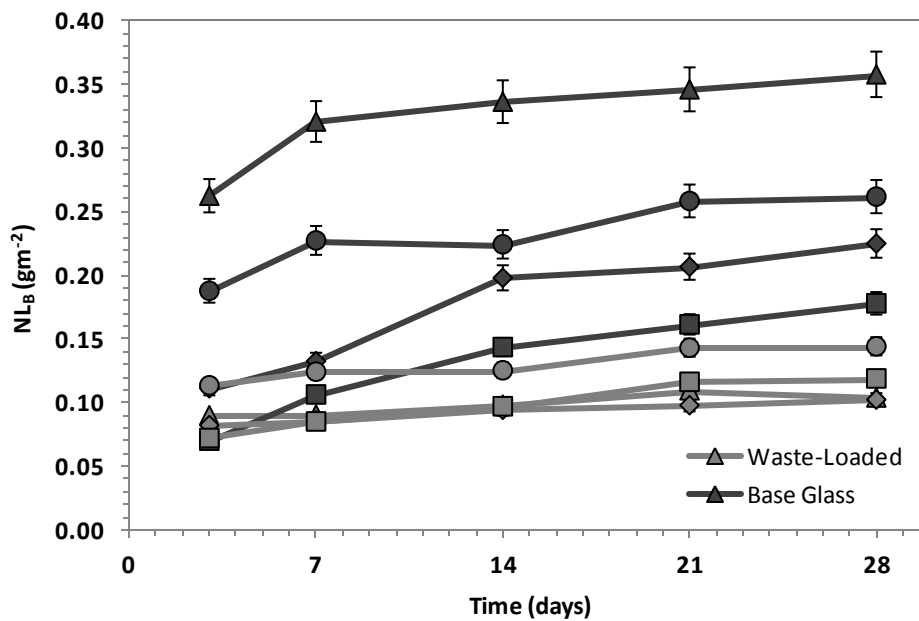


**Figure 5.1.18.** The normalised mass loss (B) against time over 28 days of glass alteration under static leach conditions at 90 °C for both waste-loaded samples and base glass samples. Triangle - AS0, Circle - ASB, Diamond - ASZ1 and Square - ASZ2.

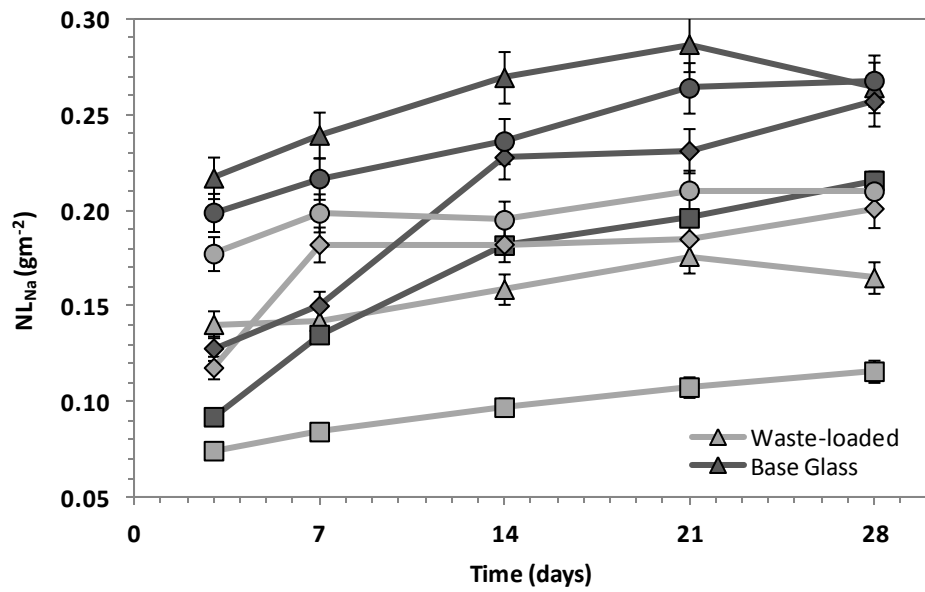


**Figure 5.1.19.** The normalised mass loss (Na) against time over 28 days of glass alteration under static leach conditions at 90 °C for both waste-loaded samples and base glass samples. Triangle - AS0, Circle - ASB, Diamond - ASZ1 and Square - ASZ2.

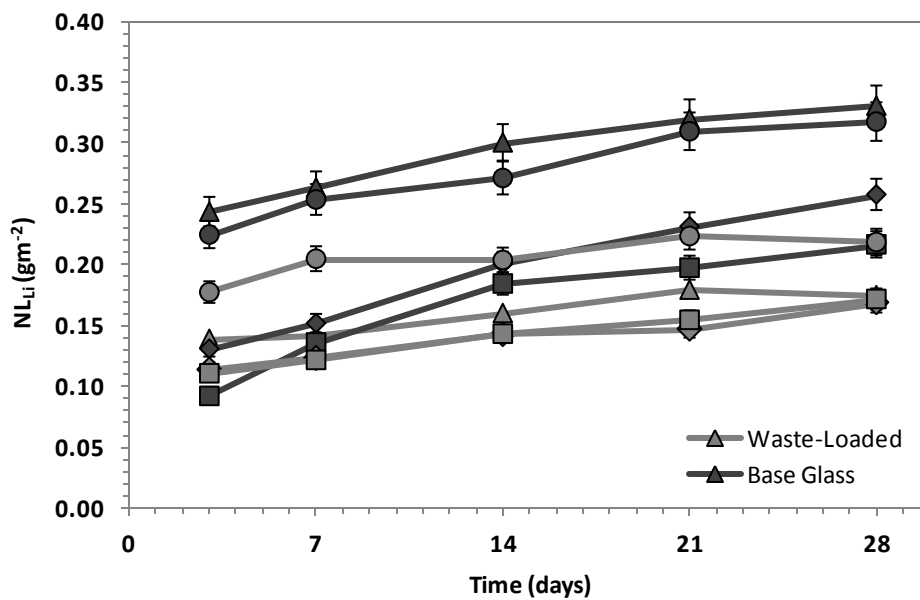


**Figure 5.2.20.** The normalised mass loss (Li) against time over 28 days of glass alteration under static leach conditions at 90 °C for both waste-loaded samples and base glass samples. Triangle - AS0, Circle - ASB, Diamond - ASZ1 and Square - ASZ2.

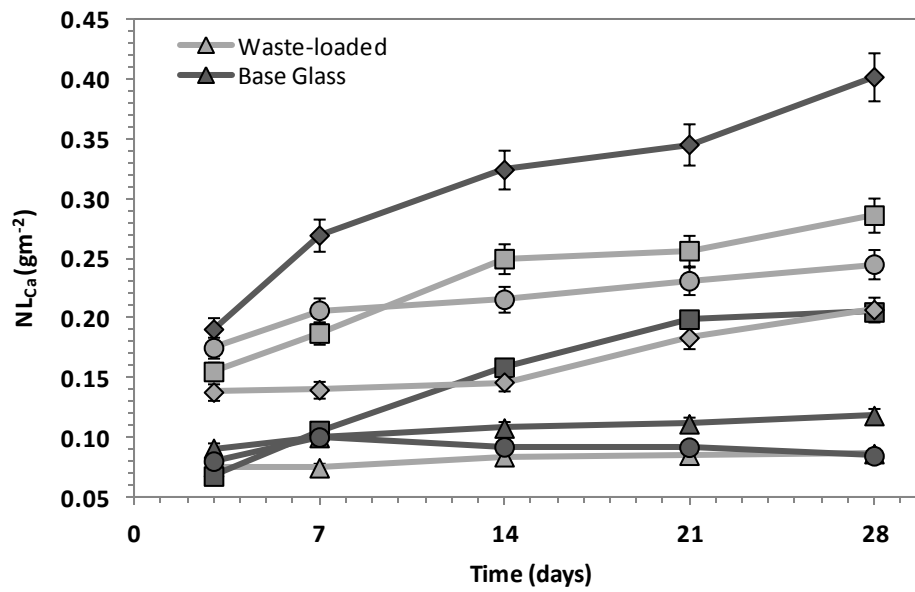


**Figure 5.2.21.** The normalised mass loss (Ca) against time over 28 days of glass alteration under static leach conditions at 90 °C for both waste-loaded samples and base glass samples. Triangle - AS0, Circle - ASB, Diamond - ASZ1 and Square - ASZ2.

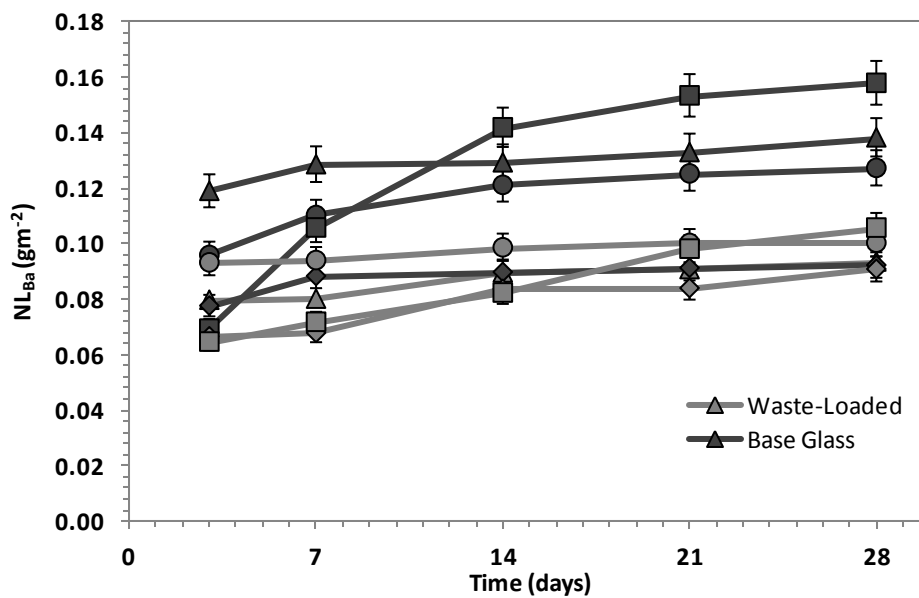


**Figure 5.2.22.** The normalised mass loss (Ba) against time over 28 days of glass alteration under static leach conditions at 90 °C for both waste-loaded samples and base glass samples. Triangle - AS0, Circle - ASB, Diamond - ASZ1 and Square - ASZ2.

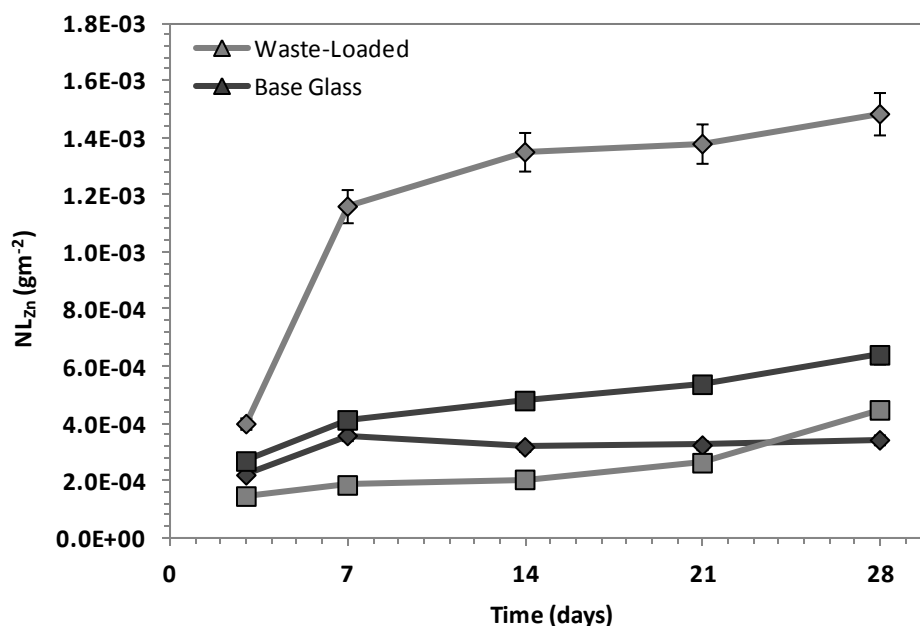


**Figure 5.2.23.** The normalised mass loss (Zn) against time over 28 days of glass alteration under static leach conditions at 90 °C for both waste-loaded samples and base glass samples. Diamond - ASZ1 and Square - ASZ2.

Finally, considering the normalised mass loss for caesium, which was also present through the waste loading of the glasses, it was apparent that comparatively low values of normalised mass loss were achieved in all four glasses. However, the ASZ1 and ASZ2 waste-forms presented the lowest values for caesium normalised mass loss over the course of the experiment, having normalised mass loss values of  $0.145 (\pm 0.03) \text{ gm}^{-2}$  and  $0.151 (\pm 0.03) \text{ gm}^{-2}$  respectively. This is important to note since radio-caesium would be the primary radio-nuclide immobilised within these waste-forms. The normalised mass loss for caesium in all four glasses can be seen in Figure 5.2.25.

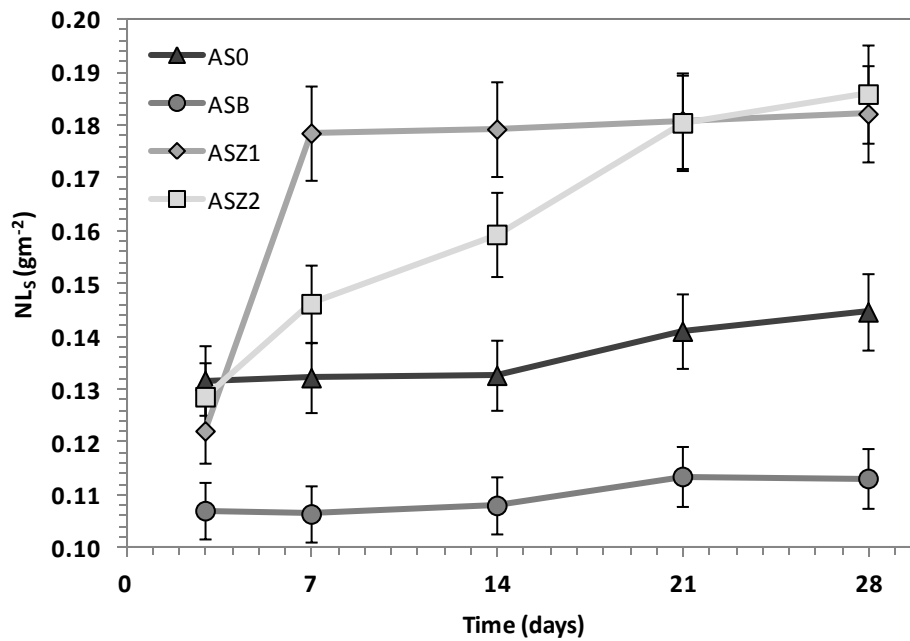


**Figure 5.2.24.** The normalised mass loss (S) against time over 28 days of glass alteration under static leach conditions at 90 °C for both waste-loaded samples and base glass samples.

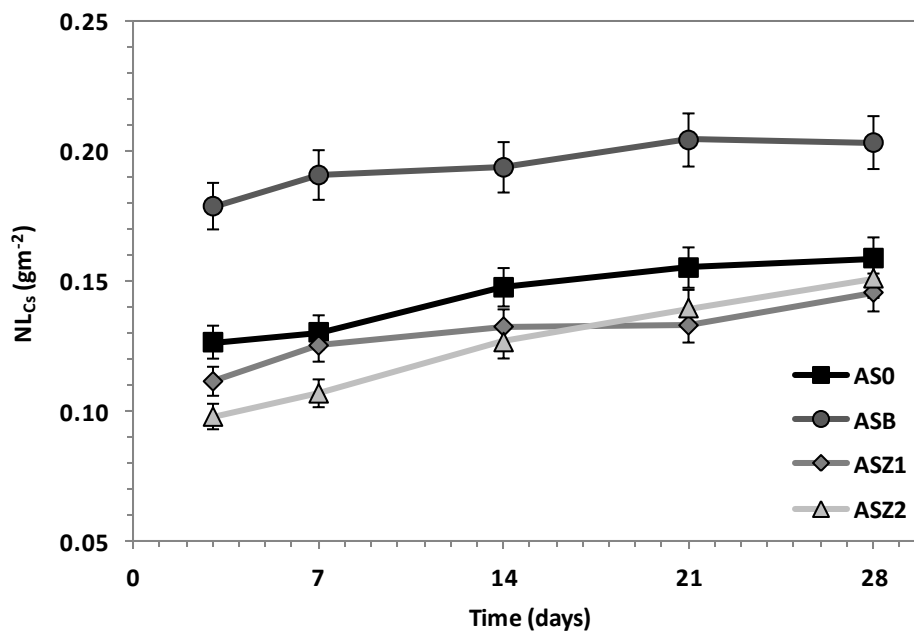


**Figure 5.2.25.** The normalised mass loss (Cs) against time over 28 days of glass alteration under static leach conditions at 90 °C for both waste-loaded samples and base glass samples.

## 5.2.3 Discussion

### 5.2.3.1 Alkali Alkaline-Earth Silicate System.

Considering the alkali alkaline-earth glasses it is apparent that the five glasses that were studied can be divided into two distinct groups. The first group, consisting of the AS0 glass and the ASB glass was characterised by the establishment of steady state dissolution kinetics, termed region 4 in the dissolution model of Grambow *et al* <sup>(149)</sup>, after shorter periods of time, generally within the first 14 days, for Si, Na, Li, Ba and Ca. This group was also characterised by the higher values for normalised mass loss that were achieved for most leached species (excluding Ca). The second group, made up from the ASZ, ASZ1 and ASZ2 glasses, were characterised by generally lower values of normalised mass loss across all elements (again excluding Ca) throughout the course of 28 days experiment, but also by the longer periods of time that were taken to achieve the steady state dissolution region, if they achieved it at all during the 28 day period. The primary compositional difference between these two groups was the replacement of 5 mol% CaO with ZnO in all glasses in the second group, indicating that either the loss of Ca or the addition of Zn is responsible for the effect seen.

The establishment of steady-state in terms of Si mass-loss implies the formation of a precipitate layer, as consistent with generally held theory on the dissolution of silicate glasses <sup>(151)</sup>. The precipitate layer has been demonstrated <sup>(151)</sup> to prevent the interaction of acidic species from the solution with pristine glass and as such is responsible for the establishment of steady-state in terms of mass-loss. Comparing the two groups of glasses, it can therefore be seen that the primary difference between the groups is the time required for the establishment of this precipitated gel layer. The first group achieves the formation of this gel layer at an earlier period than the second group, leading to the mass loss reaching steady state at 14-21 days. The higher mass loss values indicate that the rapid formation of this gel layer can be attributed to more aggressive interactions between the solution and the glasses of the first group than was seen in the second group, leading to the loss of larger concentrations of all species but resulting in the formation of the gel layer at earlier time periods. The improvement seen in the chemical durability of the second group can in principle only be attributed to the effect of zinc upon the glasses dissolution behaviour and upon the removal of calcium, since the addition of ZnO in the place of CaO is the only variation between the two groups. The reduction in Ca content, resulting in an improvement in aqueous durability, is in line with generally accepted theory with regards to the dissolution of silicate glasses, because

as an alkali earth cation, calcium is vulnerable to ion exchange processes. The addition of zinc to the system would further bolster the aqueous durability of the glass, since Zinc is well known to improve the aqueous durability of silicate glasses <sup>(59)</sup> due to the low enthalpy of hydration for zinc in glass systems. These two effects therefore explain the observed improvements in aqueous durability seen in the second group of glasses.

Regarding this anomalously high values of  $NL_{Ca}$  seen in the second group of glasses, the work of Todorvic *et al* and others has demonstrated that there is a positive effect on the aqueous durability of glasses in which a mixture of alkaline-earth species are present <sup>(152)</sup>. This can be attributed to a mixed alkaline-earth effect where the mixtures of alkaline-earth species cause interference and blockage of diffusion pathways. The presence of this effect may be used to further explain the trends in aqueous durability seen in the second group of glasses, ASZ, ASZ1 and ASZ2. In the case of the ASB and ASZ2 system, the proportion of CaO was reduced and BaO increased, resulting in a majority population of Ba cations to be present in the system. The effect of this can be seen in those two systems, which demonstrate decreased aqueous durability relative to the base glass composition and ASZ compositions that they are derived from respectively. The effect is significantly more pronounced in ASZ1 due to the greater reduction in Ca content due to the replacement of CaO with ZnO in the system. This provides an explanation for the high normalised mass loss for Ca seen in ASZ1.

The lower values of mass loss seen in the ASZ2 glass relative to the other glasses in the second group can be linked to the reduced proportion of alkali species in the system, providing an explanation for the improved durability. Alkali species are generally understood to have a detrimental effect upon the aqueous durability of silicate glass systems <sup>(151)</sup> due to their availability for ion exchange with protons in solution. As such, the reduction in alkali species improves the resistance of the ASZ2 composition to aqueous attack relative to ASZ1. Since the removal of alkali species from the system directly impairs the dissolution mechanism for the silicate glass, it has a greater impact upon the minority network-forming and intermediate species such as Zn and Fe. This provides an explanation for the lower normalised mass loss for Fe and Zn in the ASZ2 system relative to ASZ.

The normalised dissolution rates for all five glasses demonstrated that the samples achieved a steady-state dissolution regime within 3-14 days of the beginning of the leaching period. There was negligible difference between the elements present. This can be attributed to the relatively low alkali content of the system and to the rate limiting effect of the mixed alkali-earth species.

### 5.2.3.2 Alkali Borosilicate System

The alkali borosilicate glasses explored consisted of only two compositions, the glass AB0 and the modified composition ABM which possessed a higher proportion of Na<sub>2</sub>O relative to Li<sub>2</sub>O but a lower alkali content overall. Both glasses demonstrated significantly increased values of normalised mass loss relative to the other glass systems explored, which can be attributed directly to the high proportion of both Na<sub>2</sub>O and Li<sub>2</sub>O in the system, as these are highly vulnerable to ion-exchange interactions with the aqueous solution.

The modified composition demonstrated lower values of normalised mass loss for Si and Fe but higher values from Na and Li. The increase in normalised mass loss for the alkali species present in the modified glass can be attributed to the increased susceptibility to aqueous attack caused by the increased proportion of Na<sup>+</sup> cations in the composition. Sodium is known to form relatively weak bonds with the silicate network relative to those formed by Li<sup>+</sup> <sup>(59)</sup> and so is known to possess superior resistance to aqueous attack relative to sodium. The overall decrease in mass loss for the network forming (and intermediate) species Si and Fe in the modified glass shows that the reduction in alkali content overall impairs the kinetic pathway for the dissolution of these species, as is consistent with generally held theory <sup>(151)</sup>.

Notably, both glasses from this series demonstrated an extended period of ion exchange before establishing a steady-state dissolution regime, not achieving steady-state until between 14 and 21 days into the experiment. This can be attributed to the high alkali content of the system.

### 5.2.3.3 Calcium Silicate System

The calcium silicate glasses explored consisted of two compositions, the calcium aluminosilicate CA0 and the calcium ferro-silicate CF0. Normalised mass losses at 28 days for these systems demonstrated small variations in comparison to those observed in the other systems. However, a discernible difference was notable between the systems in that the CF0 system demonstrated lower values for the normalised mass losses of Ca and Si. Also, the values of NL<sub>Si</sub> for both glasses demonstrate that the CA0 glass rapidly achieved a steady-state dissolution regime within 3 days of the start of the experiment, whereas the CF0 glass took 21 days to achieve a steady state. As with the alkali alkaline-earth silicate glasses, the steady state regime, region 4 in the 5 regions of glass dissolution model <sup>(146)</sup> can be attributed to the presence of a precipitate or gel layer on the surface of the glass preventing attack by the

aqueous solution. It is apparent that such a layer was more rapidly formed in the CA0 glass than in the CF0 glass. The values of  $NL_{Al}$  and  $NL_{Fe}$  show that the presence of Al and Fe in these glasses is directly linked to the time required for the formation of the gel layer. This difference can be attributed to the relative merits of Fe over Al in terms of the stability of the intermediate hydration phases formed during dissolution. It has been shown by Jantzen *et al* <sup>(151)</sup> that the  $Ca_{0.5}FeO_2$  phase is more stable than the  $Ca_{0.5}AlO_2$  phase which would lead to the dissolution kinetics to be inhibited. In addition, the hydrated phase of Fe is known to form an insoluble precipitate at the glass surface which would further inhibit dissolution <sup>(151)</sup>.

Notably, the values of normalised mass loss reported for the CA0 and CF0 glasses were significantly lower than those reported for either of the other compositional systems explored. This can be connected to the total absence of alkali species from the CA0 and CF0 glass composition, eliminating the primary species responsible for ion exchange reaction with the aqueous solution.

#### 5.2.3.4 Waste-loaded Samples

The waste-loaded samples were seen overall to demonstrate a relatively small but significant decrease in normalised mass loss for almost all of the constituent elements of the samples. A decrease in normalised mass loss has been reported previously in response to the waste-loading of host glass compositions used for nuclear waste vitrification <sup>(153)</sup>. However, in those instances the improvement in durability can be linked to the addition of various species which are known to have durability-enhancing properties in silicate glass systems. Given the IEX resin used for waste-loading in these experiments, the decrease in normalised mass loss cannot be attributed to the same factors here. The most plausible explanation can be found in the variation in  $Q^n$  speciation which was shown to occur in chapter 4.1 on the waste-loading of these alkali alkaline-earth silicate type compositions with IEX resin wastes, where the  $Q^n$  speciation is seen to increase on waste-loading, so demonstrating an increase in network polymerisation. Increased polymerisation of the glass network can be linked to the reduced extent of normalised mass loss due to the reduction in the proportion of sites within the silicate network which are vulnerable to attack by hydroxyl cations. Therefore the increased polymerisation of the waste-loaded glasses can be seen to provide an explanation for the decreased normalised mass loss values seen throughout the waste-loaded samples.

Alongside these results however, the leaching of the waste-loaded samples also demonstrated an increase in the normalised mass loss for Ca in the ASB and ASZ2 waste-loaded samples relative to the unloaded base glass samples. This effect is likely to be connected to the similarly high release of Ca which was observed in the ASZ1 base glass,

which was attributed to the relative proportions of alkaline-earth cations present in the system. It is possible that the depletion of alkali species, caused by the formation of an alkali sulphate phase may cause the  $\text{Ca}^{2+}$  cations present in the system to become increasingly vulnerable to aqueous attack, as already exacerbated by the higher proportion of  $\text{Ba}^{2+}$  cations present in the system relative to  $\text{Ca}^{2+}$  cations. This explanation is supported by the decrease in the normalised mass loss (Ca) seen in the AS0 and ASZ1 waste-loaded samples, since the  $\text{Ca}^{2+}$  cations present in the ASZ1 base glass were already vulnerable to aqueous attack and so the effect of waste-loading would be negligible and the relative balance of  $\text{Ba}^{2+}$  and  $\text{Ca}^{2+}$  cations in the waste-loaded AS0 sample would prevent the increase in normalised mass loss (Ca) on waste-loading.

Considering the normalised mass loss of sulphur in the waste-loaded samples, it is apparent that there is again a small but significant variation in the mass loss values demonstrated. The lowest mass loss values were demonstrated by the ASB sample and to a lesser extent the AS0 glass sample, whereas the ASZ2 waste-loaded sample demonstrated a value of normalised mass loss (S) which increased steadily over the experimental period and achieved a value roughly twice as large as that seen in the ASB sample. This relative difference in normalised mass loss value may be attributable to the capacity of the glass compositions for sulphur, and in considering the data presented in chapter 4.1, it is apparent that there is a rough inverse proportion between the proportion of sulphur retained and the normalised mass loss for sulphur which implies that the same effects govern both observations. The superior normalised mass loss (S) demonstrated by the ASB glass may therefore be attributable to the higher cation field index demonstrated by that glass composition due to its increased  $\text{Ba}^{2+}$  content, since the cation field index of a glass composition has been linked to the capacity of that composition for sulphur species <sup>(31)</sup>. Similarly, the higher values for normalised mass loss (S) demonstrated by the ASZ2 waste-loaded glass may be attributed to the lower proportion of alkali species present in the glass composition which have been shown to coordinate with sulphur species in glass in chapter 4.1. Considering the ASZ1 waste-loaded sample, it is apparent that there is a significant increase occurs in normalised mass loss (S) at the 7 day mark for the PCT experiment, which was also apparent in the normalised mass loss data for Na and Zn. These results may imply the presence of micro-inclusions present within a proportion of the powder samples used for the experiment, since they are consistent for the dissolution of sulphate salts of both sodium and zinc which may have formed during the waste-loading process. However, microscopy would be required to verify this explanation.

Considering the normalised mass loss values for caesium release, it is apparent that from the significant difference between the values for the release of caesium and the release of sulphur that the two waste-species do not interact in the waste-form to any significant extent. The normalised mass loss values and trends displayed are most comparable to those of the other alkali species present in the waste-forms, Na and Li, albeit slightly lower. It is therefore plausible to suppose that the caesium content of these glasses responds to the aqueous attack of the waste-forms in a similar manner to the other alkali species, that is, through ion-exchange with the solution. The slight decrease in the normalised mass loss values seen relative to Na can be attributed to the larger size of the Cs<sup>+</sup> ion which would experience greater rate limitation due to the flow of the ions through channels in the glasses silicate network. Since the variations in caesium normalised mass loss between the four samples are consistent with the observations made for the other alkali species, it is likely that the same factors as were seen to effect the normalised mass loss of Na and Li also apply to Cs loss.

#### **5.2.3.5 Durability of Base and Development Glasses.**

Considering the leaching experiments carried out upon the unloaded base glasses and development glasses there are significant differences in the normalised mass losses between the three main glass systems explored. Figure 5.2.26 and figure 5.2.27 shows the average normalised mass loss for Si and B for each of the three systems and for the MW and SON 68 compositions after leaching under similar conditions for 28 days, as derived from literature<sup>(146-147)</sup>. It can be clearly seen that the alkali borosilicate (AB) system demonstrates the highest value for  $NL_{Si}$ , where as the alkali alkaline-earth borosilicate system (AS) and the calcium silicate system (CS) demonstrate significantly lower extents of  $NL_{Si}$ . This pattern is repeated throughout all of the components of the systems. In comparison with the data from the MW and SON 68<sup>(146-147)</sup> compositions, it is notable that both the calcium silicate and alkali alkaline-earth silicate systems demonstrate significantly lower values of normalised mass loss (Si).

These variations in normalised mass loss can be attributed to a number of general compositional factors which can provide an explanation for the differences seen. The relatively high normalised mass loss seen in the AB glass system can be connected to the comparatively high alkali content of both glasses. This causes these composition to be particularly vulnerable to aqueous attack. The AS glass system demonstrates a lower extent of normalised mass loss by virtue of a lower overall alkali content, which is generally held to

be advantageous due to the reduced proportion material vulnerable to ion exchange, and by also by virtue of its high content of alkaline-earth species. These alkaline-earth species, although being susceptible to ion exchange with the solution, are advantageous for two reasons. Firstly they form hydrated gel layers on the surface of the glass<sup>(149-151)</sup> which are known to produce a protective barrier effect for the pristine glass surface, and secondly the mixture of alkaline-earth species present in most of the AS glass samples has been demonstrated to result in inhibited ion exchange processes by means of a “mixed alkali earth effect”<sup>(152)</sup>. The lowest normalised mass losses for the three glass systems explored, in the CS system, can be attributed primarily to the total absence of alkali elements in the composition, eliminating the primary species responsible for ion-exchange interactions with aqueous solutions.

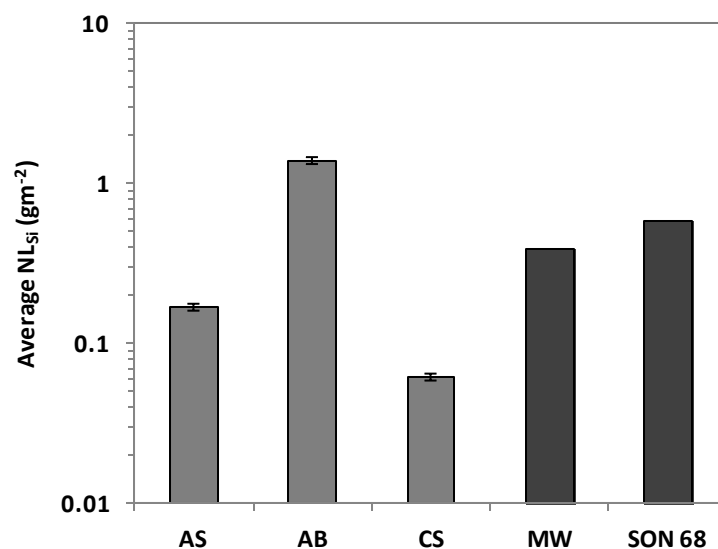


**Figure 5.2.26.** Comparison of the average normalised mass loss (Si) for the three glass systems investigated and two compositions described in literature (MW and SON 68) at 28 days. Error bars are 5% of the presented value.

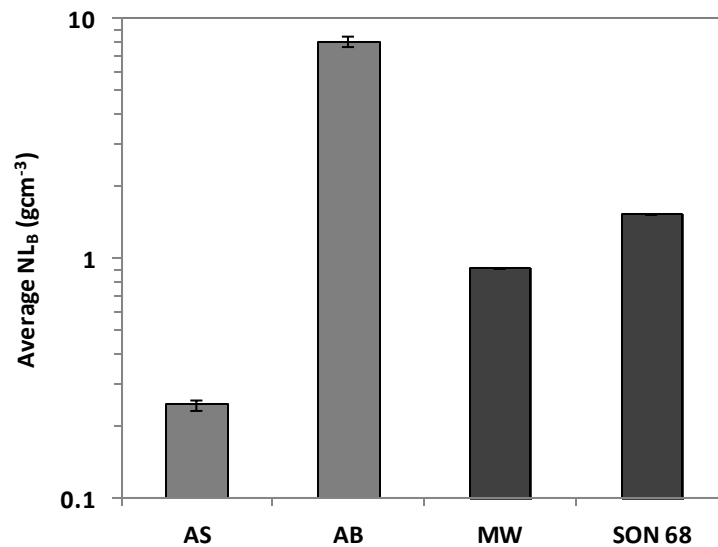


**Figure 5.2.27.** Comparison of the average normalised mass loss (B) for the two boron containing glass systems investigated and two compositions described in literature (MW and SON 68) at 28 days. Error bars are 5% of the presented value.

## 5.2.4 Conclusion

To summarise, it can be seen from this work that of the three developed glass systems presented here, glasses from both the alkali alkaline-earth silicate glass system and the calcium silicate glass system have demonstrated a resistance to aqueous attack which is comparable or superior to those glass compositions currently utilised for the vitrification of nuclear waste. In the case of the calcium silicate glasses, this effect is attributable to their lack of alkali content, reducing the effects of ion-exchange processes between the glass and solution. Similarly, the superior durability properties of the alkali alkaline-earth silicate glass samples were connected to the relatively low proportion of alkali oxides present in their composition, reducing the potential for ion-exchange reactions, and due to the presence of the mixed alkaline-earth oxides BaO and CaO, which alongside forming a buffering hydrated gel layer on the surface of the glass, creating a kinetic barrier against aqueous attack, have also been demonstrated to impair ion-exchange processes when mixed, in a form of mixed alkaline-earth effect. Further variations were apparent between the five alkali alkaline earth silicate compositions investigated, which demonstrated the effectiveness of ZnO additions in increasing the resistance of the silicate glass compositions against aqueous attack. It should be noted however that the increase in pH demonstrates that ion-exchange of alkali-earth species occurs in both alkali alkaline-earth silicate and calcium silicate glass compositions.

The alkali-borosilicate compositions which were explored demonstrated inferior properties relative to both of the other glass compositions explored and to the values found in the literature for compositions currently used in nuclear waste vitrification. These properties were connected to the high proportion of alkali oxides present in the glass composition, and to the absence of species which would form a rate retarding precipitated layer on the glass surface.

In addition to the experiments which were carried out on the developed glass composition, experiments carried out on glass samples which had been waste-loaded with a simulant ion-exchange resin waste demonstrated further improvements in terms of lower normalised mass losses. These were attributed to the effect of the waste upon the silicate network of the host glasses which was shown to increase the extent of polymerisation of the silicate network in chapter 4.1. This increase in polymerisation provided an explanation for the increased resistance to aqueous attack demonstrated by the waste loaded glass samples, due to depletion of sites in the silicate network vulnerable to attack by hydroxyl anions. In addition to this, it was found that the normalised mass loss for the sulphur content of the waste-form, originally a component of the simulant ion exchange resin waste, was determined by the same factors which determined the capacity of the host glass for sulphate species, that being the cation field index as shown by Bingham *et al* <sup>(31)</sup>. With regard to the caesium content of the waste-forms, it was found that the normalised mass loss values for caesium were highly similar to those displayed by the other alkali constituent of the waste-form, Na and Li. Although overall the normalised mass loss for Cs was found to be slightly lower than that of the other alkali species, which was attributed to the relatively large size of the caesium ion, it was found that the same trends as were apparent for alkali species in the four waste-forms were also apparent for Cs. Specifically, the compositions ASZ and ASZ2 demonstrated the highest extents of resistance to aqueous attack in general without a waste loading, although the ASZ1 glass was demonstrated to outperform the ASZ2 glass in experiments conducted with waste-loaded glass samples.

Overall it can be seen from this work that glasses from the calcium silicate glass system and alkali alkaline-earth silicate glass system demonstrate a resistance to aqueous attack that is superior to that which is demonstrated by more conventional alkali borosilicate glass compositions. Furthermore, waste-loading with simulant ion exchange resin waste has demonstrated that the overall resistance to aqueous attack is not impaired through waste-loading. As such, in terms of aqueous durability, these glass compositions are suitable for use in the vitrification of ion exchange resin wastes and may be appropriate for use in conjunction

with the vitrification of other waste streams which require long-term storage and immobilisation.

## Chapter 6. - Summary, Conclusion and Future Work

### 6.1 Summary

In summary, the work presented in Chapters 3, 4 & 5 has led to conclusions as follows.

The three sections that comprised Chapter 3 demonstrated that through the systematic compositional development of the calcium silicate and alkali alkaline-earth silicate systems investigated it was possible to produce glass compositions with physical properties which are more suitable for the vitrification of ion exchange resin wastes than existing glasses. Significant improvements were made to the alkali borosilicate system, which has already been the subject of considerable developmental work by multiple groups. In particular, in the alkali alkaline earth borosilicate glass system, it was demonstrated that by modifying the ratio of alkaline earth species present in the glass composition it was possible to effect a significant decrease ( $\sim 80$  °C) in the  $T_{liq}$  of the glass, which was attributed to the change in average modifier coordination in the silicate glass network by the mixture of alkaline-earth cations, as was indicated through solid state NMR. It was also noted the replacement of  $Ca^{2+}$  with transition metal cations, notably  $Zn^{2+}$ , resulted in both significant reduction to the  $T_{liq}$  of the glass system ( $\sim 100$  °C) and in an increased overall glass density. Furthermore, the presence of  $Zn^{2+}$  and  $Mn^{2+}$  was seen to increase the capacity of the glass for reduction by decreasing the proportion of reduced  $Fe^{2+}$  in the glass. These effects were attributed to the action of the transition metal cations as intermediate network forming cations with higher extents of coordination and a greater range of potential oxidation states available than the  $Ca^{2+}$  cation. It was found that the combination of these modifications, the replacement of  $Ca^{2+}$  cations with both  $Ba^{2+}$  and  $Zn^{2+}$  cations was found to be complimentary, due to their differing modifications to the alkali alkaline-earth silicate glass network, resulting in significant reductions in the  $T_{liq}$  of the glass ( $\sim 160$  °C below the base glass). In addition, the increased density achieved on the addition of  $Ba^{2+}$  and  $Zn^{2+}$  was further enhanced in combination, and the positive effect of the  $Zn^{2+}$  cation upon the iron oxidation state and the capacity of the glass for reduction was retained. As such, this glass composition, labelled throughout as ASZ1, demonstrates properties which are highly desirable for waste vitrification. The second glass composition, ASZ2, produced utilizing the benefits of the

ASZ1 composition with a 40% reduced alkali content, was demonstrated to have similar physical properties to the base glass composition, despite the reduction in alkali content.

The results and discussion presented in Chapter 4 demonstrated that the alkali alkaline-earth silicate glass and the compositions developed from it possessed properties suitable for the vitrification of IEX waste-loadings of up to 15 wt% in all five compositions, and 30 wt% in those compositions containing ZnO. The formation of phase-separated Na<sub>2</sub>SO<sub>4</sub> material was found to occur in the AS0 (base glass) and ASB compositions at 30 wt% loading due to the interaction of the anionic sulphate from the IEX resin with the glass. The presence of ZnO in the glass composition was found to prevent this due to the high affinity of Zn<sup>2+</sup> for sulphur species. In addition, the high affinity of the Zn<sup>2+</sup> cation for sulphur, along with the low value of cation field index for these glasses, resulted in the retention of a significant proportion of the sulphur content of the waste, potentially allowing for higher waste-loadings without the formation of phase-separated sulphate materials. All of the waste-loaded alkali alkaline-earth silicate glasses demonstrated high degrees of retention for caesium species from the IEX resin waste-loading, notably the ASZ1 glass demonstrated near total retention of Cs. The off-gas experiments demonstrated that this retention could be linked both to the lower melting temperature of the ASZ1 glass, allowing incorporation of the volatile species into the glass matrix at other temperatures, and due to the high viscosity of the glass which would inhibit the convection of glass containing volatile species from the bulk of the glass melt to the surface.

The analysis of the waste-forms and developed glasses produced for the alkali alkaline-earth silicate glass system showed that the developed glasses possessed lower values of normalized mass loss for Si, B, Na and Li over the initial 28 day period than had been demonstrated by alkali borosilicate glasses. Furthermore, waste-loaded glasses were found to have further reduced values of normalized mass loss. It was notable however that the Zn containing glasses presented higher values of normalised mass loss for Si and B after 28 days than were observed in the Zn free glass compositions. Furthermore, a sharp increase in normalized mass loss for Na, S and Zn in the ASZ1 waste-form presented possible evidence of the presence of microencapsulated phase separated material in the glass which may increase the vulnerability of waste-forms derived from this composition to aqueous attack. Due to the presence of Fe in the base glass composition, it was found that waste-forms derived from the alkali alkaline silicate system were resistant to the effect of  $\gamma$ -irradiation as would be expected from the radioactive inventory of IEX resin wastes.

The systematic development of the calcium silicate glass system explored the improvements that could be achieved through the replacement of the RO and R<sub>2</sub>O<sub>3</sub> content of the base glass system (CaO and Al<sub>2</sub>O<sub>3</sub> respectively). Significant improvements were found in glass compositions where the Al<sub>2</sub>O<sub>3</sub> content of the base glass was completely replaced by Fe<sub>2</sub>O<sub>3</sub>. The resulting calcium ferro-silicate glass was found to possess a superior capacity for reduction, due to the action of the Fe<sup>3+</sup> content of the glass as a reduction buffer, a lower melting temperature (~50 °C), and reduced viscosity due to the replacement of Al<sub>2</sub>O<sub>3</sub>. It was found that the replacement of Al<sub>2</sub>O<sub>3</sub> with Mn<sub>2</sub>O<sub>3</sub> produced similar results but to a reduced extent. It was also determined that the replacement of 10% of the CaO content with ZnO or SrO resulted in a significant (~90°C) drop in melting temperature from the base glass composition. However, it was found that this replacement reduced the glass forming ability of the system and resulted in increased incidence of crystallization in the glasses produced.

The performance of both the calcium silicate based glass (CA0) and the calcium ferro-silicate (CF0) glass on waste-loading were explored in Chapter 3. It was found that, primarily due to the high temperatures required for the melting of both glasses (~1350 °C and 1300 °C for CA0 and CF0 respectively), very low extents of sulphur retention were achieved at all waste-loadings explored. At higher waste loading (30 wt%) it was found that these glasses performed poorly with the CA0 glass, demonstrating the presence of a phase-separated sulphate phase and the CF0 glass being partially reduced to metallic iron by the organic content of the resin. Despite this poor performance upon waste-loading, in Chapter 4 it is demonstrated that these glasses demonstrated extremely low values for the normalised mass loss of Si and Ca, most probably due to the total absence of alkali species from the composition, removing the primary species vulnerable to ion exchange interactions with aqueous solutions.

The development of the alkali borosilicate composition explored the effect of varying the ratio of Na<sub>2</sub>O to Li<sub>2</sub>O in the glass system. It was demonstrated that by replacing the Li<sub>2</sub>O content with Na<sub>2</sub>O, the melting temperature could be reduced by as much as 140 °C. Replacement of a portion of the Na<sub>2</sub>O content with Li<sub>2</sub>O was shown to lead to an increase in the density of the glass and decrease in viscosity, representing an improvement to the melting properties of the glass. It was shown in Chapter 3 that the alkali borosilicate glass functioned poorly at high waste-loadings, demonstrating the formation of a significant phase separated gall layer at 30 wt% waste-loading. However, despite the poor quality of the waste-form produced, which was attributed to the interaction of the alkali content of the glass with the anionic content of the waste, the glass demonstrated a high degree of retention for Cs. Based on the observations made in chapter 3.2 this was attributed to the relatively low melting

temperature of the glass (~ 760 °C), which allowed the integration of Cs from the resin into the glass at lower temperatures. However, due to the presence of the phase separated material and unincorporated resin, it is unlikely that the full Cs content was adequately immobilized within the vitreous portion of the waste-form produced. The investigation of aqueous durability carried out in chapter 5.2 showed that the alkali borosilicate glasses investigated possessed inferior extent of aqueous durability in comparison to the other glass systems investigated. This was demonstrated most clearly in the comparison of normalized mass loss values for Si and Na with the alkali alkaline-earth silicate glass system, where the alkali borosilicate glasses demonstrated values of mass loss nearly an order of magnitude higher than those observed for glasses in the other system. This was attributed to the high alkali content of the alkali borosilicate glasses. However, despite the poor overall aqueous durability of the glass, chapter 5.1 demonstrated that, due to the presence of Fe in the base glass composition, waste-forms produced from this glass possessed an inherent resistance to damage from  $\gamma$ -ray irradiation.

In terms of scientific value section 5.1 demonstrated a significant advance in knowledge in term of how waste-forms respond to  $\gamma$ -ray irradiation, such as they would experience due to waste-loading with an active waste containing  $\gamma$ -emitting radionuclides. Most significantly it was demonstrated that upon irradiation with significant  $\gamma$ -radiation doses (equivalent of up to 8.7 years of storage), all the waste forms investigated, which included alkali borosilicate waste forms, and alkali alkaline-earth silicate waste form and a standard MW type simulant waste-form, displayed no evidence of radiation damage such as would be expected from such a large radiation dose. The glasses demonstrated no change in physical properties or to the coordination of the glass forming network. However, changes were observed in those glasses containing sulphur in the waste-loading, where significant changes in oxidation state were observed. It was also observed that the coordination of the  $\text{Fe}^{3+}$  content of the glass changed upon waste-loading. Based on that observation, and the observation that the extent of sulphur oxidation state change correlated directly to the ratio of Fe to S in the waste-form compositions, proved that the Fe content of the glass was responsible for the apparent lack of radiation induced defects. Fe and other transition metal cations have been linked to similar effects where the formation of defects though  $\beta$ -irradiation have been shown to be blocked <sup>(6,93,100)</sup>. In particular, Debnath *et al* <sup>(6)</sup> published a mechanism for this process where  $\text{Fe}^{3+}$  and  $\text{Fe}^{2+}$  cations present in a glass eliminated the free  $e^-$  and  $h^+$  produced by  $\beta$ -irradiation by switching oxidation state, preventing the formation of defects. To the author's knowledge, this is the first instance that such an effect has been found to occur in response to  $\gamma$ -ray irradiation, or for such an effect to have been reported in the context of various waste-forms for nuclear waste immobilisation.

## 6.2 Conclusion

In conclusion, it can be stated that this body of work has made a number of significant additions to the body of knowledge regarding the immobilisation of ion exchange resin wastes through vitrification, and to the wider areas of waste vitrification, the interaction of anionic species in glass and the interaction of radiation with glasses.

The two most significant outcomes of this work relate to the novel compositions developed from the alkali alkaline earth silicate glass system, most notably the ASZ1 glass composition which was developed in the course of this work, and the discovery of the  $\gamma$ -induced defect blocking mechanism of Fe in waste-forms developed for both IEX resin vitrification and in waste-forms currently utilised in industry.

The ASZ1 glass composition, and the other developed alkali-alkaline earth silicate glass compositions, could be considered to be the main output of this work in that the ASZ1 glass composition demonstrates significantly improved properties for the purpose of IEX resin vitrification. Specifically, the ASZ1 glass composition possessed a  $T_{\text{liq}}$  of  $805 \pm 10$  °C, the capacity for the incorporation of up to 50% more  $\text{SO}_3$  than observed in other glass compositions studied, a significant proportion of  $\text{Fe}_2\text{O}_3$  providing a buffer against reduction by organic species, and a proven resistance to the effects of  $\gamma$  irradiation and a high glass density, allowing for higher waste-loadings per unit volume. On waste-loading, this glass composition demonstrated a near total retention of the simulant Cs waste, which can be attributed to the low melting temperature and high viscosity of the glass. The ASZ1 glass, along with the other alkali alkaline-earth glasses investigated, was shown to demonstrate lower values of normalized mass loss under aqueous attack than have been quoted in literature for glasses currently utilised for waste vitrification. However it is important to note that at 30 wt% loading the ASZ1 glass did demonstrate the formation of an ZnO crystalline phase due to the interaction of the sulphur content of the waste with the  $\text{Zn}^{2+}$  cations present in the glass. Where the formation of this phase is preferable to the  $\text{Na}_2\text{SO}_4$  phase more typically formed due to the sulphur content of the waste, since this may be effectively re-incorporated into the glass, it still may prove to be problematic for waste vitrification on an industrial scale. However, it can be seen that this glass composition in itself represents a significant advance in terms of its capacity for anionic species, resistance to reduction and retention of volatile species as well as its apparent resistance from both aqueous attack and from radiation induced damage. The ASZ1 glass composition and the other alkali alkaline-earth silicate glass compositions therefore have the potential to significantly improve the current situation with regards to the accumulating inventory of IEX resin waste, in providing

a possible route for the vitrification of these wastes. Due to the selection of beneficial properties demonstrated by these glasses, it is also highly likely that they may be of use for the vitrification of other problematic wastes.

The discovery of the  $\gamma$ -radiation blocking mechanism of Fe in these glasses was tangential to the main aim of this work, but should also be noted as a significant output of the work due to its wide ranging implications for the long term radiation durability of any glass used in the vitrification of radioactive wastes. In demonstrating that Fe can inhibit the formation of electronic defects in a glass which is exposed to  $\gamma$  radiation, it is shown that the presence of Fe potentially can significantly improve the long term durability of a waste-form. The mechanism by which Fe prevented the formation of electronic defects in the waste-forms was identified, based upon the work of Debnath *et al* and others <sup>(6,93,100)</sup> in which similar effects have been reported to occur in glasses exposed to  $\beta$ -radiation. To the author's knowledge, this work represents the first instance of this mechanism being reported in conjunction with  $\gamma$ -irradiation or in the context of waste-forms intended for nuclear waste immobilization.

Aside from those mentioned above, a number of other outcomes from this work are of significance. The systematic development work carried out on the alkali borosilicate and calcium silicate glass systems demonstrated that improvement to the physical properties and melting properties of these glass system is possible with the effect of increasing their usefulness for the vitrification of a range of different wastes, including potentially the vitrification of IEX resin wastes, although further work would be required to eliminate the problems associated with the high melting temperature and low anion capacity of the calcium silicate and alkali borosilicate glasses respectively.

The waste-loading of the developed glasses, as reported in Chapter 4.1 demonstrated that the correlation between cation field strength index and sulphur retention, as proposed by Bingham *et al* <sup>(32)</sup> is supported by the glass compositions explored in this work, in that decreased values of cation field index were found to associate with the increased retention of sulphur species in both the alkali alkaline earth silicate and alkali borosilicate glass systems. The work presented in Chapter 4.2, with regards to the loss of sulphur and caesium through off-gas during vitrification, presented a number of important conclusions. It was demonstrated that the loss of sulphur occurred in two stages during the vitrification process, firstly through the degradation of the resin and then secondly through the volatilisation of sulphur species not incorporated into the glass. The loss of sulphur through off-gas was found to be independent of the loss of caesium through off-gas, which was observed to occur

to significant degree only above  $\sim 1000$  °C. As a consequence, it can be seen that the loss of sulphur during the vitrification of IEX resin wastes is of reduced concern and it is more important that by limiting the vitrification temperature to temperatures lower than 1000 °C higher degrees of caesium retention can be achieved. Finally, work presented in both Chapter 3.1 and 4.1 showed that the presence of  $S^{2-}$  associated with  $Fe^{3+}$  (the amber chromophore) can be detected through a characteristic Raman absorption band at  $400\text{ cm}^{-1}$  which can potentially be utilised to characterise sulphur oxidation state in glasses containing  $Fe^{3+}$ .

### 6.3 Recommendation for Future Work

In terms of future work that could be carried out based upon that presented here, the author would recommend work as follows. Firstly, due to the beneficial properties of the alkali alkaline-earth silicate glass compositions, and specifically the ASZ1 glass composition, in the context of IEX resin vitrification which have been identified in this work, the author would recommend that further studies should be carried out on these glass compositions. Specifically, this should include investigation into the vitrification of ion exchange resin waste on a larger scale utilising conventional waste vitrification technology in order to investigate the performance of the glass composition under these conditions, and identify whether or not the formation of the ZnO crystalline phase would be problematic for the use of the glass composition on an industrial scale. Secondly, given the capacity of these glass compositions for anionic species, organic production and volatile species, and their lower melting temperature and superior aqueous durability, these glass compositions possess potential for the vitrification of other problematic waste streams, both within and outside of the nuclear industry. The author would therefore recommend that work could be carried out to investigate the potential of these glasses for the vitrification of their waste streams such as PCM (plutonium containing material) waste streams and toxic industrial waste streams.

Finally, with regards to the observation made of iron-containing glasses under  $\gamma$ -irradiation and the prevention of defect formation through the action of iron, the author would recommend that three systematic studies should be carried out to further explore and understand this effect. Firstly the author would recommend the investigation of the effect of differing rates of irradiation upon the glass, in order to determine if there is a kinetic limitation to the mechanism through which defects are prevented from forming. Secondly, the author would recommend that a series be carried out with a range of iron concentrations to investigate the dependence of defect prevention upon iron content. Finally the author would recommend a series investigating the capacity of other transition metal cations with

multiple oxidation states in glass in order to determine the extent to which this defect-blocking mechanism extend to other elements, as is implied by work carried out in regards to  $\beta$ -irradiation.

## 7. References

1. **C. Cicero-Herman, P. Workman, K. Poole, D. Erich, and J. Harden**, *Proc. Int. Symp. Waste Man. Tech. Ceram. Nucl. Ind.* WSRC-MS-98-00392.
2. **N. Hutson, and C. Crawford**, *WM'02 Conference Proc.*, (2002) 1-9.
3. **P. A. Bingham, N. C. Hyatt, R. J. Hand and S. D. Forder**, *Glass Tech. A*, 54 (2013) 1.
4. **C. P. Kaushik, R. K. Mishra, P. Sengupta, A. Kumar, D. Das, G. B. Kale and K. Raj**, *J. Nuc. Mater.*, 358 (2006) 129.
5. **J. M. Schofield, P. A. Bingham, and R. J. Hand**, *Ceramic Transactions*, 207, (2008) 69.
6. **R. Debnath**, *J Mater. Res*, 16 (2001) 127.
7. **M. I. Ojovan, G. A. Petrov, S. A. Dmitriev, B. G. Trusov, K. N. Semenov and V. L. Klimov**, *IAEA Publication*, IAEA-SM-357/49
8. "Application of Ion exchange Processes for the Treatment of Radioactive Waste and Management of Spent Ion exchangers", *IAEA Technical Report No.408*
9. **R. Kunin**, "Ion exchange Resins 2<sup>nd</sup> Edition", *Wiley*, (1958)
10. **A H. Eccles**, "Nuclear Fuel Cycle Technologies – Sustainable in the Twenty First Centaury", *Solvent Extraction and Ion Exchange*, 18 633-654 (2000)
11. **C. M. Jantzen, D. K. Oeeler and C. A. Cicero**, *Westinghouse Savannah River Co.*, WSRC-MS-95-0518
12. **N. Hamodi, K. Papadopoulou, T. Loe and T. Abram**, *New Jou. of Glass and Ceramic*, 2 (2012) 111.
13. **N. C. Hyatt and M. James**, *Nucl. Eng. Int.*, 58 (1) (2013) 10.
14. **J. Tapia-Fabela, M. Pacheco-Pacheco, J. Pacheco-Sotelo, C. Torres-Reyes, R. Valdivia-Barrientos, J. Benitez-Read, R. Lopez-Callejas, F. Ramos-Flores, S. Boshle and G. Zissis**, *Plasma Science and Technology*, 9 (2007) 721.

15. **P. K. Baumgarten, M. A. Ebra, L.L Kilpatrick and L. M. Lee**, *ANS Waste Management Proc.* DP-MS-80-91 (1981)
16. **J. P. Doherty and J. C. Marek**, *US Patent*, 4840765.
17. **T. N. Sargent**, *Clemson University, Thesis*, August 1994.
18. **C. Girold, B. Barthelemy, N. Cerqueira, C. Vandensteendam and J. M. Baronnet**, *WM'01 Conference* (2001).
19. **N. E. Bibler, J. P. Bibler, M. K. Andrews and C. M. Jantzen**, *Westinghouse Savannah River Co.*, WSRC-MS-91-465.
20. **E. E. Smeltzer, and M. C. Skriba**, *US Patent* 4530723.
21. **V. A. Morozov**, "Waste Management Practices in Selected European Countries", *IAEA Publication* (1978).
22. **N.H. Hamodi and Y. Iqbal**, *J. Pakistani Mater. Sci.*, 3 (2009) 3.
23. **J. Lim, and J. Wang**, *J. Haz. Mater.*, B135 (2006) 443.
24. **F. Frizon, and C. Cau-dit-Coumes**, *J. Nuc. Mater.*, 359 (2006) 162.
25. **R. E. Streatfield**, *Proc. Int. Topical Meet. On Nuc. And Haz. Waste Mang. Spectrum* 96, (2006) 18.
26. **C. J. Shi and R. Spence**, *Crit. Rev Environ. Sci. Techno.*, 34 (2004) 391.
27. **V. Petitjean, C. Fillet, R. Boen, C. Veyer and T. Flament**, *WM'02 Conference*, (2002)
28. **I. W. Donald, B. L. Metcalfe and R. N. J. Taylor**, *Jou. Materials Science*, 32 (1997) 5851.
29. **N. D. Hutson and C. A. Herman**, *Westinghouse Savannah River Co.*, WSRC-MS-2000-00884.
30. **R. S. Juang and T. S. Lee**, *Jou. Haz. Mater.* B92 (2002) 301.

31. **P. A. Bingham and R. J. Hand**, *MRS Bulletin*, 43 (2008) 1679.
32. **D. Manara, A. Grandjean, O. Pinet, J. L. Dussossoy and D. R. Neuville**, *Mat. Res. Soc. Symp. Proc.* 932 (2006).
33. **I. A. Sobolev, F. A. Lifanov, S. V. Stefanovskii, A. P. Kobelev, V. N. Zakharenkov, N. D. Musatov and N. V. Krylova**, *Glass and Ceramics*, 47 (1990) 240.
34. **K. Choi, C. W. Kim, J. K. Park, B. C. Park, K. H. Yang, S. W. Shin, P. Brunelot and T. Flament**, *Transactions SMiRT*, 16 (2001) 01838.
35. **P. A. Bingham, N. C. Hyatt and R. J. Hand**, *Glass Tech. A*, 53 (2012) 83.
36. **R. Todd Hunter, M. Edge, A. Kalivretenos, K. M. Brewer, N. A. Brock, A. E. Hawkes and J. C. Fanning**, *J. Am. Ceram. Soc.*, 72 (1989) 943.
37. **M. Fujisawa and G. Katagiri**, *The Japan Soc. for Mech. Eng.*, 45 (2002) 621.
38. **M. A. Dubois, J. F. Dozoi, C. Nicotra, J. Serosé and C. Massiani**, *J. Analytical and Appl. Pyrolysis*, 31 (1995) 129.
39. **V. M. Manakov**, *Russian Journal of Inorganic Chemistry*, 17 (1972) 276.
40. **D. Manara, A. Grandjean, O. Pinet, J. L. Dussossoy and D. R. Neuville**, *J. Non-Cryst. Sol.*, 353 (2007) 12.
41. **A. Dietzel**, *Glastech. Ber.*, 22 (1948) 41.
42. **A. Dietzel**, *Glastech. Ber.*, 22 (1948) 81.
43. **M. I. Ojovan and W. E. Lee**, "An Introduction to Nuclear Waste Immobilisation", *Wiley*, (2005).
44. **O. J. McGann, P. A. Bingham, R. J. Hand, A. S. Gandy, M. Kavcic, M. Zitnik, K. Bucar, R. Edge and N. C. Hyatt**, *J. Nuc. Mater.*, 429 (2012) 353.
45. **J. Ramkumar, S. Chandramouleeswaran, V. Sudarsan, and R. K. Mishra**, *J. Haz. Mater.*, 172 (2009) 457.

46. **R. K. Mishra, V. Sudarasan, C. P. Kaushik, K. Raj, S. K. Kulshreshtha and A. K. Tyagi**, *J. Non-Cryst. Solids*, 353 [16-17] (2007) 1612.
47. **J. E. Shelby**, "Introduction to Glass Science and Technology 2nd Edition", RSC, (2005).
48. **H. Darwish, and M. M. Gomaa**, *J. Mat. Sci.: Mat. Electron*, 17 (2006) 35.
49. **M. Toderas, S. Filip and I. Ardelean**, *J. Optoelectron Adv. Mater.*, 8 (2006) 1121.
50. **P. Zhao, S. Kroeker and J. Stebbins**, *J. Non-Cryst. Solids*, 276 (2000) 122.
51. **M. J. Toplis, B. D. Dingwell and L. Tommaso**, *Geochim. Cosmochim. Acta.*, 61 (1997) 2605.
52. **F. Angeli, J. M. Delaye, T. Charpentier, J. C. Petit, D. Ghaleb and P. J. Faucon**, *J. Non-Cryst. Solids*, 76 (2000) 132.
53. **B. O. Mysen, D. Virgo and I. Kurshiro**, *Am. Miner.*, 66 (1981) 678.
54. **C. Rajyasree and K. Rao**, *J. Non-Cryst. Solids*, 357 (2011) 836.
55. **J. E. Shelby**, *J. App. Phys.*, 50 (1979) 8010.
56. **S. K. Lee, B. O. Mysen and G. D. Cody**, *Phys. Rev. B*, 68 (2003) 21420.
57. **M. L. Huggins and K. H. Sun**, *J. Am. Ceram. Soc.*, 26 (1943) 4.
58. **M. M. Islam, D. Holland, A. P. Howes and C. R. Scales**, *Phys. Chem. Glasses: Eur. J. Glass Sci. Technol. B*, 51 (2010) 137.
59. **M. B. Volf**, "Chemical Approach to Glass", *Elsevier*, (1984).
60. **N. A. Toropov, F. Y. Galakhov and I. A. Bondar**, *Izvest. Akad. Nauk.*, 6 (1956) 642.
61. **J. F. Stebbins, J. V. Oglesby and Z. Xu**, *Am. Miner.*, 82 (1997) 1116.
62. **B. O. Mysen, D. Virgo and F. A. Seifert**, *Am. Miner.*, 69 (1984) 834.

63. **P. A. Bingham, J. M. Parker, T. Searle, J. M. Williams and I. Smith**, *Comp. Rend. Chimie.*, 5 (2002) 787.
64. **S. Feller, T. Mullenbach, M. Franke, S. Bista, A. O'Donovan-Zacanda, K. Hopkins, D. Starkenberg, J. McCoy, D. Leipply, J. Stansberry, E. Troendle, M. Affatigato, D. Holland, M. E. Smith, S. Kroeker, V. K. Michaelis and J. E. C. Wren**, *Phys. Chem. Glasses: Eur. J. Glass Sci. Technol. B*, 53 (2012) 210.
65. **B. O. Mysen**, *An. Rev. Earth Planet Sci.*, 11 (1983) 75.
66. **V. E. Eremyashev, A. A. Osipov and L. M. Osipova**, *Glass and Ceram.*, 68 (2011) 3.
67. **J. E. Huheey, E. A. Keiter and R. L. Keiter**, "Inorganic Chemistry: Principles of Structure and Reactivity, 4th Edition," *Harper Collins*, (1993).
68. **J. Serra, P. Gonzalez, S. Liste, C. Serra, S. Chiussi, B. Leon, M. Perez-Amor, H. O. Lanen and M. Hupa**, *J. Non-Crystalline Solids*, 332 (2003) 30.
69. **P. Piscella and M. Pelino**, *Jou. Eur. Ceramic Soc.*, 25 (2005) 1855.
70. **S. A. MacDonald, C. R. Scardt, D. J. Masiello and J. H. Simmons**, *Jou. Non-Cryst. Solids*, 275 (2000) 72.
71. **M. Darby-Dyar, D. G. Agresti, M. W. Schaefer, C. A. Grant and E. C. Sklute**, *Ann. Rev. Earth Planet Sci.*, 34 (2006) 83.
72. **W. Vogel, A. Rehfeld and H. Ritschel**, *Silicate Industrie*, 32 (1967) 161.
73. **R. Lamoreaux and D. Hidenbrand**, *J. Phys. Chem. Re. Data*, 13 (1984) 152.
74. **F. C. Kracek**, *J. Am. Chem. Soc.*, 61 (1939) 2863.
75. **A. R. West**, *J. Am. Ceram. Soc.*, 59 (1976) 124.
76. **J. Zhong and P. J. Bray**, *J. Non-Cryst. Sol.* 111 (1989) 67.
77. **P. A. Bingham, R. J. Hand and C. R. Scales**, *2006 MRS Spring Meeting, MRS Proceedings* (2006) 932.

78. **W. E. Lee, M. I. Ojovan, M. C. Stennett and N. C. Hyatt**, *Adv. App. Ceramics*, 105 (2006) 3.
79. **K. Baert, W. Meulebroeck, H. Wouters, P. Cosyns, K. Nys, H. Thienpont and H. Terry**, *Jou. Raman. Spec*, 42 (2011) 1789.
80. **D. A. McKeown, I. S. Muller, H. Gan, I. L. Pegg and C. A. Kendziora**, *J. Non-Cryst. Solids*, 288 (2001) 191.
81. **W. L. Konijnendijk and J. H. J. M. Buster**, *J. Non-Cryst. Solids*, 23 (1977) 401.
82. **M. Micoulaut**, *C. R. Chimie*, 5 (2002) 825.
83. **P. A. Bingham, A. J. Connelly, N. C. Hyatt and R. Hand**, *J. Int. Mater. Rev.*, 56 (2011) 226.
84. **G. Mosel, TH. Hubert, M. Nofz, R. Brenneis, P. Kocher and G. Kley**, *Jou. Mater. Sci.*, 36 (2001) 5017.
85. **D. S. Kim and P. Harma**, *J. Am. Ceram.*, 75 (1992) 2959.
86. **M. J. Snyder, M. G. Mesko and J. E. Shelby**, *J. Non-Cryst. Sol*, 352 (2006) 669.
87. **V. A. Morozov**, *IAEA Bull.*, 21 (1979) 17.
88. **J. Sheng**, *Glass Technol. Eur. J. Glass. Sci. Technol. A*, 45 (2004) 153.
89. **W. J. Weber**, *Nucl. Inst. Meth. Phys. Res. B*, 32 (1998) 471.
90. **W. J. Weber, R. C. Ewing, C. A. Angell, G. W. Arnold, A. N. Cormack, J. M. Delaye and D. L. Griscom**, *J. Mater. Res.*, 12 (1997) 946.
91. **R. C. Ewing, W. J. Weber and F. W. Clinard Jr**, *Prog. Nucl. Energ.*, 29 (1995) 63.
92. **K. Sun, L. M. Wang, R. C. Ewing and W. J. Weber**, *Nucl. Inst. Meth. Phys. Res. B*, 218 (2004) 368.
93. **E. Malchukova, B. Boizot, G. Petite and D. Ghaleb**, *Eur. Phys. J. Appl. Phys.*, 45 (2009) 10701.

94. **T. Mizutani**, *Jour. Non-Cryst. Sol.*, 181 (1995) 123.
95. **H. Hosono and N. Matsunami**, *Nuc. Inst. Meth. Phys. Res. B*, 141 (1998) 566.
96. **G. Brown**, *J. Mater. Sci.*, 10 (1975) 1841.
97. **G. Brown**, *J. Mater. Sci.*, 10 (1975) 1481.
98. **E. A. Vanina, M. A. Chibisova and S. M. Sokolova**, *Glass Ceram.*, 63 (2006) 11.
99. **W. A. Zdaniewski, T. E. Easler and R. C. Bradt**, *J. Am. Ceram. Soc.*, 66 (1983) 311.
100. **N. A. Eissa, N. H. Sheta, W. M. El-Meligy, S. M. El-Minyawi and H. A. Sallam**, *Rad. Phys. Chem.*, 44 (1994) 35.
101. **J. A. C. Marples**, *Glass Technol.*, 29 (1988) 230.
102. **P. A. Bingham, N. C. Hyatt, R. J. Hand and C. R. Wilding**, *Sci. Basis Nuc. Was. Manag. XXXII, Mat. Res. Soc. Symp. Proc.*, 1124 (2009) 161.
103. **P. A. Bingham, A. J. Connelly, R. J. Hand and N. C. Hyatt**, *Nucl. Future.*, 6 (2010) 250.
104. **W. R. Davis**, *Trans. Brit. Ceram. Soc.*, 67 (1968) 515.
105. **H. Matzke, E. Toscano**, *J. Am. Ceram. Soc.*, C138 (1986) 69.
106. **J. Shelby**, *J. Appl. Phys.*, 51 (1980) 2561.
107. **A. J. Connelly, R. Hand, P. A. Bingham and N. C. Hyatt**, *J. Nucl. Mater.*, 408 (2011) 188.
108. **M. Kavčič, A. Karydas and Ch. Zarkadas**, *Nucl. Instr. Meth. B*, 222 (2004) 601.
109. **M. Žitnik, M. Kavčič, K. Bučar and A. Mihelič**, *Nucl. Instr. Meth. B*, 267 (2009) 221.
110. **P. A. Bingham, J. M. Parker, T. Searle, J. M. Williams and K. Fyles**, *J. Non-Cryst. Solids*, 253 (1999) 203.

111. **P. A. Bingham and C. M. Jackson**, *J. Archaeol. Sci.*, 35 (2008) 302.
112. **C. R. Bamford**, “Colour Generation and Control in Glass: Glass Science and Technology 2”, *Elsevier*, 1977.
113. **P. Piscilella and M. Pelino**, *J. Eur. Ceram. Soc.*, 25 (2005) 1855.
114. **F. H. El-Batal, E. M. Khalil, Y. M. Hamdy, H. M. Zidan, H. S. Aziz and A. M. Abdelghany**, *Silicon*, 2 (2010) 41.
115. **Y. K. Lee, Y. L. Peng and M. Tomozawa**, *J. Non-Cryst. Solids*, 222 (1997) 125.
116. **J. Kaewkhao, W. Siriprom, S. Insiripong, T. Ratana, C. Kedkaew and P. Limsuwan**, *J. Phys.: Conf. Series*, 266 (2011) 012012.
117. **P. L. King, C. D. M. Dufresne and K. N. Dalby**, *Lunar Planet Sci.*, XXXIX (2008) 2256.
118. **A. A. Ahmed, N. A. Sharaf and R. A. Condrate**, *J. Non-Cryst. Solids*, 210 (1997) 59.
119. **T. Tsujimura, X. Xue, M. Kanzaki and M. J. Walter**, *Geochim. Cosmochim. Acta*, 68 (2004) 5081.
120. **M. Lenoir, D. R. Neuville, M. Malki and A. Grandjean**, *J. Non-Cryst. Solids*, 356 (2010) 2722.
121. **K. T. Winther, E. B. Watson and G. B. Korenowski**, *Amer. Mineral*, 83 (1998) 1141.
122. **D. A. McKeown, A. C. Buechele, C. Viragh and I. Pegg**, *J. Nucl. Mater.*, 399 (2010) 13.
123. **P. McMillan**, *Amer. Mineral*, 69 (1984) 622.
124. **C. Jegou, R. Caraballo, J. De Bonfils, V. Broudic, S. Peugeot, T. Vercoouter and D. Roudil**, *J. Nucl. Mater.*, 399 (2010) 68.

125. **M. Mercier, A. Di Muro, D. Giordano, N. Metrich, P. Lesne, M. Pichavant, B. Scaillet, R. Clocchiatti and G. Montgnac**, *Geochim. Cosmochim. Acta*, 73 (2009) 197.
126. **V. Magnien, D. R. Neuville, L. Cormier, J. Roux, J. L. Hazemann, O. Pinet and P. Richet**, *J. Nucl. Mater.*, 352 (2006) 190.
127. **A. Di Muro, N. Metrich, M. Mercier, D. Giordano, D. Massare and G. Montagnac**, *Chem. Geol.*, 259 (2009) 78.
128. **B. G. Parkinson, D. Holland, M. E. Smith, C. Larson, J. Doerr, M. Affatigato, S. A. Feller, A. P. Howes and C. R. Scales**, *J. Non-Cryst. Solids*, 354 (2008) 1936.
129. **V. Magnien, D. Neuville, L. Cormier, J. Roux, J. Hazemann, D. De Ligny, S. Pascarelli, I. Vickridge, O. Pinet and P. Richet**, *Geochim. Cosmochim. Acta*, 72 (2008) 2157.
130. **M. Lenoir, A. Grandjean, S. Poissonnet and D. R. Neuville**, *J. Non-Cryst. Solids*, 355 (2009) 1468.
131. **K. Klimm and R. E. Botcharnikov**, *Amer. Mineral*, 95 (2010) 1574.
132. **S. N. White**, *Chem. Geol.*, 259 (2009) 240.
133. **G. A. Hope, R. Woods and C. G. Munce**, *Miner. Eng.*, 14 (2001) 1565.
134. **D. W. Bishop, P. S. Thomas and A. S. Ray**, *Mater. Res. Bull.*, 35 (2000) 1123.
135. **R. Cases and D. L. Griscom**, *Nucl. Instr. Meth. Phys. Res. B*, 1 (1984) 503.
136. **F. Y. Olivier, B. Boizot, D. Ghaleb and G. Petite**, *J. Non-Cryst. Solids*, 351 (2005) 1061.
137. **D. L. Griscom, C. I. Merzbacher, R. A. Weeks and R. A. Zuhr**, *J. Non-Cryst. Solids*, 258 (1999) 34.
138. **E. J. Friebele, L. K. Wilson, A. W. Dozier and D. L. Kinser**, *Phys. Stat. Sol. (B)* 45 (1971) 323.

139. **P. A. Bingham, A. J. Connelly, R. J. Hand, N. C. Hyatt, P. A. Northrup, R. Alonso Mori, P. Glatzel, M. Kavčič, K. Bučar and R. Edge**, *Glass Technol. Eur. J. Glass Sci. Technol. A*, 51 (2010) 63.
140. **D. L. Griscom**, *J. Non-Cryst. Solids*, 67 (1984) 81.
141. **E. A. Zhilinskaya, V. N. Lazukin, E. A. Bychkov and I. L. Likholit**, *J. Non-Cryst. Solids*, 119 (1990) 263.
142. **L. Backnaes, J. Stelling, H. Behrens, J. Goettlicher, S. Mangold, O. Verheijen, R. G. C. Beerkens and J. Deubener**, *J. Am. Ceram. Soc.*, 91 (2008) 721.
143. **B. Boizot, N. Ollier, F. Olivier, G. Petite, D. Ghaleb and E. Makchukova**, *Nucl. Inst. Meth. Phys. Res. B*, 240 (2005) 146.
144. **H. D. Schrieber, R. W. Fowler and C. C. Ward**, *Phys. Chem. Glasses*, 34 (1993) 66.
145. "Standard Test Methods for Determining Chemical Durability of Nuclear , Hazardous and Mixed Waste Glasses and Multiphase Glass Ceramics: The Product Consistency Test (PCT)" *ASTM Standard*, Designation: C 1285-02
146. **P. Frugier, S. Gin, Y. Minet, T. Chave, B. Bonin, N. Godon, J. E. Lartigue, P. Jollivet, A. Ayral, L. De Windt and G. Santarini**, *J. Nuc. Mater.*, 380 (2008) 8.
147. **N. J. Cassingham, P. A. Bingham, R. J. Hand and S. D. Forder**, *Glass Tech. Eur. J. Glass Sci. & Tech. A*, 49 (2008) 21.
148. **E. Vernaz, S. Gin, C. Jegou and I. Ribet**, *J. Nuc. Mater.*, 298 (2001) 27.
149. **B. Grambow and R. Muller**, *J. Nuc. Mater.*, 298 (2001) 12.
150. **S. Gin, C. Guittonneau, N. Godon, D. Neff, D. Rebiscoul, M. Cabie and S. Mostefaoui**, *Jou. Phys. Chem. C*, 115 (2011) 18696.
151. **C. M. Jantzen, K. G. Brown and J. B. Pickett**, *Int. J. of Ap. Glas. Sci.*, 1 (2010) 38.
152. **M. Todorovic and L. Radonjic**, *Ceramics Int.*, 15 (1989) 383.
153. **P. Trocellier**, *Ann. Chim. Sci. Mat.*, 26 (2001) 113.

154. **B. Voutou and E. Stefanaki**, *Physics of Advanced Materials Winter School 2008*, 1.
155. **N. V. Tkachenko**, "Optical Spectroscopy: Methods and Instrumentations", *Elsevier*, 2006.
156. **S. D. Forder, P. A. Bingham, O. J. McGann, M. C. Stennett and N. C. Hyatt**, "Mossbauer Studies of materials used to immobilise industrial wastes", *Hyperfine Interact* DOI 10.1007/s10751-012-0700-x).
157. "EPR Introductory Workshop Handbook", *National EPR Research Facility and Service*, <http://www.epr.chemistry.manchester.ac.uk/epr-handbook/> (Sept 2013).
158. **M. Duer**, "Introduction to Solid-State NMR Spectroscopy" *Blackwell Publishing*, 2004.
159. **S. D. Kelly, D. Hesterberg, B. Ravel**, *Mineralogical Methods*, Part 5 (2007).

## **8. Appendix**

### **8.1 Overview of Experimental Procedures**

#### **8.1.1 Glass Batch Preparation**

All glass batches were produced using the following procedure. Firstly, the quantities of raw chemicals required for the glass batch were calculated, with particular attention given to adjusting the quantities to account for the breakdown of certain batch components such as carbonates. Once the required quantities had been calculated, the batch was made up from powdered raw materials of a purity of 99 % or greater. Raw materials were weighed out to an accuracy of  $\pm 0.1$  g and mixed inside a sealed plastic container to ensure a reasonable degree of homogeneity within the batch. The batch material was then put into a crucible for melting. Batch sizes ranged from 100 – 300 g in mass.

#### **8.1.2 Glass Melting and Fabrication**

Each glass melt was carried out using one of two different procedures, depending on the requirement for the stirring of the glass melt or upon the risk presented by the potential of a particular melt for harmful gas emission. Regardless of the procedure used, all melts were carried out in a Zr-stabilised platinum crucible unless a significant quantity of Cl or S was present in the glass melt, in which case re-crystallised alumina crucibles were used.

In the first procedure, used for glass melts which required stirring or which did not pose a risk for gas emission, a top-loading electrical furnace was used. These furnaces were heated to temperature prior to use and maintained at a static temperature for the duration of the melt. Crucibles containing all, or a portion of, the glass batch were put into the furnace to begin the melting process and, if not all of the batch had been put in, a 'filling-on' process was used in which once the batch had melted down sufficiently, the crucible was removed from the furnace whilst hot and the remaining batch material was put into the crucible, and then the crucible was returned to the furnace. In cases where a large amount of batch was left over this process was repeated multiple times until all batch material had been input into the crucible. Once all batch material was in the furnace, the material was given 1 hour to achieve

a stable equilibrium. Subsequently a stirrer paddle was lowered into the glass melt and used to stir the melt at a rate of approximately 30 rpm. The stirrer paddle was composed from the same material as the crucible. Stirring was conducted for 2 hours, subsequent to which the stirring paddle was removed from the glass melt. At this point, the crucible was removed and the contents poured into a steel block mould which had been pre-heated to a 100 - 200 °C. The poured glass was allowed to solidify and was then put into a preheated muffle furnace for annealing. The glass block was annealed by holding the sample at its  $T_g$  for 1 hour and then allowing it cool to room temperature at a rate of 1 °C per minute. Where a re-crystallised alumina crucible and stirrer had been used, it was inspected for corrosion.

In the second procedure, used for glass melts which posed a risk of producing hazardous gas emissions, a electrical muffle furnace contained within a fume hood was used. The crucible containing the glass batch was loaded into the furnace at room temperature. The full batch was loaded into the crucible and the filling-on process was not used. Once the crucible was loaded into the furnace, this was heated to the melting temperature at a rate of 2 °C per minute. Once the melting temperature had been achieved, the temperature was maintained for three hours subsequent to which the crucible was removed from the furnace at temperature and the glass was poured. As with the previous procedure, the glass was poured into a steel block mould and then annealed by holding the glass at  $T_g$  for 1 hour and then allowing the glass to cool at a rate of 1 °C per minute. Where a re-crystallised alumina crucible was used, it was inspected for corrosion and evidence of volatile emission.

### 8.1.3 Sample Preparation

Glass samples required further preparation for the various characterisation techniques that were applied in studying the various glass compositions.

For gravimetric techniques, such as those used for the determination of density, only a small piece of sample, between 1 - 10 g in mass, was required. In order to produce this, a diamond abrasion saw was used to cut off an appropriately sized piece of glass from the glass monolith. No more preparation was required for these techniques.

For spectroscopic techniques, such as Raman and FT-IR spectroscopy, sample pieces were removed from the glass monolith utilising a diamond abrasion saw as previously. Subsequent to sectioning, the sample pieces were ground and polished upon one side of the sample. Grinding was accomplished through the use of SiC abrasion disks of with a range of

coarsenesses and a manual polishing machine. Samples were polished using 120, 400, 800 and 1200 grit SiC papers in declining order. Once samples had been sufficiently ground, they were polished using a suspension of CeO<sub>2</sub>. The polished samples were then cleaned for use in the spectroscopy.

For techniques which required powdered samples, such as DTA, XRD and EPR, samples were sectioned from the glass monolith using a diamond abrasion saw before being input into a steel percussion mortar. The percussion mortar was used to fragment the glass materials to a sufficiently small size fraction. The output of the percussion mortar was sieved to separate those particles of 75 µm in size or less, the remaining material was re-input in to the percussion mortar. This process was repeated until a sufficient proportion of sub 75 µm powder was produced for the intended experiential techniques. Before use the powdered samples were screened for contamination with steel particles from the percussion mortar through the use of a standard bar magnet.

#### 8.1.4 Density Measurement

The density of glass samples was measured through observing its displacement when submerged in water, a technique known as Archimedes method. In practice the technique simply involves measuring the mass of a piece of glass and then measuring its mass when suspended, submerged in distilled water. Using the following equation (Eqn. 8.1) the density of the glass may be ascertained. M<sub>2</sub> denotes the mass of the glass fragment with a nylon thread, M<sub>1</sub> denotes the mass of glass without a nylon thread (the nylon thread being used for the suspension of the glass in water). M<sub>3</sub> denotes the displacement mass of the glass immersed in water and M<sub>4</sub> denotes the mass of glass after submersion in water.

$$\text{BulkDensity} = \frac{\text{SolidMass}}{\text{Upthrust} + \text{PoreWaterMass}} = \frac{M_1}{(M_2 - M_3) + (M_4 - M_1)} \times \rho_{\text{H}_2\text{O}} \quad (\text{Eqn. 8.1})$$

#### 8.1.5 Liquidus Temperature Determination

The liquidus temperature (T<sub>liq</sub>) of the glass samples was measured using a relatively simple experimental method, where a sample of glass frit (usually in a long refractory boat) is melted across a temperature gradient (in a electric tube furnace), and is held at temperature for 24 hours, and then cooled rapidly forming glass or crystalline phase depending on the melt temperature as defined by the temperature gradient. If the temperature gradient has been

measured, and if the  $T_{liq}$  falls between its upper and lower limits, then the point at which the  $T_{liq}$  falls can be seen in the cooled sample and determined simply by comparing the distance along the boat at which the glass is formed to the known temperature gradient.

In the case of the experiments conducted for this work, a 10-12cm long alumina boat was heated in a tube furnace as described. The temperature gradient was recorded during each experiment by using a thermocouple inserted into the tube furnace in parallel with the sample, this thermocouple was retracted from the centre of the furnace in 1 cm intervals giving the temperature along the length of the sample boat. The  $T_{liq}$  could therefore be determined to within a 0.5 cm division, an error equivalent to approximately up to  $\pm 10$  °C. The furnace temperature was selected based upon literature information, or past experimental information relevant to the glasses being tested.

### **8.1.6 Differential Thermal Analysis**

The glass transition temperature ( $T_g$ ) of the samples was determined by the technique of the DTA (Differential Thermal Analysis), a technique which detects enthalpy changes over a range of temperatures. Since the  $T_g$  of the glass is where the glass structure changes from elastic to glassy in character (or vice versa) it has an enthalpy value, and as such this change can be observed through DTA, and a measurement of the temperature at which it occurs can be made. This allows the glass  $T_g$  to be determined with reasonable accuracy. In the case of the experiments carried out for this work, glass samples were suspended in small Pt crucibles in air, and subjected to an increasing temperature at a rate of 10 °C per minute. The heat flow detected from the sample was compared to an alumina filled reference crucible with known thermal behaviour, which allowed variation in the rate of temperature change in the sample to be determined. The resulting trace of heat flow against temperature allowed the temperature of the endothermic  $T_g$  event to be identified and through the bespoke Theta software (Dilasoft) , the  $T_g$  onset temperature could be calculated. The method allowed the  $T_g$  to be determined to within approximately  $\pm 5$  °C.

### **8.1.7 Melt Viscosity Determination**

The viscosity of glass melts was determined through the use of a viscometer setup supplied by Theta Industries. This setup involved the use of rheometer (Brookfield DV-III-Ultra) mounted above a vertically mounted electrical muffle furnace. This setup allows the

measurement of viscosity by the measurement of the torque experienced by a re-crystallised alumina spindle lowered into the glass melt over a range of temperatures. To achieve this, a re-crystallised alumina crucible is filled with fritted glass material and suspended under a rheometer on a suspended fused alumina frame above the electrical muffle furnace. The alumina frame containing the crucible is lowered in the furnace at the start of the experiment and the furnace is allowed to heat to the top end of the temperature range which is to be studied. The furnace increased in temperature at a slow rate, usually  $\sim 2$  °C per minute, in order to prevent any glass from being lost from the crucible during the re-melting of the frit. Once the furnace had reached the maximum temperature, a re-crystallised alumina spindle, connected to the rheometer, was lowered into the glass melt by a known distance in order to measure the torque it experiences and therefore determine the viscosity of the glass. The furnace temperature was decreased steadily at a rate of 2 °C per minute allowing the measurement of viscosity over the full temperature range. Once the measurement had been completed, the furnace temperature was raised to a point where the spindle could be removed and then allowed to cool to room temperature. The data was automatically tabulated by the bespoke Theta software (Dilasoft) and presented as a table of viscosity (or  $\text{Log } \eta$ ) against temperature.

### 8.1.8 X-ray Diffractometry

X-ray diffraction (XRD) was utilised to investigate any long-range order that may be present in the glass samples and determine the presence and identification of any crystal phases which may be present. XRD uses the characteristic X-ray radiation of a known wavelength and directs it across a sample at a range of angles. The X-ray radiation is diffracted by the structure of a crystalline material across these angles, which produces a pattern which can be used to identify crystalline phases present in the material. When applied to amorphous materials, a diffuse scattering pattern is generated by diffraction of the X-rays because of the randomly distributed network of the material in question. When applied to the study of glasses or amorphous materials in general, XRD can show the existence of any crystalline phase present within the glass, and allow such phase to be identified, although it is important to note that crystalline species which make up less than 5 vol% of an amorphous material may not be detected. XRD experiments were carried out using a Seimans D5000 X-ray diffractometer

### 8.1.9 Scanning Electron Microscopy and Energy Dispersive X-ray Spectroscopy

Scanning Electron Microscopy (SEM) and Energy Dispersive X-ray spectroscopy (EDX) were applied to investigate the microstructure and composition of the various samples which were produced. SEM utilises an electron beam to generate topographical and element-specific information about areas of sample on a microscopic scale. Due to the inherent low wavelength of the electron beam, this technique allows for significantly greater magnification of images than can be achieved through optical microscopy. An SEM microscope produces an image by using an electron beam produced by focusing electrons generated by an electron gun through a series of electromagnetic lenses<sup>(154)</sup>. The electron beam is then scanned over the sample producing a number of outputs including secondary electrons, electrons emitted by the sample due to stimulation by the electron beam, and backscattered electrons which are reflected from the beam in a manner which is modulated by the relative atomic mass of the elements from which they were reflected. Images are built up from these emitted secondary electrons and backscattered electrons as detected by independent detectors calibrated to the different signal sources. A scintillator and photo-multiplier are used to detect secondary electrons whereas scintillator or semi-conductor detectors placed in a ring around the electron beam are used to collect back-scattered electrons. Secondary electrons are used to generate a topographical image of the sample which is useful for the investigation of the micro-structure of a sample on scales below that which would be visible optically. In the study of vitrified materials however, topographical information is of limited value due to the lack of detail on a polished monolithic glass sample. Back-scattered electrons provide more useful information for polished glass samples, since the images they produce show variations in elemental content, with regions containing higher atomic mass species appearing as brighter signals in a Back-Scattered electron SEM image<sup>(154)</sup>. For glass samples, this means the homogeneity of a glass sample that may appear to be homogenous can be fully investigated. An example of a backscattered SEM image can be found below in Figure 8.1.1.

EDX spectroscopy operates in a similar manner to SEM in that it uses a focused electron beam to selectively excite a region of sample and stimulate the emission X-rays from target region. The energies of these emitted X-rays are connected to the energy levels of the electronic orbital of the atoms which emitted them, and so these emitted X-rays are characteristic of the elements from which they were emitted. This allows the identification of the elements excited by the electron beam from the spectrum of the X-ray emitted. This means that EDX can be used to determine the composition of the region where the X-ray beam is incident. Typically, EDX spectroscopy systems are integrated with an SEM system which allows the SEM to be used to select the precise region for study through EDX and

allows the EDX system to utilise the electron beam used by the SEM. For EDX analysis the electron beam may be scanned over an area or over a line. However, typically it is focused on a specific spot, allowing the analysis of the composition of a region identified by SEM to be analysed for composition. EDX typically will only produce qualitative information on composition, however if calibrated using a metallic standard (typically cobalt), it is possible to use EDX to provide quantitative information on the composition of a region. However, it should be noted that EDX systems cannot usually detect Li or B due to the low energy of their associated X-ray emission lines. This can be a significant drawback, especially when investigating alkali borosilicate type glass compositions.

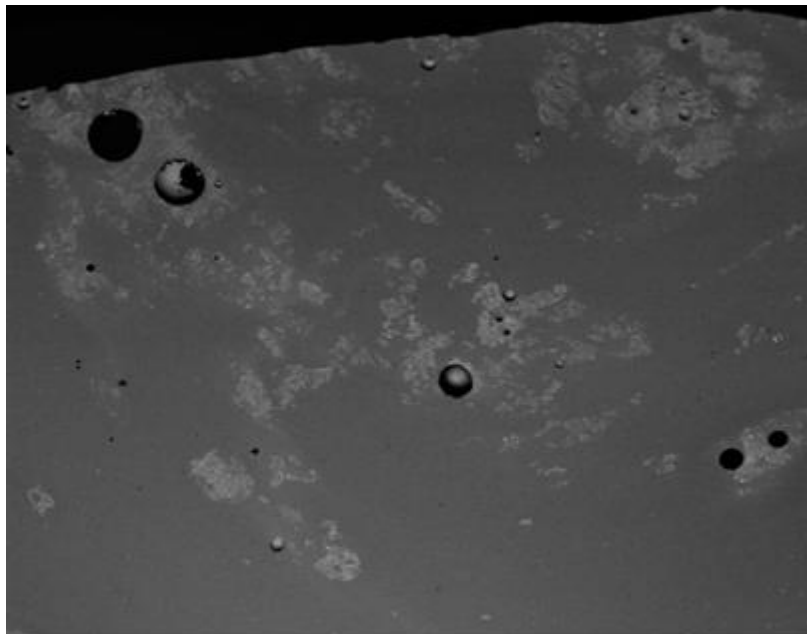


**Figure 8.1.1.** Example of an SEM image as derived using backscattered electrons. Images shows heterogeneity in a polished glass sample not discernible through topographic imaging.

Samples are prepared for SEM/EDX analysis by polishing the samples to a surface quality of 1  $\mu\text{m}$  using diamond polishing paste, and then mounting the samples in epoxy resin in order to allow the samples to be loaded into the SEM mechanism. The surfaces of the samples are carbon coated and tracks of silver DAG are applied to the surface of the sample in order to provide pathways to allow the dissipation of surface charge generated by the electron beam used by SEM.

SEM/EDX experiments carried out in this work were performed using a Philips PSEM 500 with an inbuilt EDX system.

#### **8.1.10 Fourier Transform Infrared Spectroscopy**

Fourier-transform infrared (FT-IR) spectroscopy is a form of optical spectroscopy which utilises the infrared region of the electromagnetic spectrum to study bonding in materials. FT-IR spectroscopy is widely used in chemistry and materials science as a tool for understanding the structure and bonding in materials. The fundamental principle behind FT-IR spectroscopy is the connection between the absorption of infra-red radiation by a material and the bond present in the material. The energy range covered by the infra-red spectrums covers the same range of energies as the bond vibration energies. As such, the incident infra-red light causes the excitation of the vibrational modes of the bonds present in a material, causing peaks in infrared light absorption by a sample which are characteristic of bending and stretching vibration mode linked to specific bonds within a material. In amorphous solid materials such as glasses, these vibration absorption bands are typically stretched in terms of energy over a wide range of values due to the variation in bonding throughout the amorphous material. However, in crystalline solids or liquids and gases, bond vibrations tend to be clearly defined <sup>(155)</sup>.

FT-IR instruments operate by directing an infra-red light source in such a way that the light passes through the target sample and on to a detector. The infra-red light beam, prior to reaching the sample, is passed through a Michelson interferometer (shown below in figure 8.1.2) which effectively splits the beam into two components and then recombines them in such a way that they interfere, producing an interferogram which allows a range of data to be collected over a wide range of spectra simultaneously. In circumstances where the sample is opaque and will not transmit light, it is necessary either to produce sample which sufficiently thin to allow transmission or, as is more often the case with glass monoliths which are typically opaque to IR light, a reflectance setup is used in which the laser is bounced off two mirrors and reflected off the surface of the sample itself. In this way, the IR absorption can be determined. However, when using a reflectance method it is necessary to compensate the effect of the refractive index, and so the data must undergo the mathematical Kronig-Kramers transform which allows the spectrum produced to be separated from the refractive index effects. The signal detected by the detector is subsequently de-convoluted through a Fourier-transform to produce a spectrum of absorption against wavelength <sup>(155)</sup>.

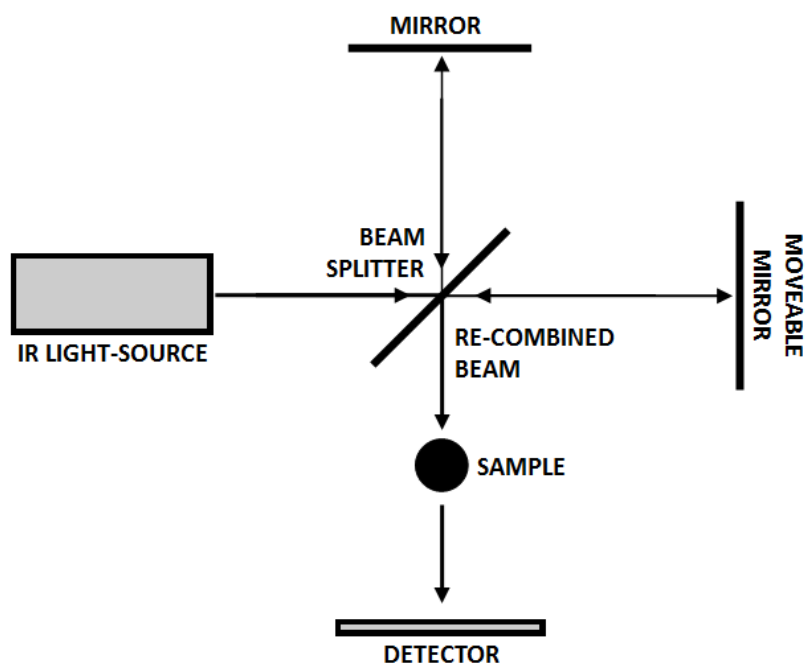


Figure 8.1.2. Schematic of a Michelson interferometer as used in FT-IR spectroscopy.

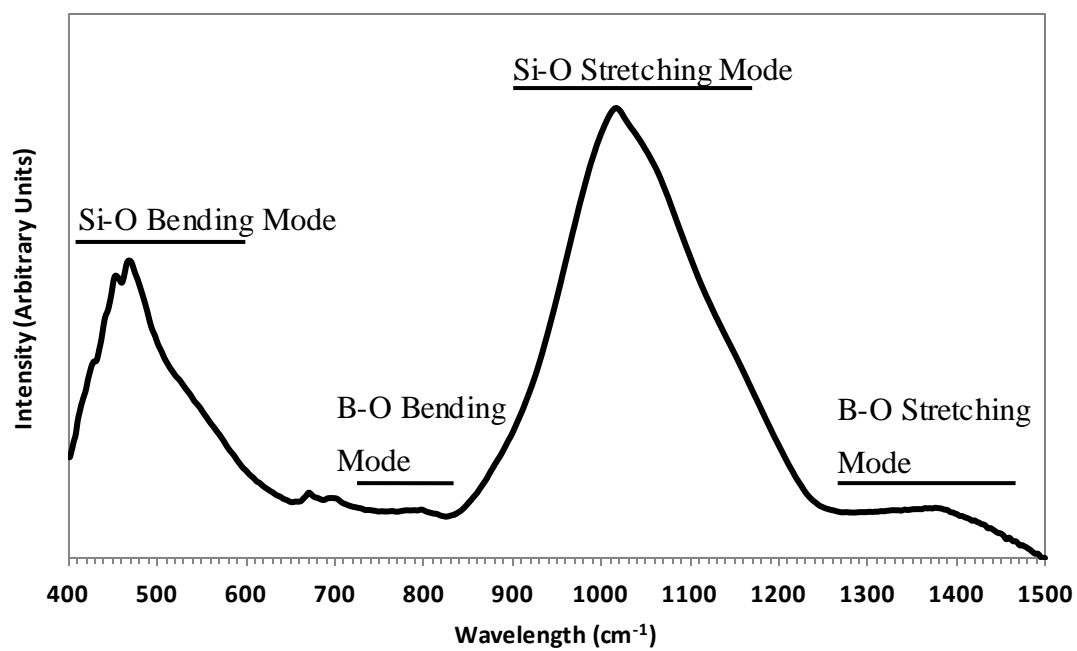


Figure 8.1.3. FT-IR spectrum associated with an alkali borosilicate glass.

In glasses, this spectrum can be de-convoluted to determine the individual bands associated with absorption by bonding species in the glass network, such as Si-O bonds which can be used to determine the  $Q^n$  speciation of the silicate network. De-convolution is achieved by means of fitting the data with line-shapes representative of the constituent bands. Commercial fitting software is available for this purpose. Figure 8.1.3 shows a typical FT-IR spectrum associated with a borosilicate type glass. FT-IR experiments were carried out with a Perkin-Elmer Spectrum 2000 FT-IR spectrometer.

### 8.1.11 Raman Spectroscopy

Raman spectroscopy makes use of the Raman effect to investigate the various vibrational, rotational and other-low frequency modes that are present in materials. These can be used to provide detailed information on the bonds present in a material. In terms of information provided, Raman spectroscopy possesses a large overlap with FT-IR spectroscopy but does feature sensitivity to some bonding species which are not detected by FT-IR. As such, it is a valuable tool for the investigation of materials in general and glasses in particular.

Raman spectroscopy relies upon the modulation of light emitted through the process of Raman scattering which occurs through the interaction of photons with polarisable molecules. Specifically Raman scattering occurs when a photon is scattered by a molecule that is already in a vibrational excited state due to prior photon interactions and which is 'Raman-active'. A molecule which is termed 'Raman active' possess vibrational modes which can be induced into become polarised giving the molecule a dipole moment which may be excited. The scattered photon gains the energy of the excited 'Raman-active' molecule which modulates the frequency of the photon in a manner which is characteristic of the scattering molecule. This modulation of the scattered photon is linked to the dipole moment of the polarised molecule which is in turn linked to the bonding of the molecule. From this it is possible to determine the nature of the bonds present in the material, by means of the de-convolution of the produced spectra and the assignment of the Raman bands which show the characteristic vibration modes of the bonds in the material <sup>(155)</sup>. It is important to note that despite the similarities in the results provided by FT-IR and Raman spectroscopy, they function by significantly different methods as FT-IR release on photon absorption whereas Raman spectroscopy relates on a light scattering phenomenon.

A Raman spectrometer typically involves a laser mounted to a microscope set above the sample. The microscope operates as a detection system collecting the scattered light produced by the Raman effect. It also serves the function of providing a means for the user to target the incident laser beam, which is directed through the microscope optics and may be focused on a particular region of a sample. The laser is focused on the sample and this leads to scattered photons being produced through the Raman effect. These photons are then collected through a detector assembly.

In glasses this spectrum can be de-convoluted, as with FT-IR, to determine the individual bands associated with absorption by bonding species in the glass network, such as Si-NB bonds which can be used to determine the Q<sup>n</sup> speciation of the silicate network. However, it can also be used to investigate more exotic bands which may not absorb in the infra-red range (such as the amber chromophore Fe<sup>3+</sup>-S<sup>2-</sup>).

Experiments were carried out utilising a Renishaw InVia Raman spectrometer with an attached microscope and automated sample stage. A 660 nm laser was utilised for all experiments.

### **8.1.12 Optical absorption spectroscopy**

Optical absorption spectroscopy makes use of the visible and near UV spectrum of light to investigate the bonds and optically absorbing species present in a system in much the same way as FT-IR spectroscopy. Species present in a material, such as Fe<sup>3+</sup> in iron-containing glass systems absorb specific frequencies of light, or ranges of frequencies due to the variation in the environs of the absorbing species. By directing a beam of light through a material, it is possible to determine which species are present through their characteristic absorption by means of the Beer-Lambert law. In this form of spectroscopy, it is necessary for light to be transmitted through the sample. Therefore, for opaque samples, these must be thinned and polished sufficiently for optical transmission to occur. In the case of glass samples with a high Fe content, this can lead to the requirement for very thin samples requiring careful preparation. As with other spectroscopic techniques, the light which is transmitted through the sample is collected by a detector which typically makes use of a prism or diffraction grating to separate the transmitted wavelengths and so allow detection of transmitted intensity across the optical spectrum explored. This produces a spectrum which through de-convolution and assignment of the absorption bands can be used to identify and to quantify, by virtue of the Beer-Lambert law <sup>(155)</sup>, the species present in the sample material.

In glasses this spectrum typically provides information on colorant species in the glass system, most typically  $\text{Fe}^{2+}$  and  $\text{Fe}^{3+}$ .

Optical absorption experiments were carried out with a Perkin Elmer Lambda 900 optical absorption spectrometer.

### 8.1.13 Mossbauer spectroscopy

Mossbauer spectroscopy is a non-destructive technique intended to study the environment of a nucleus, allowing valence, oxidation states and coordination environments to be determined. Mossbauer spectroscopy functions through the interaction of gamma radiation with atomic nuclei, which leads to the excitation of nuclear energy levels which can in turn be exploited to provide information about the environment of the atomic nuclei. Incident gamma radiation which has an energy matching the difference between nuclear energy levels may be resonantly absorbed by the nucleus which leaves the nucleus in an excited state <sup>(156)</sup>. The energy absorption that occurs can then be used to generate a spectrum providing information about the target atom's environment. However, there are two major difficulties; firstly the interactions between the nucleus and the environment are very small, in the order of  $10^{-8}$  eV, secondly the recoil of the nucleolus with gamma ray emission or absorption prevents resonance. The effect of recoil (ER) is to reduce the emitted gamma radiation energy by an amount proportional to the resonance (ER) and cause the energy for resonant absorption to be higher by the same amount (ER). In addition the energy range can be spread due to thermal motions, causing the Doppler Effect to shift gamma ray energies over a wider range. The recoil energy and Doppler energy shift overwhelm the small environment induced nuclear energy levels. In some cases, these problems can be overcome by the presence of a crystal structure which absorbs the recoil energy, and reduces the effect of thermal vibration.

For experimental applications, because the difference in energy levels is so small (10-8 eV), a very fine resolution is required. To achieve this fine resolution, the energy of the emitted gamma ray is allowed to vary over a small range tuned to cover the energy range intended for study. This is achieved by moving the gamma source in a manner which produces a Doppler shift in the emitted gamma ray energy. The number of isotopes that can have Mossbauer spectroscopy applied to them is limited, as there are only a limited number of gamma emitting isotopes suitable for showing the Mossbauer Effect; specifically, those with a low gamma ray energy, and therefore low recoil, and have a long-lived excited state,

allowing them to be useful for experimental work. As a consequence, the most commonly used target isotope is  $^{57}\text{Fe}$ . Experiments are conducted using a suitable target sample containing  $^{57}\text{Fe}$ , which has been prepared to be a suitable thickness to allow the transmission of gamma radiation. The sample is exposed to a range of gamma ray energies using the method previously described, and the absorption spectrum is recorded, the absorption pattern should reveal the interactions of the environment upon the isotope. This information is revealed in three ways; the chemical shift which provides valence information, the quadrupole splitting which indicates charge distribution, and the magnetic splitting which provides information about the magnetic environment of the isotope. These values can be determined through the fitting of the spectra produced and can be used to determine the coordination and oxidation state of the target nuclei as reported by Darby-Dyar *et al* <sup>(71)</sup> and Forder *et al* <sup>(156)</sup>. The following figure (Figure 8.1.4) shows a fitted example of a Mossbauer spectrum, with the two fitted curves representing  $\text{Fe}^{2+}$  and  $\text{Fe}^{3+}$ . From the area of these fitted curves the reduction in the glass can be quantified.

Mossbauer experiments were carried out with a WissEl  $^{57}\text{Fe}$  Mossbauer spectrometer, and data was fitted utilising the Recoil 1.03 software package.

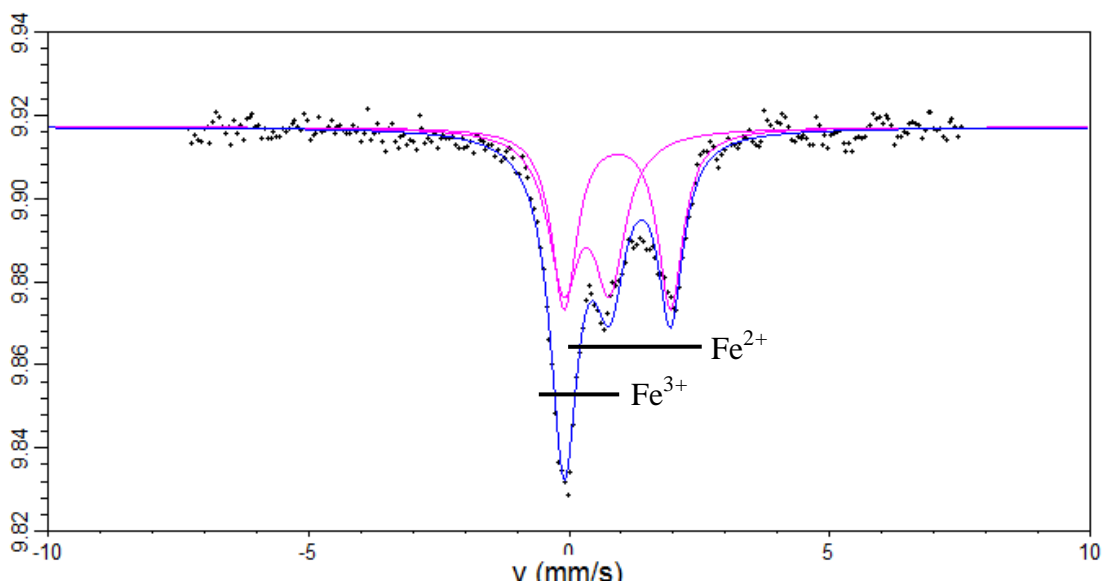


**Figure 8.1.4.** Fitted Mossbauer spectrum for glass containing both  $\text{Fe}^{2+}$  and  $\text{Fe}^{3+}$ .

### 8.1.14 Electron Paramagnetic Resonance spectroscopy

Electron paramagnetic resonance (EPR) spectroscopy is a form of spectroscopy that can be used to investigate materials which contain unpaired electrons. It is similar to NMR spectroscopy in that it relies on resonance with excited particles. However in this case, it is electrons which are excited rather than atomic nuclei<sup>(157)</sup>. EPR spectroscopy utilises the magnetic moment and quantised spin number of electrons to generate a signal. By applying a strong magnetic field to the sample, it is possible to induce a split between the energy levels between the two spin states between which an electron may move. Measurements are made using microwaves, typically of a frequency between 9-10 GHz. Whilst the microwaves are applied to the sample, the strength of the magnetic field experienced by the sample is increased and when the magnetic field causes the division in spin states to match the energy of the incident microwaves, electrons will jump from the lower spin state to the higher spin state, causing a detectable absorption in microwave energy. By varying the magnetic field in this manner it is possible to create a spectrum. This spectrum allows the resonant energy for the electrons to be determined, allowing the identification of paramagnetic species that may be present.

In glasses, due to the distribution of states that may be experienced by paramagnetic species, such as  $\text{Fe}^{3+}$ , the signal presented by EPR will typically be spread over a large area. However if defects are present, such as may be generated through irradiation, these produce strong narrow signals that are clearly defined due to their atypical electrical configuration. Therefore, EPR is uniquely useful in studying irradiation effects in glasses. Figure 8.1.5 shows the EPR spectrum of an irradiated glass sample, displaying the characteristic defect band as described by Brown *et al*<sup>(97)</sup>.

In order to generate an EPR spectrum, a sample, typically in a powdered state, is put into silica sample tube and loaded into a microwave cavity placed between two electromagnets. The quantity of sample material used is precisely weighed in order to account for variation in microwave absorption due to sample size. Once the sample is in place, measurements may be made by subjecting the sample to micro-wave radiation and varying the magnetic field incident on the sample. In order to minimise the broadening of the signal due to the effect of temperature induced motion, the sample and sample stage is typically cooled using liquid nitrogen or in some cases liquid helium<sup>(157)</sup>. EPR experiments were carried out at the EPSRC EPR research centre utilising a Bruker EPR spectrometer.

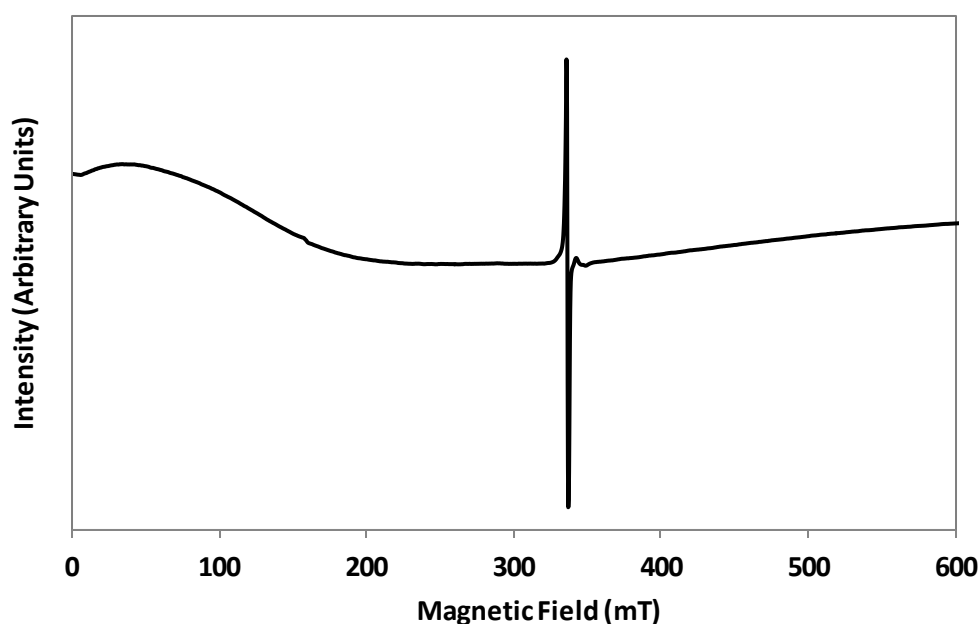


**Figure 8.1.5.** EPR spectrum of an irradiated alkali borosilicate glass.

### 8.1.15 Solid State Nuclear Magnetic Resonance spectroscopy

Solid state nuclear magnetic resonance spectroscopy (NMR) operates in a manner similar to EPR spectroscopy, relying on resonant interaction between particles and an applied electromagnetic field whilst the sample is subject to a strong magnetic field. The primary difference between the two techniques is that where EPR investigates the spin of unpaired electrons, NMR utilises the spin of atomic nuclei. The scientific basis for NMR spectroscopy relates to the magnetic moment which is inherent to all atomic nuclei that have a non-zero spin value. This magnetic moment can be utilised to cause the division of nuclear spin states in terms of energy when the nuclei are subjected to a magnetic field. By varying the incident magnetic field over a range of values, the energy gap between the two spin states is varied. An incident electromagnetic field, typically in the radio frequency range, is resonantly absorbed by the divergent spin states at specific magnetic field values associated with the environment of the atomic nucleus which is being investigated. In solid state samples, chemical shift anisotropy (CSA) can be used to provide useful information with regards to the coordination and bonding of specific elements within a solid sample. However, due to the limitation of possible configurations in the solid state, and the differing electronic environments of the atoms the NMR spectra produced are typically blurred and cannot be

interpreted <sup>(158)</sup>. As a result, for solid state samples it necessary to use the 'magic angle spinning' (MAS), method which averages the chemical shift values of the various electronic components, allowing the CSA to be interpreted for solid samples.

The spectra produced from MAS-NMR experiments can be de-convoluted in order to analyse the contributions from nuclei with differing CSA values which, in glass systems, can then be correlated to known values for specific coordination environments in glasses. As such, MAS-NMR can be utilised to provide information upon the coordination environment for any non spin-zero element or isotope present in a glass system (with the exception of magnetic species such as Fe). In the study of glasses this is a valuable tool, since it can be utilised to provide insights in to the coordination of atoms within a glass sample and so provide information about the short range order and the state of the glass-forming network within that glass system <sup>(158)</sup>.

Solid state NMR experiments were carried out at the EPSRC Solid State NMR research centre utilising a Varian VNMRs spectrometer with a 9.4 T magnet.

### **8.1.16 X-ray Absorption Near Edge Spectroscopy**

XAS was developed in the 1970s, and utilises a monochromatic X-ray source (typically from a synchrotron) to study the environment of all atoms of a particular element in a sample. The techniques can be applied to samples in wide range of forms without much difficulty and can provide detailed information about short range structure, valence, and the distribution of elements within a sample.

XAS functions by subjecting the sample to monochromatic X-rays of an energy tuned to match the X-ray absorption edge of the target element, that is, the energy limit where the X-ray photons are absorbed according to the photo-electric effect. The absorption pattern which is produced is affected by the local environment. XAS is used to describe two different techniques, XANES (X-ray absorption near edge structure) and EXAFS (Extended X-ray absorption fine structure). The former can be found close to the absorption edge and provides information with regards to the valence state and coordination, where as the latter provides the local molecular structure around the target element <sup>(159)</sup>.

XANES spectra are linked directly to the oxidation and valence state of an atom through their direct link to the outer most electron shells, those most affected by valence and

oxidation changes, and those responsible for absorption in the XANES region, EXAFS is dictated by interference and scattering of photoelectrons emitted by the absorber atoms in a sample. The relative phases of these photoelectron waves, and their interference with waves scattered from neighbouring atoms affects the probability of absorption by the absorber atom, producing the observed EXAFS spectrum. The scattered wave oscillates with a periodicity that may be used to determine the distance between coordinated atoms. Each atom at the same radial distance from the absorber contributes to the same components of the EXAFS spectrum, the number of atoms present in each shell is the coordination number of that shell, and the phase of the EXAFS signal received is determined by the distance travelled by the photoelectron to reach the absorber. As photoelectrons may be scattered off multiple atoms, it is possible for them to scatter several times before reaching the absorber atom. Where the degeneracy of a single scattering photoelectron is equivalent to the coordination of the scattering shell, a photoelectron passing through multiple shells will have a degeneracy which is a sum of those shells that it passed through. This builds up the EXAFS spectrum, which can be understood in terms of the EXAFS equation (Eqn. 8.2) .

$$\chi(k) = \sum_i \chi_i(k) \quad (\text{Eqn. 8.2})$$

Each scattering path can be written in the following form (Eqn. 8.3), and fully interpreted using (Eqn. 8.4) and (Eqn. 8.5)

$$\chi_i(k) \equiv \frac{(N_i S_0^2) F_{\text{eff}_i}(k)}{k R_i^2} \sin[2kR_i + \varphi_i(k)] e^{-2\sigma_i^2 k^2} e^{\frac{-2R_i}{\lambda(k)}} \quad (\text{Eqn. 8.3})$$

$$R_i = R_{0i} + \Delta R_i \quad (\text{Eqn. 8.4})$$

$$k^2 = \frac{2m_e(E - E_0 + \Delta E_0)}{\hbar} \quad (\text{Eqn. 8.5})$$

This equation can be utilised to understand the scattering components that contribute to the EXAFS spectrum, and from that used to determine the probable short range structure of the material being studied <sup>(159)</sup>. All XAS experiments were carried out at the ID26 beam line at ESRF, Grenoble.

### 8.1.17 X-ray Emission Spectroscopy

X-ray emission spectroscopy operates along similar lines to X-ray absorption spectroscopy in that it utilises X-rays to investigate the coordination and electron configuration of specific element within a sample. However, unlike XAS, which involves the absorption of incident X-ray radiation by a sample, XES involves the stimulation of an X-ray emission through the excitation of specific elements present in a system using a directed beam of monochromatic X-ray radiation. As with XAS, a high energy X-ray source, such as a synchrotron, is required to generate the necessary energies of X-ray radiation required for X-ray emission experiments. X-rays are directed through gratings and a monochromator in order to direct monochromatic X-ray radiation onto the target sample. The incident X-ray energy is varied utilising a monochromator over a narrow range of energies characteristic to the X-ray absorption bands of the elements intended for study <sup>(108-109)</sup>. This allows the excitation of electrons in the electron shells of the target elements exclusively. The incident X-ray radiation promotes an electron from the ground state into the continuum and generates vacancy in the electron configuration which is then filled by the decay of an electron from a higher energy level, with the emission of an X-ray. The energy of this X-ray which causes this electron promotion is modulated by the environment that the X-ray emitting electron was previously in. Therefore, by varying the energy of the incident X-ray beam and measuring the variation in the X-ray radiation generated from the sample, it is possible to collect information relating to the environment of the promoted electrons and therefore by extension the electron configuration of the target element.

The experiential setup for XES typically requires samples to be mounted onto a flat surface placed at 45° to the incident X-ray beam. An X-ray spectrometer mounted at 45° to the sample (90° to the incident X-ray beam) with a collecting crystal grating is utilised to collect X-ray emitted from the sample. Due to the potential for interactions between the X-ray beam and atmosphere, these experiments are typically conducted under a high vacuum with the full experiential setup (from the input of the X-ray beam) typically being contained within the high vacuum <sup>(108-109)</sup>.

As with X-ray absorption spectroscopy, XES is useful for the investigation of glass and vitreous waste-forms due to its capacity for providing element specific information on the electron configuration, and therefore oxidation state and coordination environment of species within the glass system. This is, therefore, a highly useful tool for understanding the interactions between waste-species and the glass network, such as occur in loaded vitreous waste-forms. Furthermore, since XES results are not impacted by diffraction effects, it means that much clearer information on the oxidation state of an element in a glass can be found than can be achieved through XANES, albeit this does mean that XES cannot provide information on short range order. As with XAS all XES experiments were carried out at the ID26 beam line at ESRF, Grenoble.

### 8.1.18 Chemical Durability (PCT)

The chemical durability of the glass samples and waste-form produced was investigated through the PCT (product consistency test) experiment. The PCT test is an ASTM standard test intended to investigate the interactions between a powdered glass sample and ultra-high purity water held at 90 °C and thereby provide a comparable measurement for the aqueous durability of glass samples. The PCT procedure is described in full in the ASTM PCT test protocol (C 1285 - 02) and several variations exist to cater for different experiential requirements<sup>(145)</sup>.

The basic PCT experiment involves the fragmentation and sieving of monolithic glass samples to provide a sample powder with particles ranging from between 75 µm and 125 µm in size. These glass powders are then cleaned by immersion and ultra-sonication in both UHQ H<sub>2</sub>O and isopropanol to remove any powdered material adhered to the surface of the sample grains. The sample material is then weighed out into pressure vessels, typically made of a material with a high aqueous durability such as Teflon. These vessels have also been previously cleaned through a series of immersions and soaks in both H<sub>2</sub>O and nitric acid at 90 °C. Once a predetermined amount of glass powder has been introduced to the vessel, the remaining volume is filled with UHQ H<sub>2</sub>O (ASTM Type 1) and is then sealed. The weight of the container is taken at all stages so the mass of H<sub>2</sub>O and glass sample present in each vessel is known precisely. The full vessels are then placed into an oven maintaining a temperature of 90 °C and left for the duration of the experiment. After the required time has expired the samples are removed from the oven, and the solution is removed using a sterile syringe with an attached syringe filter. The vessels are weighed prior to decanting and any vessels which have been found to lose greater than 5% of the initial H<sub>2</sub>O mass are removed from the

experiment. The leachant solution is then sent off for analysis, usually through either ICP-AES or ICP-MS. In order to investigate the how the interaction between the glass and solution evolves over time, sample are removed over a period of time at set intervals. The most typical time frame utilised for these experiments is 28 days. Therefore samples are removed at 3, 7, 14, 21 and 28 days. Longer experiential duration may be preformed of up to a year or longer. In addition to this, all samples are run in triplicate in order to improve accuracy ad due to the long time period involved in producing the samples, and re-producing failed samples. With each time step, two control sample (vessels containing H<sub>2</sub>O only) are produced. A typical 28 day PCT experiment therefore requires the use of 15 individual sample vessels for each glass that is investigated and 10 control samples in addition.

The ICP-AES and ICP-MS analysis provides a value for the concentration of species from the glass in the leachant solution, and so can be utilised to determine the release rate and normalised mass loss for each element present in the glass composition over the course of the experiment. In order to do this, the surface to volume ration (SA/V) ratio is calculated by dividing the surface area of the glass powder, known from the density, mass and average diameter of the glass particles, and dividing it by the leachant volume. The resultant data is then normalised for surface area to volume ratio and in combination with the known wt % composition of the glass which is being investigated is used to calculate the release rate and normalised mass loss for the various elements present in the glass using the following equations (equation 8.6 and 8.7). Where  $NR_i$  is the normalised release rate in  $g_{(waste\ form)}/(m^2\ day)$ ,  $NL_i$  is the normalised mass loss in  $g_{(waste\ form)}/m^2$ ,  $c_i$  is the concentration of element "i" in the leachant solution,  $f_i$  is the fraction of element "i" in the un-leached waste-form, SA/V is the surface area to volume ratio and  $t$  is the duration of the test in days.

$$NR_i = \frac{c_i(sample)}{(f_i) \times (\frac{SA}{V}) \times (t)} \quad (Eqn.8.6)$$

$$NL_i = \frac{c_i(sample)}{(f_i) \times (\frac{SA}{V})} \quad (Eqn.8.7)$$

This technique is clearly useful in the study of glass intended for the immobilisation of nuclear waste material since it provides a basis for the comparative evaluation of different glass compositions for their aqueous durability. Clearly, their durability will determine the extent to which the contained radionuclides remain within the waste-form during storage in a repository.

## 8.2 Tabulated Data Tables

### 8.2.1 Chapter 3.1

Table 8.2.1.1 Property variation across BaO / (BaO + CaO) series.

BaO/ (BaO + CaO) Ratio	Density (gcm <sup>-3</sup> )	Tg Onset (°C)	Tliq (°C)	Log viscosity at 1200 °C (Log( $\eta$ /dPas))	Proportion of Fe <sup>3+</sup> (Fe <sup>3+</sup> /(Fe <sup>2+</sup> +Fe <sup>3+</sup> ))
1.00	3.67 ± 0.03	532 ± 5	994 ± 10	1.12 ± 0.05	0.96 ± 0.02
0.89	3.56 ± 0.01	515 ± 5	960 ± 10	1.09 ± 0.05	0.96 ± 0.02
0.75	3.47 ± 0.01	498 ± 5	890 ± 10	1.10 ± 0.05	0.95 ± 0.02
0.61	3.34 ± 0.01	495 ± 5	962 ± 10	1.04 ± 0.05	0.95 ± 0.02
0.48	3.21 ± 0.01	491 ± 5	994 ± 10	1.13 ± 0.05	0.94 ± 0.02
0.34	3.05 ± 0.01	498 ± 5	1045 ± 10	1.09 ± 0.05	0.95 ± 0.02
0.20	2.92 ± 0.03	515 ± 5	1109 ± 10	1.15 ± 0.05	0.97 ± 0.02
0.00	2.63 ± 0.02	532 ± 5	1131 ± 10	1.26 ± 0.05	0.88 ± 0.02

Table 8.2.1.2 Q<sup>n</sup> speciation variation across BaO / (BaO + CaO) series as determined by FT-IR.

BaO/ (BaO + CaO) Ratio	Percentage Assigned Band Area			
	Q <sup>1</sup>	Q <sup>2</sup>	Q <sup>3</sup>	Q <sup>4</sup>
1.00	7.3 ± 2.0	24.3 ± 2.0	64.3 ± 2.0	4.0 ± 2.0
0.89	6.4 ± 2.0	24.6 ± 2.0	64.5 ± 2.0	4.6 ± 2.0
0.75	7.2 ± 2.0	23.8 ± 2.0	65.1 ± 2.0	3.9 ± 2.0
0.61	7.3 ± 2.0	21.9 ± 2.0	65.3 ± 2.0	5.5 ± 2.0
0.48	6.6 ± 2.0	21.3 ± 2.0	66.5 ± 2.0	5.7 ± 2.0
0.34	6.4 ± 2.0	21.1 ± 2.0	67.0 ± 2.0	5.5 ± 2.0
0.20	6.4 ± 2.0	20.1 ± 2.0	68.0 ± 2.0	5.5 ± 2.0
0.00	5.7 ± 2.0	17.8 ± 2.0	69.5 ± 2.0	7.0 ± 2.0

Table 8.2.1.3 Property variation across Ca replacement series.

Glass Composition	Density (gcm <sup>-3</sup> )	Tg Onset (°C)	Tliq (°C)	Log viscosity at 1200 °C (Log( $\eta$ /dPas))	Proportion of Fe <sup>3+</sup> (Fe <sup>3+</sup> /(Fe <sup>2+</sup> +Fe <sup>3+</sup> ))
AS + MgO	3.47 ± 0.02	506 ± 5	898 ± 10	1.14 ± 0.1	0.93 ± 0.02
AS + CaO (Base)	3.42 ± 0.02	491 ± 5	962 ± 10	1.04 ± 0.1	0.94 ± 0.02
AS + SrO	3.43 ± 0.02	516 ± 5	985 ± 10	1.34 ± 0.1	0.97 ± 0.02
AS + BaO	3.54 ± 0.02	504 ± 5	890 ± 10	1.10 ± 0.1	0.95 ± 0.02
AS + ZnO	3.50 ± 0.02	497 ± 5	852 ± 10	1.06 ± 0.1	1.00 ± 0.02
AS + MnO	3.49 ± 0.02	493 ± 5	888 ± 10	0.99 ± 0.1	1.00 ± 0.02

**Table 8.2.1.4** Property variation across alkali variation series.

Total Alkali Content (mol%)	Density (gcm <sup>-3</sup> )	Tg Onset (°C)	Tliq (°C)	Log viscosity at 1200 °C (Log( $\eta$ /dPas))	Proportion of Fe <sup>3+</sup> (Fe <sup>3+</sup> /(Fe <sup>2+</sup> +Fe <sup>3+</sup> ))
0%	3.50 ± 0.01	688 ± 5	1245 ± 10	2.06 ± 0.1	0.96 ± 0.02
4%	3.46 ± 0.01	605 ± 5	1118 ± 10	1.67 ± 0.1	0.97 ± 0.02
8%	3.44 ± 0.01	554 ± 5	1027 ± 10	1.34 ± 0.1	0.97 ± 0.02
12%	3.40 ± 0.01	491 ± 5	968 ± 10	1.04 ± 0.1	0.95 ± 0.02

**Table 8.2.1.5** Q<sup>n</sup> speciation variation across alkali variation series as determined by FT-IR.

Total Alkali Content (mol%)	Percentage Assigned Band Area			
	Q <sup>1</sup>	Q <sup>2</sup>	Q <sup>3</sup>	Q <sup>4</sup>
0%	4.8 ± 2.0	24.0 ± 2.0	68.6 ± 2.0	2.5 ± 2.0
4%	4.8 ± 2.0	26.6 ± 2.0	67.5 ± 2.0	1.0 ± 2.0
8%	7.2 ± 2.0	30.3 ± 2.0	61.5 ± 2.0	1.0 ± 2.0
12%	6.3 ± 2.0	32.7 ± 2.0	60.0 ± 2.0	1.0 ± 2.0

**Table 8.2.1.6** Q<sup>n</sup> speciation variation across BaO / (BaO + CaO) series as determined by NMR.

BaO/ (BaO + CaO) Ratio	Percentage Assigned Band Area			
	Q <sup>1</sup>	Q <sup>2</sup>	Q <sup>3</sup>	Q <sup>4</sup>
1.00	5.7 ± 5.0	29.1 ± 5.0	55.7 ± 5.0	9.6 ± 5.0
0.89	2.4 ± 5.0	25.8 ± 5.0	62.3 ± 5.0	9.6 ± 5.0
0.75	2.4 ± 5.0	26.5 ± 5.0	62.2 ± 5.0	8.8 ± 5.0
0.61	4.3 ± 5.0	25.4 ± 5.0	61.5 ± 5.0	8.8 ± 5.0
0.48	4.2 ± 5.0	25.2 ± 5.0	61.1 ± 5.0	9.5 ± 5.0
0.34	4.2 ± 5.0	25.2 ± 5.0	61.1 ± 5.0	9.5 ± 5.0
0.20	5.1 ± 5.0	21.4 ± 5.0	64.0 ± 5.0	9.5 ± 5.0
0.00	6.1 ± 5.0	21.0 ± 5.0	63.3 ± 5.0	9.6 ± 5.0

**Table 8.2.1.7** Boron ratio variation across BaO / (BaO + CaO).

<b>BaO/ (BaO + CaO) Ratio</b>	<b>Boron Ratio BO<sub>4</sub>/BO<sub>3</sub></b>
<b>1.00</b>	0.59 ± 0.10
<b>0.89</b>	0.88 ± 0.10
<b>0.75</b>	0.83 ± 0.10
<b>0.61</b>	0.60 ± 0.10
<b>0.48</b>	0.78 ± 0.10
<b>0.34</b>	0.74 ± 0.10
<b>0.20</b>	0.57 ± 0.10
<b>0.00</b>	0.34 ± 0.10

**Table 8.2.1.8** Al coordination variation across BaO / (BaO + CaO) series.

<b>BaO/ (BaO + CaO) Ratio</b>	<b>Percentage Assigned Area</b>		
	<sup>[4]</sup> Al	<sup>[5]</sup> Al	<sup>[6]</sup> Al
<b>1.00</b>	44.8 ± 0.2	49.7 ± 0.2	5.5 ± 0.2
<b>0.89</b>	41.1 ± 0.2	50.4 ± 0.2	8.5 ± 0.2
<b>0.75</b>	28.2 ± 0.2	43.7 ± 0.2	28.2 ± 0.2
<b>0.61</b>	34.6 ± 0.2	48.0 ± 0.2	17.4 ± 0.2
<b>0.48</b>	43.2 ± 0.2	44.5 ± 0.2	12.3 ± 0.2
<b>0.34</b>	38.6 ± 0.2	55.0 ± 0.2	6.40 ± 0.2
<b>± 0.20.20</b>	42.0 ± 0.2	53.6 ± 0.2	4.45 ± 0.2
<b>0.00</b>	35.0 ± 0.2	61.6 ± 0.2	3.38 ± 0.2

**Table 8.2.1.9** Boron ratio variation across CaO replacement series.

<b>Glass Composition</b>	<b>Boron Ratio BO<sub>4</sub>/BO<sub>3</sub></b>
<b>AS + MgO</b>	0.89 ± 0.10
<b>AS + CaO (Base)</b>	0.60 ± 0.10
<b>AS + SrO</b>	0.80 ± 0.10
<b>AS + BaO</b>	0.83 ± 0.10
<b>AS + ZnO</b>	0.86 ± 0.10

**Table 8.2.1.10** Al coordination variation across CaO replacement series.

Glass Composition	Percentage Assigned Area		
	<sup>[4]</sup> Al	<sup>[5]</sup> Al	<sup>[6]</sup> Al
AS + MgO	47.2 ± 0.2	36.5 ± 0.2	16.3 ± 0.2
AS + CaO (Base)	34.6 ± 0.2	48.0 ± 0.2	17.4 ± 0.2
AS + SrO	30.6 ± 0.2	51.5 ± 0.2	18.0 ± 0.2
AS + BaO	28.2 ± 0.2	43.7 ± 0.2	28.2 ± 0.2
AS + ZnO	50.5 ± 0.2	40.1 ± 0.2	9.4 ± 0.2

**Table 8.2.1.11** Q<sup>n</sup> speciation variation across Alkali depletion series.

Total Alkali Content (mol%)	Percentage Assigned Band Area			
	Q <sup>1</sup>	Q <sup>2</sup>	Q <sup>3</sup>	Q <sup>4</sup>
0%	3.8 ± 0.2	11.6 ± 0.2	73.9 ± 0.2	10.7 ± 0.2
4%	3.8 ± 0.2	15.7 ± 0.2	72.9 ± 0.2	7.6 ± 0.2
8%	3.6 ± 0.2	19.8 ± 0.2	70.1 ± 0.2	6.4 ± 0.2
12%	3.5 ± 0.2	23.8 ± 0.2	66.4 ± 0.2	6.3 ± 0.2

**Table 8.2.1.12** Al coordination variation across Alkali depletion series.

Total Alkali Content (mol%)	Percentage Assigned Area		
	<sup>[4]</sup> Al	<sup>[5]</sup> Al	<sup>[6]</sup> Al
0%	36.6 ± 0.2	32.3 ± 0.2	31.1 ± 0.2
4%	29.2 ± 0.2	38.6 ± 0.2	32.3 ± 0.2
8%	21.5 ± 0.2	38.5 ± 0.2	40.0 ± 0.2
12%	33.5 ± 0.2	48.4 ± 0.2	18.1 ± 0.2

**Table 8.2.1.13** Boron ratio variation across Alkali depletion series.

Total Alkali Content (mol%)	Boron Ratio BO <sub>4</sub> /BO <sub>3</sub>
0%	0.93 ± 0.10
4%	0.98 ± 0.10
8%	1.14 ± 0.10
12%	0.83 ± 0.10

**Table 8.2.1.14** Variation in Alkali NMR signal position across BaO / (BaO + CaO) series.

Total Alkali Content (mol%)	<sup>23</sup> Na Signal Position (ppm)	<sup>7</sup> Li Signal Position (ppm)
1.00	-11.2 ± 0.5	1.0 ± 0.1
0.89	-10.8 ± 0.5	0.9 ± 0.1
0.75	-10.4 ± 0.5	1.1 ± 0.1
0.61	-11.3 ± 0.5	1.0 ± 0.1
0.48	-11.1 ± 0.5	0.7 ± 0.1
0.34	-11.9 ± 0.5	0.7 ± 0.1
0.20	-12.4 ± 0.5	0.6 ± 0.1
0.00	-13.4 ± 0.5	0.5 ± 0.1

**Table 8.2.1.15** Variation in Alkali NMR signal position across CaO replacement series.

Glass Composition	<sup>23</sup> Na Signal Position (ppm)
AS + MgO	-9.1 ± 0.5
AS + CaO (Base)	-11.3 ± 0.5
AS + SrO	-11.4 ± 0.5
AS + BaO	-10.4 ± 0.5
AS + ZnO	-9.4 ± 0.5

## 8.2.2 Chapter 3.2

**Table 8.2.2.1.** Property variation in base, intermediate and hybrid glass compositions.

Glass Composition	Density (gcm <sup>-3</sup> )	T <sub>g</sub> Onset (°C)	T <sub>liq</sub> (°C)	Log η at 1200 °C (Log (η/dPa.s))
AS0	3.42 ± 0.034	491.0 ± 5	962 ± 10	1.044 ± 0.005
ASB	3.54 ± 0.031	503.5 ± 5	890 ± 10	1.099 ± 0.005
ASZ	3.50 ± 0.028	497.2 ± 5	852 ± 10	1.056 ± 0.005
ASZ1	3.60 ± 0.028	474.2 ± 5	802 ± 10	1.026 ± 0.005
ASZ2	3.66 ± 0.033	508.8 ± 5	987 ± 10	1.444 ± 0.005

**Table 8.2.2.2.** Variation of Fe oxidation state and coordination in base, intermediate and hybrid glass compositions.

Glass Composition	Proportion of Fe <sup>3+</sup> (Fe <sup>3+</sup> / ΣFe)	Fe <sup>3+</sup> Dipole Shift (mms <sup>-1</sup> )	Fe <sup>3+</sup> Quad. Shift (mms <sup>-1</sup> )	Fe <sup>3+</sup> Coordination
AS0	0.952 ± 0.02	0.297 ± 0.05	0.883 ± 0.05	6 fold
ASB	0.945 ± 0.02	0.312 ± 0.05	0.921 ± 0.05	6 fold
ASZ	1.0 ± 0.02	0.460 ± 0.05	1.630 ± 0.05	6 fold
ASZ1	0.974 ± 0.02	0.462 ± 0.05	1.504 ± 0.05	6 fold
ASZ2	0.971 ± 0.02	0.439 ± 0.05	1.556 ± 0.05	6 fold

### 8.2.3 Chapter 3.3

**Table 8.2.3.1** Variation in glass properties over Li<sub>2</sub>O / (Na<sub>2</sub>O + Li<sub>2</sub>O) composition range.

Li <sub>2</sub> O/ (Na <sub>2</sub> O + \Li <sub>2</sub> O) Ratio	Density (gcm <sup>-3</sup> )	Tg Onset (°C)	Tliq (°C)	Log viscosity at 1100 °C (Log(η/dPas))	Average Q <sup>n</sup> speciation
1.00	2.46 ± 0.01	488 ± 5	-	1.70 ± 0.1	2.50 ± 0.02
0.75	2.52 ± 0.01	480 ± 5	879 ± 10	1.76 ± 0.1	2.48 ± 0.02
0.50	2.53 ± 0.01	480 ± 5	702 ± 10	1.71 ± 0.1	2.52 ± 0.02
0.25	2.57 ± 0.01	503 ± 5	597 ± 10	1.79 ± 0.1	2.52 ± 0.02
0.00	2.59 ± 0.01	544 ± 5	555 ± 10	1,69 ± 0.1	2.58 ± 0.02

**Table 8.2.3.2** Variation in glass properties over Al<sub>2</sub>O<sub>3</sub> replacement series.

Glass Composition	Density (gcm <sup>-3</sup> )	Tg Onset (°C)	Tliq (°C)	Log viscosity at 1400 °C (Log(η/dPas))
CA0 (Base)	2.91 ± 0.01	770 ± 5	1349 ± 10	0.98 ± 0.1
CF0	3.14 ± 0.01	716 ± 5	1302 ± 10	0.49 ± 0.1
CMn0	3.05 ± 0.01	749 ± 5	1348 ± 10	0.49 ± 0.1

**Table 8.2.3.3** Variation in glass properties over CaO replacement series.

Glass Composition	Density (gcm <sup>-3</sup> )	T <sub>g</sub> Onset (°C)	T <sub>liq</sub> (°C)	Average Q <sup>n</sup> speciation
<b>CA0 (Base)</b>	2.91 ± 0.01	771 ± 5	1349 ± 10	2.16 ± 0.25
<b>CAS0.1</b>	2.97 ± 0.01	774 ± 5	1282 ± 10	2.27 ± 0.25
<b>CAS0.25</b>	3.12 ± 0.01	776 ± 5	1278 ± 10	2.30 ± 0.25
<b>CAZ0.1</b>	3.31 ± 0.01	686 ± 5	1250 ± 10	2.46 ± 0.25

#### 8.2.4 Chapter 4.1

**Table 8.2.4.1** Variation in density across initial waste-loading series.

Waste-Loading (wt%)	Density (gcm <sup>-3</sup> )		
	AS0	AB0	CA0
<b>Base Glass</b>	3.42 ± 0.03	2.53 ± 0.03	2.91 ± 0.03
<b>10</b>	3.4 ± 0.03	2.56 ± 0.03	2.92 ± 0.03
<b>20</b>	3.39 ± 0.03	2.54 ± 0.03	2.91 ± 0.03
<b>30</b>	3.37 ± 0.03	2.57 ± 0.03	2.91 ± 0.03
<b>40</b>	3.33 ± 0.03	2.59 ± 0.03	2.89 ± 0.03
<b>50</b>	3.23 ± 0.03	2.45 ± 0.03	2.88 ± 0.03

**Table 8.2.4.2.** Variation in T<sub>g</sub> onset across initial waste-loading series.

Waste-Loading (wt%)	T <sub>g</sub> Onset (°C)		
	AS0	AB0	CA0
<b>Base Glass</b>	491 ± 5	480 ± 5	771 ± 5
<b>10</b>	482 ± 5	469 ± 5	774 ± 5
<b>20</b>	472 ± 5	462 ± 5	770 ± 5
<b>30</b>	467 ± 5	457 ± 5	763 ± 5
<b>40</b>	466 ± 5	461 ± 5	761 ± 5
<b>50</b>	465 ± 5	460 ± 5	750 ± 5

**Table 8.2.4.3.** Variation in SO<sub>3</sub> content across initial waste-loading series.

Waste-Loading (wt%)	SO <sub>3</sub> Content (mol%)		
	AS0	AB0	CA0
Base Glass	0.29 ± 0.1	0.12 ± 0.1	0.16 ± 0.1
10	0.82 ± 0.1	0.26 ± 0.1	0.12 ± 0.1
20	1.42 ± 0.1	0.33 ± 0.1	0.10 ± 0.1
30	2.02 ± 0.1	0.44 ± 0.1	0.15 ± 0.1
40	2.11 ± 0.1	0.39 ± 0.1	0.24 ± 0.1
50	2.02 ± 0.1	0.11 ± 0.1	0.21 ± 0.1

**Table 8.2.4.4** Variation in Al<sub>2</sub>O<sub>3</sub> content across initial waste-loading series.

Waste-Loading (wt%)	Al <sub>2</sub> O <sub>3</sub> Content (mol%)		
	AS0	AB0	CA0
Base Glass	0.47 ± 0.1	0.40 ± 0.1	5.22 ± 0.1
10	0.85 ± 0.1	1.16 ± 0.1	6.78 ± 0.1
20	0.92 ± 0.1	1.27 ± 0.1	7.13 ± 0.1
30	1.34 ± 0.1	1.27 ± 0.1	7.86 ± 0.1
40	2.85 ± 0.1	2.22 ± 0.1	8.85 ± 0.1
50	3.73 ± 0.1	3.36 ± 0.1	9.99 ± 0.1

**Table 8.2.4.5** Variation Fe<sup>3+</sup> in glasses AS0 and AB0 across initial waste-loading series.

Waste-Loading (wt%)	Proportion of Fe <sup>3+</sup> (Fe <sup>3+</sup> /ΣFe)	
	AS0	AB0
10	0.97 ± 0.02	1.00 ± 0.02
30	0.39 ± 0.02	0.97 ± 0.02
50	0.51 ± 0.02	0.11 ± 0.02

**Table 8.2.4.6.** Variation in density upon waste-loading with 15 wt% and 30 wt%.

Composition	Density (gcm <sup>-3</sup> )		
	Base	15 wt%	30 wt%
<b>AB0</b>	2.53 ± 0.01	3.51 ± 0.01	2.55 ± 0.01
<b>CA0</b>	2.91 ± 0.01	3.50 ± 0.01	2.90 ± 0.01
<b>CF0</b>	3.14 ± 0.01	3.54 ± 0.01	3.01 ± 0.01
<b>AS0</b>	3.42 ± 0.01	3.62 ± 0.01	3.41 ± 0.01
<b>ASB</b>	3.54 ± 0.01	3.55 ± 0.01	3.53 ± 0.01
<b>ASZ</b>	3.50 ± 0.01	2.92 ± 0.01	3.46 ± 0.01
<b>ASZ1</b>	3.60 ± 0.01	3.10 ± 0.01	3.60 ± 0.01
<b>ASZ2</b>	3.66 ± 0.01	3.38 ± 0.01	3.63 ± 0.01

**Table 8.2.4.7.** Variation in T<sub>liq</sub> upon waste-loading at 15 wt% and 30 wt%.

Composition	T <sub>liq</sub> (°C)		
	Base	15 wt%	30 wt%
<b>AB0</b>	702 ± 10	790 ± 10	810 ± 10
<b>CA0</b>	1349 ± 10	1291 ± 10	1257 ± 10
<b>CF0</b>	1302 ± 10	1290 ± 10	1335 ± 10
<b>AS0</b>	962 ± 10	990 ± 10	1011 ± 10
<b>ASB</b>	890 ± 10	915 ± 10	967 ± 10
<b>ASZ</b>	852 ± 10	893 ± 10	1030 ± 10
<b>ASZ1</b>	802 ± 10	892 ± 10	1048 ± 10
<b>ASZ2</b>	987 ± 10	995 ± 10	1026 ± 10

**Table 8.2.4.8.** Variation in T<sub>g</sub> onset upon waste-loading at 15 wt% and 30 wt%.

Composition	T <sub>g</sub> Onset (°C)		
	Base	15 wt%	30 wt%
<b>AB0</b>	480 ± 5	479 ± 5	479 ± 5
<b>CA0</b>	770 ± 5	769 ± 5	762 ± 5
<b>CF0</b>	715 ± 5	707 ± 5	705 ± 5
<b>AS0</b>	491 ± 5	479 ± 5	474 ± 5
<b>ASB</b>	494 ± 5	478 ± 5	478 ± 5
<b>ASZ</b>	497 ± 5	478 ± 5	478 ± 5
<b>ASZ1</b>	474 ± 5	470 ± 5	473 ± 5
<b>ASZ2</b>	509 ± 5	496 ± 5	471 ± 5

**Table 8.2.4.9.** Calculated retention of Cs and S in all waste-loaded samples. *Italic values indicate values were samples were contaminated with phase separated material.*

Composition	SO <sub>3</sub> Retention (Retained SO <sub>3</sub> / Loaded SO <sub>3</sub> )		Cs <sub>2</sub> O Retention (Retained Cs <sub>2</sub> O / Loaded Cs <sub>2</sub> O)	
	15 wt% Load	30 wt% Load	15 wt% Load	30 wt% Load
<b>AB0</b>	4.9 ± 0.2 %	<i>62.5 ± 3.1 %</i>	73.2 ± 3.7 %	<i>98.4 ± 4.9 %</i>
<b>CA0</b>	2.4 ± 0.1 %	<i>40.1 ± 2.0 %</i>	70.9 ± 3.5 %	<i>33.5 ± 1.7 %</i>
<b>CF0</b>	2.6 ± 0.1 %	11.6 ± 0.6 %	68.6 ± 3.4 %	81.3 ± 4.1 %
<b>AS0</b>	31.9 ± 1.6 %	<i>41.5 ± 2.0 %</i>	78.9 ± 3.9 %	<i>66.3 ± 3.3 %</i>
<b>ASB</b>	42.4 ± 2.1 %	<i>55.4 ± 2.8 %</i>	72.1 ± 3.6 %	<i>62.1 ± 3.1 %</i>
<b>ASZ</b>	58.0 ± 2.9 %	<i>55.5 ± 2.8 %</i>	78.9 ± 3.9 %	63.7 ± 3.2 %
<b>ASZ1</b>	39.2 ± 2.0 %	84.0 ± 4.2 %	64.3 ± 3.2 %	98.2 ± 4.9 %
<b>ASZ2</b>	16.1 ± 0.8 %	34.0 ± 1.7 %	77.8 ± 3.9 %	66.3 ± 3.3 %

**Table 8.2.4.10.** Intensity of 400 cm<sup>-1</sup> and 990 cm<sup>-1</sup> Raman bands in 15 wt% and 30 wt% waste-loaded waste-forms.

Composition	Normalised Proportion of 400 cm <sup>-1</sup> band.		Normalised Proportion of 990 cm <sup>-1</sup> band.	
	15 wt% Load	30 wt% Load	15 wt% Load	30 wt% Load
<b>AB0</b>	0.00 ± 0.00	0.00 ± 0.00	0.00 ± 0.00	0.00 ± 0.00
<b>CA0</b>	0.00 ± 0.00	0.43 ± 0.02	0.00 ± 0.00	0.00 ± 0.00
<b>CF0</b>	0.02 ± 0.00	0.41 ± 0.02	0.00 ± 0.00	0.00 ± 0.00
<b>AS0</b>	0.00 ± 0.00	0.77 ± 0.04	1.00 ± 0.05	0.31 ± 0.02
<b>ASB</b>	0.00 ± 0.00	0.40 ± 0.02	0.97 ± 0.05	0.00 ± 0.00
<b>ASZ</b>	0.00 ± 0.00	0.65 ± 0.03	0.83 ± 0.04	0.44 ± 0.02
<b>ASZ1</b>	0.00 ± 0.00	1.00 ± 0.05	0.91 ± 0.04	0.00 ± 0.00
<b>ASZ2</b>	0.07 ± 0.00	0.81 ± 0.04	0.22 ± 0.01	0.00 ± 0.00

**Table 8.2.4.11.** Proportion of Fe<sup>3+</sup> (Fe<sup>3+</sup>/ΣFe) in 15 wt% and 30 wt% waste-loaded waste-forms.

Composition	Proportion of Fe <sup>3+</sup> (Fe <sup>3+</sup> /ΣFe)		
	0 wt% Load	15 wt% Load	30 wt% Load
<b>AB0</b>	1.00 ± 0.02	0.98 ± 0.02	0.96 ± 0.02
<b>CF0</b>	0.97 ± 0.02	0.74 ± 0.02	0.11 ± 0.02
<b>AS0</b>	0.97 ± 0.02	0.84 ± 0.02	0.39 ± 0.02
<b>ASB</b>	0.96 ± 0.02	0.79 ± 0.02	0.25 ± 0.02
<b>ASZ</b>	1.00 ± 0.02	0.85 ± 0.02	0.23 ± 0.02
<b>ASZ1</b>	1.00 ± 0.02	0.89 ± 0.02	0.18 ± 0.02
<b>ASZ2</b>	1.00 ± 0.02	0.91 ± 0.02	0.21 ± 0.02

**Table 8.2.4.12.** Variation in SO<sub>3</sub> incorporation in waste-forms in comparison to cation field strength index.

Glass	Cation Field Index	SO <sub>3</sub> content (mol%)	
		15 wt%	30wt%
<b>AB0</b>	1.28 ± 0.02	0.07 ± 0.02	1.84 ± 0.38
<b>CA0</b>	0.88 ± 0.02	0.03 ± 0.01	1.05 ± 0.20
<b>CF0</b>	0.87 ± 0.02	0.04 ± 0.01	0.29 ± 0.07
<b>AS0</b>	0.97 ± 0.02	0.52 ± 0.10	1.39 ± 0.28
<b>ASB</b>	0.97 ± 0.02	0.73 ± 0.14	1.94 ± 0.40
<b>ASZ</b>	0.97 ± 0.02	0.97 ± 0.20	1.87 ± 0.38
<b>ASZ1</b>	0.96 ± 0.02	0.68 ± 0.14	3.01 ± 0.60
<b>ASZ2</b>	1.01 ± 0.02	0.28 ± 0.07	1.23 ± 0.30

## 8.2.5 Chapter 4.2

**Figure 8.2.5.1** Release in all measured elements from the AS0 glass over time and temperature. All elements measured in ppm.

Time (min)	Temperature (°C)	Al	B	Ba	Ca	Fe	Li	Na	S	Si	Cs
0	0	0.00	0.00	0.00	0.00	0.00	0.00	0.00	0.00	0.00	0.00
91	455	0.02	1.11	0.23	0.04	0.10	0.02	0.14	48	0.10	0.14
104	520	0.10	0.06	0.01	0.07	0.02	0.00	0.11	14200	0.23	0.14
115	570	0.06	0.03	0.00	0.03	0.01	0.00	0.08	8560	0.04	0.07
130	640	0.05	0.03	0.00	0.03	0.01	0.00	0.08	4380	0.19	0.01
146	720	0.02	0.02	0.00	0.02	0.00	0.00	0.04	301	0.07	0.04
160	795	0.03	0.16	0.01	0.03	0.02	0.00	0.06	1440	0.33	0.60
170	850	0.02	0.02	0.00	0.00	0.00	0.00	0.03	550	0.22	0.02
180	900	0.02	0.03	0.00	0.01	0.00	0.00	0.02	594	0.13	0.03
190	950	0.03	0.03	0.00	0.01	0.00	0.00	0.05	828	0.12	0.36
202	1010	0.02	0.03	0.00	0.02	0.00	0.00	0.05	479	0.10	0.44
220	1100	0.03	0.24	0.00	0.01	0.01	0.00	0.04	469	0.14	2.11
240	1200	0.03	0.95	0.00	0.01	0.02	0.00	0.05	470	0.09	10.99
260	1200	0.08	1.33	0.01	0.02	0.02	0.00	0.08	10100	0.18	16.62
280	1200	0.02	0.82	0.00	0.01	0.00	0.00	0.03	488	0.08	8.40
300	1200	0.02	0.56	0.00	0.00	0.00	0.00	0.02	375	0.08	5.25
320	1200	0.02	0.80	0.00	0.01	0.03	0.01	0.09	16	0.07	8.98
340	1200	0.03	0.44	0.00	0.01	0.00	0.00	0.06	727	0.12	3.74
360	1200	0.04	0.29	0.00	0.01	0.00	0.00	0.07	2400	0.05	2.54
380	1200	0.04	0.04	0.00	0.01	0.00	0.00	0.06	1870	0.09	0.26
400	1200	0.01	0.00	0.00	0.00	0.00	0.00	0.00	0.00	0.00	0.00
420	1200	0.02	0.02	0.00	0.01	0.00	0.00	0.03	840	0.05	0.03

**Figure 8.2.5.2** Release in all measured elements from the AB0 glass over time and temperature. All elements measured in ppm.

Time (min)	Temperature (°C)	Al	B	Ba	Ca	Fe	Li	Na	S	Si	Cs
0	0	0.00	0.00	0.00	0.00	0.00	0.00	0.00	0	0.00	0.00
74	370	0.01	0.04	0.00	0.00	0.00	0.00	0.02	1	0.03	0.04
84	420	0.01	0.03	0.00	0.00	0.00	0.00	0.00	22	0.05	0.02
94	470	0.06	0.02	0.00	0.01	0.00	0.00	0.08	5290	0.02	0.02
104	520	0.07	0.01	0.01	0.01	0.00	0.00	0.09	7820	0.08	0.01
114	570	0.07	0.01	0.00	0.01	0.00	0.00	0.09	8960	0.07	0.22
124	620	0.07	0.01	0.00	0.01	0.00	0.00	0.09	10100	0.06	0.04
134	670	0.06	0.01	0.00	0.01	0.00	0.00	0.10	6760	0.03	0.01
144	720	0.03	0.01	0.00	0.01	0.00	0.00	0.08	2080	0.09	0.01
164	820	0.05	0.08	0.00	0.02	0.00	0.00	0.10	4650	0.03	0.02
184	920	0.04	0.04	0.00	0.01	0.02	0.00	0.07	111	0.05	0.02
204	1020	0.04	0.05	0.00	0.01	0.00	0.00	0.07	893	0.02	0.05
226	1130	0.03	0.25	0.00	0.01	0.01	0.00	0.05	1900	0.08	1.43
246	1200	0.02	0.32	0.00	0.00	0.00	0.00	0.03	103	0.02	3.57
266	1200	0.02	0.73	0.00	0.00	0.00	0.00	0.04	605	0.05	9.34
286	1200	0.03	0.38	0.00	0.00	0.00	0.00	0.05	1620	0.02	4.81
306	1200	0.04	0.19	0.00	0.01	0.00	0.00	0.06	4050	0.06	2.18
326	1200	0.08	0.13	0.00	0.02	0.00	0.00	0.08	16100	0.02	1.51
346	1200	0.02	0.17	0.00	0.01	0.00	0.00	0.05	1150	0.03	1.19
366	1200	0.02	0.13	0.09	0.03	0.01	0.01	0.04	33	0.03	0.73
386	1200	0.03	0.11	0.00	0.01	0.00	0.00	0.05	1860	0.04	0.67
406	1200	0.03	0.04	0.05	0.03	0.01	0.01	0.07	205	0.02	0.43
426	1200	0.02	0.02	0.00	0.01	0.00	0.00	0.03	560	0.03	0.10

## 8.2.6 Chapter 5.1

**Figure 8.2.6.1** Young's Modulus of control and irradiated glasses.

Glass	Youngs Modulus (GPa)		
	0 MGy	4 MGy	8 MGy
AB1	85.0 ± 9.9	82.2 ± 9.4	82.3 ± 9.5
AS0	85.2 ± 10.1	85.1 ± 10.2	86.0 ± 10.1
AB0	83.5 ± 9.7	82.0 ± 9.5	83.3 ± 9.9
MW	85.8 ± 10.2	86.7 ± 10.7	86.9 ± 9.9

**Figure 8.2.6.2** Shear Modulus of control and irradiated glasses.

Glass	Shear Modulus (GPa)		
	0 MGy	4 MGy	8 MGy
AB1		33.3 ± 5.1	32.8 ± 5.6
AS0	33.6 ± 6.2		33.9 ± 6.0
AB0	33.6 ± 5.6	33.1 ± 6.0	33.6 ± 6.2
MW	34.9 ± 6.1		34.3 ± 5.4

**Figure 8.2.6.3** Poisson's ratio of control and irradiated glasses.

Glass	Poisson's Ratio		
	0 MGy	4 MGy	8 MGy
AB1		0.23 ± 0.06	0.26 ± 0.07
AS0	0.27 ± 0.08		0.27 ± 0.08
AB0	0.24 ± 0.07	0.24 ± 0.07	0.24 ± 0.07
MW	0.23 ± 0.07		0.27 ± 0.07

**Figure 8.2.6.4** Hardness of control and irradiated glasses.

Glass	Hardness (GPa)		
	0 MGy	4 MGy	8 MGy
AB1	6.47 ± 0.58	6.33 ± 0.55	6.44 ± 0.58
AS0	6.23 ± 0.56	6.26 ± 0.55	6.10 ± 0.55
AB0	6.69 ± 0.58	6.51 ± 0.59	6.53 ± 0.58
MW	6.87 ± 0.63	7.16 ± 0.62	7.08 ± 0.69

**Figure 8.2.6.5** Fracture Toughness of control and irradiated glasses.

Glass	Fracture Toughness (MNm <sup>-3/2</sup> )		
	0 MGy	4 MGy	8 MGy
AB1	1.0 ± 0.2	1.1 ± 0.2	0.9 ± 0.1
AS0	0.7 ± 0.2	0.8 ± 0.2	0.7 ± 0.2
AB0	1.0 ± 0.1	1.1 ± 0.1	1.1 ± 0.1
MW	1.3 ± 0.2	1.4 ± 0.3	1.4 ± 0.3

**Figure 8.2.6.6** Variation in 400 cm<sup>-1</sup> Raman band area between control and irradiated glasses.

Glass	Percentage Band Area (%)		
	0 MGy	4 MGy	8 MGy
AB1	3.23 ± 0.8	2.56 ± 0.8	2.64 ± 0.8
AS0	16.27 ± 0.8	3.66 ± 0.8	5.33 ± 0.8
AB0	2.72 ± 0.8	3.77 ± 0.8	3.60 ± 0.8

**Figure 8.2.6.7** Fe<sup>3+</sup> content variation between control and irradiated glasses.

Glass	Fe <sup>3+</sup> Content (Fe <sup>3+</sup> /ΣFe)		
	0 MGy	4 MGy	8 MGy
AB1	0.43 ± 0.2	0.49 ± 0.2	0.45 ± 0.2
AS0	0.71 ± 0.2	0.75 ± 0.2	0.74 ± 0.2
AB0	0.49 ± 0.2	0.50 ± 0.2	0.49 ± 0.2

**Figure 8.2.6.8** Variation in Fe dipole and quadrupole shift in control and irradiated glasses.

Glass	Radiation Dose	Fe <sup>3+</sup>		Fe <sup>2+</sup>	
		Dipole Shift (mm/s)	Quadrupole Shift (mm/s)	Dipole Shift (mm/s)	Quadrupole Shift (mm/s)
AB1	0 MGy	0.33 ± 0.02	0.83 ± 0.02	0.96 ± 0.02	2.07 ± 0.02
	4 MGy	0.33 ± 0.02	0.84 ± 0.02	0.97 ± 0.02	2.06 ± 0.02
	8 MGy	0.33 ± 0.02	0.84 ± 0.02	0.96 ± 0.02	2.08 ± 0.02
AS0	0 MGy	0.38 ± 0.02	0.93 ± 0.02	0.97 ± 0.02	2.01 ± 0.02
	4 MGy	0.40 ± 0.02	0.96 ± 0.02	0.96 ± 0.02	2.02 ± 0.02
	8 MGy	0.37 ± 0.02	0.83 ± 0.02	0.99 ± 0.02	2.02 ± 0.02
AB0	0 MGy	0.36 ± 0.02	0.82 ± 0.02	0.94 ± 0.02	2.13 ± 0.02
	4 MGy	0.36 ± 0.02	0.83 ± 0.02	0.93 ± 0.02	2.16 ± 0.02
	8 MGy	0.34 ± 0.02	0.83 ± 0.02	0.94 ± 0.02	2.13 ± 0.02
MW-25%	0 MGy	0.28 ± 0.02	1.15 ± 0.02		
	4 MGy	0.30 ± 0.02	1.05 ± 0.02		
	8 MGy	0.30 ± 0.02	1.06 ± 0.02		

**Figure 8.2.6.9** S<sup>2-</sup> content variation between control and irradiated glasses.

Glass	S <sup>2-</sup> Content (S <sup>2-</sup> /ΣS)		
	0 MGy	4 MGy	8 MGy
AB1	0.17 ± 0.04	0.20 ± 0.04	0.21 ± 0.04
AS0	0.49 ± 0.04	0.76 ± 0.04	0.22 ± 0.04
AB0	0.37 ± 0.05	0.47 ± 0.04	0.50 ± 0.05

## 8.2.7 Chapter 5.2

**Figure 8.2.7.1** Normalised Mass Loss for Si (gcm<sup>-2</sup>)

Time (days)	AS0	ASB	ASZ	ASZ1	ASZ2	AB0	ABM	CA0	CF0
3	0.127	0.129	0.060	0.082	0.074	0.866	0.828	0.063	0.043
7	0.138	0.140	0.089	0.107	0.107	1.196	1.181	0.064	0.049
14	0.153	0.152	0.109	0.145	0.141	1.296	1.280	0.064	0.054
21	0.163	0.160	0.125	0.164	0.154	1.338	1.297	0.065	0.057
28	0.166	0.167	0.148	0.187	0.167	1.444	1.319	0.063	0.059

**Figure 8.2.7.2** Normalised Mass Loss for Al ( $\text{gcm}^{-2}$ )

<b>Time (days)</b>	<b>AS0</b>	<b>ASB</b>	<b>ASZ</b>	<b>ASZ1</b>	<b>ASZ2</b>	<b>CA0</b>
<b>3</b>	0.022	0.016	0.037	0.030	0.033	0.069
<b>7</b>	0.022	0.015	0.028	0.049	0.039	0.068
<b>14</b>	0.023	0.014	0.034	0.048	0.026	0.073
<b>21</b>	0.020	0.010	0.025	0.042	0.023	0.073
<b>28</b>	0.041	0.009	0.030	0.039	0.021	0.071

**Figure 8.2.7.3** Normalised Mass Loss for B ( $\text{gcm}^{-2}$ )

<b>Time (days)</b>	<b>AS0</b>	<b>ASB</b>	<b>ASZ</b>	<b>ASZ1</b>	<b>ASZ2</b>	<b>AB0</b>	<b>ABM</b>
<b>3</b>	0.262	0.187	0.063	0.111	0.069	4.177	4.896
<b>7</b>	0.320	0.227	0.103	0.132	0.106	5.571	5.897
<b>14</b>	0.336	0.224	0.143	0.197	0.143	6.507	6.651
<b>21</b>	0.390	0.258	0.170	0.206	0.161	7.206	7.259
<b>28</b>	0.357	0.261	0.204	0.224	0.177	8.039	8.081

**Figure 8.2.7.4** Normalised Mass Loss for Fe ( $\text{gcm}^{-2}$ )

<b>Time (days)</b>	<b>AS0</b>	<b>ASB</b>	<b>ASZ</b>	<b>ASZ1</b>	<b>ASZ2</b>	<b>AB0</b>	<b>ABM</b>	<b>CF0</b>
<b>3</b>	0.000	0.000	0.000	0.000	0.000	0.324	0.249	0.001
<b>7</b>	0.000	0.000	0.000	0.000	0.000	0.489	0.508	0.000
<b>14</b>	0.000	0.000	0.004	0.000	0.000	0.610	0.541	0.000
<b>21</b>	0.000	0.000	0.003	0.000	0.000	0.560	0.188	0.000
<b>28</b>	0.000	0.000	0.009	0.000	0.000	0.713	0.407	0.000

**Figure 8.2.7.5** Normalised Mass Loss for Na ( $\text{gcm}^{-2}$ )

<b>Time (days)</b>	<b>AS0</b>	<b>ASB</b>	<b>ASZ</b>	<b>ASZ1</b>	<b>ASZ2</b>	<b>AB0</b>	<b>ABM</b>
<b>3</b>	0.217	0.199	0.075	0.128	0.092	2.983	4.170
<b>7</b>	0.239	0.217	0.121	0.150	0.135	3.997	5.022
<b>14</b>	0.270	0.236	0.153	0.198	0.182	4.581	5.721
<b>21</b>	0.287	0.264	0.180	0.231	0.196	5.081	6.266
<b>28</b>	0.290	0.268	0.216	0.257	0.216	5.708	7.068

**Figure 8.2.7.6** Normalised Mass Loss for Li ( $\text{gcm}^{-2}$ )

<b>Time (days)</b>	<b>AS0</b>	<b>ASB</b>	<b>ASZ</b>	<b>ASZ1</b>	<b>ASZ2</b>	<b>AB0</b>	<b>ABM</b>
<b>3</b>	0.243	0.224	0.078	0.130	0.092	3.493	4.711
<b>7</b>	0.263	0.253	0.126	0.151	0.136	4.621	5.614
<b>14</b>	0.300	0.271	0.160	0.231	0.184	5.377	6.267
<b>21</b>	0.319	0.309	0.189	0.231	0.197	5.933	6.654
<b>28</b>	0.296	0.317	0.227	0.257	0.216	6.685	7.357

**Figure 8.2.7.7** Normalised Mass Loss for Ca ( $\text{gcm}^{-2}$ )

<b>Time (days)</b>	<b>AS0</b>	<b>ASB</b>	<b>ASZ</b>	<b>ASZ1</b>	<b>ASZ2</b>	<b>CA0</b>	<b>CF0</b>
<b>3</b>	0.091	0.080	0.040	0.191	0.068	0.044	0.033
<b>7</b>	0.100	0.100	0.077	0.269	0.106	0.047	0.035
<b>14</b>	0.108	0.092	0.110	0.324	0.159	0.049	0.036
<b>21</b>	0.112	0.092	0.127	0.345	0.199	0.051	0.038
<b>28</b>	0.118	0.085	0.156	0.402	0.205	0.055	0.039

**Figure 8.2.7.8** Normalised Mass Loss for Ba ( $\text{gcm}^{-2}$ )

<b>Time (days)</b>	<b>AS0</b>	<b>ASB</b>	<b>ASZ</b>	<b>ASZ1</b>	<b>ASZ2</b>
<b>3</b>	0.116	0.117	0.043	0.075	0.069
<b>7</b>	0.133	0.135	0.081	0.091	0.106
<b>14</b>	0.125	0.121	0.111	0.062	0.142
<b>21</b>	0.128	0.126	0.132	0.088	0.153
<b>28</b>	0.119	0.096	0.154	0.077	0.158

**Figure 8.2.7.9** Normalised Mass Loss for Zn ( $\text{gcm}^{-2}$ )

<b>Time (days)</b>	<b>ASZ</b>	<b>ASZ1</b>	<b>ASZ2</b>
<b>3</b>	0.00028	0.00022	0.00027
<b>7</b>	0.00029	0.00036	0.00041
<b>14</b>	0.00989	0.00032	0.00028
<b>21</b>	0.01079	0.00032	0.00054
<b>28</b>	0.01851	0.00034	0.00025

**Figure 8.2.7.10** Normalised Mass Loss for Si in waste-loaded samples ( $\text{gcm}^{-2}$ )

<b>Time (days)</b>	<b>AS0</b>	<b>ASB</b>	<b>ASZ1</b>	<b>ASZ2</b>
<b>3</b>	0.070	0.086	0.071	0.065
<b>7</b>	0.070	0.094	0.069	0.075
<b>14</b>	0.076	0.094	0.080	0.084
<b>21</b>	0.081	0.097	0.081	0.098
<b>28</b>	0.080	0.097	0.084	0.103

**Figure 8.2.7.11** Normalised Mass Loss for B in waste-loaded samples ( $\text{gcm}^{-2}$ )

<b>Time (days)</b>	<b>AS0</b>	<b>ASB</b>	<b>ASZ1</b>	<b>ASZ2</b>
<b>3</b>	0.089	0.113	0.082	0.071
<b>7</b>	0.090	0.124	0.085	0.084
<b>14</b>	0.098	0.125	0.094	0.096
<b>21</b>	0.109	0.142	0.097	0.116
<b>28</b>	0.103	0.144	0.102	0.118

**Figure 8.2.7.12** Normalised Mass Loss for Fe in waste-loaded samples ( $\text{gcm}^{-2}$ )

<b>Time (days)</b>	<b>AS0</b>	<b>ASB</b>	<b>ASZ1</b>	<b>ASZ2</b>
<b>3</b>	0.0007	0.0001	0.0004	0.0002
<b>7</b>	0.0001	0.0001	0.0007	0.0002
<b>14</b>	0.0001	0.0013	0.0002	0.0001
<b>21</b>	0.0001	0.0001	0.0001	0.0001
<b>28</b>	0.0002	0.0003	0.0001	0.0001

**Figure 8.2.7.13** Normalised Mass Loss for Na in waste-loaded samples ( $\text{gcm}^{-2}$ )

<b>Time (days)</b>	<b>AS0</b>	<b>ASB</b>	<b>ASZ1</b>	<b>ASZ2</b>
<b>3</b>	0.140	0.177	0.118	0.074
<b>7</b>	0.142	0.199	0.182	0.084
<b>14</b>	0.159	0.195	0.182	0.097
<b>21</b>	0.176	0.210	0.185	0.108
<b>28</b>	0.165	0.210	0.201	0.116

**Figure 8.2.7.14** Normalised Mass Loss for Li in waste-loaded samples ( $\text{gcm}^{-2}$ )

<b>Time (days)</b>	<b>AS0</b>	<b>ASB</b>	<b>ASZ1</b>	<b>ASZ2</b>
<b>3</b>	0.139	0.177	0.113	0.110
<b>7</b>	0.141	0.204	0.123	0.121
<b>14</b>	0.160	0.203	0.142	0.143
<b>21</b>	0.179	0.223	0.147	0.154
<b>28</b>	0.174	0.218	0.169	0.171

**Figure 8.2.7.15** Normalised Mass Loss for Ca in waste-loaded samples ( $\text{gcm}^{-2}$ )

<b>Time (days)</b>	<b>AS0</b>	<b>ASB</b>	<b>ASZ1</b>	<b>ASZ2</b>
<b>3</b>	0.076	0.175	0.138	0.155
<b>7</b>	0.075	0.206	0.166	0.187
<b>14</b>	0.084	0.216	0.146	0.250
<b>21</b>	0.085	0.231	0.184	0.256
<b>28</b>	0.087	0.206	0.207	0.286

**Figure 8.2.7.16** Normalised Mass Loss for Ba in waste-loaded samples ( $\text{gcm}^{-2}$ )

<b>Time (days)</b>	<b>AS0</b>	<b>ASB</b>	<b>ASZ1</b>	<b>ASZ2</b>
<b>3</b>	0.081	0.093	0.071	0.064
<b>7</b>	0.080	0.098	0.068	0.072
<b>14</b>	0.089	0.100	0.083	0.082
<b>21</b>	0.091	0.100	0.084	0.098
<b>28</b>	0.093	0.094	0.091	0.105

**Figure 8.2.7.17** Normalised Mass Loss for Zn in waste-loaded samples ( $\text{gcm}^{-2}$ )

<b>Time (days)</b>	<b>ASZ1</b>	<b>ASZ2</b>
<b>3</b>	0.0004	0.0001
<b>7</b>	0.0012	0.0002
<b>14</b>	0.0014	0.0002
<b>21</b>	0.0014	0.0003
<b>28</b>	0.0015	0.0004

**Figure 8.2.7.18** Normalised Mass Loss for S in waste-loaded samples ( $\text{gcm}^{-2}$ )

<b>Time (days)</b>	<b>AS0</b>	<b>ASB</b>	<b>ASZ1</b>	<b>ASZ2</b>
<b>3</b>	0.132	0.107	0.122	0.129
<b>7</b>	0.132	0.106	0.178	0.146
<b>14</b>	0.133	0.108	0.179	0.159
<b>21</b>	0.141	0.114	0.181	0.180
<b>28</b>	0.145	0.113	0.182	0.186